
A multi-technique hierarchical X-ray phase-based approach for the characterization and quantification of the effects of novel radiotherapies

Mariele Romano



München 2022

**A multi-technique hierarchical X-ray
phase-based approach for the charac-
terization and quantification of the ef-
fects of novel radiotherapies**

Mariele Romano

Dissertation
an der Fakultät für Physik
der Ludwig-Maximilians-Universität
München

vorgelegt von
Mariele Romano
aus Roma, Italy

München, den 15 Juni 2021

Erstgutachter/in: Prof. Dr. Paola Coan

Zweitgutachter/in: Prof. Dr. Guido Cavaletti

Tag der mündlichen Prüfung: 22. Juli 2021

*“Nothing in life is to be feared,
it is only to be understood.
Now is the time to understand more,
so that we may fear less.”*

Maria Skłodowska-Curie

Abstract

Cancer is the first or second leading cause of premature deaths worldwide with an overall rapidly growing burden. Standard cancer therapies include surgery, chemotherapy and radiotherapy (RT) and often a combination of the three is applied to improve the probability of tumour control. Standard therapy protocols have been established for many types of cancers and new approaches are under study especially for treating radio-resistant tumours associated to an overall poor prognosis, as for brain and lung cancers. Follow up techniques able to monitor and investigate the effects of therapies are important for surveying the efficacy of conventionally applied treatments and are key for accessing the curing capabilities and the onset of acute and late adverse effects of new therapies.

In this framework, this doctoral Thesis proposes the X-ray Phase Contrast Imaging - Computed Tomography (XPCI-CT) technique as an imaging-based tool to study and quantify the effects of novel RTs, namely Microbeam and Minibeam Radiation therapy (MRT and MB), and to compare them to the standard Broad Beam (BB) induced effects on brain and lungs. MRT and MB are novel radiotherapies that deliver an array of spatially fractionated X-ray beamlets issued from a synchrotron radiation source, with widths of tens or hundreds of micrometres, respectively. MRT and MB exploit the so-called dose-volume effect: hundreds of Grays are well tolerated by healthy tissues and show a preferential effect on tumour cells and vasculature when delivered in a micrometric sized micro-plane, while induce lethal effects if applied over larger uniform irradiation fields. Such highly collimated X-ray beams need a high-resolution and a full-organ approach that can visualize, with high sensitivity, the effects of the treatment along and outside the beamlets path. XPCI-CT is here suggested and proven as a powerful imaging technique able to determine and quantify the effects of the radiation on normal and tumour-bearing tissues. Moreover, it is shown as an effective technique to complement, with 3D information, the histology findings in the follow-up of the RT treatments.

Using a multi-scale and multi-technique X-ray-based approach, I have visualized and analysed the effects of RT delivery on healthy and glioblastoma multiforme (GBM)-bearing rat brains as well as on healthy rat lungs. *Ex-vivo* XPCI-CT datasets acquired with isotropic voxel sizes in the range $3.25^3 - 0.65^3 \mu\text{m}^3$ could distinguish, with high sensitivity, the idiopathic effects of MRT, MB and BB therapies. Histology, immunohistochemistry, Small- and Wide-Angle X-ray Scattering and X-ray Fluorescence experiments were also carried out to accurately interpret and complement the XPCI-CT findings as well as to obtain a detailed structural and chemical characterization of the detected pathological features. Overall, this multi-technique approach could detect: *i)* a different radio-sensitivity for the MRT-treated brain areas; *ii)* Ca and Fe deposits, hydroxyapatite crystals formation; *iii)* extended and isolated fibrotic contents. Full-organ XPCI-CT datasets allowed for the quantification of tumour and microcalcifications' volumes in treated brains and the amount of scarring tissue in irradiated lungs.

Herein, the role of XPCI-CT as a 3D virtual histology technique for the follow-up of *ex-vivo* RT effects has been assessed as a complementary method for an accurate volumetric investigation of normal and pathological states in brains and lungs, in a small animal model. Moreover, the technique is proposed as a guidance and auxiliary tool for conventional histology, which is the gold standard for pathological evaluations, owing to its 3D capabilities and the possibility of virtually navigating within samples. This puts a landmark for XPCI-CT inclusion in the pre-clinical studies pipeline and for advancing towards *in-vivo* XPCI-CT imaging of treated organs.

Zusammenfassung (abstract in German)

Weltweit gilt Krebs als häufigste bzw. zweithäufigste Ursache eines zu früh erfolgenden Todes, wobei die Zahlen rasch ansteigen. Standardmäßige Krebstherapien umfassen chirurgische Eingriffe, Chemotherapie und Strahlentherapie (radiotherapy, RT); oft kommt eine Kombination daraus zur Anwendung, um die Wahrscheinlichkeit der Tumorkontrolle zu erhöhen. Es wurden Standardtherapieprotokolle für zahlreiche Krebsarten eingerichtet und es wird vor allem in der Behandlung von strahlenresistenten Tumoren mit allgemein schlechter Prognose wie bei Hirn- und Lungentumoren an neuen Ansätzen geforscht. Nachverfolgungstechniken, welche die Auswirkungen von Therapien überwachen und ermitteln, sind zur Überwachung der Wirksamkeit herkömmlich angewandter Behandlungen wichtig und auch maßgeblich am Zugang zu den Fähigkeiten zur Heilung sowie zum Auftreten akuter und verzögerter Nebenwirkungen neuer Therapien beteiligt.

In diesem Rahmenwerk unterbreitet diese Doktorarbeit die Technik der Röntgen-Phasenkontrast-Bildgebung über Computertomographie (X-ray Phase Contrast Imaging - Computed Tomography, XPCI-CT) als bildverarbeitungsbasiertes Tool zur Untersuchung und Quantifizierung der Auswirkungen neuartiger Strahlentherapien, nämlich der Mikrobeam- und Minibeam-Strahlentherapie (MRT und MB), sowie zum Vergleich derselben mit den herkömmlichen durch Breitstrahlen (Broad Beam, BB) erzielten Auswirkungen auf Gehirn und Lunge. MRT und MB sind neuartige Strahlentherapien, die ein Array räumlich aufgeteilter Röntgenstrahlenbeamlets aus einer synchrotronen Strahlenquelle mit einer Breite von Zehnteln bzw. Hunderteln Mikrometern abgeben. MRT und MB nutzen den sogenannten Dosis-Volumen-Effekt: Hunderte Gray werden von gesundem Gewebe gut vertragen und wirken bei der Abgabe in einer Mikroebene im Mikrometerbereich vorrangig auf Tumorzellen und Blutgefäße, während sie bei einer Anwendung über größere gleichförmige Strahlungsfelder letale Auswirkungen aufweisen. Solche hoch kollimierten Röntgenstrahlen erfordern eine hohe Auflösung und einen Zugang zum gesamten Organ, bei dem die Auswirkungen der

Behandlung entlang und außerhalb der Beamletpfade mit hoher Empfindlichkeit visualisiert werden können. Hier empfiehlt und bewährt sich die XPCI-CT als leistungsstarke Bildverarbeitungstechnik, welche die Auswirkungen der Strahlung auf normale und tumortragende Gewebe feststellen und quantifizieren kann. Außerdem hat sich gezeigt, dass sie durch 3-D-Informationen eine effektive Technik zur Ergänzung der histologischen Erkenntnisse in der Nachverfolgung der Strahlenbehandlung ist.

Anhand eines mehrstufigen und multitechnischen röntgenbasierten Ansatzes habe ich die Auswirkungen der Strahlentherapie auf gesunde und von Glioblastomen (GBM) befallene Rattenhirne sowie auf gesunde Rattenlungen visualisiert und analysiert. Mit isotropen Voxelgrößen im Bereich von $3,5^3$ bis $0,65^3 \mu\text{m}^3$ erfasste *Ex-vivo*-XPCI-CT-Datensätze konnten die idiopathischen Auswirkungen der MRT-, MB- und BB-Behandlung mit hoher Empfindlichkeit unterscheiden. Es wurden auch Experimente zu Histologie, Immunhistochemie, Röntgenklein- und -weitwinkelstreuung und Röntgenfluoreszenz durchgeführt, um die XPCI-CT-Erkenntnisse präzise zu interpretieren und zu ergänzen sowie eine detaillierte strukturelle und chemische Charakterisierung der nachgewiesenen pathologischen Merkmale zu erhalten. Im Allgemeinen wurde durch diesen multitechnischen Ansatz Folgendes ermittelt: *i*) eine unterschiedliche Strahlenempfindlichkeit der mit MRT behandelten Gehirnbereiche; *ii*) Ca- und Fe-Ablagerungen und die Bildung von Hydroxylapatitkristallen; *iii*) ein ausgedehnter und isolierter Fibrosegehalt. XPCI-CT-Datensätze des gesamten Organs ermöglichten die Quantifizierung der Volume von Tumoren und Mikroverkalkungen in den behandelten Gehirnen und der Menge des Narbengewebes in bestrahlten Lungen.

Dabei wurde die Rolle der XPCI-CT als virtuelle 3-D-Histologietechnik für die Nachverfolgung von *Ex-vivo*-RT-Auswirkungen als ergänzende Methode für eine präzise volumetrische Untersuchung des normalen und pathologischen Zustands von Gehirnen und Lungen im Kleintiermodell untersucht. Darüber hinaus wird die Technik aufgrund ihrer 3-D-Fähigkeiten und der Möglichkeit zur virtuellen Navigation in den Proben als Leitfaden und Hilfstool für die herkömmliche Histologie vorgeschlagen, die der Goldstandard für die pathologische Evaluierung ist. Dies markiert einen Meilenstein für die Übernahme der

XPCI-CT in die Pipeline präklinischer Studien und für den Übergang zur *In-vivo*-XPCI-CT von behandelten Organen.

Table of contents

Abstract	VI
Zusammenfassung (abstract in German)	VIII
Table of contents	XII
Acknowledgements.....	1
List of abbreviations.....	3
Introduction: Thesis motivations and outline	5
1 Cancer statistics, therapies and follow-up techniques.....	9
1.1 Cancer statistics worldwide	9
1.2 Standard cancer therapies.....	11
1.2.1 X-ray radiotherapy	12
1.3 Novel radiation therapies: X-ray microbeam and minibeam radiation therapy.....	15
1.3.1 The lateral dose profile	18
1.3.2 The dose-volume effect.....	19
1.4 Imaging techniques for cancer follow-up.....	20
1.4.1 Brain follow-up techniques	21
1.4.2 Lung follow-up techniques	23
1.4.3 Histology as the gold standard for pathology assessment.....	24
1.4.4 XPCI-CT as a 3D virtual histology follow-up technique	26
2 X-ray scattering-based imaging modalities.....	29
2.1 Imaging with X-rays	30
2.1.1 X-ray absorption and phase contrast theory	30

2.1.2	Propagation-based X-ray Phase Contrast Imaging.....	34
2.1.3	Phase retrieval problem.....	41
2.1.4	X-ray Phase Contrast Computed Tomography.....	43
2.1.5	Applications of X-ray phase contrast imaging.....	46
2.1.6	X-ray sources for XPCI.....	47
2.2	Small and Wide-Angle X-ray Scattering.....	47
2.2.1	SAXS/WAXS profiles analysis	50
2.2.2	Applications of SAXS/WAXS.....	54
3	Irradiation experiments at the European Synchrotron.....	55
3.1	The European Synchrotron Radiation Facility	55
3.1.1	The ID17 biomedical beamline	57
3.2	The irradiation experimental procedures.....	59
3.2.1	The irradiation spectrum	61
3.2.2	The dosimetry procedure	62
3.2.3	Animal positioning and beam delivery.....	63
3.2.4	Animal follow-up after the irradiation and sample collection	69
3.3	Monte Carlo dose simulations	70
3.3.1	Simulation parameters definition.....	73
3.3.2	Choice of the radiotherapy protocols	75
3.3.3	Dose maps.....	77
4	X-ray imaging and scattering experiments.....	79
4.1	Sample preparation	79
4.1.1	Sample preparation for XPCI-CT	79
4.1.2	Sample preparation for histology and SAXS/WAXS.....	82
4.2	PB-XPCI-CT experiments.....	83
4.2.1	The tomography setup of ID17 - ESRF	83

4.2.2	The SLS TOMCAT PB-XPCI-CT setup	88
4.2.3	The PETRA III P05 PB-XPCI-CT setup	90
4.3	Histology and immunohistochemistry examination	92
4.4	SAXS/WAXS and XRF experiments	94
5	Image processing and volumetric data analysis	97
5.1	XPCI-CT image reconstruction	98
5.1.1	Phase retrieval optimization with the RMS contrast evaluation ..	102
5.2	Images post-processing	104
5.2.1	Artefacts correction	104
5.2.2	Stack piling and normalization	108
5.2.3	Maximum projection intensity	109
5.2.4	Local CT stitching	110
5.2.5	Data masking	111
5.3	Segmentation and quantification of the features of interest within the examined specimens	112
5.3.1	Threshold segmentation	112
5.3.2	Morphological watershed-based segmentation	115
5.3.3	Volume quantification of under-sampled 3D datasets	121
5.4	3D volume rendering	126
5.5	SAXS/WAXS data analysis	128
6	Characterization of the effects of BB, MRT and MB irradiations on rat brains 131	
6.1	Introduction	131
6.2	Dose maps for BB, MRT and MB brain irradiations	132
6.3	Radio-induced effects on healthy treated samples	134
6.4	Effects of spatially fractionated radiotherapy on glioblastoma-bearing animals	141

6.4.1	Survival curves.....	141
6.4.2	XPCI-CT: a multi-scale imaging approach	142
6.5	Quantitative analysis and 3D rendering.....	145
6.6	SAXS/WAXS and XRF study of microcalcifications	157
6.7	Discussion	163
6.7.1	Effects of treated healthy rat brains	163
6.7.2	Effects on GBM-bearing rat brains.....	164
6.7.3	Microcalcification study	165
6.7.4	A full 3D characterization and quantification of RT-induced effects 167	
6.8	Data exclusion from the study	168
6.9	Limitations of the study	169
6.10	Conclusions and future perspective.....	169
7	Evaluation of healthy lung alterations after BB, MRT and MB irradiation	171
7.1	Introduction	171
7.2	XPCI-CT for healthy rat lung anatomy.....	172
7.3	Dose maps for BB, MRT and MB irradiations	175
7.4	Imaging of the effects of MRT on lungs.....	177
7.5	Imaging of the effects of MB on lungs	181
7.6	Imaging of the effects of BB radiotherapy on lungs	185
7.7	Segmentation of the scarring tissue.....	187
7.8	Discussion	189
7.9	Limitations of the study	192
7.10	Conclusion and future perspectives.....	192
	Conclusions	193
	Bibliography	197
	Annexes.....	231

Annex 1: An ideal protocol for preclinical radiotherapy follow-up.....	231
Annex 2: List of publications produced within this Ph.D. work	233
Annex 3: list of oral talk and poster presentations related to this Thesis work	234

Acknowledgements

I would like to express my sincere gratitude to Prof. Dr. Paola Coan who supervised this Ph.D. project. I wish to thank her for being a great scientific guide, for always encouraging critical thinking and for her dedicated involvement in every step throughout this process. I would also acknowledge her for allowing me being part of a big and international group, for permitting me travelling around the world attending conferences and performing experimental sessions. No less important, I thank for her comprehension, support, kindness and trust accorded to me.

I offer my special thanks to Dr. Alberto Bravin who taught me how to run a synchrotron imaging experiment and who has always been a source of fruitful discussion and wise suggestions.

I am particularly grateful for the friendly assistance given by Dr. Alberto Mittone in many aspects of the practical realization of the experimental procedures at the ESRF.

I would also like to thank Alicia Eckhardt for her help in the data analysis; Luca Fardin for being always ready to help; Francesca di Lillo and Paolo Pellicoli for the nice moments we shared in Grenoble.

I would like also to thank all the people who collaborated to this project and in particular the ESRF, SLS, PETRA III, LMU, CNR, University of Bern and TUM co-workers for giving their precious contribution to this Ph.D. project.

This work would have been impossible without the support of the funding institutions: the German Research Foundation (DFG) and especially the GRK2274 Research Training Group, that I would like to acknowledge.

Acknowledgements

La mia più sincera gratitudine va ai miei genitori e a mia sorella Angela, base solida sulla quale ho sempre potuto appoggiarmi. Grazie per avermi amorevolmente accompagnata in questo percorso, soprattutto nei momenti più difficili.

Voglio inoltre ringraziare Elga, Aldo, Emilia Genangeli e Sergio Ciattaglia per avermi accolto a Monaco come parte della loro famiglia.

Infine, voglio ringraziare i miei amici per avermi dimostrato che l'affetto va oltre le distanze fisiche. Una menzione speciale la meritano Pauline, il mio punto fermo da sempre, Valerio che ha saputo essermi vicino esattamente nel modo in cui avevo bisogno e Maria Cristina che è sempre stata pronta a condividere con me momenti di svago, riflessioni e consigli. Non di minore importanza è stata la presenza di Claudio, Alis, Silvia, Luca, Andrea, Consuelo, Claudia ed Ilaria che voglio infinitamente ringraziare.

Semplicemente grazie,

Mariele

List of abbreviations

Acronym	Definition
1D	One-Dimension
2D	Two-Dimensions
3D	Three-Dimensions
ABI	Analyser-Based Imaging
AMG	Amygdala
AW	Adjusted Windowing
BB	Broad Beam
BFV	Blood Filled Vessel
BV	Blood Vessel
C.L.	Confidence Level
CNS	Central Nervous System
COR	Centre Of Rotation
CP	Caudate Putamen
c-t-c	Centre-To-Centre
CTX	Cortex
D	Day
DF	Dark Field
DNA	Deoxyribonucleic Acid
EBS	Extremely Brilliant Source
EH	Experimental Hutch
ESRF	European Synchrotron Radiation Facility
FBP	Filtered Back Projection
FFV	Formalin Filled Vessel
FOI	Field Of Irradiation
FReLON	Fast Readout Low Noise
FWHM	Full Width at Half Maximum
GBM	Glioblastoma Multiforme
Gd	Gadolinium
GFAP	Anti-glial Fibrillary Acidic Protein
GI	Grating Interferometric
H&E	Haematoxylin and Eosin
HAP	Hydroxyapatite
HIP	Hippocampus

List of abbreviations

HYP	Hypothalamus
ID	Insertion Device
LINAC	Linear Accelerator
LOR	Line Of Response
LUS	Light Ultrasound
MB	Minibeam Radiation Therapy
MCS	Monte Carlo Simulations
mcs	Microcalcifications
MIP	Maximum Intensity Projection
MRI	Magnetic Resonance Imaging
MRT	Microbeam Radiation Therapy
MSC	Multi-Slit Collimator
nec	Necrosis
NICE	Networked Interactive Computing Environment
PBI	Propagation-Based Imaging
PBS	Phosphate Buffered Saline
PB-XPCI-CT	Propagation-Based X-Ray Phase Contrast Imaging - Computed Tomography
PCA	Principal Component Analysis
PET	Positron Emission Tomography
PFA	Paraformaldehyde
PMMA	Polymethylmethacrylate
PVDR	Peak-to-Valley Dose Ratio
RMS	Root Mean Square
ROI	Region Of Interest
RT	Radiotherapy
SAXS	Small-Angle X-Ray Scattering
sCMOS	scientific Complementary Metal–Oxide–Semiconductor
SLS	Swiss Light Source
SPECT	Single Photon Emission Computed Tomography
SR	Synchrotron
TH	Thalamus
TIE	Transport of Intensity Equation
TRI	Masson-Goldner Trichrome
US	Ultrasound
WAXS	Wide-Angle X-Ray Scattering
WF	White Field
XPCI-CT	X-Ray Phase Contrast Imaging - Computed Tomography
XRF	X-Ray Fluorescence

Introduction: Thesis motivations and outline

This Thesis work has the aim of proposing a new imaging-based methodology for monitoring the effects of radiotherapy (RT), which can provide simultaneously improved sensitivity and detail in three-dimensions (3D) and thus fill the gaps of standardly used laboratory tools. The objective is to develop and test a method to depict and analyse anatomy, pathology and treatments with high spatial and contrast resolutions, without the need of staining media and with a multiscale approach allowing full organ-coverage and magnified sub-region investigation. Ultimately, the purpose is to establish an effective and complementary X-ray-based procedure for virtual 3D histology that can be included in the pipeline for pre-clinical examinations and that has the potential of being used in future preclinical and clinical studies.

At the time when I began this doctoral work, the main methods conventionally used in preclinical research as well as in clinical practice to investigate pathologies and the effects of RT treatments were, on one side, sample-destructive, two-dimensional (2D) and based on the use of staining agents as histology and immunohistochemistry, or, on the other side, based on imaging techniques that enable 3D full-organ visualization but characterized by limited sensitivity and/or spatial resolution. In this scenario, this Thesis proposes X-ray Phase Contrast Imaging - Computed Tomography (XPCI-CT) as a valuable imaging method to investigate in 3D, with high sensitivity and spatial resolution, the effects of novel RTs, namely Microbeam and Minibeam Radiation Therapy (MRT and MB), which are spatially fractionated RTs delivering highly collimated arrays of X-ray beamlets.

In this work I present original results obtained by applying innovative experimental and analysis methodologies based on the use of state-of-the-art XPCI-CT imaging setups installed at three different European synchrotron facilities, namely the European Synchrotron Radiation Facility (ESRF, Grenoble, France), the Swiss Light Source (SLS, Villigen, Switzerland) and PETRA III (Hamburg, Germany), with the purpose of: *i*) investigating the efficacy and side-effects of

MRT and MB and *ii*) comparing them to standard seamless broad beam (BB) RT. For the first time, the effects of MRT, MB and BB irradiations are investigated and quantified at high resolution with a full-organ-coverage approach on healthy and glioblastoma multiforme (GBM) bearing brains and on healthy lungs in a rat animal model. Histology and immunohistochemistry investigations were also performed to interpret and validate the XPCI-CT findings, while Small- and Wide-Angle X-ray Scattering (SAXS/WAXS) and X-ray Fluorescence (XRF) experiments were carried out to obtain a detailed structural and chemical characterization of the radiation-driven effects. The two target organs were chosen because of the high fatality for both lung and brain tumours and, specifically, because of the poor prognosis after GBM diagnosis and the high incidence rate of lung cancer. For these reasons, brain and lung tumours have a high medical relevance in the field of radio-oncology.

The outline of this doctoral Thesis is composed as follows:

Chapters 1-2 are dedicated to the presentation of the scientific background of the Thesis project and report on the up-to-date statistics of cancer burden, and the standardly used therapies and follow-up methods. XPCI-CT is introduced as a valuable tool for 3D virtual histology and the fundamentals of this imaging technique as well as of SAX/SWAXS are given.

In **Chapter 3** the treatment planning, via Monte Carlo Simulations (MCS), and the experimental details of small animal *in-vivo* irradiation of brains and lungs are explained. **Chapter 4** describes the experimental setups and parameters used in the synchrotron XPCI-CT imaging experiments, the histology and immunohistochemistry protocols as well as the details of synchrotron SAXS/WAXS and XRF measurements. **Chapter 5** lists and explains all the data analysis and processing tools applied and developed within the different projects of the work.

Chapter 6 reports the results of a study in which the multi-scale and multi-technique approach described in the previous chapters is used to investigate, classify and quantify the effects of MRT, MB and BB on healthy and GBM-bearing brains; **Chapter 7** presents the first application of spatially fractionated MRT and MB on healthy lungs and the detailed volumetric investigation of the radiation-driven effects on this tissue by 3D virtual histology in comparison to standard 2D lab-based histology.

Final remarks and recapitulation of the main results, future perspectives and the limitations of the studies are presented and are also given in the **Conclusions**. The outline of an ideal protocol for RT follow-up in pre-clinical investigations is given in **Annex 1**, while **Annex 2** lists the publications produced within this Ph.D. work and **Annex 3** gives the details of the oral talks and poster presentation held at international conferences.

Chapter 1

Cancer statistics, therapies and follow-up techniques

1.1 Cancer statistics worldwide

Noncommunicable diseases have become the leading cause of death worldwide and cancer is the first or second cause (after cardiovascular diseases) of premature death, at ages between 30 and 69 years, in 134 of 183 countries and it ranks third or fourth in other 45 countries (Wild, 2020; WHO, 2018)¹, as visible in Figure 1.1.

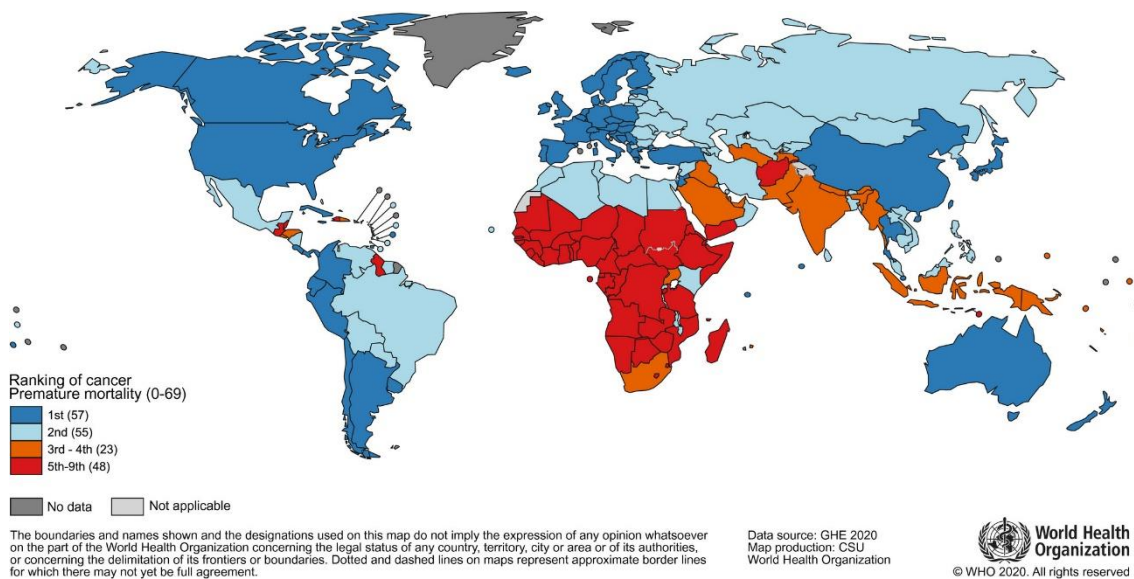


Figure 1.1: Global map of cancer ranking as a cause of premature death at ages of 30 – 69 years. Next to each ranking, the number of countries associated to that ranking is reported in parentheses. Image from (Sung, 2021).

Anyhow, cancer mortality trends strongly vary between countries and across specific cancer types due to the environment, lifestyle, exposure to known or supposed risk factors, available medical practices, infrastructures and so on. Indeed,

¹ COVID-19 does not appear as the leading cause of death worldwide in the recent years since about the 60% of the COVID-19 related deaths occurred in the age group over 80 years. Data from <https://www.euro.who.int>.

in most countries with high human development index, cancer mortality rates are declining, while in countries in transition, mortality rates are increasing or stabilizing (DeSantis, 2015; Siegel, 2014; Center, 2012). In 2020, one-half of all diagnosed cases and the 58.3% of cancer deaths occurred in Asia while e.g. Europe accounted for the 22.8% of the cases and 19.6% of the registered cancer deaths (Sung, 2021).

As visible in Figure 1.2 (data from (Sung, 2021)), the leading cancer incidence cases worldwide are breast, lung, colorectum and prostate cancers, while for deaths, lung cancer ranks first (18.0% of total deaths) and is followed by colorectum, liver and stomach cancers. Data for each sex are available too (see Figure 1.2c-d). Female breast cancer was in 2020 the first case of global tumour incidence overtaking lung cancer that was, in 2018, the overall first case of both global incidence and mortality (Bray, 2018).

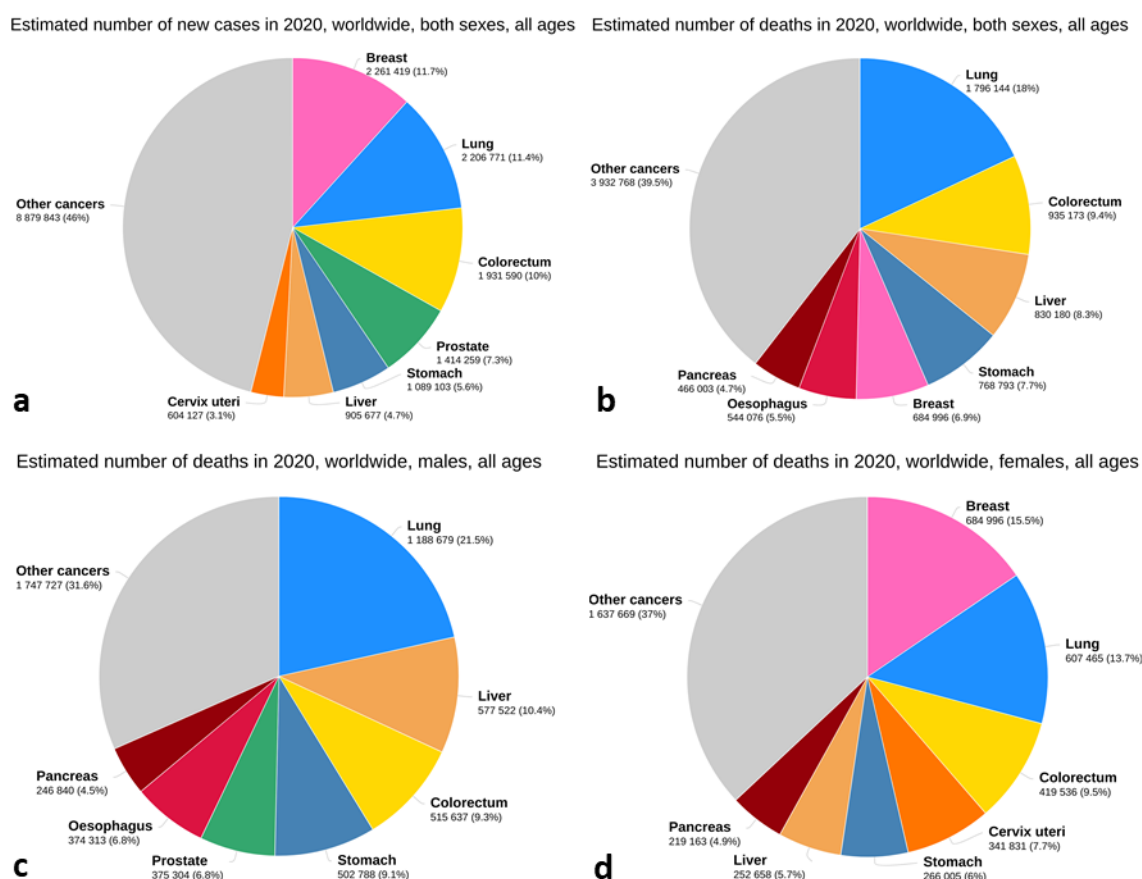


Figure 1.2: estimated number of cancer incidence (a) and deaths (b) for both sexes in 2020. Cancer deaths for men (c) and women (d) in 2020 for the different types of cancer. Each cancer type is associated with a specific colour. Graphs from <https://gco.iarc.fr/today> (accessed on 02.07.2021) and data from (Sung, 2021).

Lung tumour still remains the principal cause of cancer death representing approximately one in 10 cancers diagnosed and one in 5 deaths (Sung, 2021); incidence and mortality rates are about two times higher in men than in women, with occurrence reflecting the maturity of the tobacco epidemics among countries. Last, it has to be noted that patterns in lung cancer mortality are close to the one of the incidences because of the high fatality rate. Furthermore, several cancer types are radioresistant (e.g. gliomas and osteosarcomas) or the survival is still low when a combination of standard cancer therapies is applied. As an example, brain cancer and particularly GBM have a poor prognosis and a low long-term survival probability. Cancers of the central nervous system (CNS) ranked in 2020 as the 19th tumour case for incidence and 13th for fatality (Sung, 2021). Among all, GBM is the most common and aggressive intra-axial primary tumour, accounting for about 60% of the cases (Leao, 2020), and has a survival ranging from 7 months (Caiazzo, 2015) to 12-15 months (Delgado-Lopez, 2016; Witthayanuwat, 2018) with a long-term survival probability of about 3-5% (Furnari, 2007; Ostrom, 2018).

1.2 Standard cancer therapies

Cancer treatment involves medical procedures to control or remove primary or metastatic cancer tissue and preventing the recurrence or spread of the primary cancer. Cancer treatments can be divided into curative and palliative treatments that respectively aim at curing the tumour or reducing the tumour sizes and side effects by relieving symptoms and suffering. The main curing cancer treatments are surgery, chemotherapy and RT (Baskar, 2012; DeVita, 2008; Sullivan, 2015). Overall, a combination of treatments, called multimodal treatment, is often used in clinical routine to improve the likelihood of cure and to reduce healthy tissues damages (Wang, 2019a).

Surgery removes part or all of the cancerous tissue and a small amount of healthy tissue around the tumoral mass to obtain adequate margins. If needed, lymph nodes close to the tumour location can be removed too (Wang, 2019a). Surgery works well with localized cancers and as a first step of a multimodal treatment for non-localized tumours concurring to reduce the overall tumour mass (NCI, National Cancer Institute).

Chemotherapy is a systematic therapy that targets cells throughout the body using anti-cancer drugs to eradicate or control the growth of cancer by interfering with deoxyribonucleic acid (DNA) synthesis and mitosis and can be both used to sterilize the remaining tumour cells after surgery or RT or to shrink the tumour volume before surgery (DeVita, 2008). The main drawback is that chemotherapeutic drugs affect both healthy and cancerous cells causing toxicity to healthy tissues and side effects. However, healthy tissues are able to repair and chemotherapy effects result to be selective, with time, on the tumour.

RT uses ionizing radiations such as X-rays, gamma rays, protons and other radiation types to sterilize cancer by damaging cells and causing reactions that will lead to the cell death. More precisely the DNA of cells is either directly or indirectly damaged, mainly through the formation of free-radicals, leading to damages such as the generation of abasic sites, single and double strand breaks (Baskar, 2012). As chemotherapy, the delivered radiation acts on both cancer and surrounding healthy cells, thus early or late side effects are possible after RT sessions. Therefore, **accurate treatment plans have to be developed and set for each patient to avoid vital organ irradiation and to protect as much as possible healthy tissues from irradiation.**

1.2.1 X-ray radiotherapy

X-ray RT can be divided into two main categories: external beam radiotherapy and brachytherapy, where the radiation source is placed at a certain distance from the patient or is at direct contact with the tumour volume, respectively. The most common photon sources used in radiation oncology are X-ray tubes, linear accelerators (LINACs) and teletherapy radioisotopes (Baskar, 2012).

The X-ray dose deposition within a tissue-equivalent phantom or a patient is reported in Figure 1.3 as a function of depth and it results from the superimposition of the X-ray beam attenuation as the inverse square law (as it would undergo in vacuum) and the attenuation and scattering experienced within the traversed tissues (Podgorsak, 2005). The X-ray beam enters the patient and delivers to the entrance surface a small percentage of the maximum deposited dose. This effect is called skin-sparing effect and avoids provoking severe damages to the skin of the patient when treated with X-rays. Photons scattered from the collimators and air, backscattered from the patient and high energy electrons produced in the

vicinity of the patient contribute to the surface dose. Beneath the entrance surface, the dose rises rapidly (buildup region), reaches the maximum value and then decreases almost exponentially. The buildup region results from the (relatively) long range of secondary charged particles that are produced after X-ray interactions that deposit their kinetic energy in the target. The higher the X-ray beam energy, the deeper the position of the maximum dose is (Parsai, 2008) because of the higher penetrating power of the secondary charged particles. The dose delivered at the beam exit point causes the dose-depth curve to slightly curve downwards due to the missing scattering contribution from points beyond the tissue (Podgorsak, 2005). This is a minor effect and is not reported in Figure 1.3.

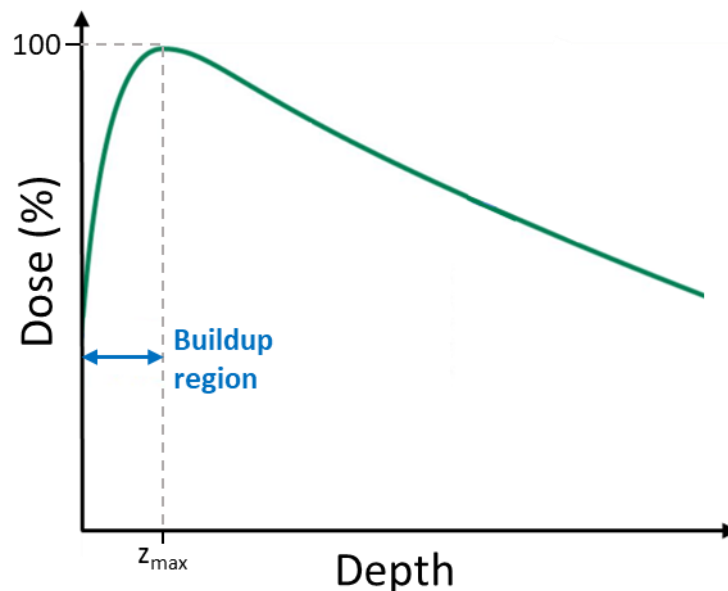


Figure 1.3: dose depth deposition for and X-ray beam into a patient (or a phantom). At the entrance surface the deposited dose is a fraction of the maximum dose that is reached at a certain depth (z_{max}) after the so-called buildup region. When the maximum dose deposition is reached, the dose falls exponentially as a function of the depth.

The key objective of RT is to maximize the radiation dose delivered to cancer cells while minimizing damage to the surrounding healthy tissue. The probability of tumour cure increases with increasing the radiation dose but, since healthy surrounding tissues are irradiated together with the cancer mass, the probability of severely damaging healthy tissue increases too (Barnett, 2009), as visible in Figure 1.4. Here, the dose response curves for tumour and normal tissues are represented by steep-sigmoids and the optimum treating dose is indicated by the dot-

ted line; a trade-off between the tumour control and the normal tissue complication probabilities is obtained, in the presented case, with a 60% of tumour control and healthy tissue damages of 5%.

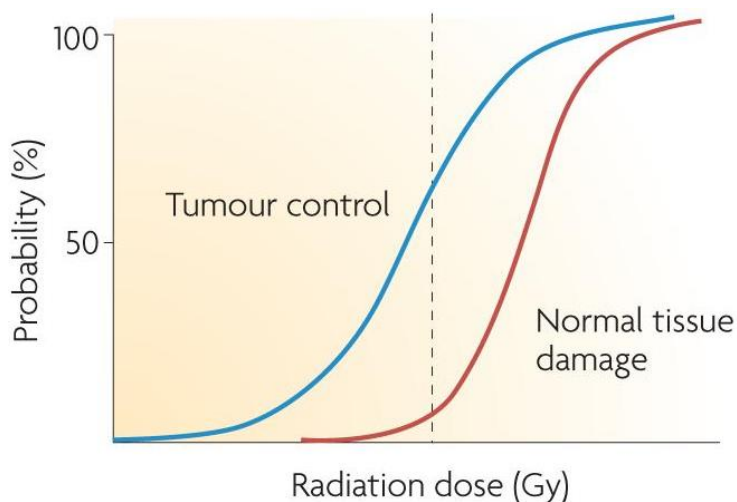


Figure 1.4: probability curves of tumour control and damages to normal tissues as a function of the delivered dose. Figure from (Barnett, 2009).

Over the past decades, many technological advances have been made to maximise the dose to the tumour while minimizing the healthy tissues damages. Among all, the most frequently implemented techniques to reduce the dose to healthy tissues are those using multiple cross-firing beams and dose temporal fractionation. The first method is usually employed to distribute the total amount of delivered dose to normal tissues over a wide area by means of multiple beams that overlap in the volume to be treated creating a brick-shaped central region of high dose distribution (i.e. in the tumour area) and limiting the exposure of the surrounding healthy tissue (Taylor, 2004). The second modality, the dose temporal fractionation, enables normal tissue to recover between two fractions empowering cell repopulation (important for improving the healing of the healthy tissue) and tumour oxygenation that results in an increase of the tumour radiosensitivity at the subsequent irradiation (Gragoudas, 2013). Further improvements in the therapeutic ratio have been made with the advent of e.g. image-guided RT (van Herk, 2007; Dawson, 2006), intensity-modulated RT (Hong, 2005; Rehman, 2018) and stereotactic radiosurgery. The first two RT strategies conform the dose around the tumour target achieving great healthy tissue sparing and facilitating the implementation of high-dose hypo-fractionated RT protocols; stereotactic ra-

diagnosis is applied by means of e.g. a Gamma Knife (Desai, 2020), where several highly collimated ^{60}Co sources are arranged around the region to be treated in a circular array within a heavily shielded device.

Despite impressive progresses, the efficacy of standard cancer therapy has reached a plateau for most solid tumours (Prasad, 2004). Thus, **there is an increasing interest in new curative approaches to improve the efficacy of cancer therapies and to reduce the recurrence of primary tumours**. Many approaches have been proposed, in both pre-clinical and clinical applications, such as hormonal and biological therapies, hadrontherapy, brachytherapy, fast neutron or boron neutron capture therapy as well as spatially fractionated X-rays and proton RTs. **In this Thesis, the role of MRT and MB as novel spatially fractionated RTs as potential method for treating radio-resistant tumours is investigated via a 3D virtual histology imaging technique and a multi-modal X-ray-based approach**. In the following paragraphs the basic principles of MRT and MB are given (section 1.3) together with an up-to-date review of the imaging techniques currently used for RT treatment follow-up with a special focus on techniques used for brain and lung monitoring (section 1.4). Furthermore, the role of a new X-ray imaging modality, XPCI-CT is discussed and the state-of-the-art applications are given as a basis for proposing, with this work, XPCI-CT as a 3D virtual histology modality for RT follow-up, which can complement conventional lab-based techniques.

1.3 Novel radiation therapies: X-ray microbeam and minibeam radiation therapy

MRT is a novel radiosurgery method, which was first dedicated to the treatment of brain tumours (Slatkin, 1992). It was developed at the Brookhaven National Laboratory in New York, USA (Laissue, 1992; Slatkin, 1995) and then at the ESRF (Bräuer-Krisch, 2003; Laissue, 2001). It was initiated with the use of deuteron microbeams (Zeman, 1961; Curtis, 1967) to simulate the possible effects of high-dose radiation, such as cosmic X-rays, on biological tissues, a problem that arose on the occasion of the first space exploration with humans. This research triggered further studies also thanks to the availability of highly collimated spatially fractionated synchrotron X-ray beams that enable the delivery of both MRT and MB. By using specially designed multi-slit collimators, X-ray MRT and MB reshape

the synchrotron laminar beam into an array of quasi-parallel beamlets of width ranging from 25 to 100 μm for MRT and from 500 to 700 μm for MB, as shown in Figure 1.5a. Centre-to-centre (c-t-c) distances are from tens to hundreds of micrometres for MRT and of the order of the millimetre for MB. A typical MRT lateral dose profile is shown in Figure 1.5b and is characterized by a spatially and periodically alternating microscopic dose deposition following an inhomogeneous geometric pattern with sharp falloff between the so-called peak and valley dose zones. Thus, two main regions of dose deposition can be recognized: the **peak region**, which corresponds to the dose delivery from the multi-slit collimator apertures, with a release of high doses, and the **valley region**, which is the area wedged between the peaks that is exposed to the lowest dose and results from the scattering of photons and secondary electrons from the adjacent peaks.

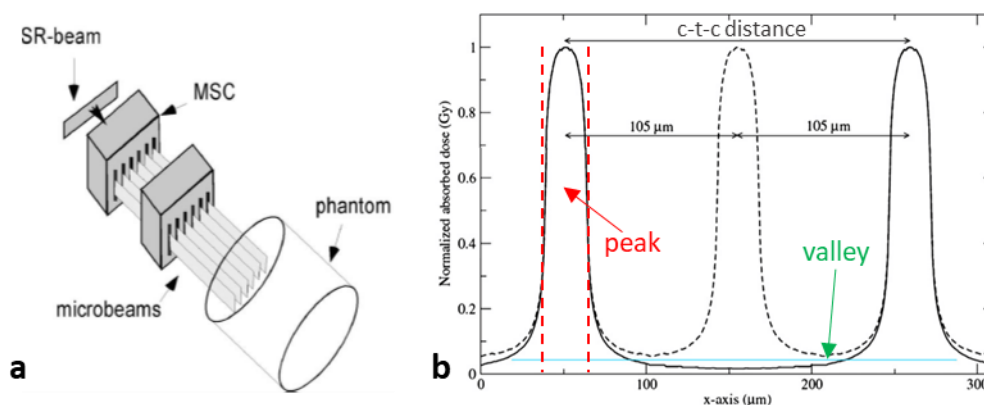


Figure 1.5: (a) reshape of the synchrotron (SR) laminar beam into an array of quasi-parallel microbeams by means of two multi-slit collimators (MSCs). (b) MRT lateral dose profile for two different centre-to-centre (c-t-c) distance values with arrows pointing at the peak and valley regions; the cyan line is the healthy tissue tolerance dose. Images are adapted from (Bräuer-Krisch, 2010) and (Bräuer-Krisch, 2005).

This spatially-fractionated irradiation geometry relies on the so called dose-volume effect (see paragraph 1.3.2) with the result that high dose deposition in a micrometric window (hundreds of Gray within the peak regions) are well tolerated (Slatkin, 1995; Serduc, 2008). Due to the micrometric width of the single beamlet, very short irradiation time (high dose rates) are needed to obtain a precise MRT dose distribution in the tissue since any movement of the target would cause the smearing of the MRT lateral dose profile. X-ray beams issued at third and fourth generation synchrotron facilities are particularly adapted for this treatment because of their inherent high collimation and fluxes (i.e. dose rates). This condition can be relaxed when MB are used. Indeed, MB was developed as

an alternative to MRT to overcome these difficulties (Prezado, 2015) since small movements occurring during irradiations will not merge the millimetre-distant MB beamlets.

The hypothesis underlying MRT irradiations is that damaged microvasculature is better repaired in normal than in cancerous tissues when irradiated with microbeams (Laissue, 1999; Bouchet, 2013). Therefore, cancer cells in between the tracks of microbeams will undergo necrosis because of the decreased oxygen supply induced by the vasculature damage. On the contrary, healthy tissue vasculature show high radioresistance for peak doses of hundreds of Gray (Bouchet, 2010; Serduc, 2008). The assumption is that the repair of microscopic lesions occurred within the peak areas is helped by the minimally irradiated cells that are placed in the valleys (Dilmanian, 2002). The valley region is thought to play a crucial role in healthy tissue healing. The key point is that the value of dose in the valleys has to be kept under the tolerance dose level of the irradiated healthy tissues. This condition is achieved by opportunely setting the values for microbeams width and c-t-c distance. The large area of the interface between intensely (peak) and minimally (valley) irradiated tissues ensures widespread contact between reparative cells in the valleys and damaged tissues in the peaks facilitating the repair (Laissue, 2007). Another reason for the preferential effect of MRT on tumour seems to be possibly attributed to the bystander effect or cellular communication (Crosbie, 2010): tumour cells showed extensive migration starting from one day post-irradiation facilitating the induction of double-strand breaks within the tissue, while healthy peak-irradiated cells exhibit limited migration up to 3.5 days post-irradiation. Nevertheless, **the processes that contribute to the efficacy of MRT treatments is still a partially open question and imaging techniques able to investigate the effects on different tissues with high detail and volumetrically can help in answering this query.**

Another important parameter in MRT is the peak-to-valley dose ratio (PVDR), namely the ratio between the dose value at the centre of the peak and the dose value in the valley (Bräuer-Krisch, 2005). High PVDR, together with a suitable MRT geometry, ensures the sharp falloff of the peak dose and has been found to play an essential role in the tissue sparing in biological experiments (Bräuer-Krisch, 2010). Overall, PVDR increases by increasing the beam c-t-c distance and, within the field of irradiation (FOI), is larger at the sides of the array than at the

centre due to the presence or absence of the overlap of the different microbeams tails (De Felici, 2005).

1.3.1 The lateral dose profile

As already mentioned, the lateral dose profile of a typical MRT irradiation geometry is composed by alternating peaks and valleys and its shape depends on the spectrum of the X-rays as well as on the width and c-t-c distance of the beamlets. Figure 1.6 shows, on a logarithmic scale, the simulated lateral dose profile of a single 25 μm wide beam within a cylindrical polymethylmethacrylate (PMMA) phantom from monochromatic and polychromatic radiation sources. The plateau region corresponds to the peak area (the X-ray beamlet) then the valley region starts and the dose profile drops exponentially. For monochromatic photon beams, the absorbed dose profile in the valley is characterized by two shoulders. The first shoulder is due to the Compton (incoherent) scattering electrons (in fact, the coherent scattering has a very low probability of occurrence), while the second shoulder results from the photoelectric absorption, of which electrons have a longer mean free path and contribute to the dose deposition after a certain distance from the beam axis (Spiga, 2007). The lateral dose profile for a polychromatic beam has a smooth appearance due to the fact that the probability of having Compton scattering and photoelectric effect changes with the X-ray radiation energy; thus, the two shoulders are broadened.

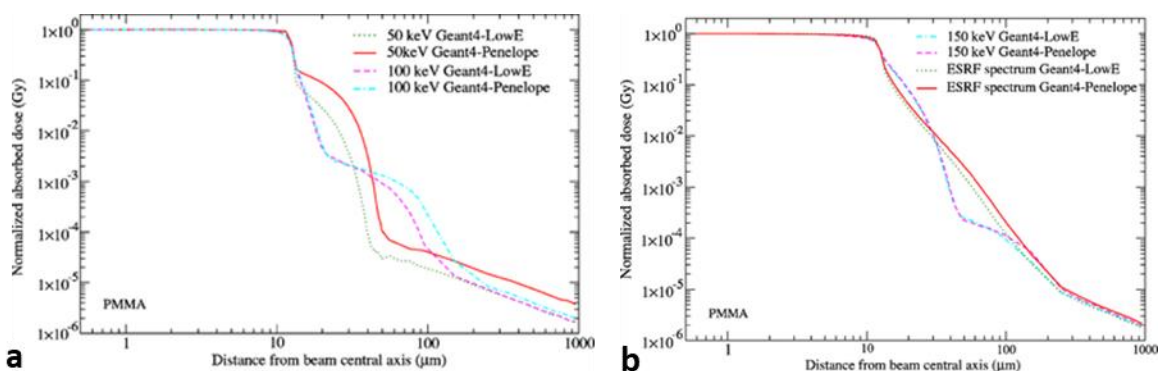


Figure 1.6: Monte Carlo dose simulations for the lateral dose profile distribution in a cylindrical PMMA of one single 25 μm wide beam of varying monochromatic energy (a) and the comparison of the lateral dose distribution, for the same beam, for a monoenergetic and polychromatic X-ray beam. Images from (Spiga, 2007).

1.3.2 The dose-volume effect

A first proof of the dose-volume effect on which MRT relies was given by Zeman *et al.* (Zeman, 1961) by irradiating the mouse visual cortex with single deuteron beamlets of 1 mm, 250, 75 and 25 μm of width, respectively, and peak doses from 24 to 200000 Gy. As shown in Figure 1.7, a peak dose of 280 Gy delivered in a 1 mm wide beam produced the complete destruction of the tissue and surrounding tissue necrosis, while the 25 μm wide beam produced a destruction of nerve cell bodies but preserved nerve fibres, vessels and interstitial glial cells despite the delivered dose of 4000 Gy. This experiment demonstrated that **the tissue sensitivity is inversely related to the irradiated volume, i.e. high doses are better tolerated by tissues if delivered in a narrow-micrometric window, while they cause the complete tissue destruction if delivered in a mm-size beam.**

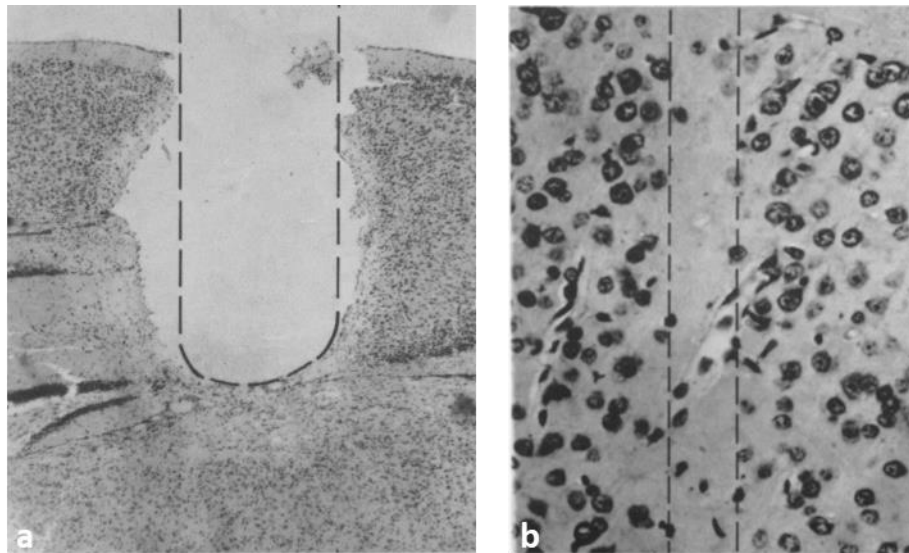


Figure 1.7: comparison of the effects of micrometre and millimetre-wide deuteron beams represented by the dashed lines. (a) tissue destruction corresponding to the delivery area of a 1 mm wide beam with peak dose of 280 Gy. Rarefication of the nerve cells is also visible in the cavity vicinity. (b) complete loss of nerve cells within the beam delivery area and normal appearing vein for a 4000 Gy, 25 μm -wide beam delivery. Figures adapted from (Zeman, 1961 © 2022 Radiation Research Society).

The dose-volume effect was also seen in X-ray MRT irradiation by (Serduc, 2009) where two orthogonal intersecting MRT arrays were delivered *in-vivo* on healthy and GBM-bearing rats with a c-t-c distance of 211 μm and beam widths of 25, 50 and 75 μm . The peak dose was chosen in order to obtain a valley dose of 18 Gy in all the configurations. The survival curves showed early death for both healthy

and GBM-bearing rats irradiated with 25 μm wide beams indicating that the delivered peak dose (860 Gy) is too large to be well tolerated by healthy tissues. On the contrary, good survival were obtained for arrays with 50 and 75 μm wide beams that delivered a peak dose of 480 and 320 Gy, respectively. Furthermore, the blood–brain barrier disruption was observed to increase with the peak dose.

Overall, MRT can exploit at maximum the dose-volume effect and has the potential of sterilizing radio-resistant tumours. The main drawback is that its clinical implementation is currently limited because of the high dose rate needed to avoid the beamlets smearing (Prezado, 2015). MB have instead the advantage of not needing dose rates as high as MRT, but, to avoid lethal effects, peak doses should be kept under a certain tolerance level that depends on the beamlets width and c-t-c distance.

1.4 Imaging techniques for cancer follow-up

Early cancer detection and well-established follow-up methodologies are key for a successful cancer treatment. Treatment follow-up is essential to facilitate the early detection of cancer recurrence, monitoring the outcome of the ongoing treatment, detecting and managing possible side-effects (Rose, 2009; Lewis, 2009). Follow-up is also important for providing supportive care to patients and their families such as information, reassurance, advises and identifying psychosocial or practical problems (Donnelly, 2007). Therefore, cancer treatment follow-ups are both clinical investigations and psychological and social support.

As for both clinical and preclinical therapy monitoring, several imaging methods can be used depending on the organ to be checked and an overview of the most used ones is given in Figure 1.8. Especially in pre-clinical research applications specific follow-up methods are needed to accurately investigating and monitoring, with high specificity and resolution, the effects of newly developed treatments. In this Thesis, RT side effects on brain and lung organs of a small animal model have been monitored; thus, the most widely used follow-up modalities for these two organs are presented.

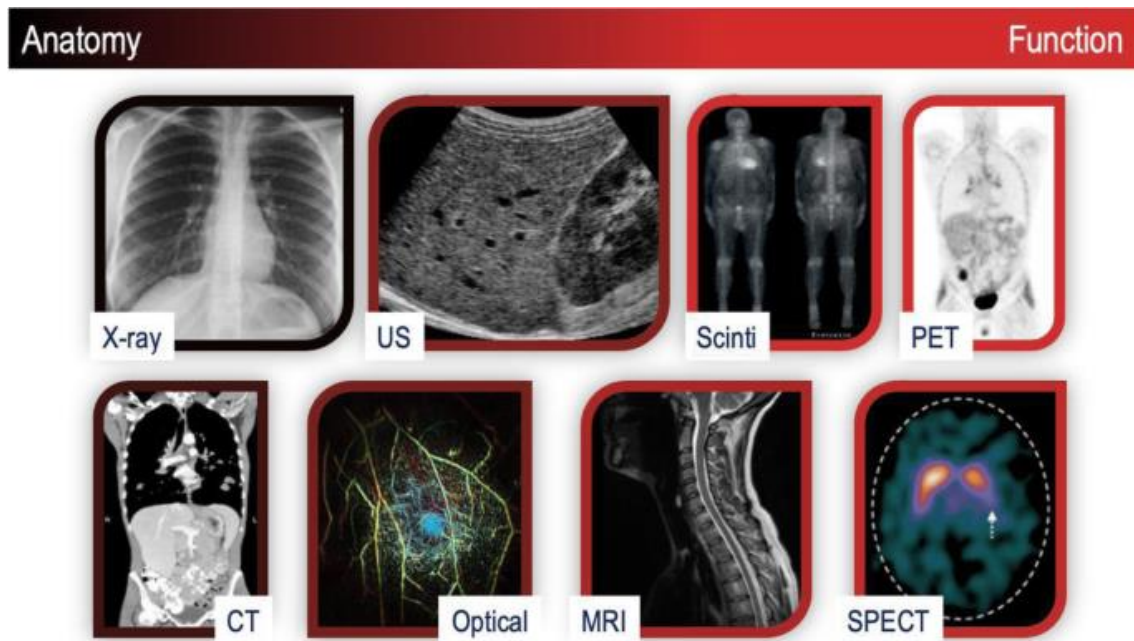


Figure 1.8: most-commonly used imaging modalities for clinical investigations and treatment follow-up in clinical practice, i.e. X-ray radiograph, Ultrasound (US), scintigraphy, Positron Emission Tomography (PET), Computed Tomography (CT), optical imaging methods, Magnetic Resonance Imaging (MRI) and Single Photon Emission Computed Tomography (SPECT). The image show, for each technique, the colour-coded ability to depict anatomical and/or functional information. Figure reproduced from (Beyer, 2020) under the Creative Commons licence: <http://creativecommons.org/licenses/by/4.0/>.

1.4.1 Brain follow-up techniques

The most widely used techniques in clinical routine for the monitoring of brain tissue, and more generally of the CNS, are Magnetic Resonance Imaging (MRI), CT, Positron Emission Tomography (PET), Single Photon Emission Computed Tomography (SPECT) and combinations of the mentioned techniques as PET-MRI and PET-CT (Alliance, 2018). All these techniques can attain a 3D visualization of the organ with consequent 3D localization of lesions, tumours and organ pathological states. MRI is used to study changes in the whole-brain networks as both a volumetric and morphometric methodology (Goodman, 2021). The MRI contrast formation mechanisms has considerably improved due to the recent developments in magnetic field strength, tailored sequence development, and optimized post-processing methods; voxel sizes down to $176 \times 132 \times 600 \mu\text{m}^3$ were consequently obtained at fields of 9.4 T (Loureiro, 2018). However, MRI is often used together with specific contrast agents to enhance the contrast between the region to be investigated (e.g. the tumour) and the surrounding tissues. As an

alternative, CT is widely employed for clinical imaging providing detailed volumetric and morphological information with an in-plane resolution of ~ 0.5 mm but out-of-plane resolutions of the order of the millimetre (Muschelli, 2020). Functional brain investigations can instead be obtained via PET or SPECT. PET is used for imaging the brain glucose metabolism (Sarıkaya, 2015) and to assess glial activation and neuroinflammation in the brain (Turkheimer, 2015), while SPECT is applied for studying the blood flow into veins and arteries and thus to detect injured sites with reduced blood flow. The main limitations of the two functional techniques are that: *i*) glucose metabolism PET shows only modest performance as a brain RT follow-up due to the high intrinsic uptake of the brain cortex and therapy-related hypermetabolism (la Fougère, 2011); *ii*) SPECT imaging has a low spatial resolution if compared to PET (Sadaghiani, 2021); *iii*) they both rely on the use of nuclear medicine radiotracers, which have a limited availability due to their short half-life, for the evaluation of brain lesion and neoplasms and are intrinsically characterized by a lack of precise anatomic details.

Overall, to obtain a good functional and morphological information, PET, MRI or SPECT images are often co-registered to CT scans to obtain simultaneously morphological and functional data, as visible in Figure 1.9.

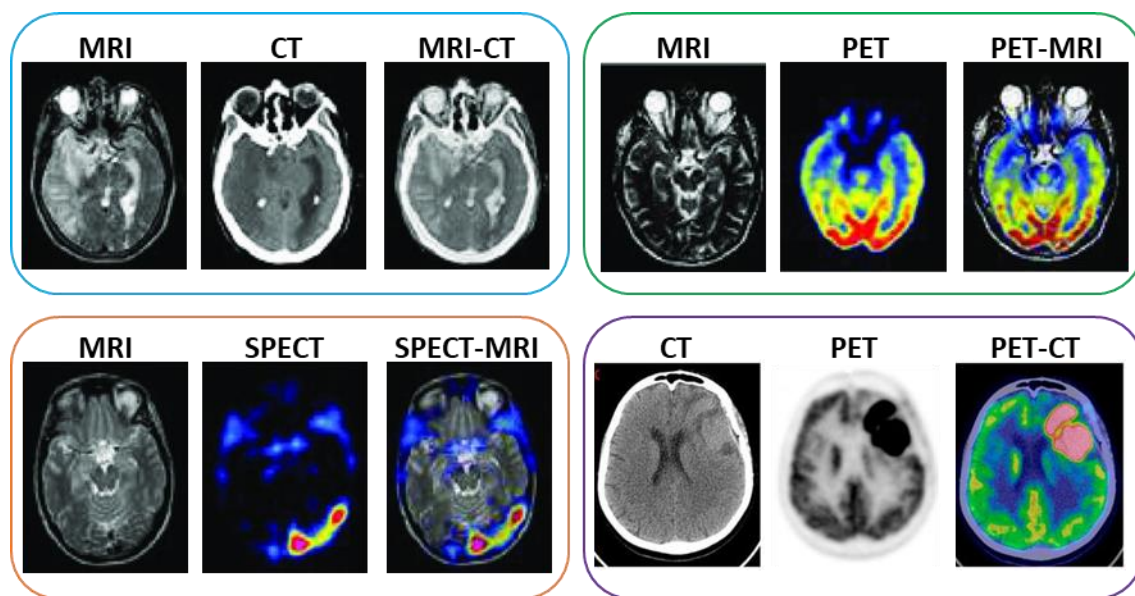


Figure 1.9: examples of multi-modal clinical imaging. Figure adapted from (Du, 2015) and (Quartuccio, 2020).

1.4.2 Lung follow-up techniques²

Standard diagnostic techniques currently used for lung monitoring are radiography, PET, light ultrasounds (LUS), MRI and CT. Due to the fact that lung diseases such as fibrosis, emphysema and cancer affect the density and structural integrity of lung tissue, radiographic imaging is the principal diagnostic technique in clinical practice, but the early-stages of lung diseases are often difficult to detect (Kitchen, 2005). LUS is a non-invasive, repeatable and reproducible bedside technique. It has the great advantage of being ionizing radiation free and is suitable for the diagnosis of alveolar-interstitial syndrome, lung consolidation, pleural effusion and pneumothorax (Lichtenstein, 2004; Bouhemad, 2007). Nevertheless, LUS provides only 2D images and does not meet the clinical imaging standards for obese patients or in the presence of subcutaneous emphysema (Chiumello, 2013). PET has been used to monitor cellular metabolic activity linked to the presence of inflammatory cells (Chiumello, 2013), vascular perfusion, capillary filtration or inflammation (Hsia, 2010) providing with both static and dynamic information derived from the used radio-tracer kinetics. This technique results in morphological information and partial anatomical details, such as lung aeration, that requires the compensation for lack of morphological details with an additional MRI or CT scan. In such a way, a complete 3D information of the lung functioning can be provided. An example of a multi-modal lung imaging (PET/CT and PET/MRI) is visible in Figure 1.10. MRI imaging of the lungs is challenging because of the low tissue density (low water content in the lung tissue), which severely limits the signal-to-noise ratio, and the many air-tissue interfaces of the alveoli and bronchioles that create local magnetic field inhomogeneities leading to shortening of some relaxation times (Schuster, 2004) and thus, to image artefacts. To overcome some of those weaknesses, hyperpolarized noble gases, such as ^3He and ^{129}Xe are used as gaseous inhaled contrast agents to improve the signal-to-noise ratio (Fain, 2010). MRI can achieve a relatively high 3D spatial and temporal resolution, especially in comparison to PET. Despite that, typical values are 1 mm in-plane and 5-10 mm out-of-plane for *in-vivo* human lungs and 0.5^3 mm^3 as isotropic voxel size for small animals (Felder, 2017), while *ex-vivo* MRI can reach up to $110^3 \mu\text{m}^3$ voxel size for the entire animal scanning

² The text of this paragraph is reproduced form (Romano, 2021b)

and $25^3 \mu\text{m}^3$ for imaging isolated organs; both configurations are achieved with the help of suited contrast agents (Johnson, 2002). MRI is well suited for assessing the regional pulmonary functional gas exchange by means of oxygen as contrast agent to diagnose cystic fibrosis, chronic obstructive pulmonary disease and asthma (Voskrebenzev, 2020). Nevertheless, for some respiratory diseases, CT imaging still remains the gold standard for an imaging-based diagnosis and monitoring: this is the case of lung fibrosis (Voskrebenzev, 2020), emphysema and interstitial lung disease (van Rikxoort, 2013). State-of-the-art CT systems can now produce images with a spatial resolution of 50-100 μm (Schuster, 2004). However, these micro-CT (Blocker, 2020) devices are not capable to resolve microscopic lung structures such as alveoli. Furthermore, conventional X-ray absorption-based CT or micro-CT are intrinsically characterized by poor soft-tissue sensitiv-

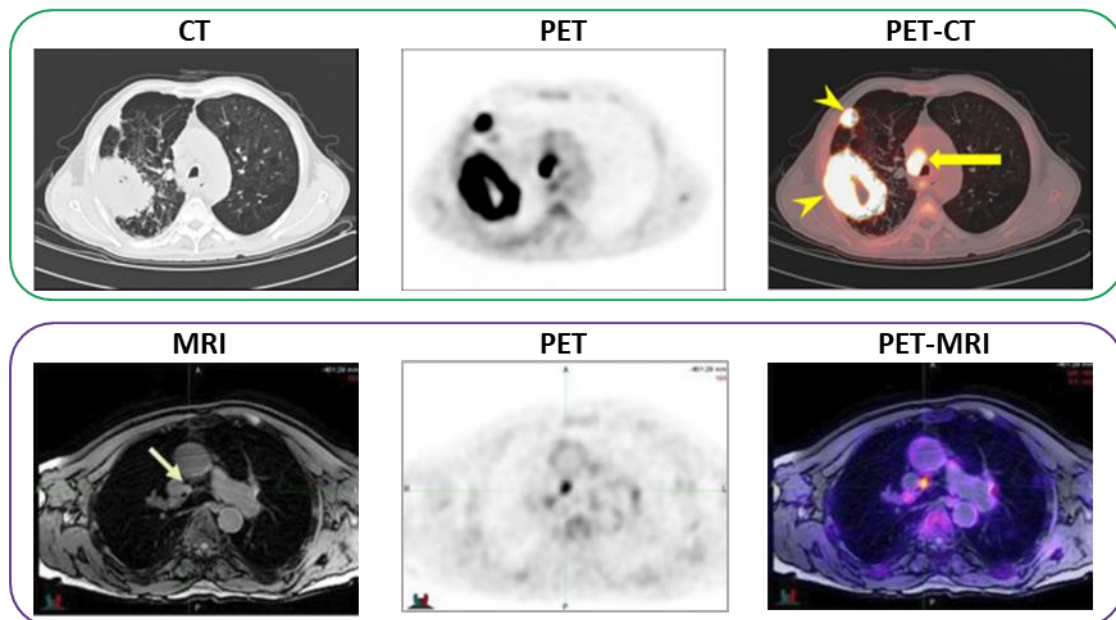


Figure 1.10: examples of multi-modal clinical imaging for lungs. Arrows point at cancerous lesions in the tissue. Figure adapted from (Xu, 2020; Herrmann, 2013)

ity if compared, for instance, with MRI and even more with XPCI-CT that will be presented in the followings.

1.4.3 Histology as the gold standard for pathology assessment

Despite the numerous advances in imaging techniques, histology and immunohistochemistry are considered the clinical gold-standards for diagnosis (Müller, 2018; Albers, 2018a) and are used to benchmark or confirm findings in biomedical

research applications. Histological investigations, i.e. the study of the composition and the structure of the microscopic anatomy of tissues in relation to their specialized functions, are indispensable to identify and classify several types of tissues and pathological states providing a multitude of staining protocols for labelling and recognizing the different structures, including cancerous cells. However, histology presents also important drawbacks in that: *i*) it is a destructive macroscopic analysis method, *ii*) it is laborious, time demanding and highly relying on skilled operators (Töpperwien, 2018a) and *iii*) it provides, intrinsically, 2D information. Histological resolution is only achievable in 2D, while, in the third dimension, the thickness of the cut slice determines the sampling step and thus the spatial resolution (Töpperwien, 2018a). In addition, localisation and histological analysis of regions of interest within the specimen are hampered by the poor visibility of the tissue embedded within the histologic paraffin block (Albers, 2018b). This limitation can only be overcome with serial sectioning and staining that are, anyhow, very time consuming. To allow for a more detailed analysis of the tissue, an accurate 3D reconstruction of the volume, based on histological sections, is needed. However, during the slicing phase, tissues can be damaged leading to inhomogeneous deformations and artefacts like tearing, shrinking, stretching or other morphological rearrangements of the tissues (Chakravarty, 2003). Thus, creating a 3D atlas of an organ by stacking the 2D histological slices will involve morphological inconsistencies in the reconstructed volume; a slice-to-slice alignment results to be a labour-intensive procedure.

3D virtual histology has recently appeared as able to overcome these limitations and to provide datasets of images that can be virtually sectioned in any direction. Several so-called virtual histology approaches have recently emerged (Müller, 2018), each with their own limitations: confocal microscopy, light sheet microscopy, micro-MRI and micro-CT. Among all, **synchrotron X-ray based virtual histology** has been shown to provide datasets down to sub-micron isotropic spatial resolution even for soft tissue samples by means of XPCI-CT (Saccomano, 2018; Barbone, 2020a). Among the different examined tissues with XPCI-CT, applications to brain, lung, breast, cartilage and spinal cord above all, have produced relevant results both *ex-vivo* (Barbone, 2018; Norvik, 2019; Saccomano, 2018) and *in-vivo* (Croton, 2018; Fardin, 2021; Willer, 2021). Therefore, this technique has been studied and is here proposed as a valuable candidate for monitoring the

effects of RTs with histology-like resolution in 3D, obtaining full organ image datasets at high contrast and sensitivity and without the need of stainings. XPCI-CT images were also compared to SAXS/WAXS and XRF data to achieve, for the first time, an accurate morphological and chemical interpretation of the radio-induced effects of MRT and MB treated tissues.

1.4.4 XPCI-CT as a 3D virtual histology follow-up technique

To overcome the intrinsic low sensitivity to soft-tissues of conventional CT and micro-CT, XPCI-CT has been introduced in the field of biomedical imaging about 30 years ago; since then it has been applied to a large number of medical questions (Russo, 2017). In addition to conventional X-ray absorption information, XPCI-CT exploits the refractive properties of biological tissues allowing enhanced image contrast and sensitivity by using sophisticated experimental and image processing methods (Bravin, 2013; Lewis, 2005; Coan, 2013). An example showing the enhanced soft-tissue contrast for XPCI-CT with respect to absorption CT is given, for an excised rat brain organ, in Figure 1.11.

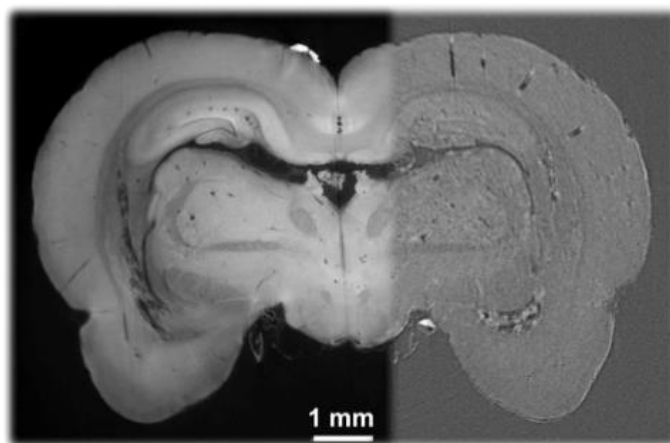


Figure 1.11: XPCI-CT (left) and absorption CT (right) coronal image of a rat brain. XPCI-CT significantly improves soft tissue contrast. Image reproduced from <https://www.gratxray.com/learn-more/technology> and adapted from (McDonald, 2009).

Among the developed setups, propagation-based XPCI-CT (PB-XPCI-CT) has been extensively applied in biomedicine using both synchrotron radiation setups (Bravin, 2013) and lab-based micro-focus X-ray sources (Wilkins, 1995; Krenkel, 2016) mainly in *post-mortem* investigations, but also in *in-vivo* applications (Momose, 2020), see section 2.1.5. Owing to its extremely high brilliance and coherence, synchrotron radiation offers unique possibilities for XPCI-CT in terms

of achievable spatial resolution (today reaching the nanometre range) and contrast resolution, being a valuable technique for treatment follow-up of full organs in 3D with histology-like resolution.

Chapter 2

X-ray scattering-based imaging modalities

The use of X-rays for imaging the internal structure of solid objects dates back to November 8, 1895 when Wilhelm Conrad Röntgen took the first X-ray radiograph (Röntgen, 1895). The use of X-rays quickly spread out and, within a year, became an established routine for diagnosis and therapy in clinical practice (Linton, 1995; Drury, 1896). Until 1912, when the wave nature of X-rays was discovered by von Laue (Friedrich, 1912), the basic principle underlying the use of X-rays was their absorption, i.e. intensity modulation derived from the interaction with electrons of the object they pass through. The von Laue's discovery allowed the wave conception of X-rays to be officially accepted by providing an experimental proof of that X-rays interacting with a crystal interfere and produce diffraction patterns. X-ray crystallography and the exploitation of physical processes inherent to the scattering were then initiated.

Nowadays, X-ray imaging is a standard tool for the non-destructive inspection of the internal structure of samples finding application in the most disparate fields: medicine, biology, engineering, palaeontology, food industry, art, security and many others. Despite the outstanding progresses derived from improvements in X-ray source technology and detection system as well as from the introduction of CT, the working principle has remained unchanged for over a century: contrast at the detector is generated by the sample absorption (photoelectric effect), while scattering (Compton, Thompson and Rayleigh effects) is considered a parasitic effect to be taken under control. Thanks to the Bonse and Hart discovery (Bonse, 1965) of X-ray interferometry, a new X-ray imaging modality was extensively studied: XPCI, of which first application was realized by Ando et al. (Ando, 1971) in the early seventies. Since then, this new X-ray imaging technique has been widely studied both theoretically and experimentally. The possibility of performing imaging by exploiting the scattered X-rays emerging from the sample

to be analysed enables the visualization of the inner structure of weakly-absorbing materials that might be undetectable with conventional X-ray absorption modalities. That opened the potential of X-ray imaging to a wide set of new applications making today scattering-based X-ray techniques as XPCI largely used for pre-clinical biomedical research and in some cases bringing these setups close to clinical practice.

In this chapter, the basic principles of XPCI as well as of SAXS/WAXS will be presented and an overview of the major applications of these techniques is provided. Both methods exploit the elastic scattering of X-rays within matter: the electrons in the sample are caused by the X-rays to resonate elastically producing secondary X-ray waves, which interfere and lead to a scattering signal (Hémonnot, 2017) that is processed afterwards.

2.1 Imaging with X-rays

2.1.1 X-ray absorption and phase contrast theory

Let's consider, as in a conventional radiography setup, an X-ray beam passing through an object and an image receptor placed just downstream it. On the image receptor, the internal structure of the analysed object is reported as differences in the transmitted X-ray beam intensity. Supposing the X-rays propagate along the z axis and that the object placed between the source and the detector is non-homogeneous, as shown in Figure 2.1, the intensity at the detector can be described by the Beer's law (Born, 1999):

$$I(x, y, z = 0) = I_0(x, y) e^{-\int \mu(r) dl} = I_0(x, y) e^{-\mu T_{obj}(x, y)} \quad 2.1$$

where $I_0(x, y)$ is the intensity of the impinging beam, μ is the absorption coefficient and T_{obj} the projected thickness of the object. The absorption coefficient is integrated along the beam path to account for the different materials that may constitute the object.

Furthermore, if the source is polychromatic, an integration over the energy is required since μ and I_0 are both energy dependent:

$$I(x, y, z = 0) = \int I_0(x, y, \lambda) e^{-\mu(\lambda) \cdot T_{obj}(x, y)} P(\lambda) \cdot d\lambda \quad 2.2$$

with λ the X-ray wavelength and $P(\lambda)$ a factor accounting for the detector energy response. With this new formulation of the law, every energetic component participates in the image formation with a proportionality factor ruled by its probability of emission and detection (Born, 1999).

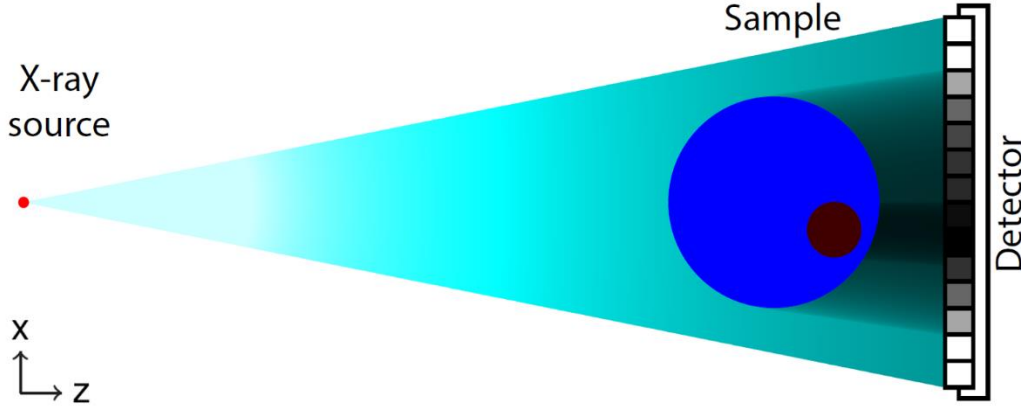


Figure 2.1: schematic aerial representation of a conventional absorption-based X-ray imaging setup. The source beam propagates along the z direction and interacts with a non-homogeneous sample. Just after the sample, an image receptor is placed to record the beam intensity variations. Image modified from (Lundström, 2014).

If we now use the wave formalism to describe the problem, the plane wave representation holds for a monochromatic beam travelling in the vacuum:

$$\Psi = \psi_0 e^{ikz} \quad 2.3$$

where ψ_0 is the wave amplitude and $k = |\mathbf{k}| = 2\pi/\lambda$ is the modulus of the wave vector that should be replaced by nk when travelling through a matter with a complex refractive index n . When Ψ interacts with an object, the exiting wave can be written as:

$$\Psi_{out} = \Psi T(x, y) = \psi_0 e^{ikz} T(x, y) \quad 2.4$$

where $T(x, y)$ is the complex transmission factor that modulates the incident wave and depends on the traversed object index of refraction $n = 1 - \delta(x, y, z) + i\beta(x, y, z)$ (Paganin, 2006) as:

$$\begin{aligned} T(x, y) &= e^{ik \int (n-1) dz} = e^{-k \int \beta(x, y, z) dz} e^{-ik \int \delta(x, y, z) dz} \\ &= e^{-k \int \beta(x, y, z) dz} e^{i\varphi(x, y)}. \end{aligned} \quad 2.5$$

Equation 2.5 reveals that the impinging wave is modified in the amplitude by β and the phase shift factor is ruled by $\varphi(x, y) = -k \int \delta(x, y, z, \lambda) dz$.

By using this formalism, the problem becomes more general with the introduction of both absorption and phase shift as a consequence of the interaction of X-rays with matter. Nevertheless, by going back to the conventional absorption X-ray imaging, it is possible to retrieve the intensity projected on the detector by applying the square modulus of equation 2.4, which results again in the Beer's law:

$$|\Psi_{out}|^2 = |\Psi T(x, y)|^2 = \psi_0^2 e^{-2k \int \beta(x, y, z) dz} \quad 2.6$$

with $\beta = \mu/2k$.

Going back to the definition of n , it is possible to express β and δ as a function of the electron density ρ of the object and the radiation wavelength λ as (Born, 1999):

$$\delta(\lambda) = \rho \frac{r_e \lambda^2}{2\pi} \quad 2.7$$

$$\beta(\lambda) = \mu(\lambda) \frac{\lambda}{4\pi} \quad 2.8$$

where r_e is the classical electron radius. **For biomedical imaging applications**, X-rays have energies between 10 and 100 keV and biological tissues are composed of elements with low atomic numbers ($Z \leq 20$), thus $\delta \approx 10^{-6} - 10^{-7}$ **with an energy dependence of E^{-2} , while $\beta \approx 10^{-10}$ and depends from the energy as E^{-4}** . The δ dependency from the energy can be trivially derived given that $E = hc/\lambda$, with h and c the Plank constant and the speed of light in vacuum, respectively. For determining the explicit energy dependence of β , one should consider that $\mu(\lambda) \propto E^{-3}$, with the photoelectric effect carrying the strongest energy dependence among all the process that a photon can undergo, resulting in $\beta \propto E^{-4}$. The big difference between δ and β is the reason why phase contrast imaging, which is sensitive on both the intensity modulation and the phase shift, can theoretically provide much higher image contrast and thus sensitivity with respect to purely absorption-based radiography. As shown in Figure 2.2, δ assumes larger values with respect to β in the energy range of biomedical applications and at energies higher than the K-edge values of biological materials. Furthermore, the different energy dependence of δ and β enables the use of energies higher than the ones implied with absorption-based X-ray imaging, keeping the phase contribution predominant over that of the absorption. As a result, phase-contrast modalities

can generate significantly higher image contrast compared to conventional radiograph (Zhou, 2008).

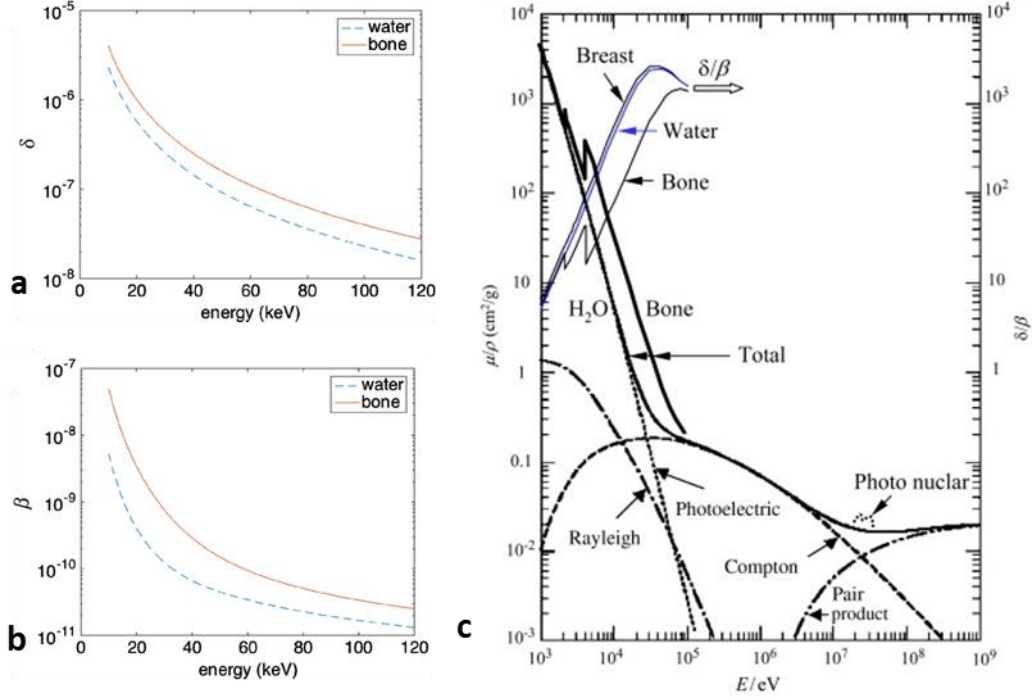


Figure 2.2: (a) and (b) are the representation of the real and imaginary part of the complex index of refraction, respectively, as a function of the X-ray energy. (c) is the dependence on the X-ray energy of the absorption coefficient and the δ/β ratio for breast tissue, water and bone. Images are reproduced from (Endrizzi, 2018) and (Zhou, 2008).

Recalling equation 2.5, the phase shift caused by the object can be written as:

$$\varphi(x, y, \lambda) = -k \int \delta(x, y, z, \lambda) dz = -\frac{2\pi r_e}{k} \int \rho(x, y, z) dz \quad 2.9$$

in the geometrical optics approximation (Wilkins, 1996). Thus, using δ values as expressed above, the refraction angles results typically in very small angles (few arcseconds) and the angular deviation of the wave front with respect to the normal direction is:

$$\Delta\alpha \approx \frac{1}{k} |\nabla_{xy} \varphi(x, y, z)| = |\nabla_{xy} \int dz \cdot \delta(x, y, z, \lambda)| \quad 2.10$$

where ∇_{xy} is the gradient operator in the object plane. This equation provides a direct link between the object-induced phase shift and the refraction angle, which is a measurable physical quantity and puts the basis for phase-sensitive techniques that exploit the possibility of transforming the angular deviations into intensity modulation to be recorded on the detector.

Several techniques have been developed during the past 30 years to exploit the phase-contrast with X-ray beams and they can be classified into five main methods (Bravin, 2013): crystal-based interferometric methods (Bonse, 1965; Momose, 1996), analyser-based imaging (ABI) (Förster, 1980; Davis, 1994), propagation-based imaging (PBI) (Snigirev, 1995), grating interferometric (GI) (Weitkamp, 2005) and non-interferometric (Olivo, 2007) methods. By using appropriate image acquisition procedures and *ad-hoc* developed mathematical algorithms (Diemoz, 2010; Bravin, 2013), these techniques enable the separation of the absorption and phase contrast contributions to the signal; in addition, ABI and GI methods can discriminate the small angle scattering (dark field) signal, which, over the recent years, has been shown to offer new valuable possibilities for pathologies in specific organs (e.g. lung, as it will be mentioned again in section 2.1.5).

Within the framework of this Thesis, the PBI-XPCI technique was used and thus, only this method will be described in both its theory and experimental realization. The citations given above constitute a reference for the other techniques.

2.1.2 Propagation-based X-ray Phase Contrast Imaging

Among the different XPCI techniques, the PBI method uses the simplest experimental setup: it essentially consists of an X-ray beam, an object to be imaged and a 2D imaging detector placed downstream the object similarly to standard absorption-based radiography. The two main differences, which are crucial for making this setup an XPCI setup are: 1) the X-ray beam needs to have a high degree of spatial coherence (see the following subparagraphs) and 2) the sample to detector distance is increased with respect to conventional radiography, as shown in Figure 2.3a. Owing to this experimental configuration, when two parts of the wavefront, which experienced different angular deviations, propagates sufficiently far, the small differences in the phase propagation direction cause interference and variations of intensity are observed at the image plane (Fresnel diffraction). Figure 2.3 shows a schematic view of a synchrotron-based PBI experimental setup where a highly spatially coherent monochromatic X-ray beam impinges on the sample (Figure 2.3a) and the intensity modulation induced by the object is then recorded by the detector (Figure 2.3b). Polychromatic synchrotron beams are often monochromatized by using perfect crystal systems (for instance

in Bragg-Bragg or Laue-Laue configuration) to select a narrow spectral range ($\lambda/\Delta\lambda \approx 10^{-4}$) and achieve a good temporal coherence for improving the final image contrast. PB-XPCI applications also exist with polychromatic sources and conventional X-ray tubes; further details are given in paragraph 2.1.6.

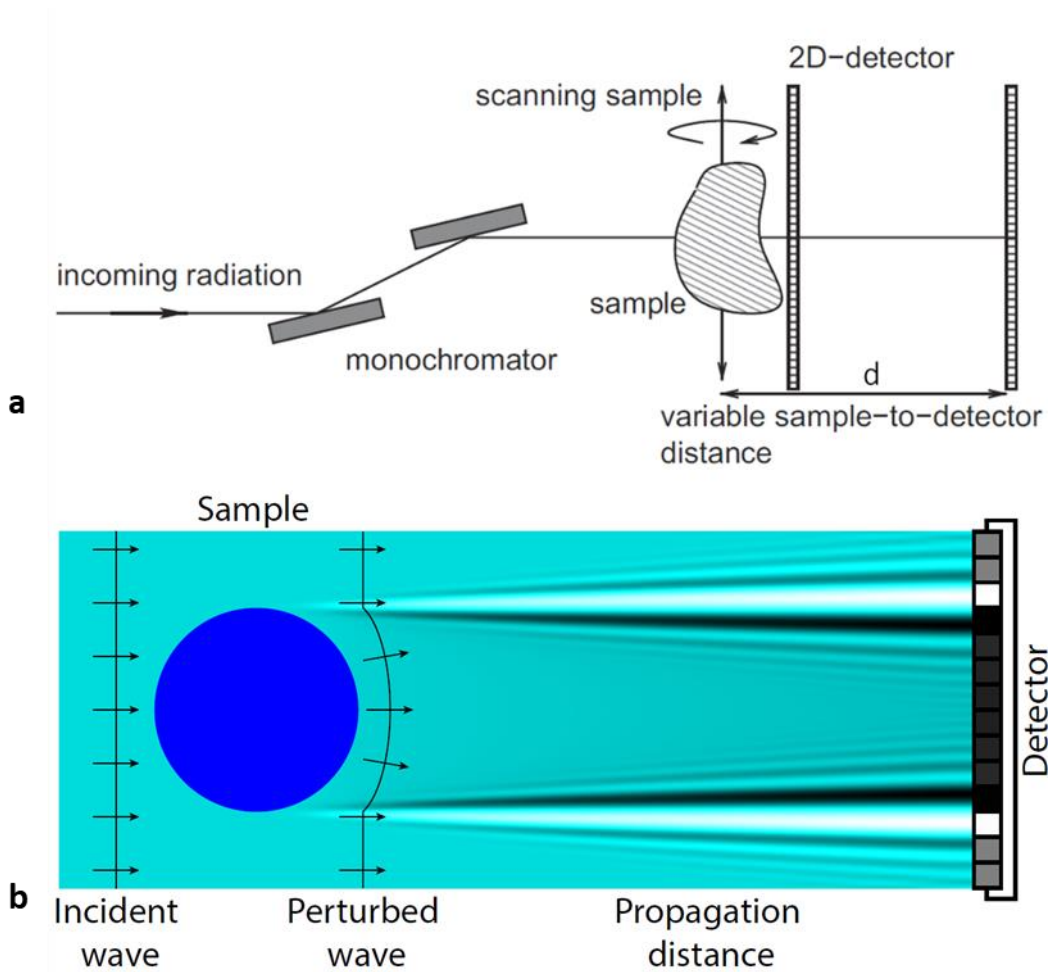


Figure 2.3: (a) schematic representation of a PB-XPCI experimental setup at a synchrotron facility. The highly spatially coherent incoming X-ray radiation is monochromatized by a two-crystal system and afterwards impinges on the sample. The resulting intensity modulations are recorded at a variable distance by a two-dimensional (2D) detector. (b) is an aerial view of the same setup reporting the wave modification after the beam passes a homogeneous sample. Images reproduced from (Keyriläinen, 2010) and (Lundström, 2014).

Let us now use the wave-optical approach of the problem to obtain a formulation for the intensity recorded on the detector plane in a PB-XPCI experiment. Beginning with the equation 2.4 and using the formulation obtained with the Fresnel diffraction integral, we obtain (Paganin, 2006):

$$\psi_d = \psi(x, y, z = d) = e^{ikd} \mathcal{F}^{-1} e^{\frac{-id(k_x^2 + k_y^2)}{2k}} \mathcal{F} \psi_{z=0}, \quad d > 0. \quad 2.11$$

Here, \mathcal{F} is the Fourier transformation with respect to x and y , \mathcal{F}^{-1} is the inverse Fourier transformation and (k_x, k_y) are the Fourier coordinates dual to (x, y) . This means that to obtain the wave function in the Fresnel approximation after a propagation distance of d , we have to take the Fourier transformation of the unpropagated field, multiply the result by the above written free-space propagator and take the inverse Fourier transform of the result. If the propagation distance d is small enough, the Fresnel propagator can be approximated as:

$$e^{\frac{-id(k_x^2+k_y^2)}{2k}} \approx 1 - \frac{id(k_x^2+k_y^2)}{2k} \quad 2.12$$

and the equation 2.11 becomes:

$$\psi_d = e^{ikd} \mathcal{F}^{-1} \left(1 - \frac{id(k_x^2+k_y^2)}{2k} \right) \mathcal{F} \psi_{z=0} = e^{ikd} \left(1 + \frac{id}{2k} \nabla_{x,y}^2 \right) \psi_{z=0} \quad 2.13$$

with $\nabla_{x,y}^2$ the Laplacian in the x, y plane. $\psi_{z=0}$ is now generally written as: $\psi_{z=0} = \sqrt{I_{z=0}} e^{i\varphi_{z=0}}$ and equation 2.13 results in:

$$\psi_d = e^{ikd} \left(1 + \frac{id}{2k} \nabla_{x,y}^2 \right) \sqrt{I_{z=0}} e^{i\varphi_{z=0}}. \quad 2.14$$

Thus, to obtain the intensity at the detector, the square modulus of equation 2.14 is taken:

$$I_d = I_{z=0} + 2Re \left(\sqrt{I_{z=0}} e^{i\varphi_{z=0}} \cdot \frac{id}{2k} \nabla_{x,y}^2 \sqrt{I_{z=0}} e^{i\varphi_{z=0}} \right) \quad 2.15$$

where the quadratic terms in d have been neglected considering a propagation distance sufficiently small (Paganin, 2006). Equation 2.15 can be adjusted as follows:

$$I_d = I_{z=0} - \frac{d}{k} \nabla_{x,y} (I_{z=0} \nabla_{x,y} \varphi_{z=0}) \quad 2.16$$

or alternatively, by explicating all the spatial dependencies, as:

$$I(x, y, z = d) = I(x, y, z = 0) - \frac{d}{k} \nabla_{x,y} [I(x, y, z = 0) \nabla_{x,y} \varphi(x, y, z = 0)] \quad 2.17$$

which is the transport of intensity equation (TIE) of (Teague, 1983). **This is the key result of this section since explicitly provides the recorded intensity at the detector as a function of both the phase and intensity variation of the initial wave.**

For low-absorbing objects and thus if the intensity $I_{z=0}$ varies slowly with x and y , its Laplacian can be neglected and, by introducing the geometrical magnification factor $M = (d + l)/l$ accounting for the relative positions of source, object and detector (being l and d the distances of the sample to the source and the detector, respectively), equation 2.17 becomes (Wilkins, 1996):

$$I(x, y; M, k) = \frac{I_{z=0}}{M^2} \left[1 + \frac{d}{kM} \nabla_{x,y}^2 \varphi(x, y; l, k) \right] = \frac{I_{z=0}}{M^2} \left[1 - \frac{2\pi r_e d}{k^2 M} \nabla_{x,y}^2 \int \rho(x, y, z) dz \right] \quad 2.18$$

where the last statement holds by using equation 2.9. As it can be seen, the phase term is directly proportional to the propagation distance d and **the beam monochromaticity is not essential**. The PBI technique can indeed use either monochromatic and collimated synchrotron radiation (Cloetens, 1996) or polychromatic beams from microfocus X-ray tubes (Wilkins, 1996; Shovkun, 2006).

PBI is a differential phase technique that requires the second derivative of the phase to be different from zero. Indeed, a homogeneous phase gradient corresponds to an overall deflection of the beam and will not be detectable. As a consequence, this imaging method is particularly sensitive to edges and interfaces in the object providing an edge-enhancement effect in the images (Gureyev, 2008) that largely varies with the propagation distance. By moving the detector far from the sample, the *edge-detection regime* holds with interference fringes becoming visible on the detector and being directly correlated to the sample edges. When the propagation distance is further increased, we enter the so-called *holographic regime* and the image obtained at the detector appears deformed and does not carry direct and precisely-linked information about the object; specific image processing algorithms based on the image formation mechanism are used to recover the information. Usually, PB-XPCI is experimentally realized by recording Fresnel diffraction patterns of the object at different sample to detector distances and applying retrieval algorithms to bring back the phase signal of the object, but XPCI images can be also obtained, under certain assumptions, by using just one propagation distance (paragraph 2.1.3).

The optimal contrast for phase features of frequency f is obtained when:

$$2\lambda D f^2 \approx 1 \quad 2.19$$

with the defocusing distance $D = \frac{d \cdot l}{d+l}$ (Cloetens, 1996). Typically, l is large if compared with d and D turns out to be approximately equal to d . Being the λ of X-

rays of the order of a few Angstrom, the optimum distance falls in a range that well accommodates the experimental needs (centimetres to millimetres).

Propagation-based Phase Contrast Imaging with a polychromatic source

Up to now, it has been assumed that the incoming X-rays are monochromatic, but an equation equivalent to 2.18 can be derived for the case of a polychromatic beam.

Being a polychromatic beam a superimposition of monochromatic waves, the dependency of equation 2.17 on λ is explicated as follows:

$$I_{\omega,d} = \frac{I_{\omega,z=0}}{M^2} \left[1 - \frac{cd}{\omega M} \nabla_{x,y}^2 \varphi_{\omega}(x, y; l, k) \right] \quad 2.20$$

were $\lambda = 2\pi c/\omega$ was used, with c the speed of light in vacuum and ω the frequency of the monochromatic radiation.

Let us make some assumptions: *i)* the polychromatic beam is made of planar incident waves, *ii)* the object is weakly absorbing, *iii)* thin enough so that the projection approximation can be used (the local direction changes of the wave vector within the sample are negligible) and *iv)* is composed of N different materials associated with N refractive indexes $n_{\omega,j} = 1 - \delta_{\omega,j}$ with $j = 1, 2, \dots, N$. As a consequence, equation 2.9 becomes:

$$\varphi_{\omega}(x, y, \lambda) = -k \sum_{j=1}^N \delta_{\omega,j} \cdot T_{\omega,j}(x, y) = -\frac{\omega}{c} \sum_{j=1}^N \delta_{\omega,j} \cdot T_{\omega,j}(x, y) \quad 2.21$$

with $T_{\omega,j}(x, y)$ the projected thickness of each j^{th} material. Finally, equation 2.19 can be generally written as:

$$\bar{I}(x, y; M, k) = \frac{\bar{I}_{z=0}}{M^2} - \frac{d}{M^3} \sum_{j=1}^N \left[\int \delta_{\omega,j} I_{\omega,j} d\omega \right] \nabla_{x,y}^2 T_{\omega,j}(x, y). \quad 2.22$$

Here, \bar{I} is the averaged intensity of the polychromatic beam and $I_{\omega,j}$ are the different spectral weights of the monochromatic waves. Once more, **the intensity recorded with a polychromatic beam undergoing phase contrast modulations is related to the Laplacian of the projected thickness of the N materials.**

Coherence requirements

As discussed above, the monochromaticity of the X-ray beam (temporal coherence) is not a stringent requirement for PB-XPCI, but some spatial coherence constraints are a necessary condition to obtain images with a good level of contrast. The key condition is that the X-ray radiation has a certain spatial, or lateral, coherence so that the phase of two different points on the same wavefront are highly correlated (Wilkins, 1996). The lateral coherence length, or the propagation distance within which the wave is considered coherent, is defined as:

$$c_l = \frac{\lambda l}{\vartheta_s} = \frac{\lambda}{\gamma} \quad 2.23$$

with ϑ_s the source size and γ the angular width of the source as seen from the detector. A high degree of spatial coherence can be thus obtained with a point-like source and/or by placing the sample at a large distance from the source provided that the total flux is appropriate. An incoherent beam will form images at the detector that are shifted by an amount that is proportional to the distance d and ϑ_s , here interpreted as the angle between the two incoherent sources. Thus, the condition for observing the frequency f under optimum condition is $d\vartheta_s \approx D\vartheta_s < 1/f$ and substituting equation 2.19 into equation 2.23, we obtain:

$$\vartheta_s < 2f\lambda. \quad 2.24$$

Thus, **the finite source size puts a limit for the minimum observable spatial frequency and c_l determines the minimal size of an object detail that can be discriminated via XPCI** (Keyriläinen, 2010).

In terms of the spatial coherence, synchrotron facilities are optimum laboratories where to perform XPCI due to the small beam emittance (lateral dimensions), large source to sample distance and the highly intense flux of the produced X-ray beam. Indeed, until now, most of the XPCI developments have been carried out at synchrotron facilities but laboratory and table-top sources for XPCI applications are also in use and many technological progresses have been realized (see paragraph 2.1.5-2.1.6).

Figure 2.4 reports how the source size (ϑ_s) and the detector to sample distance (d) influence the obtainable PBI signal and thus the final result of a PB-XPCI image (from (Paganin, 2019)).

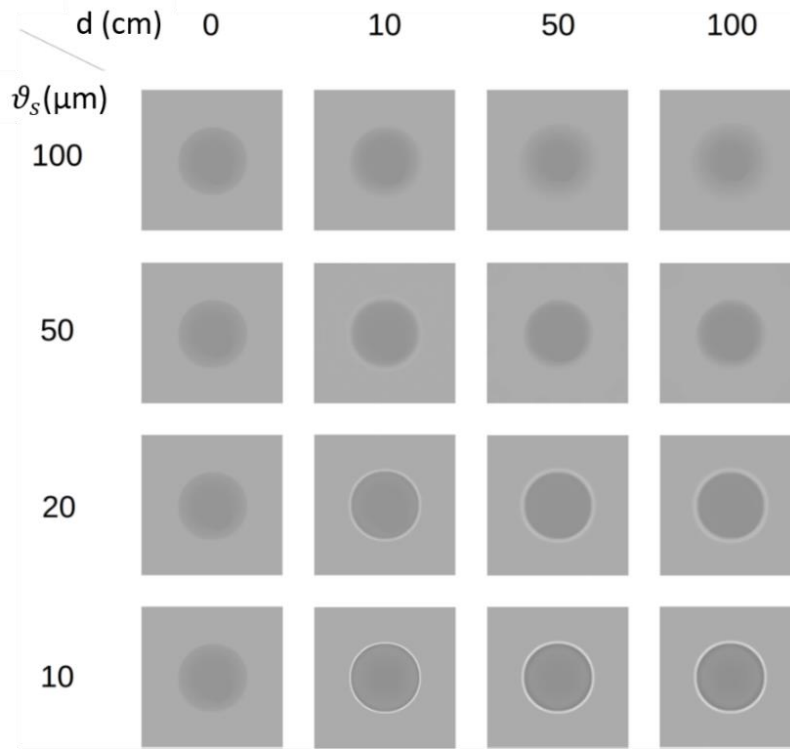


Figure 2.4: simulated propagation-based X-ray phase-contrast images of a solid carbon sphere by varying the source size ϑ_s and the object to detector distance until reaching the optimum distance where the sphere is completely resolved. ϑ_s increases from top to bottom and d increases as one moves from left to right. Figure adapted from (Gureyev, 2009).

Image resolution

Another important requirement for PB-XPCI is that the spatial resolution of the imaging system is sufficiently high to resolve the interference fringes. One can write (Gureyev, 2008):

$$\vartheta_x^2 \approx \left(1 - \frac{1}{M}\right)^2 \vartheta_s^2 + \frac{\vartheta_d^2}{M^2} + \vartheta_m^2 \quad 2.25$$

with ϑ_x and ϑ_d the standard deviation of the system and detector point-spread functions, respectively, ϑ_s the standard deviation of the source intensity distribution and ϑ_m the diffraction term:

$$\vartheta_m = \frac{1}{2} \sqrt{\frac{\lambda d}{2}} \quad 2.26$$

that becomes less significant for increasing X-ray energies, but still remains a limiting factor for ideal systems with small ϑ_d and ϑ_s .

In most applications using biological samples, the number of Fresnel, $N_F = a^2/\lambda d \gg 1$ (Bravin, 2013), puts an upper limit for the propagation distance and a lower limit for the minimum detectable feature of interest (a), often identified with the experimental pixel size. Furthermore, the image resolution depends on the applied image processing and phase retrieval, which may degrade the spatial resolution.

2.1.3 Phase retrieval problem

In the previous sections, the forward problem of X-ray phase contrast imaging was described and a formulation was derived for the intensity variation that the sample will form at the detector when illuminated by a partially coherent X-ray beam. Now, we intend to solve the inverse problem retrieving the sample characteristics ideally performing single phase contrast images, meaning that both phase shift and attenuation are derived from equation 2.18 starting from a single PB-XPCI image acquired at a given sample to detector distance. This problem is known as phase retrieval or phase-amplitude retrieval. As always, solving the inverse problem is more difficult than solving the associated direct one and no closed-form solution exists in general (Paganin, 2019).

Usually, phase retrieval requires at least two measurements of the intensity taken at two different distances from the detector to obtain distinct distributions of the propagated intensity modulation. As a consequence, the contributions generated by the X-ray absorption and the elastic scattering can be untangled (Paganin, 2019). As previously said, solving the problem is still possible by capturing only one image and thus fixing the sample to detector distance. However, the solution that can be obtained is not unique: it is possible to find either a pure phase or absorption object that would produce the same intensity at the detector and, generally, most objects induce both amplitude (X-ray absorption) and phase (refraction) modulations. To solve the phase retrieval problem, many approaches have been proposed and details of the most used algorithms have been described in (Burvall, 2011). As an example, to retrieve the phase and amplitude from one single image, some *a priori* assumptions can be made as: *i*) the object is homogeneous, *ii*) the absorption is constant and thus can be discarded, *iii*) β and δ are proportional to each other.

In the followings, the method presented by Paganin *et al.* in 2002 (Paganin, 2002) will be discussed since it is the method I used in this Thesis work for the phase retrieval of the acquired PB-XPCI datasets.

The phase retrieval method introduced by Paganin starts with the TIE equation (equation 2.18) for monochromatic beams written as:

$$-k \frac{\partial}{\partial z} I(x, y, z) = \nabla_{xy} [I(x, y, z = 0) \nabla_{x,y} \varphi(x, y, z = 0)] \quad 2.27$$

with the assumption of using a **point-source of X-rays placed at infinite distance** l ; this results in a collimated sample illumination and unitary magnification factor M . The second assumption is the **homogeneity of the sample**, i.e. the imaged object is composed of a single material.

Using equation 2.9 and being the object sufficiently thin, the phase at $z = 0$ is proportional to the projected thickness of the homogeneous object:

$$\varphi(x, y, z = 0) = -k \delta(x, y, z, \lambda) T_{obj}(x, y). \quad 2.28$$

If we now use equation 2.1 and equation 2.28, the TIE equation 2.27 becomes:

$$-k \frac{\partial}{\partial z} I(x, y, z) = -k \delta \nabla_{xy} [I_0 e^{-\mu T_{obj}(x,y)} \nabla_{x,y} T_{obj}(x, y)]. \quad 2.29$$

Rearranging each of the two expressions on the two sides we obtain:

$$\frac{\partial}{\partial z} I(x, y, z) \approx \frac{I_d - I_0 e^{-\mu T_{obj}(x,y)}}{d} \quad 2.30$$

and

$$\delta I_0 \nabla_{xy} [e^{-\mu T_{obj}(x,y)} \nabla_{x,y} T_{obj}(x, y)] = -\frac{\delta}{\mu} I_0 \nabla_{xy}^2 e^{-\mu T_{obj}(x,y)} \quad 2.31$$

resulting in:

$$\frac{I_d - I_0 e^{-\mu T_{obj}(x,y)}}{d} = -\frac{\delta}{\mu} I_0 \nabla_{xy}^2 e^{-\mu T_{obj}(x,y)} \quad 2.32$$

and thus:

$$\left(-\frac{\delta d}{\mu} \nabla_{xy}^2 + 1 \right) e^{-\mu T_{obj}(x,y)} = \frac{I_d}{I_0}. \quad 2.33$$

Let's now consider the Fourier integrals of both $I(x, y, z = 0)$ and $I(x, y, z = d)$:

$$I(x, y, z = 0) = I(\mathbf{r}, z = 0) = I_0 e^{-\mu T_{obj}(\mathbf{r})} = \frac{I_0}{2\pi} \iint \mathcal{F}\{e^{-\mu T_{obj}(\mathbf{r})}\} e^{-i\mathbf{k}\cdot\mathbf{r}} d\mathbf{k} \quad 2.34$$

$$I(x, y, z = d) = I(\mathbf{r}, z = d) = \frac{1}{2\pi} \iint \mathcal{F}\{I(\mathbf{r}, z = d)\} e^{-i\mathbf{k}\cdot\mathbf{r}} d\mathbf{k} \quad 2.35$$

and now substitute them into equation 2.33 (Paganin, 2002) obtaining:

$$\mathcal{F}\{e^{-\mu T_{obj}(\mathbf{r})}\} = \frac{1}{I_0} \frac{\mathcal{F}\{I(\mathbf{r}, z=d)\}}{1 + \frac{\delta d}{\mu} |\mathbf{k}|^2}. \quad 2.36$$

Finally, for retrieving a formulation for $T_{obj}(\mathbf{r})$, the inverse Fourier transform of equation 2.36 must be taken:

$$T_{obj}(\mathbf{r}) = -\frac{1}{\mu} \ln \left(\mathcal{F}^{-1} \left\{ \frac{1}{I_0} \frac{\mathcal{F}\{I(\mathbf{r}, z=d)\}}{1 + \frac{\delta d}{\mu} |\mathbf{k}|^2} \right\} \right). \quad 2.37$$

The result of **equation 2.37 is the central result of this section that correlates the projected sample thickness to the intensity and phase at the sample exit surface.**

If we now relax the constraint on the source at infinite distance, the magnification factor modifies equation 2.37 as follows:

$$T_{obj}(\mathbf{r}, M) = -\frac{1}{\mu} \ln \left(\mathcal{F}^{-1} \left\{ \frac{1}{I_0} \frac{\mathcal{F}\{M^2 I(M, \mathbf{r}, z=d)\}}{1 + \frac{\delta d}{M\mu} |\mathbf{k}|^2} \right\} \right) \quad 2.38$$

where the term $\left(1 + \frac{\delta d}{M\mu} |\mathbf{k}|^2\right)^{-1}$ can be viewed as an operator to be applied to the Fourier transform of $I(\mathbf{r}, z = d)$ or as a filter in the frequency domain (see equation 2.8) (Burvall, 2011).

2.1.4 X-ray Phase Contrast Computed Tomography

We now have retrieved both the equation for the forward- (equation 2.18) and back-propagation (equation 2.37) of the X-ray wave exiting the sample. Since PB-XPCI is also used in tomographic mode, let's recall the basics of the image reconstruction procedure.

In computed tomography, hundreds to thousands of 2D projection images of the object are taken in fast succession while either the object or the source-detector system is rotated by 360° or 180° . In XPCI-CT, the reconstruction of the CT dataset can be performed either on the acquired angular projections directly, in this case the signal of the CT images is a mixture of the different contrast contributions (absorption, refraction and scattering), or on the phase retrieved images obtained after the application of a phase retrieval algorithm (e.g. the Paganin's one) to the

acquired angular projections. Different CT reconstruction algorithms (algebraical methods, iterative algorithms and Fourier-based approaches) can then be used to reconstruct the CT dataset. In this Thesis work, I have used the filtered back projection (FBP) algorithm that it is here described.

As already said, a tomographic dataset requires many projections to be acquired at different angles ϑ . From a mathematical point of view, each projection is the line integral of the object spatial distribution:

$$R_{\vartheta}(x, y) = \int f(x, y, z, \vartheta) dz = \int f(x \cos \vartheta - z \cos \vartheta, y, z \cos \vartheta) dz \quad 2.39$$

better known as the Radon transform of the distribution f with y the rotation axis of the sample.

The next step to reconstruct a 3D tomographic slice implies that the Radon transform has to be inverted to obtain the object distribution from a series of recorded $R_{\vartheta}(x, y)$ at different angles. As first, if the assumption of parallel beam geometry holds, every slice to be reconstructed is associated with one unique value of y and can be treated independently. Thus, a 3D problem of reconstructing the full 3D object distribution reduces to a 2D issue for each y value. As an example, Figure 2.5 provides a schematic view of the Radon transform obtained projecting a nonhomogeneous sample along a certain angle. Once all the Radon transforms along all the available angular directions are arranged together, the resulting image is called sinogram, which illustration is reported in the Figure 2.5b.

The further step of a CT reconstruction consists in back-projecting, or assigning, a R_{ϑ} value at each point of the sample, which is not a trivial issue. To do this, the relation between the Radon and Fourier transforms is useful:

$$\mathcal{F}\{R_{\vartheta}(s)\} = P(\omega) = \frac{1}{2\pi} \int_{-\infty}^{\infty} R_{\vartheta}(s) e^{-i\omega s} ds \quad 2.40$$

and the Fourier-slice theorem must be invoked:

$$\mathcal{F}_{1D}\{R(\vartheta_1, s)\} = \mathcal{F}_{2D}\{f(x, y)\}_{|\vartheta=\vartheta_1} \quad 2.41$$

meaning that the one-dimensional (1D) Fourier transform of a projection at a given angle ϑ_1 equals the 2D Fourier transform of the function $f(x, y)$ representing the sample; otherwise written as: **the Fourier transform of the projection, or the Radon transform of the function $f(x, y)$, taken at an angle ϑ_1 gives a slice at an angle ϑ_1 of the 2D Fourier transform of $f(x, y)$.**

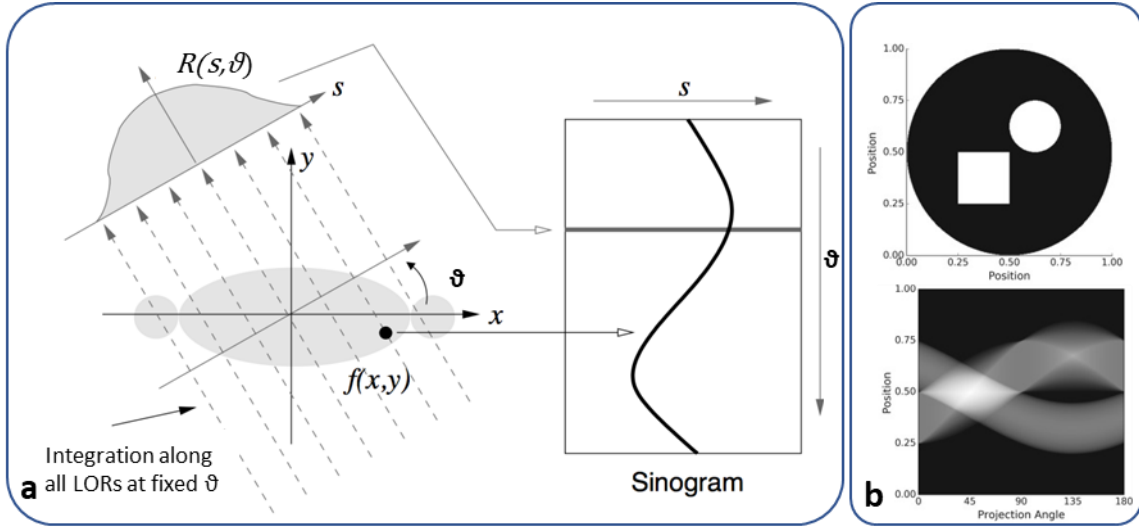


Figure 2.5: (a) sketch of a Radon transform for a nonhomogeneous sample. Each projection, obtained by integrating along all the lines of response (LORs) at a fixed angle ϑ , produces a line in the final sinogram of varying s and fixed ϑ . Indeed, a single object, as the dark circle, is represented in the sinogram as a curved line of varying s and ϑ . (b) showcases how a phantom composed of two different materials is depicted in a sinogram. Figures adapted from (Lecoq, 2020) and (Swan, 2017).

Overall, the function $f(x, y)$ can be written via its inverse Fourier transform:

$$f(x, y) = \mathcal{F}_2^{-1}\{G(u, v)\} = \int_{-\infty}^{\infty} du \int_{-\infty}^{\infty} dv \cdot G(u, v) e^{2\pi i(ux+vy)} \quad 2.42$$

and by using the polar coordinates $u = \omega \cos \vartheta$ and $v = \omega \sin \vartheta$, with $du dv = \omega d\omega d\vartheta$, it becomes:

$$\begin{aligned} f(x, y) &= \int_0^{2\pi} d\vartheta \int_0^{\infty} d\omega \cdot \omega G(\omega \cos \vartheta, \omega \sin \vartheta) e^{2\pi i\omega(x \cos \vartheta + y \sin \vartheta)} \\ &= \int_0^{\pi} d\vartheta \int_{-\infty}^{\infty} d\omega \cdot |\omega| P(\omega) e^{2\pi i\omega s}. \end{aligned} \quad 2.43$$

Equation 2.43 states that $f(x, y)$ can be retrieved by:

- taking the Fourier transform of the projection: $P(\omega) = \mathcal{F}\{R_{\vartheta}(s)\}$;
- multiplying by a frequency filter $|\omega|$;
- taking the inverse Fourier transform of the product;
- projecting it at a value of $s = x \cos \vartheta + y \sin \vartheta$;
- integrating over all the filtered projections.

Thus, from a complete set of 1D projections the original 2D distribution of the sample is retrieved, at a given y , without loss of information. The procedure can be iterated for every y leading to a 3D reconstruction of the imaged object.

2.1.5 Applications of X-ray phase contrast imaging

XPCI applications span over a wide range of research fields: material science, palaeontology, biology, food science, cultural heritage preservation, pre-clinical and clinical studies and many others. In the past years, several review papers have been published presenting and discussing the main XPCI applications (Bravin, 2013; Momose, 2020; Lewis, 2004; Mayo, 2012).

Biomedical applications of XPCI-CT are strongly linked to the investigation of the effects of diseases on biological tissues and organs of both animal and human origin. Impressive results on *pre-clinical* investigations were obtained in the following applications:

- *ex-vivo* human cartilage and bone imaging for degenerative joint diseases, osteoarthritis and rheumatoid arthritis (Li, 2003; Mori, 1999; Wagner, 2005; Muehleman, 2004; Horng, 2014) and *ex-vivo* imaging of the inner structure of human cartilage (Coan, 2008; Coan, 2010; Cooper, 2011);
- *ex-vivo* human breast imaging (Pisano, 2000; Keyriläinen, 2010; Arfelli, 2000);
- *ex-vivo* (Saccomano, 2018; Borisova, 2020) and *in-vivo* (Lewis, 2005; Bayat, 2006; Bayat, 2009; Hooper, 2009; Lovric, 2017a) small-animal lung imaging and airway liquid clearance;
- *ex-vivo* small-animal (McDonald, 2009) and human (Schulz, 2010) brain imaging for the discrimination of different brain anatomical parts, *post-mortem* small-animal model imaging for brain tumour (Pfeiffer, 2007; Barbone, 2018), Alzheimer's disease (Connor, 2009; Pinzer, 2012; Massimi, 2020) and *in situ* brain visualisation in a small-animal model (Croton, 2018);
- *ex-vivo* human (Barbone, 2020b) and small-animal (Bartels, 2015; Cao, 2016; Khimchenko, 2018; Barbone, 2020a) spinal cord imaging for neuron and vascular visualization at high resolution and *ex-vivo* imaging of a multiple sclerosis (Cedola, 2017) and experimental autoimmune encephalomyelitis (Palermo, 2020) small-animal model.

In parallel to pre-clinical studies, some attempts to address XPCI into clinical practice have been made. Clinical trials have started and are running for some

specific applications, such as: *i*) for PB-XPCI mammography and breast CT with both synchrotron sources and conventional X-ray tubes (Dreossi, 2008; Castelli, 2011; Tanaka, 2005); *ii*) for the diagnosis of arthritis with GI (Tanaka J, 2013; Yoshioka, 2020); and *iii*) for the detection of lung diseases as fibrosis (Yaroshenko, 2015) and chronic obstructive pulmonary disease (Hellbach, 2015; Willer, 2021) with X-ray dark field GI- imaging.

2.1.6 X-ray sources for XPCI

Many of the mentioned applications are studies carried out at synchrotrons because the produced intense and highly spatially coherent X-ray beams meet the basic requirements for an XPCI experiment. To bring XPCI investigations into clinical practice, efforts have to be made in developing XPCI methods that can be implemented with existing X-ray sources or with new X-ray sources with intrinsic high coherence and without excessively reducing the available flux. Among the XPCI modalities working well under more relaxed spatial coherence conditions, it is worth to mention the ABI (Connor, 2012), Talbot-Lau interferometers developed for conventional, low-brilliance X-ray sources (Pfeiffer, 2006; Stampanoni, 2011), laboratory-based edge illumination XPCI systems (Olivo, 2013; Marenzana, 2012), grating-based non-interferometric imaging set-up (Wang, 2019b) and speckle phase contrast imaging (Labriet, 2019). As for the new sources, the main results were obtained with inverse Compton approaches (Oliva, 2010), compact laser accelerators (Najmudin, 2014), compact synchrotrons (Van Heekeren, 2011; Töpperwien, 2018b) and liquid metal jet X-ray tubes (Larsson, 2012; Larsson, 2016).

2.2 Small and Wide-Angle X-ray Scattering

SAXS/WAXS is a technique where X-rays are elastically scattered at small angles (typically $0.1^\circ - 5^\circ$) and wide angles (typically $> 5^\circ$) (Liu, 2013) by an inhomogeneous sample where the sub-structures of the dimensions of the nanometre cause the scattering. SAXS/WAXS, being sensitive to molecules of different dimensions, provides information as the shape, size and distribution of macromolecules and characteristic distances of partially ordered materials: SAXS is sensitive to mineral structures with dimensions between 1 and 200 nm, whereas WAXS can retrieve information at atomic length scales between 0.33 nm and 0.49 nm, depending on the available experimental setup. SAXS/WAXS applications are very

broad and include colloids of metals, composites, cement, oil, polymers, plastics, proteins, foods, and pharmaceuticals. Experimentally, this technique requires an intense and collimated monochromatic X-ray beam with a good stability and a solid mechanical setup because of the used small beam sizes (Bolze, 2018). Furthermore, since it is based on the elastic scattering of X-rays when passing through the sample, any source of parasitic scattering must be minimized to achieve sufficient sensitivity for weakly scattering structures. Although lab-based experimental setups are available and widely used, synchrotron facilities are ideally suited to SAXS/WAXS due to the intrinsic high beam brilliance and coherence.

The SAXS/WAXS technique exploits the interference phenomena that occurs between an X-ray beam of a given energy (wavelength comparable to atomic spacings) and the period lattice of the sample, most commonly known as Bragg diffraction. The Bragg law is written as:

$$n\lambda = 2d \sin \vartheta \tag{2.44}$$

and relates the periodically re-occurring distances of lattice planes (d -spacings) to the beam wavelength λ and the Bragg (scattering) angle ϑ ; n is an integer number. As shown in Figure 2.6, a constructive interference pattern is only produced when the difference in terms of optic path travelled by two incident waves that are reflected by two parallel lattice planes in a crystal equals $n\lambda$. Thus, the diffraction angle under which a reflection is observed is 2ϑ .

Theoretically, the outcome of the Bragg diffraction are sharp peaks where the d -spacing and the reflection angles are univocally defined, but in experimental sessions many factors account for a peak broadening as the detector response and the sample imperfections e.g. crystallite size, microstrain and stacking faults.

The intensity of the diffraction pattern is given by the Debye's equation:

$$I(q) = \sum_{ij}^N f_i f_j \frac{\sin(qr_{ij})}{qr_{ij}} e^{-2\sigma_{ij}^2 q^2} \tag{2.45}$$

with f_i and f_j the scattering factors of the i^{th} and j^{th} atom, r_{ij} the distance between the two considered atoms, $q = 2\pi / d$ the scattering vector and σ_{ij} the atomic mean-square displacement.

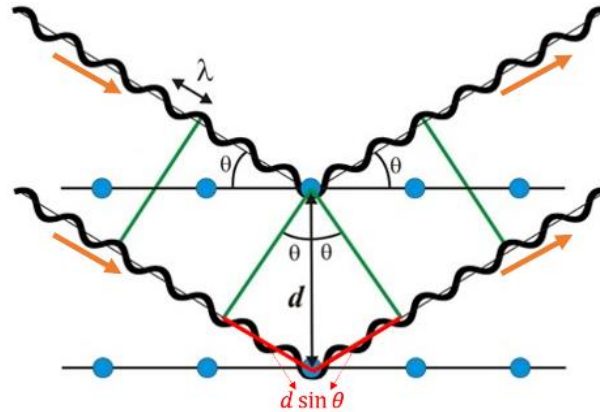


Figure 2.6: representative scheme of the Bragg's law: two waves, impinging on the surface of a crystal, are reflected by two parallel lattice planes. The difference in travelled path is $2d \sin \vartheta$ and causes constructive interference if equal to $n\lambda$.

SAXS/WAXS microscopy uses a setup like the one sketched in Figure 2.7. A monochromatic beam of $\sim 100 \mu\text{m}^2$ of area is typically focused by a bent mirror and delivered to the sample that is raster scanned to obtain the full sample view. SAXS and WAXS data are collected by moving the detector at two different distances with respect to the sample: the closer to the sample, the wider the angles of scattering that are detected.

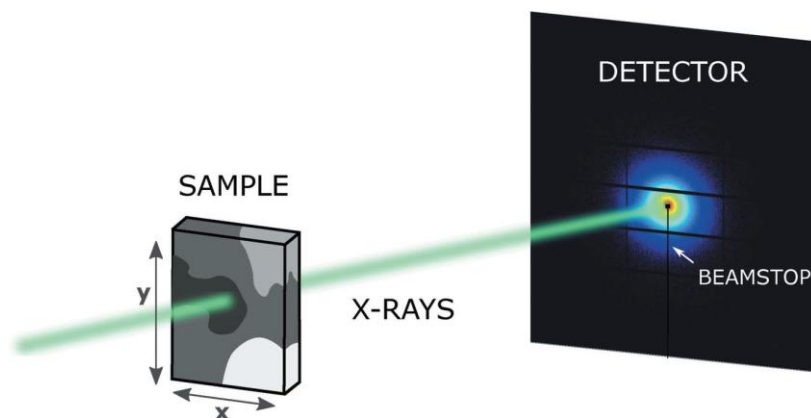


Figure 2.7: simplified view of the SAXS/WAXS experimental setup. The incident monochromatic X-ray beam is focused and delivered through a sample that is placed perpendicular to its travelling direction. The resulting scattering is ruled by the Bragg law and the interference pattern is recorded over 360° by a detector placed at a suitable distance for either SAXS or WAXS experiments. The centre of the detector has a beamstop allowing for recording an X-ray transmission microscopy image. Figure reproduced from (Lutz-Bueno, 2018).

2.2.1 SAXS/WAXS profiles analysis

After a SAXS/WWAXS experimental session, the acquired raw data consist in hundreds of thousands 2D frames. Figure 2.8 displays two representative 2D SAXS/WAXS patterns from different portions of a bone tissue sample: (a) signal from a region of the sample without bone, (b) signal showing a characteristic hydroxyapatite (HAP) frame (Giannini, 2012). Each 2D frame can be azimuthally or meridionally integrated to obtain 1D patterns, which report the detected intensity as a function of the scattering vector q . Depending on the direction of integration along the image, one can retrieve information on the packing of the structure under study along different directions (see Figure 2.8, where WAXS profiles are reported as a showcase).

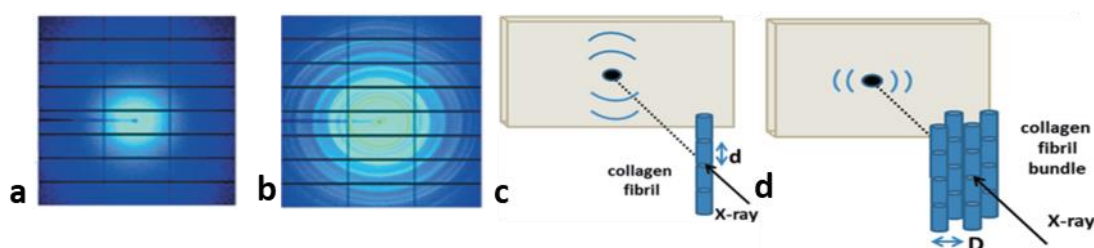


Figure 2.8: typical WAXS 2D profiles for a bone sample taken at different positions in the tissue. (a) is originated from a sample portion where no bone is present, while (b) is the result of the scattering from the mineral component of the bone. The two cartoons (c) and (d) show that the meridional and azimuthal information of the 2D patterns are linked to the studied structure packing along different symmetry axes. The images are referred to a structure containing collagen and calcium minerals and are reproduced from (Giannini, 2014).

Once a 1D profile is obtained from the integration of each 2D frame, a data reduction process is applied. In order to select the important spectra out of the big amount of data produced, from each profile $I_i(q)$ some interesting structures are identified by focusing on the inflection points, i.e. areas of the spectrum where Bragg peaks or intensity slope variations are present and where the first or second derivative of the intensity is zero (Lutz-Bueno, 2018).

To further reduce the number of variables, the Principal Component Analysis (PCA) is applied as described in (Lutz-Bueno, 2018). This and the further steps in data reduction are listed here:

- A set of m principal components are obtained. The different principal components PC_i with $i=1, \dots, m$ are related to the functions that produce the maximum variance by subtracting the i^{th} component from the initial

or residual dataset with the constraint that any selected component is uncorrelated from all the lower order components.

- The number of considered PCs is obtained by plotting the portion of the total variance accounted for the i^{th} component as a function of PC_i .
- As showed in Figure 2.9a, an L-shaped curve is obtained. Here, the position of the knee indicated by the arrow defines the number m of PCs representative of the dataset.
- Now, the obtained principal components are grouped into clusters representing each a main type of signal originated by the scattering with the sample.
- The suitable number of clusters is chosen by the *k-means* method (Lloyd, 1982) applying the silhouette graphical display criterion (Rousseeuw, 1987) showing which signals lie well into a cluster and which ones are located among them. From that, it is also possible to distinguish if each cluster is isolated or not. Using a Euclidean distance metrics, each signal is assigned to a value between -1 and 1, where 1 accounts for the best matching of the signal with its own cluster. The average of the values is computed as a function of the selected clusters number as in Figure 2.9b.
- The optimum number of clusters is then chosen as the one that maximises the curve (Lutz-Bueno, 2018).
- At each cluster is then assigned a representative signal $S_k(q)$ depending on the nature of the cluster. If a cluster is isolated, the representative signal will be the average of all the signals belonging to it. On the contrary, if some cluster have a mixed nature, and thus signals belonging to more than one cluster, $S_k(q)$ is identified from the subset containing the most uncorrelated signals avoiding the overlapping interfaces between clusters.
- The n $S_k(q)$ signals are thus representative of the entire specimen and an example is given in Figure 2.9c.
- The identification of n representative signals is used to divide the scanning SAXS/WAXS measurements into n segments, assigning to each pixel

of the 2D detector one cluster and segmenting the image of the sample into n regions as in Figure 2.9d.

- Then, a whole profile fitting, the Rietveld analysis, is performed on each 1D profile and it accounts for the crystal structure model and possible shape anisotropies. Figure 2.9e showcases the Rietveld analysis on a typical WAXS representative signal where the different Bragg peaks originate from the scattering of the represented material at different angles and thus along different directions in the crystalline structure.

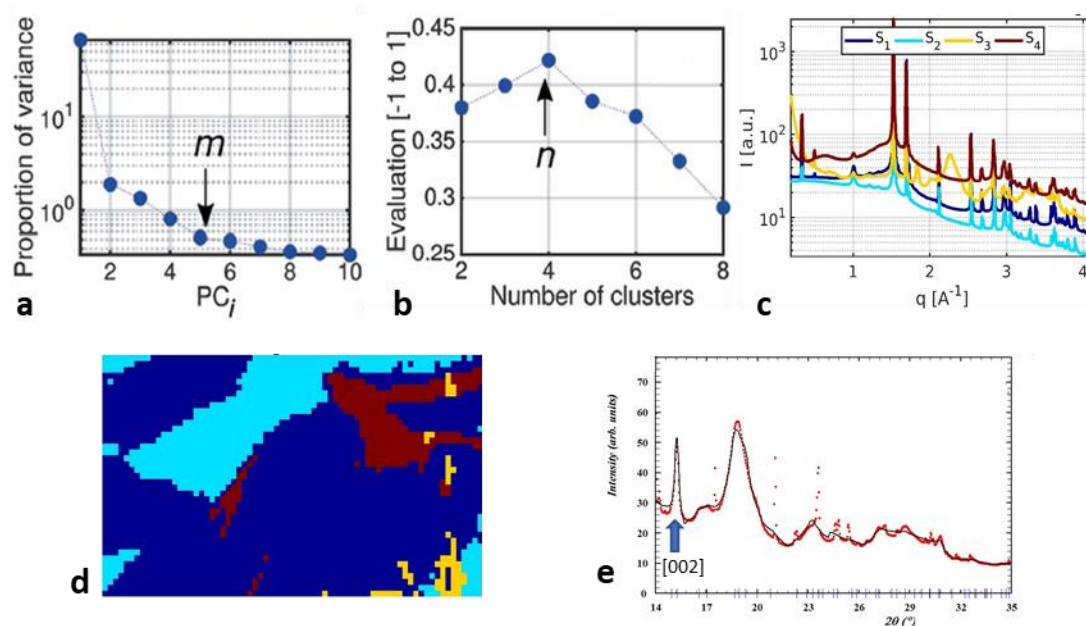


Figure 2.9: (a) L-shaped curve resulting from the Principal Component Analysis displaying the portion of variance as a function of the principal components. The knee point defines the number of m principal components to consider for the sample under study. (b) graphic representation of the evaluation of the optimum number n of cluster. (c) representative signals of the selected clusters, (d) scanned sample image segmented and coloured according to the cluster results and (e) Rietveld analysis of one representative signal. The arrow indicates the reflection along the 002 crystallographic direction. Figures a-b adapted from (Lutz-Bueno, 2018).

The Rietveld analysis is based on the Scherrer formula and considers all the detected reflections, originating from the material represented by the signal, and extracts the crystalline domain values of this material along the different crystallographic directions. Furthermore, the material associated with each 1D profile can be univocally identified by detecting the position of the most predominant peaks along specific crystalline domains that correspond to particular angles of

scattering (or q values). The identification is based on a crystallography information file released by the International Union of Crystallography and implemented in dedicated analysis software.

The Scherrer formula is the simplest way to estimate the dimension of the crystalline domain (single-peak measurement) from the full width at half maximum (FWHM) of the peak along a selected crystallographic direction. Thus, the size of the crystalline particles (i.e. crystalline domain) for a specified material, analysed along a single diffracted peak is (Scherrer, 1918):

$$D = \frac{\lambda}{\Delta(2\vartheta) \cdot \cos\vartheta} = \frac{\lambda}{FWHM \cdot \cos\vartheta} \quad 2.46$$

with λ the wavelength of the incident radiation and ϑ the half value of the Bragg angle. More precisely, a volume weighted domain size is computed as (David, 2010):

$$\langle D \rangle_v = \frac{p\lambda}{\Delta(2\vartheta) \cdot \cos\vartheta} \quad 2.47$$

with p the Scherrer constant, which considers the crystallite shape and is normally taken as 0.9 (Monshi, 2012). This latter equation is valid for gaussian profiles, but experimental peaks are better adaptable to a Voigt function, which is the convolution of a Gaussian with a Lorentzian one (David, 2010). To overcome this problem, a more general Scherrer formula is based on substituting the FWHM with the integral breadth, which is defined as the area of a peak divided by its height (Stokes, 1942). Furthermore, the peak broadening caused by both the detecting instrument and possible lattice strains has to be kept under consideration. Let B be the detected profile and β be the FWHM of the single SAXS/WAXS peak and thus the width of the pure signal, the detector broadening is accounted through the parameter b as $B = b + \beta$ or $B^2 = b^2 + \beta^2$ for a Lorentz or Gaussian profile shape, respectively. The contribution due to crystallite size is considered by means of β_n as $\beta' = \beta^2 + \beta_n^2$ or $\beta' = \beta + \beta_n$ if both terms of the equations are Gaussian or Lorentz, respectively (Monshi, 2012). For the strain contribution it is also possible to write (Danilchenko, 2002):

$$\varepsilon = \left| \frac{\Delta d}{d} \right| = \frac{\beta_n}{4 \cdot \tan\vartheta} \quad 2.48$$

where $\Delta d/d$ is the change in d -spacing, the structure packing, that occurs in a strained sample with respect to the unstrained case.

Thus, separating the size and strain contributions:

$$\beta' = \frac{\lambda}{L \cdot \cos \vartheta} + 4\varepsilon \cdot \tan \vartheta. \quad 2.49$$

2.2.2 Applications of SAXS/WAXS

The SAXS/WAXS technique is applied in many different fields to understand the inner structure of materials improving the control of chemical-physical and biologic processes of complex (bio-)materials at the molecular length scales (Lombardo, 2020). Some of the main applications in the biomedical domain are:

- bone hierarchical structure with the study of the orientation of HAP within the collagen fibres (Fratzl, 1997; Giannini, 2012; Giannini, 2014; Danilchenko, 2002);
- bundles and networks of cytoskeletal keratin intermediate filament proteins (Hémonnot, 2016; Weinhausen, 2012);
- actin fibre structure and myosin II concentration (Priebe, 2014);
- structural orientation of differentiated stem cells and naive human mesenchymal stem cells (Bernhardt, 2016);
- malignant microcalcification formation in breast (Vanna, 2020);
- representation of gene disruption in laboratory mice after papaver somniferum extracts administration as analgesic (Manglik, 2012; Sayers, 2017).

Chapter 3

Irradiation experiments at the European Synchrotron

In this chapter the description of the animals' irradiation experiments as well as of the methods used for the RT follow-up is provided. All RT sessions were conducted at the biomedical beamline ID17 of the ESRF and thus a brief description of the ESRF (as before the recent upgrade) is included in this chapter as a showcase of third-generation synchrotron source. A short mention of the ESRF upgrade to a fourth-generation source (realized in 2019-2020) is also reported.

3.1 The European Synchrotron Radiation Facility

In 1988 the ESRF was built as a collaborative effort of twelve European countries to obtain the first third-generation synchrotron in the world. In 2018, the ESRF counted twenty-two partners, thirteen Member States, nine Associate countries and forty-four operating beamlines dedicated to various applications.

The ESRF, as the other synchrotron facilities, is designed with four main components: an electron source, a LINAC, a booster and a storage ring, as shown in Figure 3.1. The **electron source** is an electron gun placed at the beginning of the LINAC that produces electrons thanks to the thermoionic emission. Electrons are then inserted into a short standing wave buncher and then into the **LINAC** consisting of two 6 m long accelerating sections. At the end of the LINAC, 200 MeV electrons are injected into the **first transfer line** (16 m long) and into the **booster ring**, a 300 m long accelerating section where electrons reach the energy of 6 GeV and an emittance of the order of 10^{-7} mrad. The booster ring only operates for the storage ring refill occurring a few times a day, depending on the synchrotron operation mode. A **second transfer** line, 66 m long, connects the booster to the storage ring. The **storage ring** has a circumference of 844 m and stores electrons at 6 GeV; the energy losses due to the emission of radiation are compensated by 4 radiofrequency chambers. For further details, see <https://www.esrf.eu>.

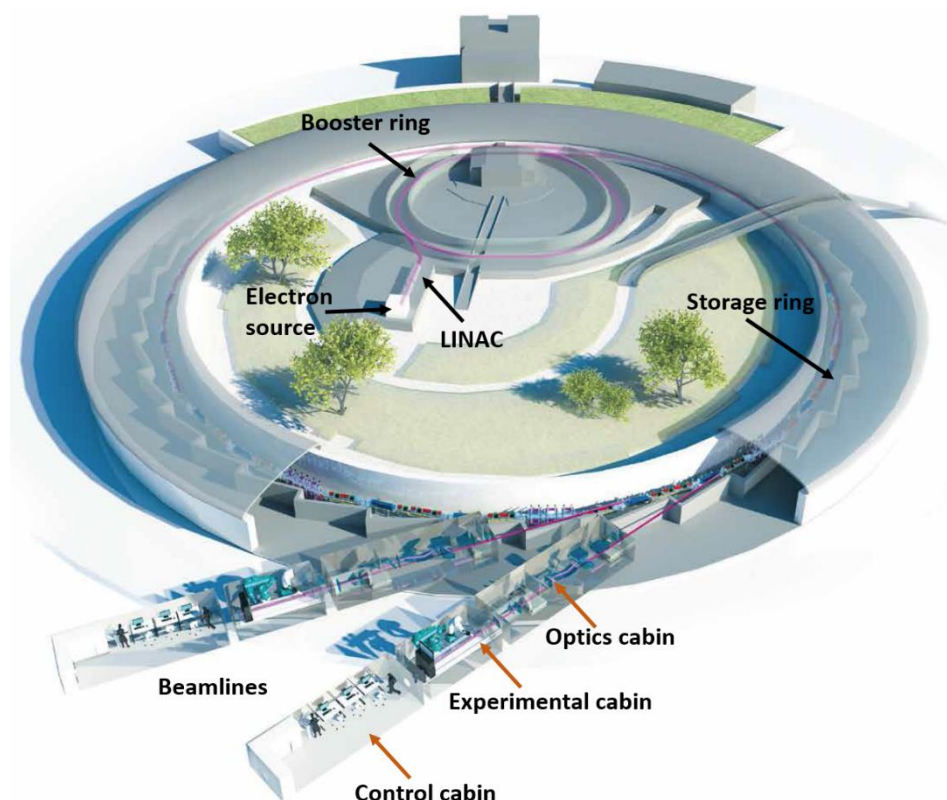


Figure 3.1: scheme of the ESRF composed by a 200 MeV linear accelerator (LINAC), a booster ring to reach the nominal electron beam energy, a 6 GeV storage ring and several beamlines with optics, experimental and control cabins. The magenta line shows the electron and afterwards the X-rays paths through the facility. Figure adapted from <https://www.esrf.eu>.

Key component to obtain synchrotron light into the beamlines are the dipoles, or otherwise named bending magnets, and the so-called insertion devices (IDs), which can be either a wiggler or an undulator, all forcing the beam to change trajectory and to produce X-rays tangentially. Depending on the used device, the X-rays are emitted and delivered to the beamlines with different properties (for details see (Wiedemann, 2015; Clarke, 2014)). The emitted X-ray beams are directed towards the beamlines (see Figure 3.1) that are built tangentially to the storage ring. The first part of the beamline is the optics cabin, where the beam is geometrically and spectrally adjusted to fit the requirements of the specific technique the beamline is designed for. The experimental cabin is where the experiment takes place and the control cabin is equipped for remote controlling the beam delivery and the experimental setup. In the following sections, a detailed description of the biomedical beamline ID17 is given.

Synchrotron sources are, nowadays, widely used in different research fields for the high flux (i.e. high brilliance), coherence and small angular divergence of the

produced X-ray beams. For RT purposes, the high flux allows the realization of fast and high-dose RT protocols while for XPCI-CT applications, the optimization of the three aforementioned parameters is crucial for obtaining images of thick samples with high contrast (i.e. high sensitivity) and at spatial resolution down to the micrometre or nanometre.

With the ESRF upgrade to the Extremely Brilliant Source (EBS), the brilliance and coherence of the produced X-rays in some beamlines has been increased by a factor of 100 thanks to a completely new magnetic lattice installed in the storage ring (see Figure 3.2). Some of the main improvements obtained with the ESRF-EBS upgrade are reported in Table 3.1.

Table 3.1: ESRF and ESRF-EBS main parameters (<https://www.esrf.eu>).

	ESRF	ESRF-EBS
Operational emittance (H-V) (pm)	4000 - 5	110 - 5
Energy spread	$1.06 \cdot 10^{-3}$	$0.93 \cdot 10^{-3}$
Energy loss/turn (MeV)	4.90	2.52

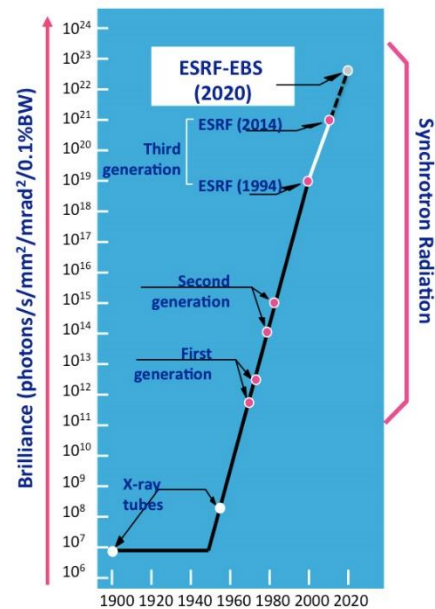


Figure 3.2: Brilliance of the ESRF, ESRF-EBS and other X-ray sources. Figure from <https://www.esrf.eu>.

3.1.1 The ID17 biomedical beamline

The ID17 beamline is one of the “long” beamlines of the ESRF that is mainly used for biomedical-related applications ranging from MRT, radiobiology, *ex-vivo* and *in-vivo* XPCI planar and CT imaging and K-edge subtraction imaging. Typical biological samples are small animal models and human organs/tissues. A schematic view of the beamline layout is given in Figure 3.3.

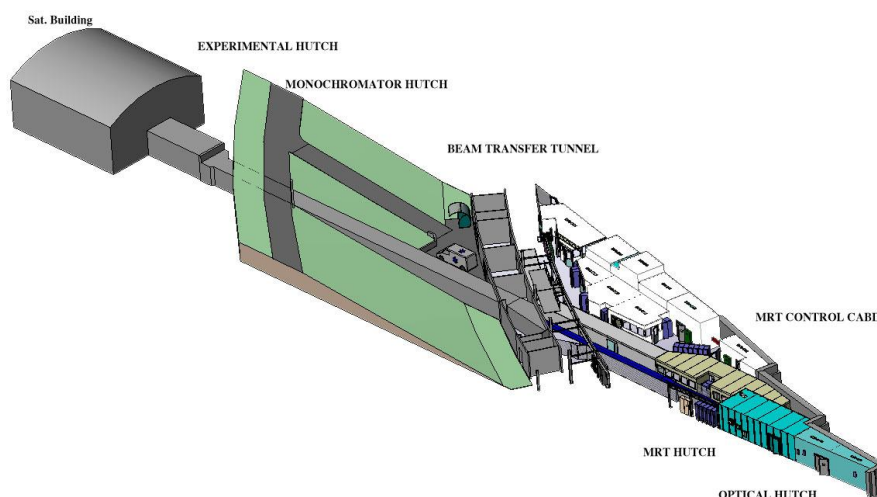


Figure 3.3: scheme of the ID17 beamline. The X-ray beam obtained from the two wiggler sources is driven in the first experimental hutch (MRT hutch – EH1) where a polychromatic beam is available, or delivered to the second experimental hutch (monochromator hutch – EH2) after the beam is monochromatized. Figure from www.esrf.eu.

The X-ray source are two wigglers, $w150$ and $w125$, that can operate simultaneously. The $w150$ is a multi-pole wiggler magnet with 21 poles, a period of 15 cm and maximum magnetic field of 1.6 T with the gap at the minimum value, i.e. 24.8 mm. The $w125$ is a 22-pole wiggler with a period of 12.5 cm (maximum magnetic field of 1.8 T with the minimum gap, i.e. 11 mm). The maximum settable gap is 200 mm for both the wigglers. The beamline has two experimental hutches (EH1 and EH2), as showed in Figure 3.3, located at ~ 38.5 m and ~ 148.5 m from the $w150$ source, respectively. EH2 is placed outside the experimental hall in a satellite building and a 100 m long beam transfer tunnel connects the two hutches. The X-ray beam can be alternatively used in one of the two experimental hutches: EH1 receives the intense polychromatic X-ray beam from the wigglers (after filtration the beam is referred to as “pink beam”), while EH2 presently works only with monochromatic radiation. To transfer the X-ray beam from the source to the EH1, some vacuum sections are present and separated by two beryllium windows; afterwards, vertical and horizontal slits are used to shape geometrically and in dimensions the X-ray beam, while remotely controlled filters (Al, W, C, Cu) are used to shape the beam energetically. A fast shutter and a personnel safety shutter are added to prevent unwanted radiation in the experimental hutch.

The EH1 hosts the experimental setups for MRT irradiation and high resolution (down to sub-micrometre) XPCI-CT imaging (in propagation-based phase contrast mode). If an MRT irradiation experiment has to be performed, a multi-slit collimator, to spatially fractionate the beam, is placed upstream to a kappa-type goniometer (Huber, Germany) used for animal positioning and irradiation. Conversely, if a “pink beam” imaging experiment has to be performed, an in-air fast shutter, consisting of two rotating tungsten carbide blades is activated and the tomography setup is installed after the goniometer at a distance between 42.6 and 45.5 m from the source (Mittone, 2020). The fast shutter is synchronized with the tomographic acquisition to prevent the sample and detector exposure during imaging dead times. A beam shutter is placed at the end of the hutch to prevent the radiation to leak in the rest of the beamline (Elleaume, 1999).

When the X-ray beam needs to be transported up to the EH2, in the EH1 two beryllium windows can be connected by a long pipe to create an additional vacuum section to transport the beam in the satellite building. The long distance between the two hutches and the natural horizontal divergence of the beam (~ 1 mrad) allows obtaining a wide fan beam in the EH2. The second optics hutch has installed a set of slits, absorbers, beam monitors and monochromators. For XPCI-CT purposes, a double crystal system monochromator is used. The system is a pair of bent Laue-Laue Si(111) crystals that can select energies in the range of 25-150 keV. Just before the EH2, a fast shutter is placed. Other monochromator systems (e.g. a single bent Si Laue crystal) are installed and used for other kinds of experiments.

3.2 The irradiation experimental procedures

The irradiation of animals realized within this Ph.D. work have been performed at the ID17 beamline, which is the unique place in Europe where it is possible to apply MRT. Furthermore, the ID17 beamline hosts an animal facility that can provide animal care, housing, follow-up and sample preparation after animal euthanasia. As already mentioned, irradiations take place in the EH1. Pictures of the setup and goniometer stage used for animal positioning are shown in Figure 3.4.

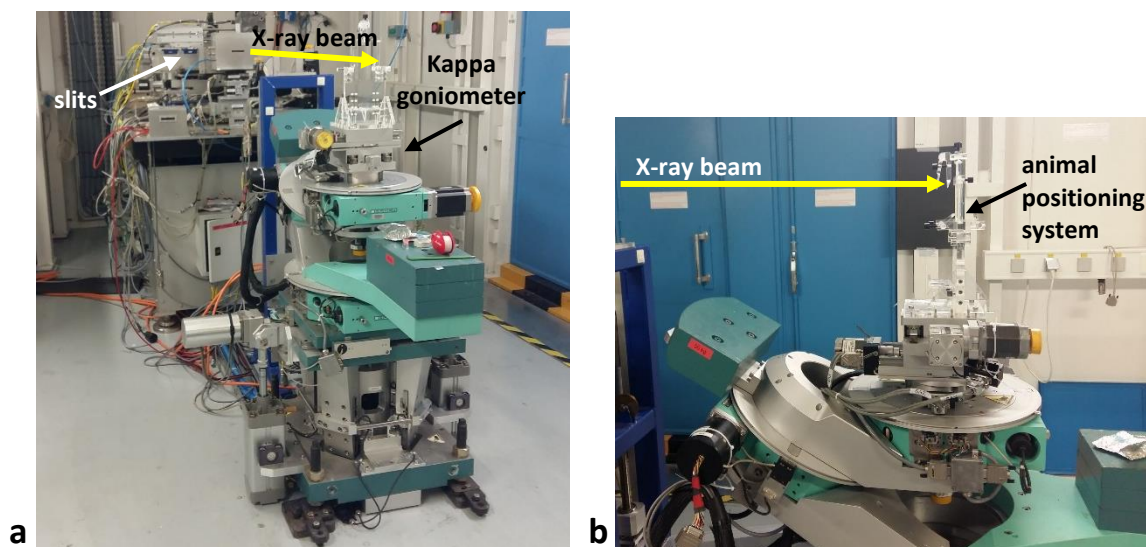


Figure 3.4: pictures of the EH1 for in-vivo animal irradiation. The X-ray beam, indicated by the yellow arrow, is filtered by some metal absorbers and shaped by slits collimators to the desired vertical and horizontal dimensions. The goniometer allows for the precise positioning of the animal by means of translation and rotation motor stages that are remotely controlled. Figure (b) reproduced from (Romano, 2021a).

A set of remotely controlled filters (C, Al and Cu) placed in the first optics cabin allows removing the low energies from the X-ray beam and obtaining a spectrum as the one shown in section 3.2.1. In the EH1, the photon beam is geometrically adjusted in its vertical and horizontal dimensions by means of slits and further fractionated by a multi-slit collimator (Bräuer-Krisch, 2009) for MRT and MB irradiations. About 80 cm downstream, the animal to be treated is positioned on the high-precision goniometer thanks to a custom-made animal holder. The goniometer allows for the animal rotation and positioning with six degrees of freedom. At this position, the maximum beam dimensions are 2.5 mm in height and 41 mm in width, approximately (Prezado, 2011a) and the vertical beam intensity distribution is gaussian; the available set of tungsten slits is used to vertically reshape the beam down 0.5 mm to obtain a uniform irradiation field. On the opposite side of EH1 with respect to the beam entrance, a Fast Readout Low Noise (FRLoN) camera (Coan, 2006) is placed for image guidance. Beam filters, slits and the movements of the goniometer are all remotely controlled by the operator in the control cabin.

3.2.1 The irradiation spectrum

Within the framework of this Thesis, BB, MRT and MB irradiations were performed on rat brains and lungs. Details on the experimental settings to obtain the “standard” MRT-ESRF spectrum that was used in the experimental sessions are given in Table 3.2. The resulting spectrum calculated with the *XOP* software (del Rio, 2004) is shown in Figure 3.5 and has a peak energy at 84 keV.

Table 3.2: beam parameters used for BB, MRT and MB irradiations.

Irradiation beam parameters	
<i>w</i> 150 gap	24.76 mm
<i>w</i> 125 gap	200 mm
Ring current (mean value) ³	88 mA
Beam filters	C = 1.15 mm, Al = 1.52 mm, Cu = 1.04 mm

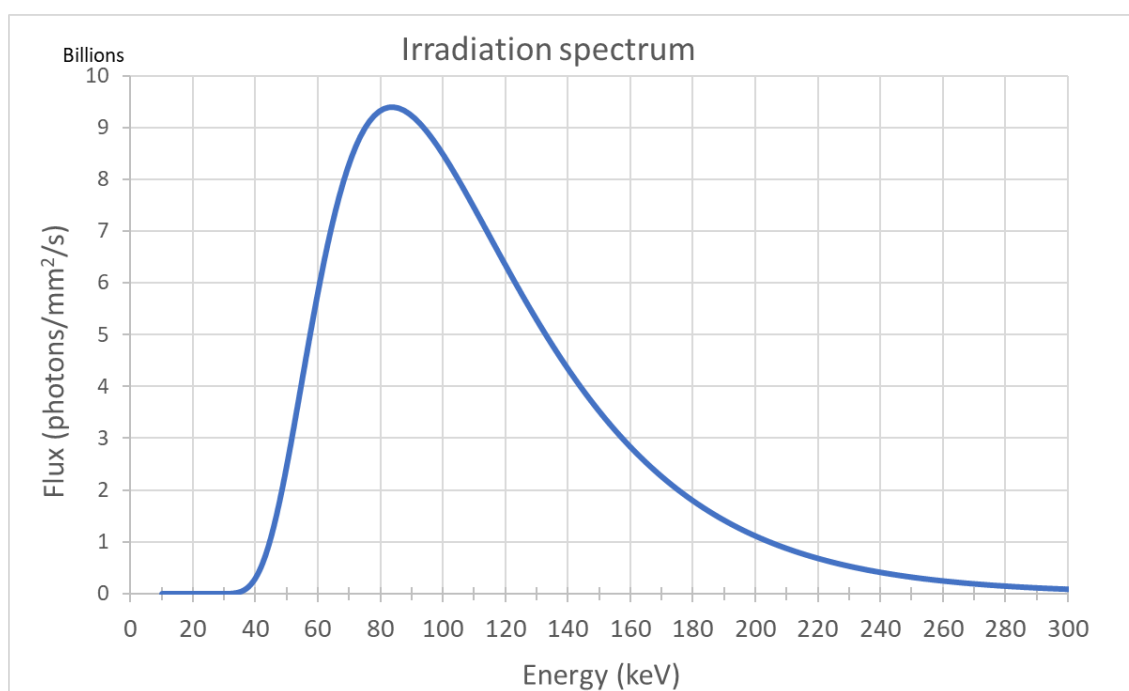


Figure 3.5: An example of the typical ESRF-ID17 irradiation spectrum. The low energy components are removed by the applied filters and the resulting peak energy is 84 keV.

³ This mean value is obtained with a top-up filling mode where the beam in the storage ring is refilled every 20 minutes obtaining a nearly constant beam current.

3.2.2 The dosimetry procedure

Before any irradiation session, the X-ray beam is calibrated in terms of radiation dose with the help of an ionization chamber. It is worth to say that since the ID17 beam is limited in height (the beam is laminar), irradiations are performed by vertically swiping the target through the beam at constant speed. Thus, dosimetry is performed by scanning the ionization chamber with a constant speed, which was proven to be equivalent to a uniform irradiation of the dosimeter (Prezado, 2011b). A PTW semiflex ionization chamber (PTW31002) of 0.125 cm³ in volume was used for dose measurements together with a homogeneous RW3 (Goettingen White Water) solid water phantom of 18x18x18 cm³ of volume. The first step consists in determining the absorbed dose under reference conditions according to (IAEA, 2005), i.e. in a 2x2 cm² irradiation field. The centre of the PTW ionization chamber, chosen as the chamber reference point, was placed at 2 g·cm⁻², that is the reference depth. The obtained absorbed dose for the beam quality Q is:

$$D_Q = M_Q N_{Q_0} K_{Q,Q_0} \tag{3.1}$$

where M_Q is the chamber output corrected for air pressure and temperature, the ion collection efficiency and polarization voltage effect; N_{Q_0} is the calibration factor obtained for a beam quality Q_0 in the calibration laboratory with the chamber in water; K_{Q,Q_0} is a factor taking into account the differences between the calibration beam quality Q_0 and the used one Q . This procedure was used to calibrate the BB irradiation in my Thesis experiments.

For the MRT and MB irradiations, scatter factors were included in order to translate the dose deposited by a full BB into the one delivered within the peaks of MRT and MB beamlets. The scatter factors are those of the collimator (S_c) and of the phantom (S_p) and account for the contribution to the absorbed dose of the scattered radiation from these two objects. Due to the distance between the collimator and the animal, the collimator scattering factor can be neglected (Prezado, 2011b). As a result, the deposited dose at 2 cm of depth by one single beamlet is:

$$D_{peak,2\text{ cm}} = D_Q \cdot S_p \cdot f_{array} \tag{3.2}$$

with D_Q the dose obtained with equation 3.1 and f_{array} a factor accounting for the contribution of the valleys to the peak when an array of beamlets is used. Both S_p and f_{array} were assessed by MCS.

3.2.3 Animal positioning and beam delivery

After the beam dosimetry is accomplished, the area to be treated and the FReLON camera are correctly aligned with the beam. Sub-millimetric precision in the alignment is crucial. Thus, every animal has to be correctly positioned and this is checked via an X-ray imaging protocol to be applied before the irradiation.

Before the experiment, animals are anaesthetised and fixed by the skull on the animal positioning system as shown in Figure 3.4 and Figure 3.6. In this work, brain and lung irradiations were performed with dose prescriptions assessed by MCS as explained in the paragraph 3.3. The rat positioning for brain irradiations is presented in Figure 3.6, while the positioning system for lung irradiation is slightly different due to the fact that the animal is connected to a respirator to control the breathing and to arrest the organ motion during the irradiation.



Figure 3.6: rat positioning for the MRT irradiation in the EH1 of the ID17 beamline. The X-ray beam path is identified by the yellow arrow that points at the RT target which is, in this case, the right brain hemisphere. The zoomed picture shows how the rat head is blocked.

After the animal positioning, a Gafchromic film is placed just before the area to be irradiated to verify the effective irradiation. The RT target is then aligned with the beam. As described in (Nemoz, 2016), the horizontal and vertical slits are fully opened and the *w150* gap is set to 100 mm. A radiographic image is then acquired and the centring of the irradiation target is obtained by means of a dedicated software. For the brain RT of my Thesis, the reference feature on the animal skull for the alignment is the bregma point (Figure 3.7). The beam centre is vertically centred with the bregma, while is displaced of 3.5 mm horizontally in order to only irradiate the right hemisphere. Figure 3.7 shows (a) the monitoring system of the rat (three cameras allow for the animal monitoring) and the radiograph used for aligning the irradiation target; (b) the radiograph together with the bregma indication and the FOI; (c) the scheme of the rat skull with the bregma point indication; (d) the rat head with the resulting MB trace on a Gafchromic film after the RT.

Once the FOI centring is realized, the wiggler gap and the absorber filters are modified according to the parameters given in Table 3.2. The horizontal and vertical slits are closed to obtain the desired FOI, the multi-slit collimator is eventually inserted and the FReLON camera is moved behind a lead cabinet to prevent its exposure. During the irradiation, the animal is moved vertically in order to cover the full volume to be treated. Depending on the needed dose rate the translation speed ranges from 30 to 80 mm/s and is kept constant by a feedback system (Serduc, 2010). High dose rate ($\sim 14\text{kGy/s}$) and fast translation speed are important to avoid the beam smearing due to cardiosynchronous movements of the tissues (Requardt, 2010). Precise alignment and fast irradiations are of paramount importance when microbeams with a width of the order of $50\ \mu\text{m}$ are delivered, since even small movements might provoke the beams smearing. The delivery of such highly collimated arrays of X-ray beamlets is presently most easily done at third-generation synchrotron sources due to the available high dose rates that enable fast high dose irradiations. Established research programs are running at the ESRF (Bravin, 2015) and the Australian Light Source (Stevenson, 2017).

In this Thesis BB, MRT and MB irradiations were delivered on brains and lungs of Fisher rats with the ESRF-ID17 source as before the EBS upgrade; details are given in the followings.

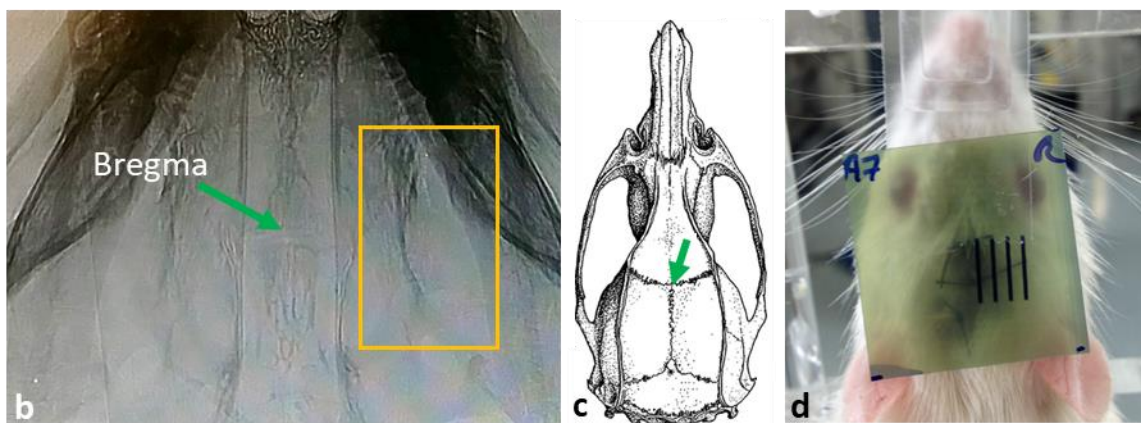
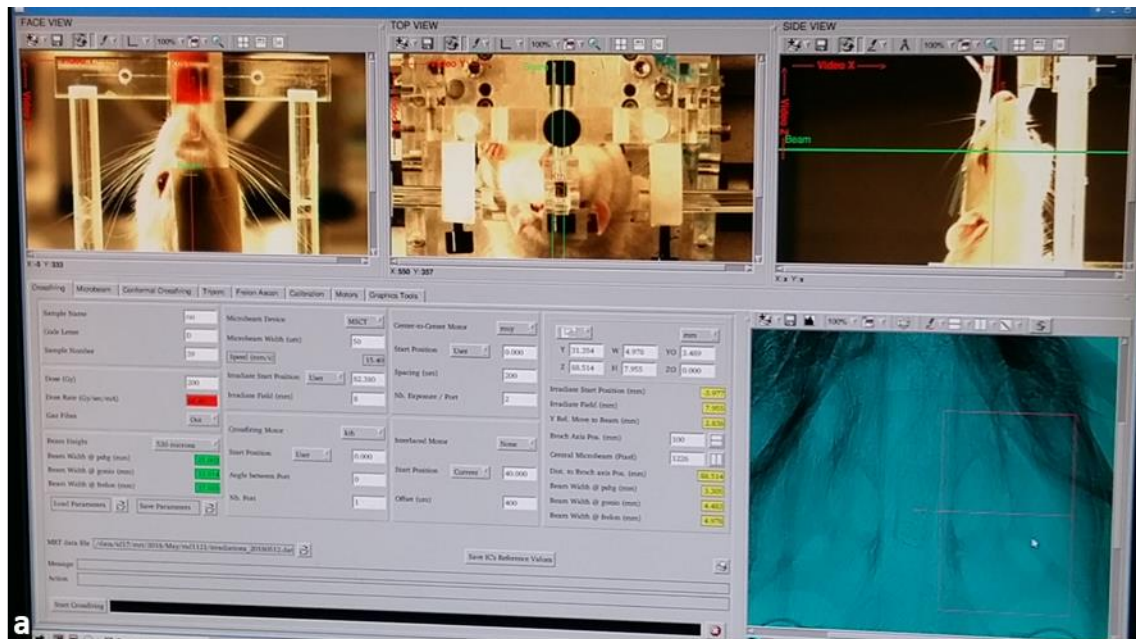


Figure 3.7: (a) animal control and RT delivery software. Three different cameras point at the animal and allow for checking its status and position. The image in the bottom-right corner of the screen is the animal radiograph taken just before the radiotherapy delivery to centre the correct target area with the beam. (b) A rat radiograph with the indication of the bregma point (green arrow) and the field of irradiation; (c) a scheme of the rat skull with the indication of the bregma; (d) picture of an irradiated rat with a Gafchromic film placed just before the animal for checking the correct delivery of the X-ray beam. Figure (d) reproduced from (Romano, 2021a).

Rat brain irradiations

Rat brain irradiations were realized in two different experimental sessions at ID17, in which I have participated, involving a total of eighty-three male Fisher rats. At the age of 8 weeks, fifty-eight of these animals were implanted with 9L glioblastoma cell-line according to reported protocols (Régnaud, 2008a; Régnaud, 2008b). The 9L cell-line was chosen since it is the most widely used rat brain tumour model (Barth, 1999) that closely simulates glioblastoma multiforme when

implanted *in vivo* (Ghods, 2007). The day of the implantation is, for all the animals, the starting point of the experiment, namely day 0 (D0). At D10, all healthy and tumour-bearing rats, but the control groups, were irradiated under anaesthesia with different irradiation protocols, as listed in Table 3.3.

Table 3.3: irradiation groups and beams parameters for BB, MRT and MB brain irradiations. MRT and MB have a different horizontal FOI to ensure an integer number of beamlets in the FOI: 24 for MRT, 7 and 4 for MB with c-t-c distances of 1000 and 2000 μm , respectively.

Group name	FOI HxV (mm ²)	Peak dose (Gy)	Valley dose (Gy)	Beam width (μm)	c-t-c distance (μm)	GBM-implanted animals	Healthy animals
BB5	5x8	5	-	-	-	2	3
BB10	5x8	10	-	-	-	4	3
BB15	5x8	15	-	-	-	7	4
MRT200	5x8	200	7.0	50	200	6	2
MRT400	5x8	400	14.0	50	200	6	2
MRT600	5x8	600	21.0	50	200	9	2
MB180	6.5x8	180	7.2	500	1000	4	2
MB350	6.5x8	350	14.0	500	1000	8	3
MB150	6.5x8	150	2.9	500	2000	4	0
MB450	6.5x8	450	8.8	500	2000	4	0
Control (untreated)	-	-	-	-	-	4	4
Total	-	-	-	-	-	58	25

Three dose values for the BB irradiations were chosen below the tolerance limit for seamless radiotherapies of about 20 Gy (Dilmanian, 2002), while the MRT and MB peak doses were chosen for granting a corresponding valley dose within the

same limit by means of MCS (see section 3.3). Two animal groups, one for healthy and one for GBM-bearing animals, were not irradiated and left as control to check the natural tumour evolution and to have a reference of the rat brain morphology without any tumour or delivered RT. For disambiguation, the two control groups are named healthy- and GBM-control, respectively. The pre-RT anaesthesia protocol included isoflurane inhalation (4% for two minutes) for induction and an intraperitoneal injection of xylazine/ketamine (64.5/5.4 mg/kg) cocktail for maintenance. All the irradiations were performed in the antero-posterior direction (see Figure 3.6 and Figure 3.7d) avoiding to have the eye in the FOI.

The groups for the RT are not homogeneous in terms of number of animals due to the fact that the first experimental session was also meant to study the survival of the different groups and that the number of animals per group in the second experimental session was tuned on the previously obtained results, i.e. some irradiation geometries or dose levels were not used in the second irradiation session because a too low survival was obtained.

The beam reshaping for the MRT and MB cases was achieved by using a multi-slit collimator (paragraph 3.2.1). For MRT irradiations a collimator providing beamlets with the exact planned dimensions was available, while for the MB case it was used a collimator with apertures of 500 μm and c-t-c distance of 4000 μm and the irradiations with 2000 μm and 1000 μm c-t-c distances were realized with two and three subsequent irradiations, respectively, displacing the animal in the horizontal direction.

Rat lung irradiations

Rat lung irradiations were realized at ID17 in one single experimental session involving a total of thirty-three male, eight weeks-old, healthy Fisher rats. Irradiations were performed in the framework of a collaboration with the ESRF, Varian Medical Systems Inc. and the Institute of Anatomy of the University of Bern, Switzerland. Three different RT beam patterns were delivered: BB, MRT and MB for a total of 11 groups with three animals each. RT specifications are given in Table 3.4, where peak and valley doses were assessed by MCS (see section 3.3).

The irradiation was performed at D10 targeting, for all the groups, 1x1 cm² within the right lung, with the beam delivered in the antero-posterior direction, as shown in Figure 3.8. The beam centring was done in a way that vital organs in the surroundings like liver, heart and spinal cord were spared during the treatment. I did not personally participate in these irradiation experiment, which was realized before the starting of my Ph.D., but I analysed the specimens collected afterwards (more details in Chapter 7).

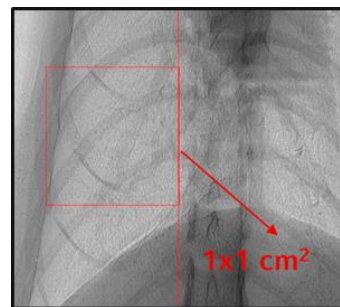


Figure 3.8: field of irradiation chosen for the RT protocols (red box) superimposed to a rat thorax radiograph (radiologic view).

Table 3.4: irradiation groups and parameters for healthy lungs RT. Every group is composed by three rats.

Group name	Peak dose (Gy)	Valley dose (Gy)	Beam width (μm)	c-t-c distance (μm)
BB30	30	-	-	-
BB50	50	-	-	-
MRT50	50	1.2	50	400
MRT100	100	2.4	50	400
MRT300	300	7.3	50	400
MRT600	600	14.6	50	400
MB50	50	0.7	500	4000
MB100	100	1.3	500	4000
MB300	300	4.0	500	4000
MB600	600	7.9	500	4000
Control (untreated)	-	-	-	-

3.2.4 Animal follow-up after the irradiation and sample collection⁴

After the irradiation, all animals were housed and daily monitored at the ESRF animal facility until their sacrifice. All rats involved in the lung study were sacrificed after 12 months. The sacrifice time point for the animals of the brain study was set to D138, while for each GBM-bearing group, was set accordingly to the animals' monitoring protocol including animal daily care, a weekly weight check and *in-vivo* MRI sessions (see Table 3.5). MRI was performed on the implanted animals to follow up the tumour growth and evolution. A first MRI was done close to the irradiation date (2-3 days after the irradiation) to investigate the initial size and shape of the tumour and possible intra-animal variabilities. A second MRI was performed at D35 to check the tumour status.

Table 3.5: sacrifice days set for GBM-bearing treated groups according to the animal monitoring protocol. * D26, 41 and 61 where fixed as sacrifice points to study the tumour and microcalcifications evolution.

RT group (GBM-bearing animals)	Sacrifice day
BB5	20-23
BB10	29-38
BB15	42-44
MRT200	15-31
MRT400	43-59
MRT600	26, 41, 61, 55-138*
MB180	26-30
MB350	15-16
Controls	20-26

All MRI sessions were performed at the 4.7 T IRMaGe MRI facility (Avance III console; Bruker, Ettlingen, Germany) in Grenoble using an actively decoupled

⁴ Part of this paragraph is reproduced from (Romano, 2021a).

cross-coil setup. Animals were anesthetized with 4% isoflurane for induction and 2% for maintenance. The tail vein was equipped with a catheter to deliver the Gadolinium (Gd) MRI contrast agent (0.4 $\mu\text{l/g}$ of the animal weight). During the whole MRI session, the rat temperature was maintained at 37.0°C, by means of pre-heated water-filled tubes, and the breath rate at about 60 breath/min by modulating the gaseous isoflurane delivery. The following imaging sequences were applied:

- anatomical imaging was performed with a T₂-weighted spin-echo sequence: voxel size = 117x117x1000 μm^3 , 19 slices, echo time = 40 ms, flip angle = 90°; number of averages = 2, repetition time = 2500 ms, 2:40 min of total acquisition time;
- T₁-weighted spin-echo sequence was performed before and 30s after the injection of the Dotarem® Gd contrast agent (0.4 $\mu\text{l/g}$) through the tail vein and flushed with 500 μL of sterile saline solution. The used parameters are: voxel size = 234x234x1000 μm^3 , 19 slices, echo time = 5, flip angle = 90°; number of averages = 4, repetition time = 800 ms, 1:17 min of total acquisition time.

After animals' euthanasia, the brain was dissected out and fixed in 4% paraformaldehyde (PFA) in phosphate buffered saline (PBS) solution for immersion; irradiated lungs were extracted together with the heart as a single block of tissue and fixed similarly to the brains. Organs were kept in the PFA fixating bath for at least one week to allow the solution penetrate and fix the full tissue avoiding its degradation over time.

All procedures related to animal care conformed to the guidelines of the French government and were approved by the ESRF Internal Evaluation Committee for Animal Welfare and Rights (authorization number #01261.02 for the brain RT study and licenses 380325 and B3818510002 for the lung RT investigations).

3.3 Monte Carlo dose simulations

The assessment of the dose distribution is a key task to ensure the best radiotherapy outcome. Well-established procedures exist for the evaluation and validation of dose distributions for a conventional BB radiotherapy (Brahme, 1984; ICRU, 1976), while dose evaluation for spatially fractionated radiation, in particular for MRT, is more challenging. The small beamlets dimensions and the differences in

dose deposition between peaks and valleys place high demand on dose calculations (Bartzsch, 2020). MCS rely on tracking each interaction arising from primary particles (see Figure 3.9). Thus, MCS, after being benchmarked with experimental dosimetry, can reach a high degree of accuracy but need long computation times for processing a number of source particles adequate to reach a low statistical uncertainty for dose maps of micrometric resolution. Up to now, accurate MCS based on Geant4, EGS4 and PENELOPE have been used for MRT dose calculations, but new approaches are raising such as kernel-based and hybrid approaches. The principle of operation of the three methods is sketched in Figure 3.9 showing how the dose deposition for the same simulated event is handled.

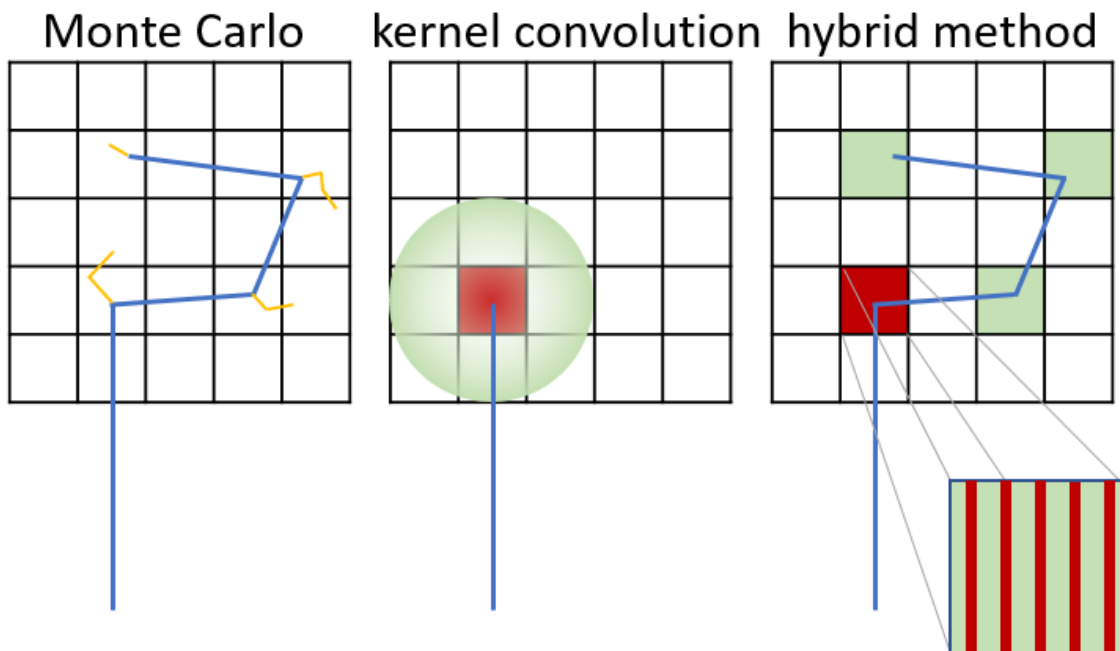


Figure 3.9: photons (blue paths) and electrons (yellow paths) interactions handled by the Monte Carlo, kernel-based and hybrid approaches for the same impinging primary photon. Monte Carlo follows individually all the particles tracks and interactions; a smaller voxel size is required to resolve all the interactions. Kernel-based methods only follow the primary photon interaction, where the red coloured pixel is the one where the primary interaction takes place, and secondary interactions are implemented with a kernel convolution (green shadowed area); uncertainties in the dose deposition are intrinsically added. The hybrid method uses Monte Carlo tracking for photons and kernels for electron convolution. The coloured voxels represent whether a primary or secondary photon-mediated event is registered. The voxel zoom shows that, when an MRT primary beam is used, the events contributing to peaks can be clearly discriminated from scattering events.

Kernel-based algorithms generally separate the energy transport of the primary beam from the energy transport of secondary photons and electrons (Donzelli, 2018). After the energy release from primary interactions is computed, scatter

kernels, derived to account for the mean spatial distribution of energy release from secondary particles, are convoluted over the density of primary interactions. Overall, kernel-based simulations are faster than MCS but can lead to some inaccuracy in the dose estimation, as in Figure 3.9.

The hybrid method represents a trade-off between MCS and kernel-based approaches: dose maps with micrometric resolution are obtained with limited computational efforts. The hybrid algorithm separates photon- and electron-mediated energy transport that are handled respectively by MCS and kernels. MCS track the photons on a grid equal to the target voxel size, typically in the mm range. For dose maps of RTs on humans or small animals the target voxel size often corresponds to the CT voxel size of the irradiated area. A macroscopic grid is sufficient even for MRT dose distributions since only photons are considered by MCS, improving the computation times. Thus, when the photon track is followed, scores of energy deposition are recorded and stored separately in the $D_{primary}$ or $D_{scatter}$ variables depending on whether the event is generated by a primary photon or by a scattered one. Kernels handle the dose deposited by electrons computing their transport within each voxel on a micrometre grid. The microbeam structure can be resolved under the assumptions that within a single voxel the beam intensity and spectrum as well as the voxel material are assumed to be homogeneous (Donzelli, 2018). It can be thus considered that peaks are built up with electrons produced in interactions of primary photons, while the valley dose is obtained from energy absorbed from scattered photons and electrons. Electrons energy deposit subsequent to scattered photons are neglected since their range is much smaller than a typical voxel size (Debus, 2017). The dose within a single voxel can thus be calculated as:

$$D(\mathbf{r}) = D_{scatter}(\mathbf{r}) + D_{primary}(\mathbf{r}) \cdot [K_{el}^{3D}(\mathbf{r}) * \tau(\mathbf{r})] \quad 3.3$$

where $K_{el}^{3D}(\mathbf{r})$ is the scatter kernel and $\tau(\mathbf{r})$ is the distribution of events of photon-to-electron energy transfer within the voxel.

Overall, it can be concluded that: pure MCS need small voxel size to correctly track the interactions, the kernel-based method is less accurate than MCS and the hybrid method can be a good trade-off between the first two tools. The hybrid method output for an MRT irradiation is the total valley and peak dose evaluated

in each target pixel, but the information of how peak and valley doses are distributed on a submillimetre grid can still be retrieved, as visible in the zoom of Figure 3.9.

In this Thesis, the hybrid approach was used to compute the dose distributions for BB, MRT and MB irradiations with *3D Slicer* (Fedorov, 2012). This part of the work was performed in collaboration with Prof. S. Bartzsch (TUM, Munich). The MCS part is computed via the *GEANT4* toolkit (Agostinelli, 2003) with the *PE-NELOPE* physics model for low energy photons, while for the electron dose deposition the algorithm of (Debus, 2017) was used. As first, I used the MC hybrid simulations results to define the doses to be delivered in the BB, MRT and MB irradiations and then to obtain representative dose distribution maps, as explained in the following paragraphs.

3.3.1 Simulation parameters definition

By using the *3D Slicer* user interface, it is possible to define the source beam to be used during the simulations. The CT images of the target to be irradiated are loaded and the beam definition is subsequently performed. The parameters to be inserted are: the beam centre with respect to the target irradiation, the transverse beam dimensions, the angle of delivery and the beam energy spectrum. All the parameters are visualized in 2D and in 3D on the target volume as showcased in Figure 3.10. If MRT or MB geometries are used, the beam width and c-t-c distance have to be set too. As last, the number of particles composing the beam and the voxel size for the dose scoring, if different from the CT voxel size, have to be set.

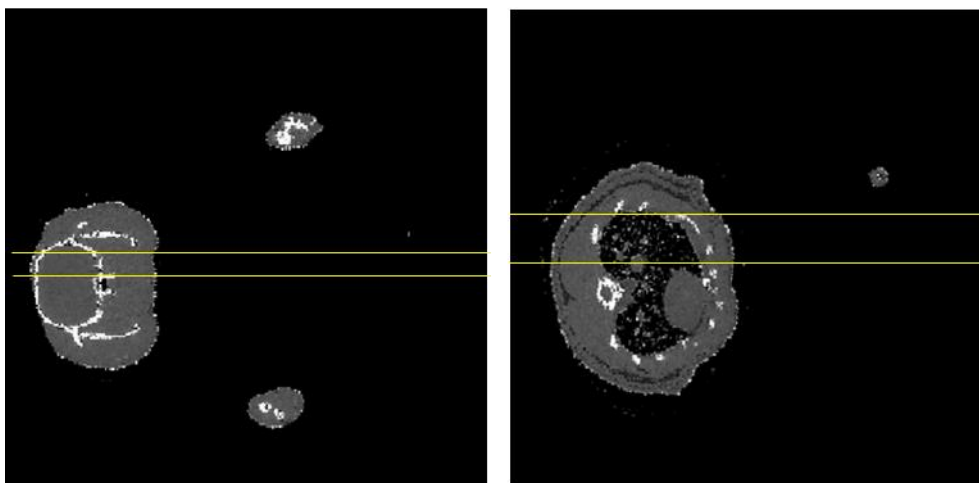


Figure 3.10: example of axial 2D views produced with *3D Slicer* of the RT beam delivered on a rat brain and lung. Yellow lines indicate the FOI borders and the beam entrance is placed at left.

Simulations are performed by directly using the source beam spectrum as used in the irradiation experiments without the need of modelling the source and the optical elements placed between the source exit and the target. The results will be then calibrated using the experimental dosimetry procedure carried out before the irradiation experiment and the output values of the calibration MCS. Calibration MCS is obtained by using the same irradiation spectrum as for the irradiation simulations and replacing the CT target with a solid water phantom, as the one used for the experimental dosimetry, and delivering a seamless irradiation beam of 2x2 cm². Thus, the hybrid MCS output dose calibration is obtained, for each pixel, with the following equation:

$$D_{real} = D_{MC} \cdot \left(\frac{bw}{ctc} \cdot \frac{FOI_{exp}}{FOI_{cal}} \cdot \frac{D_{exp-cal}}{D_{MC-cal}} \right) \quad 3.4$$

where D_{real} and D_{MC} are respectively the delivered dose, relative to 1 Gy under reference conditions, during the experimental irradiation and the dose calculated by the hybrid MCS for that pixel; bw the beam width and ctc the c-t-c distance for spatially fractionated beams; FOI_{exp} and FOI_{cal} the FOI respectively used for the RT experiment and for the experimental calibration; $D_{exp-cal}$ the dose measured at the reference point during the experimental calibration and D_{MC-cal} the dose computed by the calibration MCS at the reference point.

MCS are usually run with targets built with 3D shapes filled with specific predefined materials; thus, the Hounsfield units associated to each voxel of the target volume are transformed into materials e.g. bone, skin and air by means of a dedicated tool in *3D Slicer*. Simulations are run on a dedicated cluster; the output for MRT or MB irradiations consist of two files containing the total peak and valley dose values for each CT pixel. These results can be individually visualized as an overlay on the CT images for obtaining 2D dose maps. For BB geometries, only one output file is produced with the dose scored on all the target voxels. Finally, 1D plots of the transverse and depth dose profiles can be extracted from the 2D dose maps.

3.3.2 Choice of the radiotherapy protocols

Within this Thesis, hybrid MCS were used to choose the experimental settings for the delivery of BB, MRT and MB geometries to rat lungs and brains (paragraph 3.2.3). For each RT protocol, a simulation was performed with $2 \cdot 10^8$ source particles scoring the dose on a grid of $0.992 \times 0.992 \times 1.350 \text{ mm}^3$, corresponding to three times the used rat CT voxel size ($0.331 \times 0.331 \times 0.450 \text{ mm}^3$). The $2 \cdot 10^8$ particles were spectrally distributed according to the experimental irradiation spectrum displayed in section 3.2.1.

The first evaluation made on the dose simulations was the peak and valley doses and the PVDR (see paragraph 1.3) for the selected MRT and MB pitches. Table 3.6 shows the values obtained with the hybrid MC code for the brain irradiations. The reported values are normalized according to equation 3.4 and are thus relative to 1 Gy under reference conditions. Therefore, it is sufficient to multiply both the peak and valley values for the desired nominal dose to be delivered to obtain the real doses administered during the RT experiments. For brain irradiations, MRT and MB dose prescriptions were chosen in order to obtain valley doses similar to the BB irradiation values and with valley values below the tolerance level. For the lung irradiations, PVDR, peak and valley doses for the chosen beam geometries were computed too: high BB doses were chosen in order to explore the tolerance of the healthy tissue, but MRT and MB protocols were selected keeping the valleys below the tolerance and with peak values not higher than 600 Gy.

Table 3.6: peak dose, valley dose and PVDR for brain irradiations, relative to 1 Gy under reference conditions, obtained with the hybrid MC method. MRT 50/200 refer to microbeams with 50 μm of width and 200 μm as c-t-c distance. MB 500/100 and MB 500/2000 refer to minibeam with 500 μm of width and 1000 or 2000 μm as c-t-c distance, respectively.

RT protocol	Peak dose (Gy)	Valley dose (Gy)	PVDR
MRT 50/200	0.99 ± 0.04	0.0038 ± 0.004	26.3 ± 4.0
MB 500/1000	1.10 ± 0.06	0.044 ± 0.005	25 ± 4
MB 500/2000	1.15 ± 0.05	0.023 ± 0.003	49 ± 9

By averaging the peak and valley values scored in the pixels placed at a certain depth and within the FOI, it was possible to draw the depth-dose curves for peaks and valleys as in Figure 3.11 where the brain irradiation results are displayed starting from the X-ray beam entrance surface and along the whole path within the rat head. Here, the normalized results relative to 1 Gy under reference conditions are displayed. To explain the dose enhancement, i.e. the three peaks, the scheme of the brain CT given in the same figure has to be considered: the first peak (magenta dashed line) is due to the dose entrance (buildup effect and presence of the skull); the second, at about 12 mm in depth indicated by the green dashed line, is due to the presence of a second bone layer; the third is at about 22 mm depth and is mainly an artefact caused by the dose averaging above all the pixels placed at that depth, where a non-sharp transition between tissue and air is present.

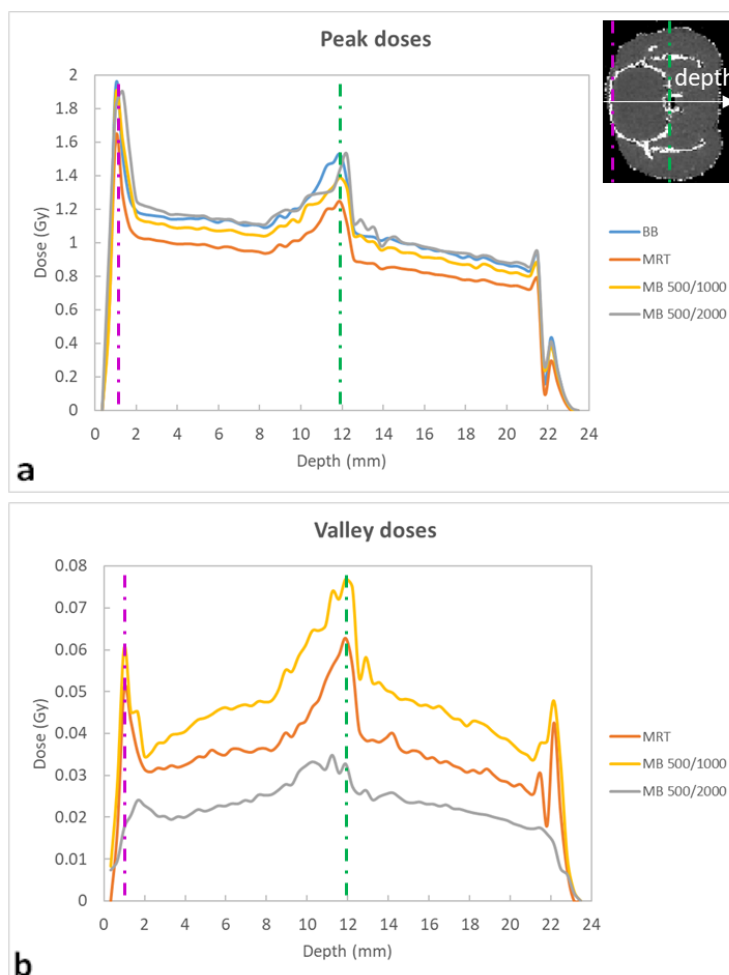


Figure 3.11: depth-dose curves for peaks (a) and valleys (b) for the rat brain irradiation for all the used geometries. BB dose curve is reported together with the peaks of the spatially fractionated protocols. The rat brain CT helps in identifying the position of the dose peaks within the rat anatomy.

In Figure 3.11 peak curves are similar for all the geometries and show an enhanced dose deposition in the bone tissue (~ 0 and ~ 12 mm depth) due to its higher effective atomic number, as also seen in (Prezado, 2011a). Within the brain (area between the peaks indicated by the magenta and green lines), an almost constant dose deposition is obtained. The valley doses for MRT and the two MB configurations exhibit similar curves; an enhancement of the scattering within the bone is present also in these curves. Overall, it is visible how the valley dose increases, for MBs, by decreasing the inter-beam spacing.

3.3.3 Dose maps

2D dose maps are obtained with the software *Amide* (Loening, 2003). Binary files containing the rat CT and the dose values for all the voxels are loaded and displayed with a coloured lookup table accordingly to the needs. Figure 3.12 shows the *Amide* user interface for displaying target CT and the 2D dose maps displayed along the three anatomical planes. Here, an example of a dose map is given for a BB brain irradiation. Similar dose maps are obtained for all the irradiation geometries and are displayed in Chapters 6-7.

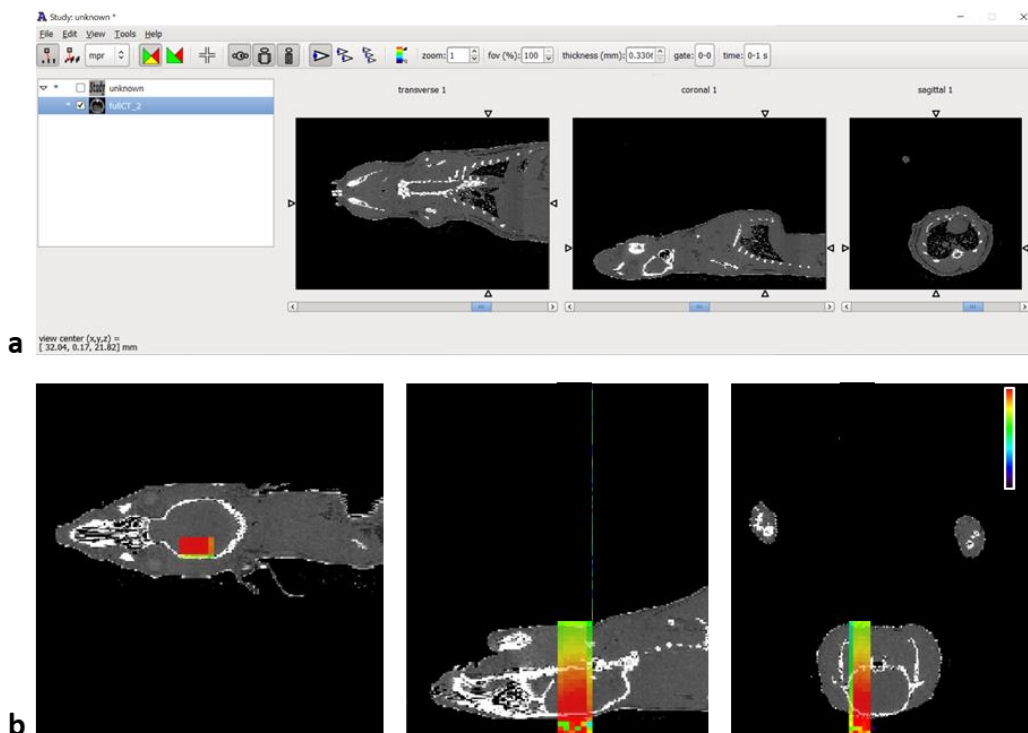


Figure 3.12: (a) *Amide* software user interface for dose maps visualization with the rat CT uploaded. (b) an example of 2D dose maps overlaid to the rat CT for a BB RT along the three main anatomical planes.

Chapter 4

X-ray imaging and scattering experiments

This chapter will focus on the experimental aspects of the morphological and structural analysis techniques I used in the framework of this Thesis to investigate the effects of radiotherapies on rat brain and lung. The portfolio of the used experimental methods includes: XPCI-CT, histology, SAXS, WAXS and XRF. The sample preparation procedures for the different techniques are presented and afterwards, the experimental setups and procedures are described.

4.1 Sample preparation

Sample preparation is a crucial step to be attentively carried out before the experiments. Particular procedures have to be put into practice to guarantee the needed experimental standards.

4.1.1 Sample preparation for XPCI-CT

When imaging biological materials with hard X-rays, adapted sample environments are required, which, ideally, should mimic the physiological conditions of the studied specimen as much as possible. Generally, excised and fixed organs are placed in cylindrical sealed plastic containers immersed in a buffer solution to avoid abrupt index of refraction variations between the sample and air. In fact, XPCI-CT of a specimen in air will produce images with evident organ borders and a compression of the greyscale palette, together with numerous streak artefacts, which will be discussed in section 5.2.1. Thus, the sample is placed in a liquid or solid solution with refraction properties similar to the sample to be investigated e.g. PFA, ethanol, PBS, paraffin or agar-agar gel. The substrate needs to be chosen accordingly to the X-ray beam to be used: it has to be radiation resistant, transparent for X-rays and compatible with the biological samples.

Brain samples preparation

After the organ extraction and PFA fixation, few days before the XPCI-CT imaging experiment all the brain samples were dehydrated in an increasing ethanol

series (50%, 60% and 86% in volume) for four hours each and then kept in the highest concentration solution. This protocol was chosen after an experimental XPCI-CT session where I tested the quality of the images obtained with healthy brains fixed with PFA and stored in different liquids: PFA, 50%, 86% and 100% ethanol baths. All the ethanol concentrations above 50% were achieved by multiple baths of increasing concentration. 86% ethanol was chosen as imaging buffer solution as it provides an optimum image quality and is ideal for storing the samples for several months. Nevertheless, ethanol produces many air bubbles at the interface with the tissue when the sample is immersed in it. Thus, I explored several sample preparation protocols and the final chosen one follows:

- brain positioning in an empty cylindrical plastic container;
- 86% ethanol solution pouring into the container;
- application of small vibration to the container in a way the air bubbles detach from the tissue, if needed a vibrating plate can be used;
- container sealing.

Figure 4.1 shows two different fixed rat brain samples (a and b) together with their positioning into the plastic containers (c and d). Air bubbles must be avoided during the sample preparation procedure since each bubble constitutes an air-liquid interface and will produce streak artefacts in the XPCI-CT images, as shown in Figure 4.1e-f; here, a picture of a sample and an XPCI-CT image are presented for a brain prepared with a sub-optimum protocol.

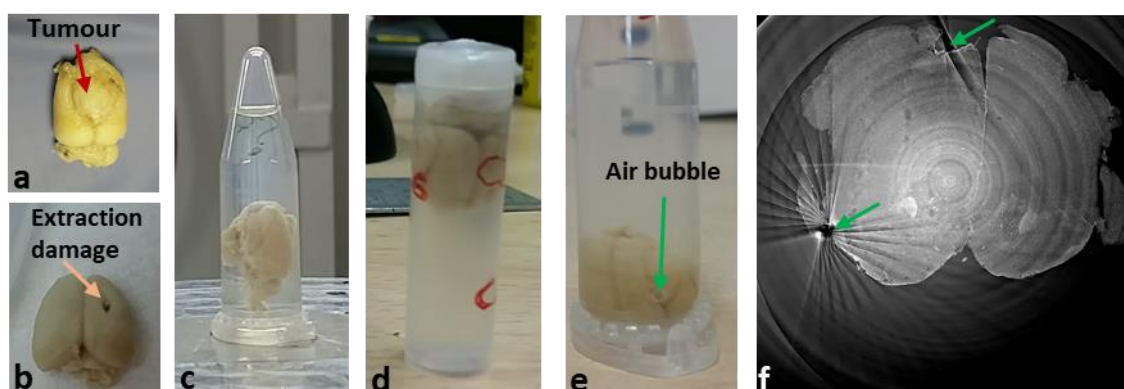


Figure 4.1: rat brain samples (a)-(b) after extraction and formalin fixation. (a) is a tumour-bearing brain while (b) is a healthy brain sample where extraction damages are visible as pointed by the orange arrow and by the absence of the cerebellum. (c)-(d) are two different samples placed in sealed plastic containers and immersed in 86% ethanol as a buffer liquid for imaging. (e) showcases the formation of air bubbles at the liquid-tissue interface producing streak artefacts like in (f) when the sample is imaged with XPCI-CT.

After the sample exposure to X-rays, some air bubbles can be produced within the ethanol solution, but it was experimentally seen that this formation is typically associated with a fast bubble burst and no artefacts are observed. Nonetheless, this effect has to be taken into account when long image acquisitions are performed (e.g. 2-3 h for a full-organ scan).

Lung samples preparation

After animals' euthanasia, lungs and heart were extracted and fixed with PFA as a single block of tissue. Afterwards, the heart was removed, left and right lungs were separated and embedded in two different paraffin blocks (Figure 4.2a). The procedure for paraffin embedding should be carried out properly by experts in order to avoid incorporating air bubbles between tissue and paraffin. In Figure 4.2b the XPCI-CT signal from air bubbles within the paraffin-embedded lung tissue is shown. Paraffin sample enclosure has the great advantage of safely storing tissues for long periods (e.g. years), guaranteeing a stable sample positioning and, at the same time, samples are already prepared for the histological processing.

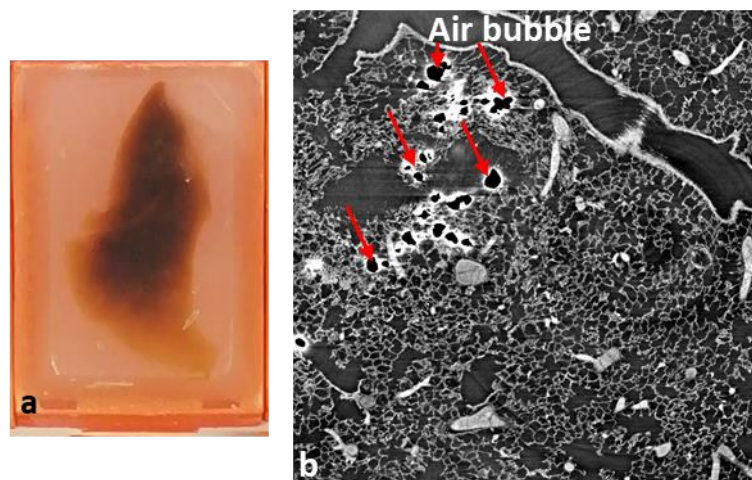


Figure 4.2: (a) rat lung embedded in a paraffin block. (b) portion of lung tissue imaged with XPCI-CT showing some air bubbles within the block producing big phase shift and thus saturation and streak artefacts.

Paraffin blocks have normally a parallelepiped shape, thus, before imaging, the edges of the blocks are usually rounded and smoothed in order to avoid artefacts in the CT images due to corners.

4.1.2 Sample preparation for histology and SAXS/WAXS

After the XPCI-CT experiments, samples underwent either histology and/or SAXS/WAXS examination and thus needed to be all embedded in paraffin and then sectioned in slices by means of a microtome.

Brain samples were embedded in paraffin blocks similarly to lung organs. Each sample block, either rat brain or lung, was frozen (to facilitate the sectioning of paraffin and tissue) and then placed in the block housing of a Leica SM2010R Sliding Microtome (Leica Microsystems GmbH, Wetzlar, Deutschland) as shown in Figure 4.3a. Sections of a thickness of approximately 3 μm were cut and immersed in a Leica HI1210 water bath at 48°C (Figure 4.3b) for stretching and drying the sections. Finally, slices were placed on glass slides to be processed for the histology staining.

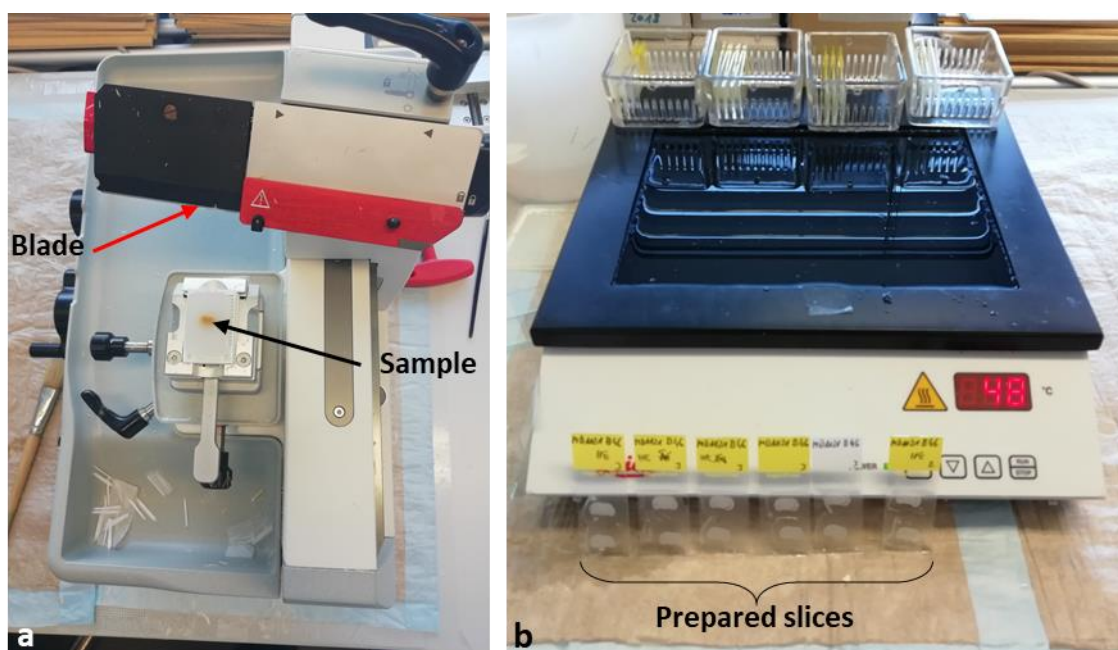


Figure 4.3: (a) Leica SM2010R Sliding Microtome for samples sectioning in thin slices. The arrows point at the cutting blade and at the rat brain sample. (b) Leica HI1210 water bath for slices stretching and drying. Some ready to stain brain slices are also visible.

SAXS/WAXS samples were only collected from selected rat brain samples. Similarly to the histology protocol, 80 μm thick brain slices were cut and placed on glass slides for drying. Just before the experiment took place, the tissue slices were removed from the glass slides and placed in Ultralene sachets to avoid the

spurious contribution of glass in the measured signal. The same brain slices used for SAXS/WAXS were then analysed with XRF.

All the healthy brains and some selected GBM-bearing samples were cut in specific areas in order to only select the features of interest. The navigation within the sample was done using the available XPCI-CT datasets as a reference for precisely locating the features of interest within the samples and thus choosing the depth where to cut the slices.

Lungs underwent serial cutting for histology purposes producing, for each sample, 11-13 slice series of 5 subsequent slices each, with 125 μm of spacing between the series and a slice thickness of 3 μm .

4.2 PB-XPCI-CT experiments

Ex-vivo propagation-based XPCI-CT imaging experiments were performed at ID17, at the TOMCAT-X02DA beamline (Stampanoni, 2006; Stampanoni, 2007) of the SLS and at the P05 beamline (Ogurreck, 2013; Wilde, 2016) of the PETRA III synchrotron to achieve different spatial resolutions. For all the imaging sessions the general setup is composed of a synchrotron X-ray beam source, a sample CT stage and an X-ray detecting system placed at due distance from each other. Samples are placed on a sophisticated system of translating and rotating motors allowing the sample alignment with the beam and detector and acquisition of the CT datasets. Additional details are provided in the following paragraphs together with the description of the procedure for adjusting the detector focus and the sample stage in use at ID17, here presented as a showcase; the other beamlines apply similar protocols.

Brain samples were all imaged at the ESRF at $3.25 \times 3.25 \times 3.25 \mu\text{m}^3$ voxel size (in the following indicated as $3.25^3 \mu\text{m}^3$, being the voxel isotropic) and afterwards, a selection of interesting cases was analysed at the other facilities at higher isotropic spatial resolutions. Lung specimens were all imaged at SLS.

4.2.1 The tomography setup of ID17 - ESRF

The tomography setup of the ESRF ID17 beamline is shown in Figure 4.4. The subfigure (a) illustrates the first part of the EH2 hutch indicating the X-ray beam propagation direction and the sample on its motorized stage, while the picture in (b) shows the sample stage and the detector placed at a certain distance from each

other. The sample stage consists of a tower of motorized stages with six degrees of freedom that can be remotely piloted from the beamline control cabin for sample alignment and rotation for CT acquisition.

The available motors are visible in Figure 4.4c and allow for:

- the vertical and lateral displacement of the sample for its alignment, but also for removing the sample from the beam to acquire the reference and detector noise images;
- the sample movement along the three main axes, used for imaging purposes (to target the part to be imaged);
- the rotation of the sample around an axis aligned with the detector, used for sample rotation of 180° or 360° during the CT acquisition;
- the stage angular fine alignment with the X-ray beam and detector by means of a $\pm 15.5^\circ$ motorized “circle-segment” alignment stages.

Depending on the sample lateral dimensions with respect to the detector FOV, two different acquisition modes are used. The so-called “*full acquisition*” CT modality is used when the sample fully fits in the FOV and is obtained by aligning the rotation axis to the detector central pixel column and acquiring CT projections over 180°. Conversely, if the sample is larger than the detector FOV, the so-called “*half acquisition*” modality is used: the projections are collected over 360° and the rotation axis is set to the first or last detector pixel column thus, the beam illuminates almost half of the sample in each CT projection and the detector horizontal FOV is almost doubled.

The imaging detector is a scientific complementary metal-oxide-semiconductor (sCMOS) PCO.Edge 5.5 camera (2560x2160 pixels, 6.5x6.5 μm^2 pixel size) (Mittone, 2017) coupled with a scintillator screen and indirect conversion optics (Optique Peter, France) achieving pixel sizes down to 0.65 μm . The optical system is a 1x, 2x, 5x or 10x system of lenses, allowing a pixel size according to the used magnification. The scintillator screen to be used depends on the experimental

conditions and requirements. In the experiments of this Thesis a 40 μm thick GGG:Eu ($\text{Gd}_3\text{Ga}_5\text{O}_{12}:\text{Eu}$) and a 50 μm thick LuAG:Ce ($\text{Lu}_3\text{Al}_5\text{O}_{12}$) were used.

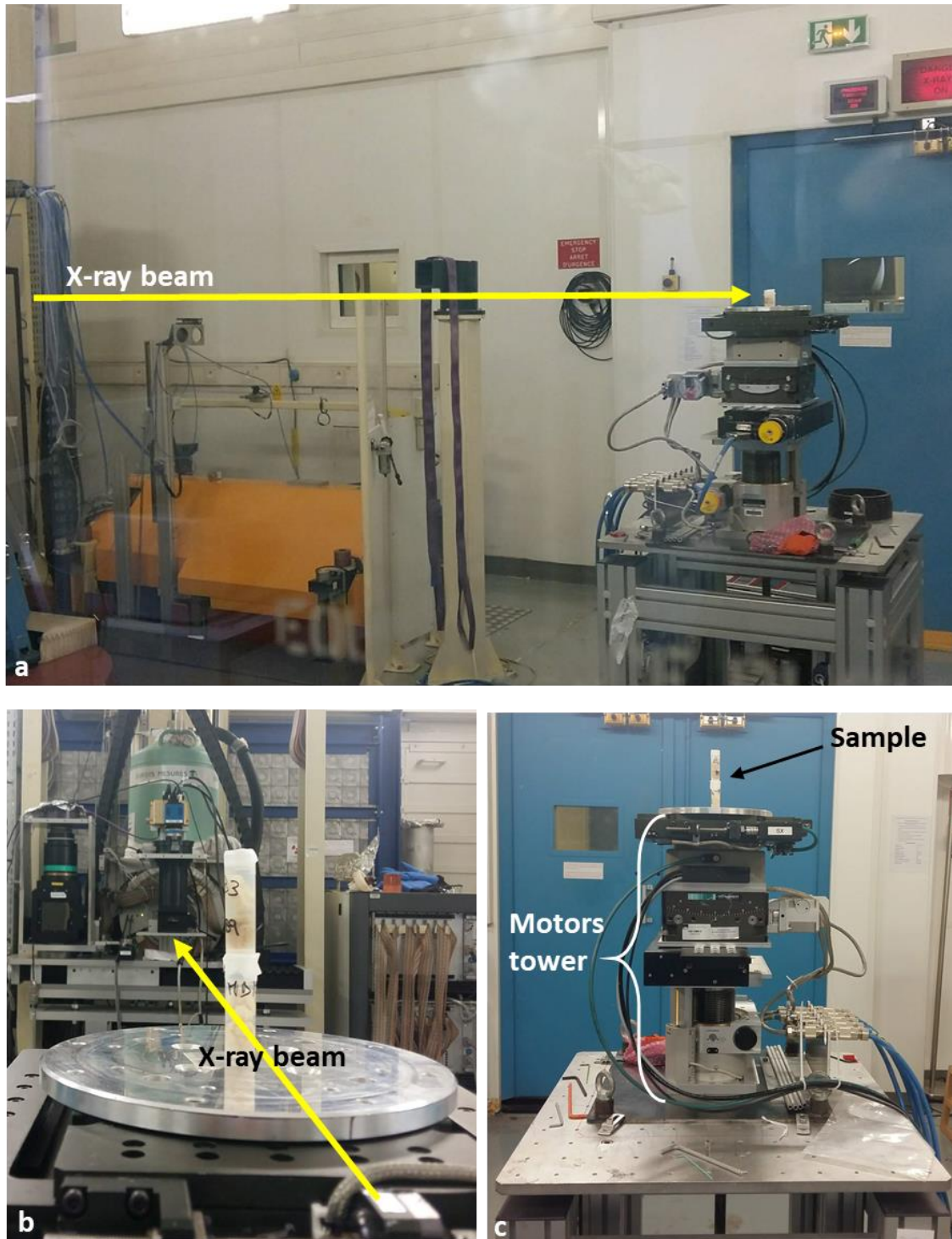


Figure 4.4: EH2 XPCI-CT imaging setup. (a) beamline configuration from the X-ray entrance into the hutch up to the sample stage; (b) sample-detector system: a PCO.Edge 5.5 sCMOS camera is placed downstream the sample stage together with its optic system. The sample is placed on a motorized stage tower (c) allowing movements along for six degrees of freedom.

These scintillator screens are chosen since their emission occurs at 595 nm and at 535 nm, respectively that perfectly match the detector quantum efficiency, as shown in Figure 4.5.

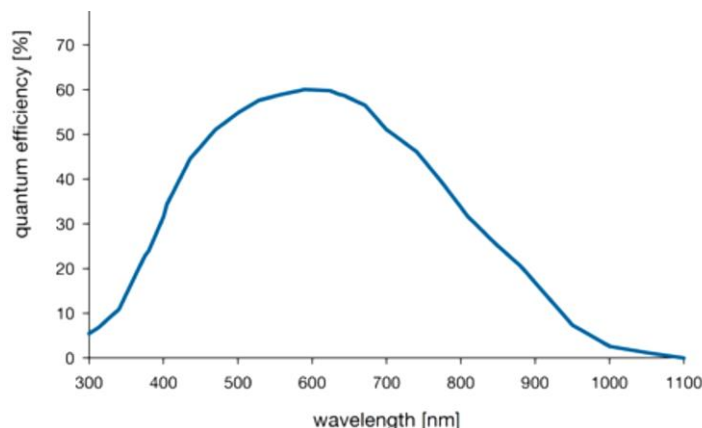


Figure 4.5: PCO.Edge 5.5 sCMOS quantum efficiency for visible light. Image adapted from https://www.pco.de/fileadmin/user_upload/pco-product_sheets/pco.edge_55_data_sheet.pdf

To improve the radiation resistance of the detection system, a mild N₂ flow is generated in between the scintillator and the optical mirror inside the optics, as described in (Zhou, 2018). The PCO.Edge 5.5 can be either coupled with one single optics system or with a double optics (for a fast pixel size change), as shown in Figure 4.6.

The optics system is realized in a way the X-ray beam impinges on the scintillator screen, which converts X-rays in visible light, and the transmitted residual X-ray beam is stopped by an opaque diaphragm. The visible light is then reflected on a slanted screen allowing the signal reaching the camera, placed perpendicularly to the beam direction, through a lenses system. The single optics setup can be used in both the experimental hutches while the two optics structure is typically equipped with the 10x and 2x magnifications and it is mainly used in the EH1 with the *pink beam*.

Monochromatic PB-XPCI-CT

PB-XPCI-CT acquisition with the 3.25³ μm³ voxel size were carried out in the EH2 hutch with a monochromatic 35 keV X-ray beam. The experimental details are summarized at the end of the paragraph in Table 4.1.

The projections were taken uniformly over 360° in *half acquisition* modality and 20 noise and 20 beam images were acquired before and after the CT of the sample by moving the sample out from the detector FOV. The noise images, or dark field (DF) images, contain the electronic noise signal of the detector, while the beam

images, also called white field (WF) images, are used to compensate for any spatial beam inhomogeneity. Every sample was entirely imaged with 5-6 vertical CT scans (each corresponding to a 7 mm vertical FOV, i.e. perpendicular to the beam direction) with a suitable overlap between adjacent CT stages, while the organ fits within the horizontal (lateral) detector FOV. Every two subsequent CT vertical stages were acquired with a certain overlap to ensure that small failures in the motor vertical movement will still result in a full organ coverage.

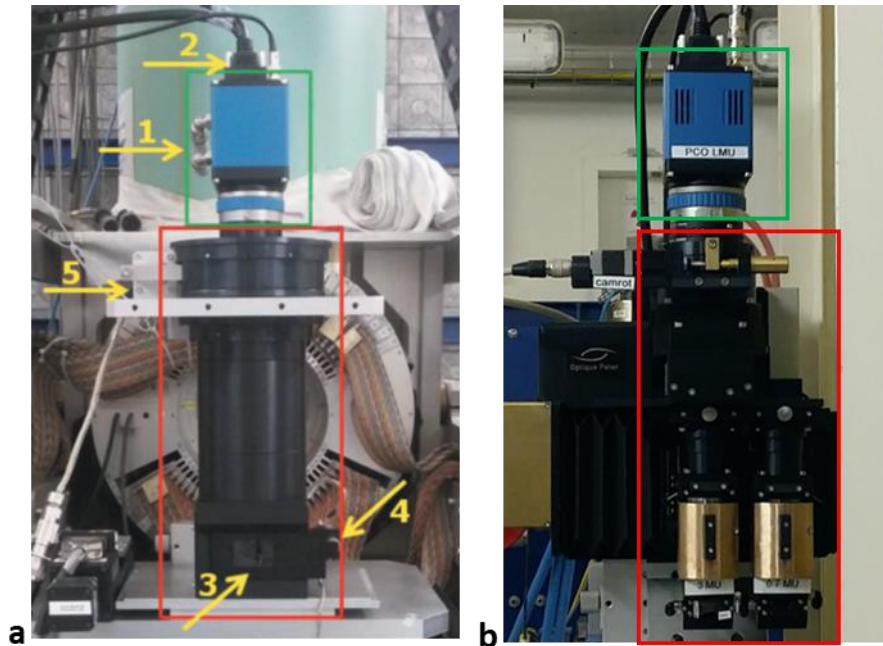


Figure 4.6: the water-cooled PCO.Edge 5.5 camera mounted on the 2x optic system (a) and on the double optics system 2x and 10x (b). The red rectangles indicate the optic system and the green rectangles indicate the PCO camera. In (a) it is possible to distinguish the different components of the detection system: (1) connectors to the Peltier detector cooling system, (2) camera link cables for the signal transfer to the detector server, (3) carbon window for the scintillator protection, (4) motor for the focus adjustment, (5) motor for the camera alignment to the sample stage. (a) is reproduced from (Mittone, 2017).

Pink beam PB-XPCI-CT

In the EH1, *ex-vivo* brain imaging was performed using the detection system shown in Figure 4.6b with magnifications leading to $3.25^3 \mu\text{m}^3$ (2x) and $0.65^3 \mu\text{m}^3$ (10x) voxel size images. The detector was placed at a distance from the sample that is a compromise between the optimum sample-to-detector distance for resolving the interference fringes with the two spatial resolutions. One CT stage (2.3 mm vertical FOV) was acquired with the 2x magnification to identify the region of interest (ROI) to be then imaged with the 10x magnification. Details on the imaging parameters are given in Table 4.1.

The X-ray imaging spectrum is obtained by filtering the polychromatic beam from the source with C (1.15 mm), Al (1.52 mm) and Cu (0.69 mm). The wiggler gaps were set to 73 mm for $w150$ and 200 mm for $w125$. A graph of the used spectrum was obtained via the *XOP* software and is displayed in Figure 4.7

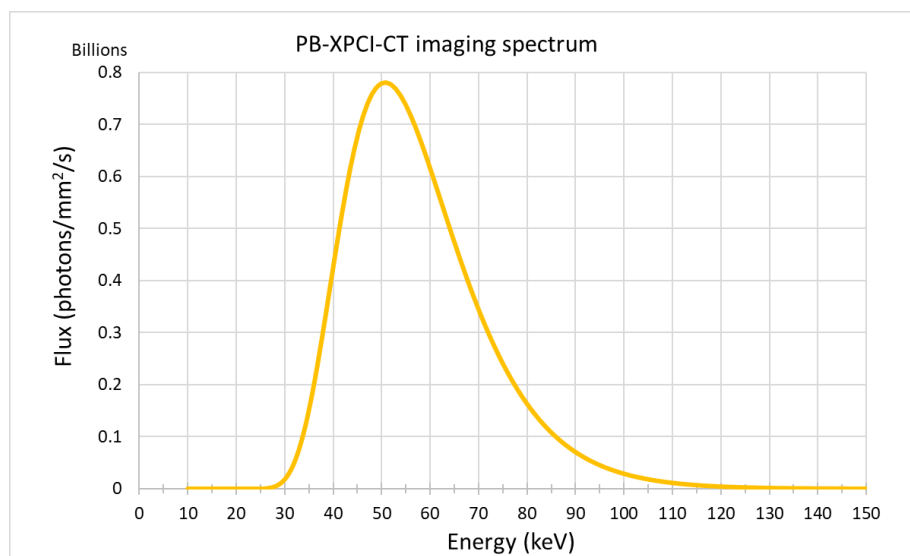


Figure 4.7: pink beam spectrum for PB-XPCI-CT imaging in the EH1 hutch. The FWHM of the filtered beam ranges from 39 to 68 keV and the peak energy is at 50.8 keV.

4.2.2 The SLS TOMCAT PB-XPCI-CT setup

PB-XPCI-CT experiments (on both the rat brains and lungs) at the TOMCAT - X02DA beamline were realized with the setup shown in Figure 4.9. X-ray photons, coming from a 2.9 T superbending magnet, are filtered by a fixed-exit double crystal multilayer monochromator allowing the sample to be illuminated by a 20 keV quasi-coherent monochromatic beam. The sample is placed on a remotely controlled, automatized CT stage for sample centring, movement and alignment with the detector (a PCO.Edge 5.5 sCMOS). One of the two available video cameras is used for the sample centring, as illustrated in Figure 4.8. Sample centring is typically checked at 0° and 90° for full acquisition, i.e. at the location in which the sample is mounted and by rotating it of 90° . In this, case the camera allows for centring the sample at 90° without the need of sample rotation: the camera FOV equals the detector one. Wax markers are placed on the lung sample ROI to ease the correct sample centring.

Details on the used parameters for imaging both lungs and brains at 1.63^3 and $0.65^3 \mu\text{m}^3$ isotropic voxel sizes (4x/10x magnification) are given in Table 4.1.

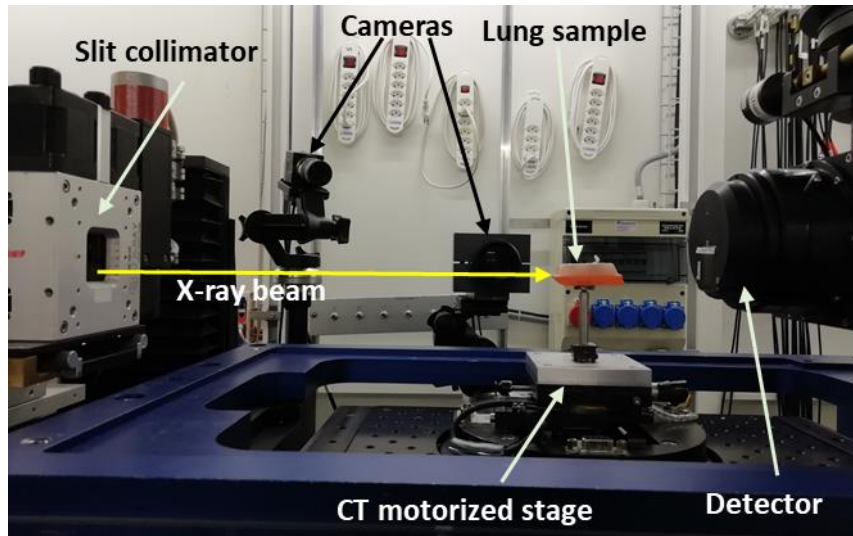


Figure 4.9: PB-XPCI-CT setup of the TOMCAT-X02DA beamline at the SLS. The slits collimator shapes the beam to be delivered, the motorized stage is placed in between the collimator and the detector allowing for the sample rotation and movement and is equipped with a custom-made magnetic sample holder. Two video cameras monitor the sample and enable its centring with the detector.

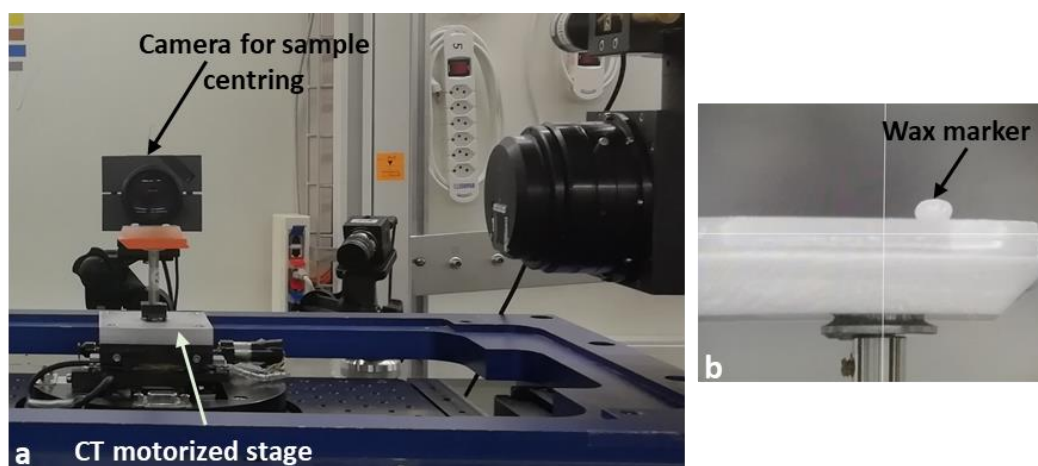


Figure 4.8: sample centring system for lung samples (a) and sample view from the camera (b). Thanks to the detector and the video camera placed in a perpendicular direction to the X-ray beam path, it is possible to centre the sample ROI in the two directions without need of rotating the sample. The camera view shown in (b) corresponds to the detector FOV once the sample is rotated of 90° . Wax markers are placed on top of the sample ROI to facilitate the centring.

All the lung samples were imaged with the 4x magnification and some selected interesting regions were analysed with the 10x magnification, both leading to partial organ coverage. For brain samples, the 4x microscope was only used for identifying the ROIs to be imaged at $0.65^3 \mu\text{m}^3$ voxel size. For every lung sample a mosaic image was acquired using a grid of $n \times m$ $1.63^3 \mu\text{m}^3$ voxel size micro-CTs

distributed in the horizontal plane (parallel to the beam direction) that were subsequently reconstructed and stitched together by using the NRStitcher software (Miettinen, 2019) resulting in a high-resolution wide-field tomographic dataset. Each pair of subsequent CT dataset were acquired with an overlap of 15%, allowing for a good match of the structures on the borders: e.g. a 2x2 stitching procedure gives a 7.2x7.2 mm² CT image. A single 1.6³ μm³ voxel-size CT image has a FOV of 4.2x4.2 mm² thus, the n and m values for the mosaic images were decided and set for each sample, according to its horizontal dimensions. One CT stage (3.35 mm vertical FOV) was sufficient to cover the full sample thickness.

4.2.3 The PETRA III P05 PB-XPCI-CT setup

The experimental setup for PB-XPCI-CT imaging at the P05 micro-tomography beamline of PETRA III is presented in Figure 4.10. The X-ray beam is obtained from an undulator source placed 81 m downstream the experimental hutch and monochromatized to 30 keV by a Bragg-Bragg double crystal monochromator Si[111]/Si[311]. The CMOS KIT detector was coupled with a 5x custom made optics system to image the brain samples with 1.2³ μm³ isotropic voxel size. Samples were positioned on a remotely controlled CT motor stage and typically 2-3 vertical stages were acquired to cover specific ROIs; one vertical stage corresponds to about 1.2 mm of vertical FOV, in this configuration. Further details are given in Table 4.1.

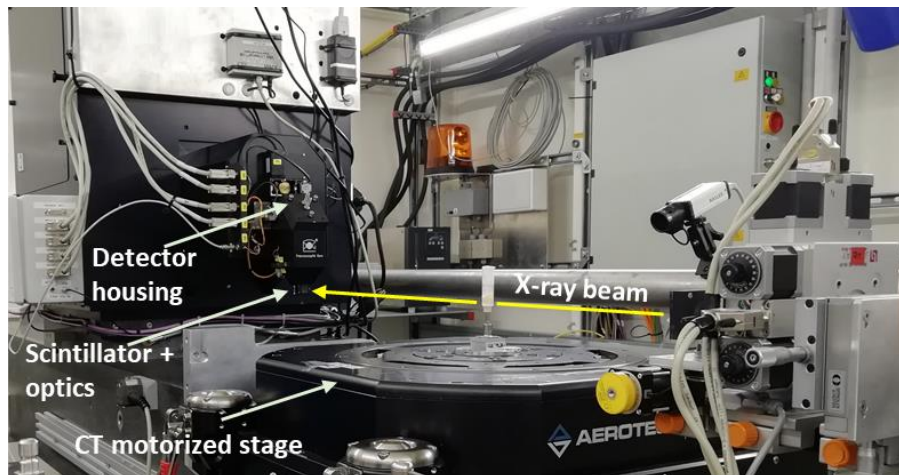


Figure 4.10: PETRA III P05 beamline XPCI-CT setup. The X-ray source pipeline is reported at right, then a motorized CT stage is placed together with a rat brain sample and at left is present the detecting system, which is composed by scintillator, optics and a CMOS detector.

Table 4.1: PB-XPCI-CT imaging parameters at the beamlines ID17 (ESRF), TOMCAT (SLS) and P05 (PETRA III).

Imaging parameters	ID17 - EH2	ID17 - EH1	TOMCAT	P05
Beam energy	35 keV	<i>pink beam</i>	20 keV	30 keV
Nominal ring current	200 mA	180 mA	400 mA	100 mA
Detector camera	PCO.Edge 5.5	PCO.Edge 5.5	PCO.Edge 5.5	CMOS KIT
Optics	Optique Peter 2x	Optique Peter 2x; 10x	UPLAPO 4x; UPLAPO 10x	5x (custom made)
Pixel size	$3.25^3 \mu\text{m}^3$	$3.25^3 \mu\text{m}^3$ (2x); $0.65^3 \mu\text{m}^3$ (10x)	$1.63^3 \mu\text{m}^3$ (4x); $0.65^3 \mu\text{m}^3$ (10x)	$1.2^3 \mu\text{m}^3$
Scintillator screen	40 μm thick GGG:Eu	40 μm thick GGG:Eu (2x); 50 μm thick LuAG:Ce (10x)	20 μm thick LuAG:Ce	100 μm thick LuAG:Ce
Sample to detector distance	1.8 m	1.22 m	20 cm (4x); 5 cm (10x)	50 cm
Acquired projections	4000 over 360°	5000 over 360°	1801 over 180°	6000 over 360°
WD and DF	20	20	50	20
Exposure time	30 ms	50 ms	150 ms	55 ms

4.3 Histology and immunohistochemistry examination

Histologic and immunohistochemistry analyses were performed on both brain and lung samples. All the healthy-treated rat brain slices were stained with Haematoxylin and Eosin (H&E), Alizarin Red (for Ca deposits), Perls' Prussian Blue (for Fe particles) and monoclonal mouse anti-glial fibrillary acidic protein (GFAP) (for gliosis detection). In addition, some tumour bearing brains were prepared for histology; a serial slice cutting was performed for GFAP staining to validate the tumour presence or sterilization. For lung samples, the serially cut slices were stained for histologic examination with H&E, Masson-Goldner Trichrome (TRI) and Fe stainings. Brain histologies were realized in collaboration with Prof. J. Herms and M. K. Schmidt (LMU Zentrum für Neuropathologie und Prionforschung), Prof. J. Ricke, Dr. M. Alunni-Fabroni and Dr. H. Hirner-Eppeneder (LMU-Klinikum Experimental Radiology Laboratory).

The cut slices were transferred on glass slides, dewaxed and rehydrated following standard protocols: preheating to 60°C for 10 min, Neo Clear xylene substitute 2x10 min, Ethanol graded series (100%, 96%, 90%, 80% and 70%), 1x each for 5 min, water 1x5 min). The details of the staining protocols are given in the followings.

H&E staining procedure

H&E staining was obtained with a multi-step procedure:

- nuclear staining placing the slides in Mayer's Haemalaun solution (1x5 min), rinsing in ddH₂O and washing for 10 min under running tap water;
- cytoplasm staining by immersing in 0.5% Eosin for 10 – 12 s and briefly rinsing with ddH₂O;
- differentiating with several baths of 80% EtOH; e) drainage with 90% and 96% EtOH baths (1 x 30 s each), 100% EtOH (2 x 2 min), NeoClear (2 x 5 min).

Results: cell nuclei are stained blue-black while the cytoplasm appears pink.

Alizarin Red staining procedure

Alizarin Red staining was obtained following the protocol described in (McGee-Russell, 1958):

- immerse sections in 50% EtOH and rinse rapidly in distilled water;
- cover sections with Alizarin Red S solution at 2% diluted with ammonia and follow the staining by transmitted light, on the stage of a staining microscope;
- calcium sites will be covered with a vivid orange-red calcium-alizarin lake within a period of 30 seconds to 5 minutes. The end point should be chosen when the deposit is heavy but not too diffused;
- shake off excess stain and blot carefully with filter paper or alternatively drain very thoroughly;
- place immediately into Acetone for 10 – 20 seconds followed by Acetone-Xylene for 10 -20 seconds;
- clear in Xylene and mount in Depex or Cedar wood Oil.

Results: calcium sites are covered and surrounded by a heavy orange-red precipitate, which is birefringent between crossed polaroids. The background appears faint pink.

Perls' Prussian Blue staining procedure for brains

Immerse each slice in:

- Perls' Prussian Blue solution for 30 min, rinse in distilled water for 5 min;
- a 0.1% Nuclear Fast Red solution is used for 10 min, ascending alcohol series and Xylene.

Results: Iron deposits in their ferric form are stained bright blue, the cells nuclei in red and cytoplasm in pink.

Fe staining procedure for lungs

Immerse the sections in:

- 2% Potassium ferrocyanide - $3K_4Fe(CN)_6$ 1x20 min and rinse with distilled water;
- Nuclear Fast Red Solution 1x10 min;
- steep shortly in 50% EtOH, 80% EtOH, 95% EtOH, 100% EtOH and in 100% EtOH 1x1 min and Xylene 2x5 min.

Results: Fe deposits are stained in blue while the background is red.

Masson- Goldner Trichrome staining procedure

Immerse the sections in:

- Ponceau Acid Fuchsin 1x10min, rinse in acetic acid 1%;
- Phosphomolybdic Acid-Orange G 1x10 min and rinse in acetic acid 1%;
- Light Green Stock Solution for 10 min and rinse in acetic acid 1%;
- 95% and 100% EtOH shortly, 100% EtOH 1x1 min, Xylene 2x5 min.

Results: cell nuclei are stained dark brown-black, cytoplasm in brick red, muscles in bright red, connective tissue in green and erythrocytes in bright orange.

Monoclonal mouse anti-glia fibrillary acidic protein staining procedure

Immerse the sections in:

- 0.1 M Citrate Buffer, pH6 and irradiate with microwave at 600 W;
- incubated with the rabbit anti-GFAP antibody (clone E4L7M, Cell Signaling, Frankfurt am Main, Germany; 1:100) over night at 4°C;
- process using the EnVision System HRP (DAB) kit (Agilent, Frankfurt am Main, Germany) according to the manufacturer's instructions;
- Mayers Haemalaun for counterstain;
- cover with Kaiser's Glycerine Gelatine.

Results: astrocytes, ependymal cells and corresponding tumours are stained brown.

4.4 SAXS/WAXS and XRF experiments⁵

SAXS/WAXS scanning microscopy data were collected at the cSAXS beamline of the SLS synchrotron facility (Bunk, 2009; Giannini, 2019) within the framework of a collaboration with Prof. C. Giannini (Università degli Studi di Bari Aldo Moro, Bari, Italy) and Dr. O. Bunk (SLS, PSI, Villigen). The data collection was achieved using a monochromatic X-ray beam of 13.589 keV of energy and 2.4×10^{11} photons/s selected by means of a liquid N₂-cooled fixed-exit Si(111) monochromator with bendable second crystal for horizontal focusing to about 45 μm FWHM,

⁵ The text of this paragraph is reproduced from (Romano, 2021a).

focused by a Rh coated mirror for vertical focusing to about 25 μm FWHM. SAXS/WAXS data were collected with a Pilatus 2M area detector (Henrich, 2009), while XRF maps were collected with Ketek VIAMP KC00-C1T0-H030-ML8B 133 Silicon drift detector with the signal processing done by XIA FALCONX electronics. The setup is shown in Figure 4.11a.

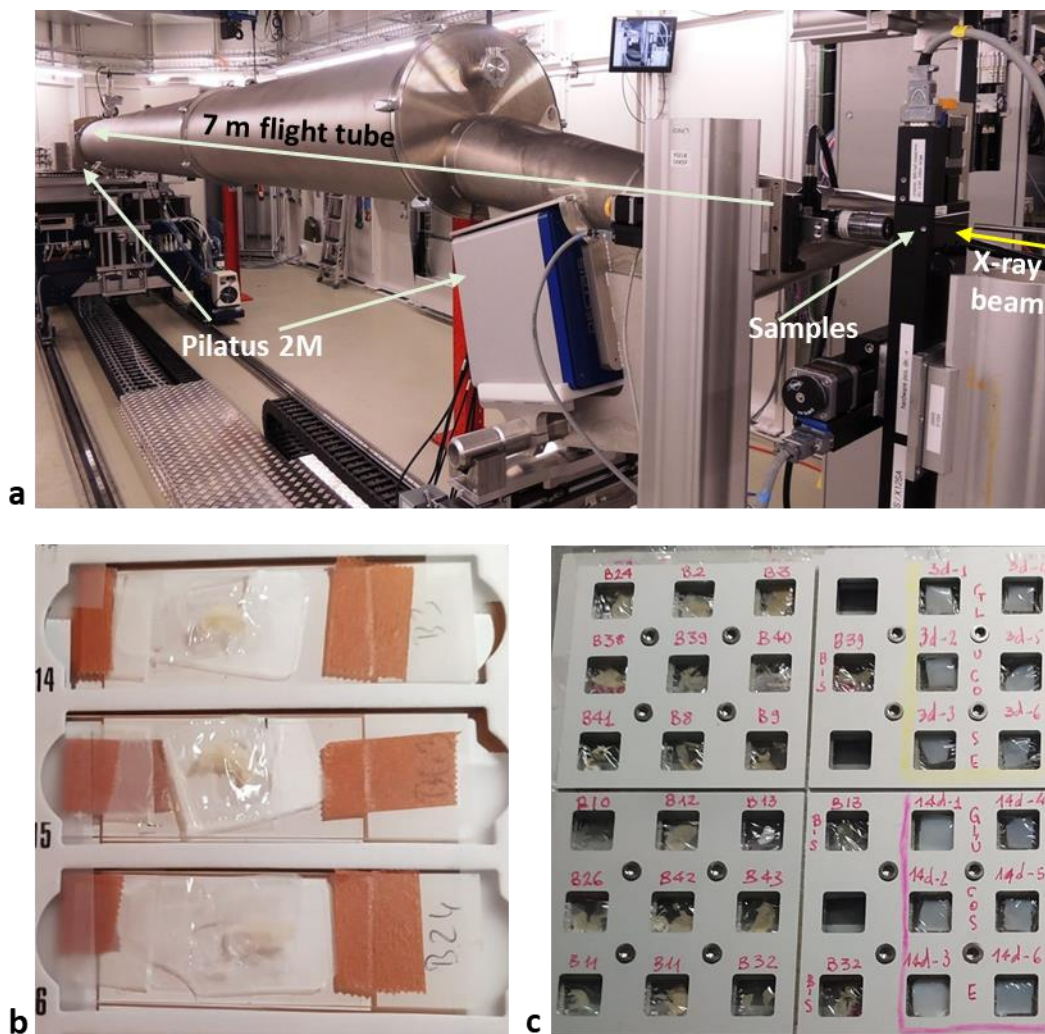


Figure 4.11: (a) cSAXS beamline layout for SAXS/WAXS combined measurements. (b) is a picture of rat brain slices into Ultralene sachets and (c) the samples mounted on their custom-made sample holder.

Measurements were first done in the SAXS geometry and then in the WAXS geometry. Calibration samples were used to define the energy-windows to integrate the P, Ca, and Fe signal. Samples were put in Ultralene sachets (see Figure 4.11b) and mounted on a custom-made sample holder (Figure 4.11c) placed onto a motorized 2D translation stage oriented perpendicularly to the beam direction.

The sample-to-detector distance was set to 7.1 and 0.24 m for SAXS in combination with XRF and WAXS, respectively, with exposure times of 0.4 s for SAXS and XRF and 0.3 s for WAXS. Data collection was performed in continuous vertical lines with the sample moving at constant speed and the detector synchronously recording the data frames with in-line rates of 1/0.405 Hz for SAXS and XRF and 1/0.305 Hz for WAXS. For SAXS data collection, a 7 m long air-evacuated tube was inserted between the sample and the Pilatus 2M detector allowing for combined SAXS/WAXS measurements. The flight tube has a ~ 7 μm thick entrance mica window and a 300 μm thick exit mylar window matching the size of the detector. SAXS and WAXS 2D data were calibrated by using silver behenate (SAXS) and NIST SRM640b (WAXS), and folded into 1D profiles. The intense transmitted, unscattered, X-ray beam was blocked from impinging onto the area detector by a beam stop placed close to the centre of the detector.

Chapter 5

Image processing and volumetric data analysis

This chapter gives the details of all the methods that were applied to the collected raw XPCI-CT data for the reconstruction of CT slices, for reducing the spurious contributions and image artefacts, to enable the segmentation of interesting features and for the 3D rendering (sections 5.1-5.4). I have set up a global workflow, shown in Figure 5.1 as a block diagram, to be applied to the acquired raw XPCI-CT projections to extract relevant qualitative and quantitative information by means of: publicly available tools, adapting existing macros to the needs of this study and developing, testing and implementing new procedures and tools. Each step of the scheme of Figure 5.1 is then described in detail in a dedicated paragraph within this chapter.

SAXS/WAXS data analysis specifics are also reported. This part of the data processing has been realized as a collaborative work with Dr. O. Bunk (SLS, PSI, Switzerland) and Prof. C. Giannini (Università degli Studi di Bari Aldo Moro, Bari, Italy) (see section 5.5).

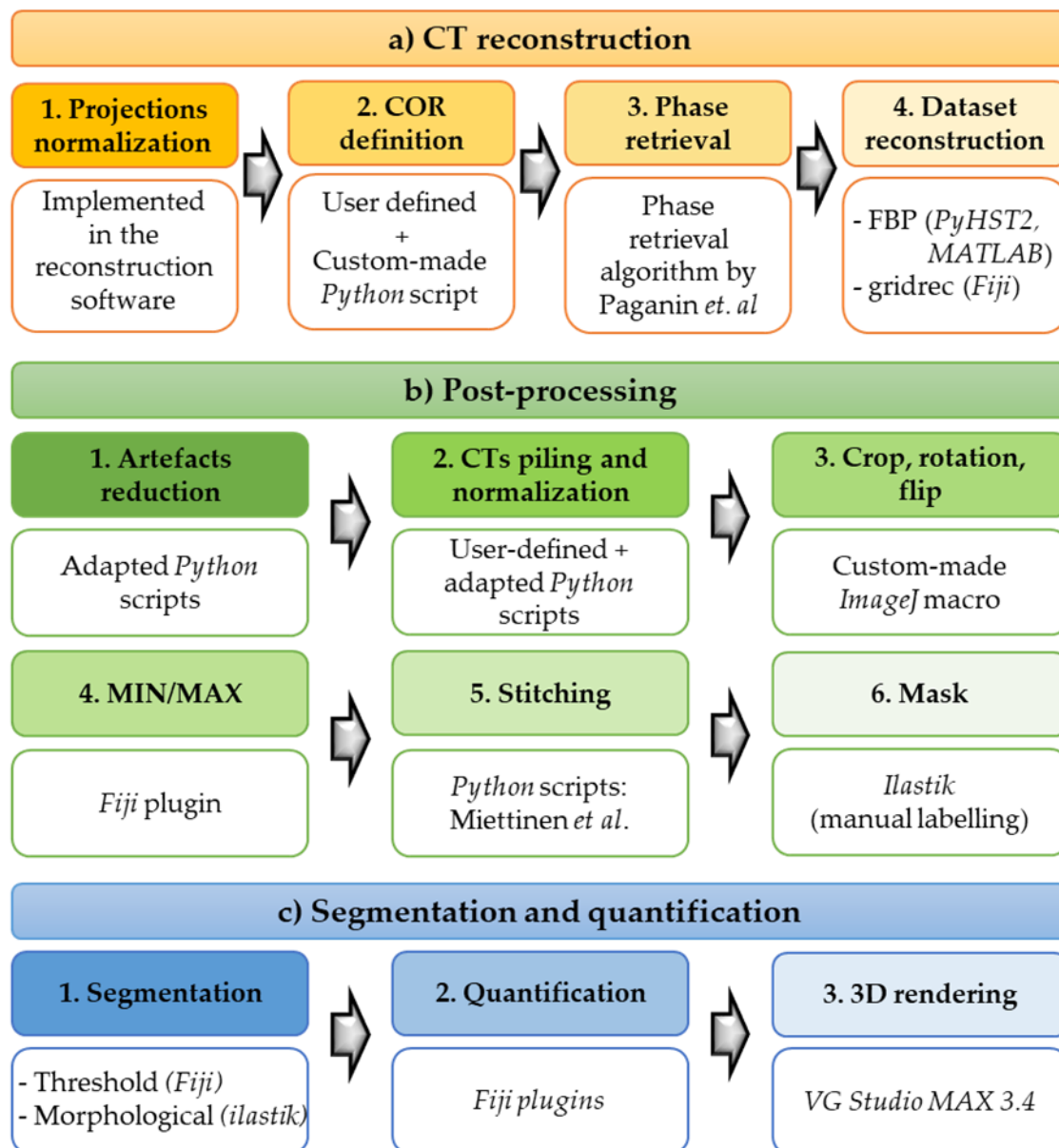


Figure 5.1: scheme of the workflow adopted in this thesis for XPCI-CT data reconstruction, processing and features segmentation and quantification. Each step is reported together with the used scripts or software.

5.1 XPCI-CT image reconstruction

All the XPCI-CT datasets acquired in this Thesis work were reconstructed with either the FBP or gridrec algorithm after the application of the single-distance Paganin's phase retrieval to the raw angular projections, as described in sections 2.1.3 and 2.1.4. Every synchrotron beamline used in this work has its own dedicated software; the ones I used for XPCI-CT images reconstruction are:

- The *PyHST2* package (Mirone, 2014), used at the ESRF-ID17, assumes a monochromatic X-ray beam with a small divergence and the propagation through

the sample to be kinematic, i.e. scattering from each atom is independent from all other atoms and afterwards the X-rays pass beyond without further scattering. The software includes the Paganin's phase retrieval and the FBP algorithms.

- The *gridrec* based *Fiji* plugin (Marone, 2012; Marone, 2017) is used at the SLS-TOMCAT beamline. It is based on the Fourier Transform method and Paganin's phase retrieval. The reconstruction procedure maps the Fourier space onto a Cartesian grid after convolution with the Fourier transform of a certain function $w(x, y)$, of which contribution is removed after the 2D inverse FFT.
- A dedicated MATLAB script (Moosmann, 2014; MATLAB, 2010), based on FBP algorithm and Paganin's phase retrieval, is used at the PETRA III-P05 beamline.

As visible in Figure 5.1, the reconstruction process is composed of four different sub-steps: 1) the projections normalization, 2) the centre of rotation (COR) definition, 3) the phase retrieval and 4) the final dataset reconstruction.

The first procedure the collected raw projections undergo is the normalization with the average of the acquired dark field and white field images as follows:

$$Normalized\ proj = \frac{Raw\ proj - DF}{WF - DF}$$

where the DF subtraction removes the electronic noise and the division by the also corrected WF compensates for possible X-ray beam inhomogeneities.

During the reconstruction procedure and before the final CT images are obtained, the user has to define two main parameters: the COR and the δ and β values for the object under study. Both parameters are given as input values from the user to the reconstruction software.

The **COR definition** is the procedure of settling the horizontal pixel value, within the projections, at which the CT rotation axis (i.e. axis of rotation of the sample) lies. An incorrect COR value will produce half-circle artefacts around the features within the sample as shown in Figure 5.2, where the same image with different COR values is reported; the direction of these half-circles depends on whether the selected COR is larger or smaller than the actual value. The circles semi-aperture equals the value of pixels to be incremented or decremented for reaching the true COR value. Due to

the high-resolution optics under use in this Thesis and possible small mis-alignments between subsequent CT stages, the COR has to be determined for every CT stage. For all the three reconstruction software I have defined the correct COR by generating different previews of the CT images; a dedicated tool is already implemented in each software.

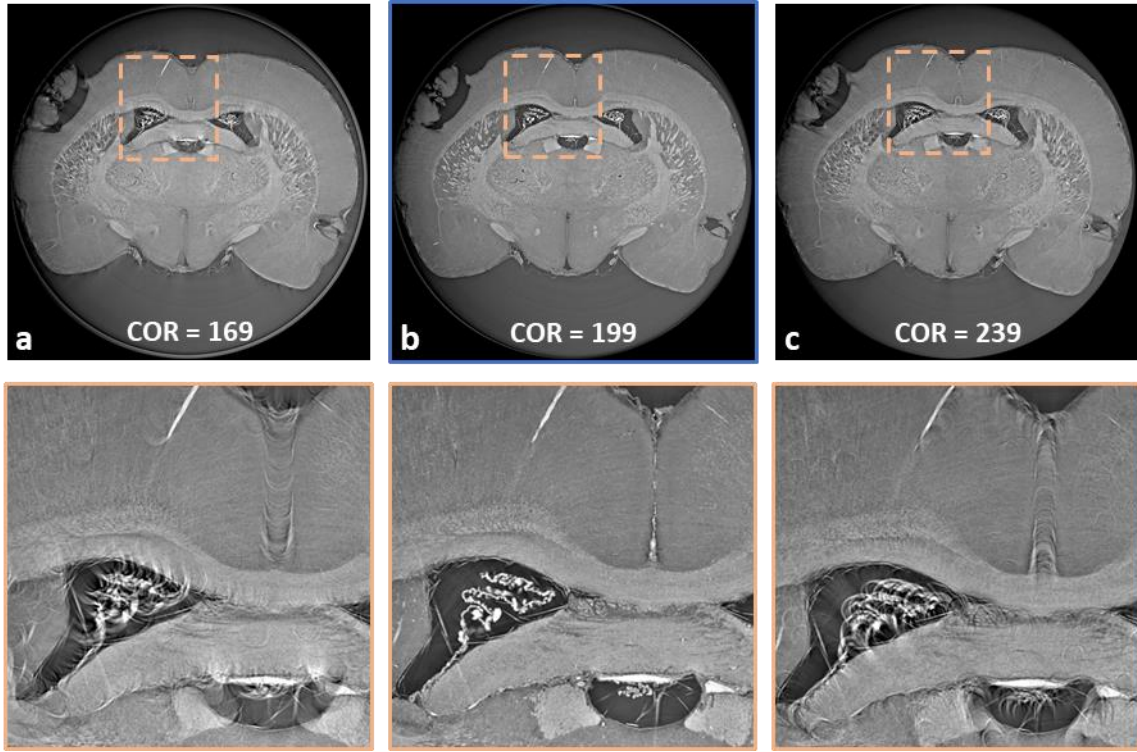


Figure 5.2: $3.25^3\mu\text{m}^3$ voxel size XPCI-CT coronal image of formalin fixed healthy rat brain reconstructed with three different centre of rotation (COR) values. The COR increases from (a) to (c) and reaches its optimum value in (b). Incorrect COR values produce half circles artefacts, as shown in the zooms, which direction depends on if the COR is larger or smaller than the true value. The larger the distance of the selected COR to the actual value, the larger their aperture.

The δ and β values are to be determined for every sample type to be studied; viable values for both lung and brain specimens are $\beta \sim e^{-10}$ and $\delta \sim e^{-7}$. For the phase retrieval, the SLS-TOMCAT and PETRA III-P05 dedicated software require δ and β values as inputs, while the ESRF-ID17 *PyHST2* uses the Paganin length parameter P_L , which has to be set by the user:

$$P_L^2 = \pi\lambda d \frac{\delta}{\beta}$$

where λ is the X-ray beam wavelength and d the sample-to-detector distance, both given in μm . The study of the P_L parameter is visible in Figure 5.3, where a

$3.25^3 \mu\text{m}^3$ voxel size brain XPCI-CT coronal image is reconstructed with six different P_L values. The correct P_L value allows optimizing the contrast between the different materials and the anatomy visibility on XPCI-CT images (Figure 5.3d); under-filtering confers marginal benefit (Figure 5.3a-c), but over-filtering produces blurring and feature visibility loss (Figure 5.3e-f). In this Thesis I assessed the P_L value to be used for CT reconstructions by: *i*) qualitatively evaluating the features contrast and limiting structures blurring; *ii*) calculating, according to (Peli, 1990), the overall image root mean square (RMS) contrast for different P_L values. These two evaluations were performed on the same image reconstructed with different P_L and the procedure was repeated for several images belonging to different samples.

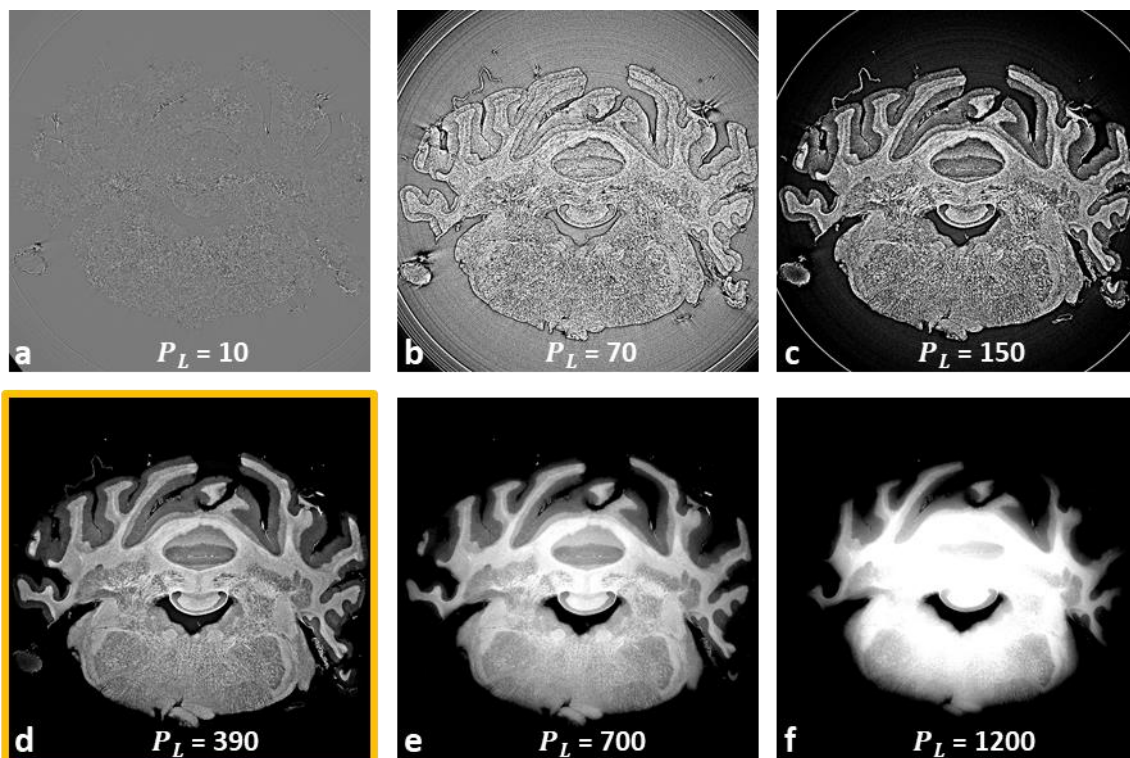


Figure 5.3: a rat brain XPCI-CT image at $3.25^3 \mu\text{m}^3$ voxel size reconstructed with the PyHST2 package with different values of Paganin length (P_L) for phase retrieval. For low P_L values the brain anatomy is not distinguishable (a) or visualized in an edge-enhanced modality (b)-(c). The correct P_L value (d) features the brain details at best, while P_L values higher than the true one (e)-(f) blurs out the image losing the phase-based contrast typical of XPCI-CTs.

5.1.1 Phase retrieval optimization with the RMS contrast evaluation

Following the qualitative P_L evaluation, I studied the image RMS contrast, i.e. the standard deviation of the image pixel intensities on a set of images belonging to different samples in order to validate the qualitative P_L evaluation and thus to estimate the contrast of the features within the images. The RMS contrast for an entire image is defined as (Peli, 1990):

$$C_{RMS} = \sqrt{\frac{1}{N-1} \sum_{j=0}^N (I_j - \bar{I})^2}$$

where N is the total number of pixels in the image, I_j the normalized grey-value for the j^{th} pixel such that $0 < I_j < 1$ and \bar{I} the mean normalized grey value of the image. I have developed a *Python* script to evaluate the RMS contrast of which application to the coronal brain XPCI-CT image of Figure 5.3d is showcased in Figure 5.4a. The obtained results confirm an improvement of the image contrast by increasing the P_L value (and thus the δ/β ratio) for sub-optimal P_L values; this trend then stabilizes after the optimum value is reached. Furthermore, the histograms of Figure 5.4b-c report the grey level distribution for the images reconstructed with $P_L = 10$ (under-filtering) and $P_L = 390$ (optimum filtering) revealing the extent of the available grey-level range utilized by the image and confirming the results of Figure 5.4a. The under-filtered case (Figure 5.4b) results in a majority of pixels being grouped in the centre of the histogram (grey values between 100 and 140), which severely limits the dynamic range and contrast of the image, while a larger dynamic range is available for the image with the true P_L value (Figure 5.4c) resulting in the separation of the different structures (high-contrast image). Thus, **Paganin's phase retrieval improves the separation among the different grey levels and therefore the contrast of the image features.**

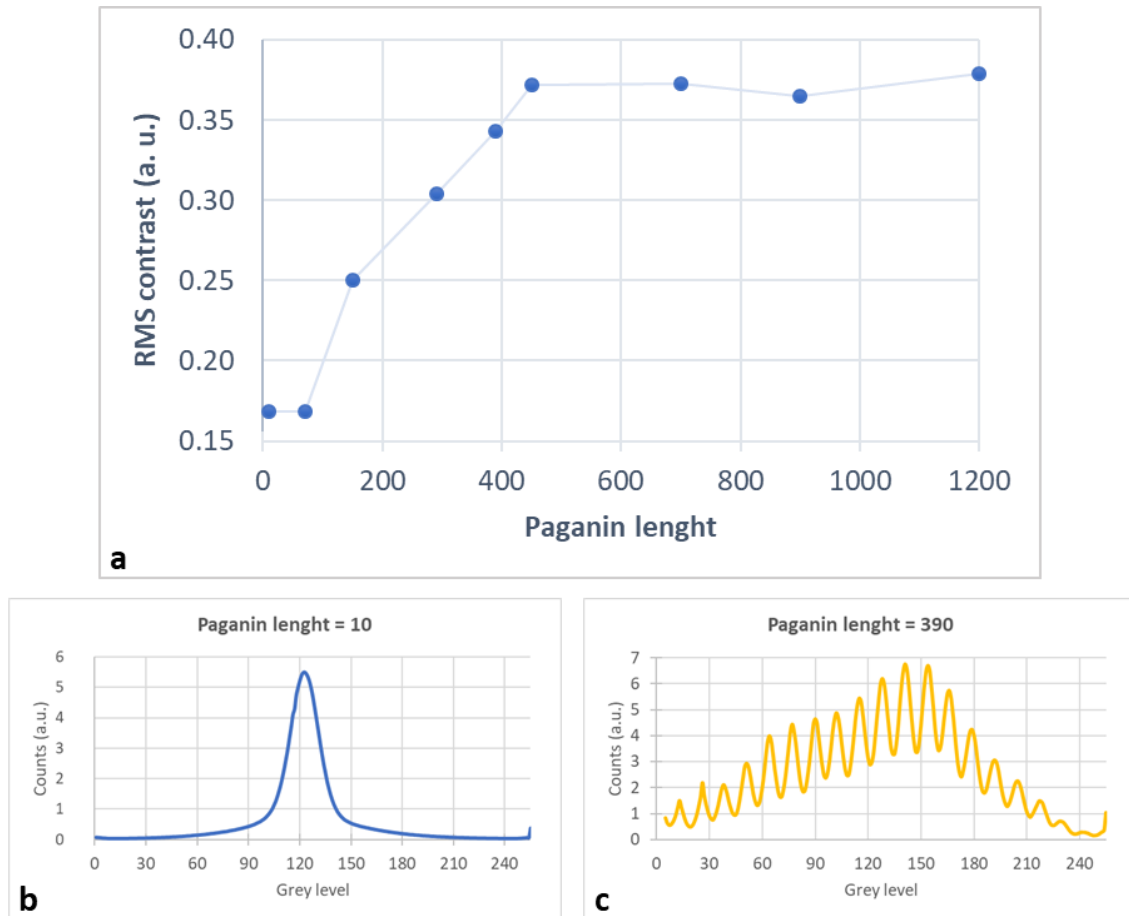


Figure 5.4: (a) root mean square (RMS) contrast evaluation of the same brain slice reconstructed with different Paganin length (P_L) values showing increasing contrast as P_L augments and a contrast stabilization after the optimum P_L value, where all the structures are resolved and induced blurring starts. (b) and (c) are the histograms of the grey levels of the images reconstructed with $P_L=10$ and $P_L=390$, respectively. (b) is characteristic of a low-contrast image where the object features and the background are all displayed with the same grey values, while (c) is representative of a high-contrast image where the different features are well separated.

After the COR and the phase retrieval parameters are optimized, the full CT datasets can be reconstructed. If the reconstruction is performed with the *PyHST2* software, CT images are saved in the “EDF” file format. Thus, a conversion of the images to “TIF” files is commonly applied for enabling post-processing and easing their visualization. The TOMCAT and P05 software directly produce “TIF” CT images.

5.2 Images post-processing

5.2.1 Artefacts correction

XPCI-CT data and consequently reconstructed XPCI-CT images can be affected by a number of different artefacts that can have various origins, such as the sample preparation, X-ray beam inhomogeneities and defects or misalignment of the components of the imaging setup (Barrett, 2004; Schulze, 2011). The optimization of the setup and of the protocols for sample preparation and fixation on the CT stage are thus crucial steps. In the presence of image artefacts, *ad hoc* image post-processing procedures can be developed and used to reduce or remove these unwanted effects. In this section, the most common source of artefacts, which were encountered in this work, is discussed together with possible ways of reduction that I have implemented and tested. Other sources of artefacts to be considered are the image noise and the angular under-sampling. The first has been already discussed (image normalization), while the angular under-sampling can be avoided by studying the optimum number of needed angular projections for a given sample, which directly depends on the portion of the detector lateral FOV occupied by the sample. Angular under-sampling will produce aliasing with the appearing of fine stripes resulting in sub-optimal visualization of sharp edges and small objects information.

Cupping artefact

Cupping artefacts are commonly seen when using a polychromatic X-ray beam. By passing through the sample, polychromatic X-rays undergo a selective attenuation of lower energy photons that ‘hardens’ the beam increasing the X-rays mean energy as the beam passes through the object. Thus, details of the imaged sample placed at different depths are imaged with a varied beam, impairing efficient grey scale windowing and posing a problem in volume visualization (Altunbas, 2007). Interestingly, a similar effect is obtained when only a local region of the object is imaged (local CT acquisition); the fact that the sample is larger than the detector FOV, causes the acquisition of truncated projections that are misinterpreted by the FBP reconstruction algorithm (Gompel, 2004).

The effect of the cupping artefact on XPCI-CT images is shown in Figure 5.5 where a 3.25^3 um^3 voxel size rat brain XPCI local CT image obtained with the ID17 *pink beam* is shown in its original reconstructed form with two different

choices of the grayscale window (Figure 5.5a-b). The first windowing is attained by optimizing the contrast for the central part of the image, obtaining a limited visibility at the image borders, and the latter was chosen for visualizing the entire imaged tissue. Figure 5.5a illustrates the typical appearance of an XPCI-CT image suffering from a cupping artefact, of which profile, drawn along the yellow dashed line, is far from an ideal flat profile (Figure 5.5d) (as expected from a quasi-uniform specimen as a rat brain).

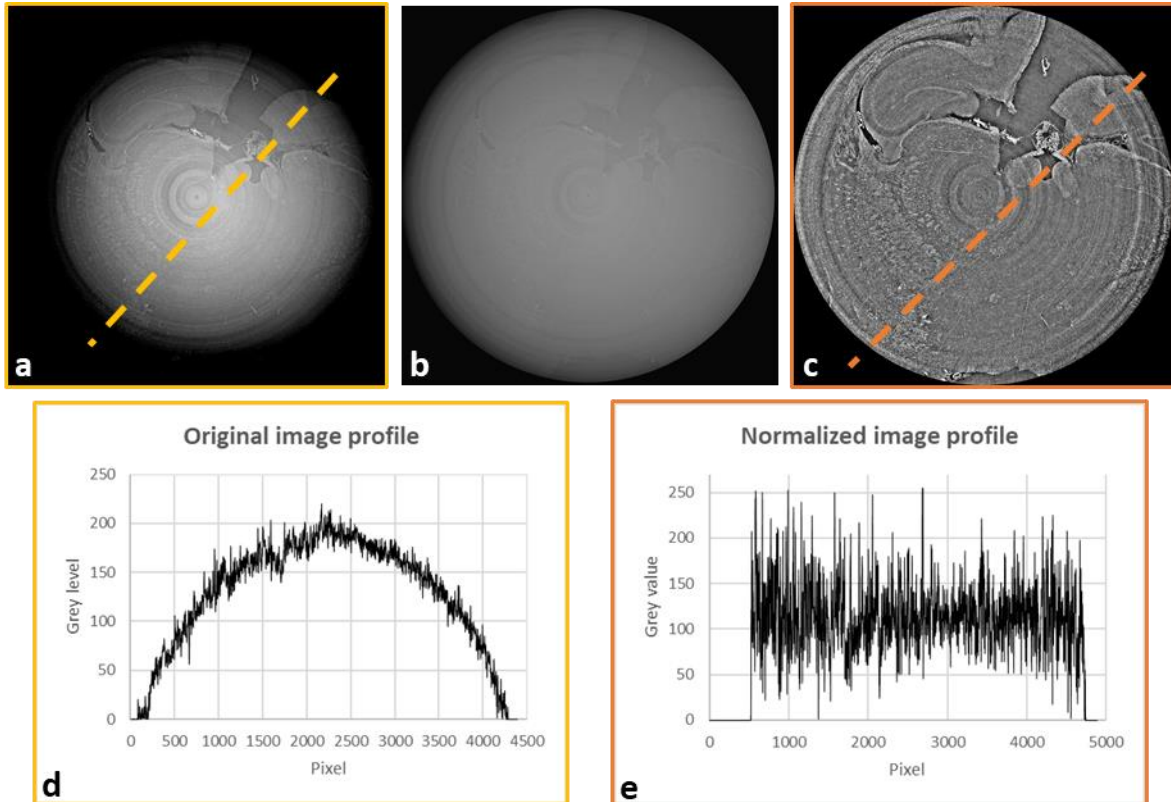


Figure 5.5: cupping artefact on a 3.25^3 um^3 voxel size rat brain XPCI-CT image with two different windowing (a) and (b); normalized image by its gaussian blurred counterpart (c). (d) and (e) are the grey level profiles, obtained along the dashed lines, for the images (a) and (c), respectively. (d) reports the typical cup-like profile, while the normalized image shows a restored flat, but noisy, profile.

Cupping artefacts can be avoided or mitigated by inserting suitable metal filters between the X-ray source and the sample to pre-harden the spectrum. Nevertheless, residual cupping artefacts can still be present and can be corrected in post-processing phases. The method I used in this Thesis implies the normalization of the image by its blurred version. The blurred image is obtained via the Fiji (Schindelin, 2010) “Gaussian Blur” filtering acting on the image as a low-frequency filter. The original image pixels are convoluted with their neighbours by means of a Gaussian function, of which standard deviation value is set by the

user, producing a map of the low-frequencies. The original image is then divided by its gaussian blurred version to filter-out the unwanted cup profile, as visible in Figure 5.5c. The result is a sub-optimal contrast between different features, but the edges of the different details are well discriminated and the entire sample is visible without needing different windowing adjustments. Figure 5.5e shows the grey-values profile of the normalized image of Figure 5.5c: a flat, but noisy, profile is restored.

The gaussian normalization of the image, obtained in this Thesis by adapting a publicly available *Python* script, represents a valuable technique for obtaining morphologically detailed representations of the samples that can be used for quantitative analyses such as features segmentation (based on the borders detection) and volume evaluation within the sample.

Streak artefact

Streak artefacts can have different origin such as the beam hardening, the presence of sharp edges within the imaged object or abrupt discontinuities in the sample composition/density distribution (Croton, 2018). The two latter cases cause mild to strong X-ray deviations and scattering giving rise to bright and dark streaks as the one showed in Figure 4.1f and Figure 4.2b in section 4.1.1. In this Thesis, streak artefacts have been mainly caused by air bubbles at the tissue-buffer liquid interface or within the paraffin formed during the inclusion procedure. These artefacts can be mitigated with a careful sample preparation.

Motion artefacts

Motion artefacts are caused when the object moves during the CT imaging process. These movements of the samples can be derived from a not perfect fixation of the sample or of its container on the CT stage or of the sample inside the container. Another source of motion artefact is also the degradation of the sample (e.g. shrinkage) or of the environment in which the sample is embedded, induced by the radiation (e.g. degassing of the liquid buffer); this effect is more important the higher the exposure and the dose used for the imaging examination is. The result is that projections taken before and after any movement are inconsistent and different parts of the reconstructed CT image seem to have different CORs; i.e. there is no a single COR value giving a perfectly reconstructed CT slice. Indeed, the lines along which the backprojection takes place do not correspond to

the lines along which the attenuation had been recorded simply because the object has moved during the acquisition. Obviously, the smaller the used voxel size, the smaller the movement necessary to create the artefact. An example of a motion artefact is given in Figure 5.6, where a $3.25^3 \mu\text{m}^3$ voxel size XPCI-CT coronal image of a rat brain is shown. The failure in finding a unique COR for the full image reveals that the sample or parts of it has moved during the acquisition of the angular CT projections. Motion artefacts can be thus prevented with an *ad hoc* sample preparation.

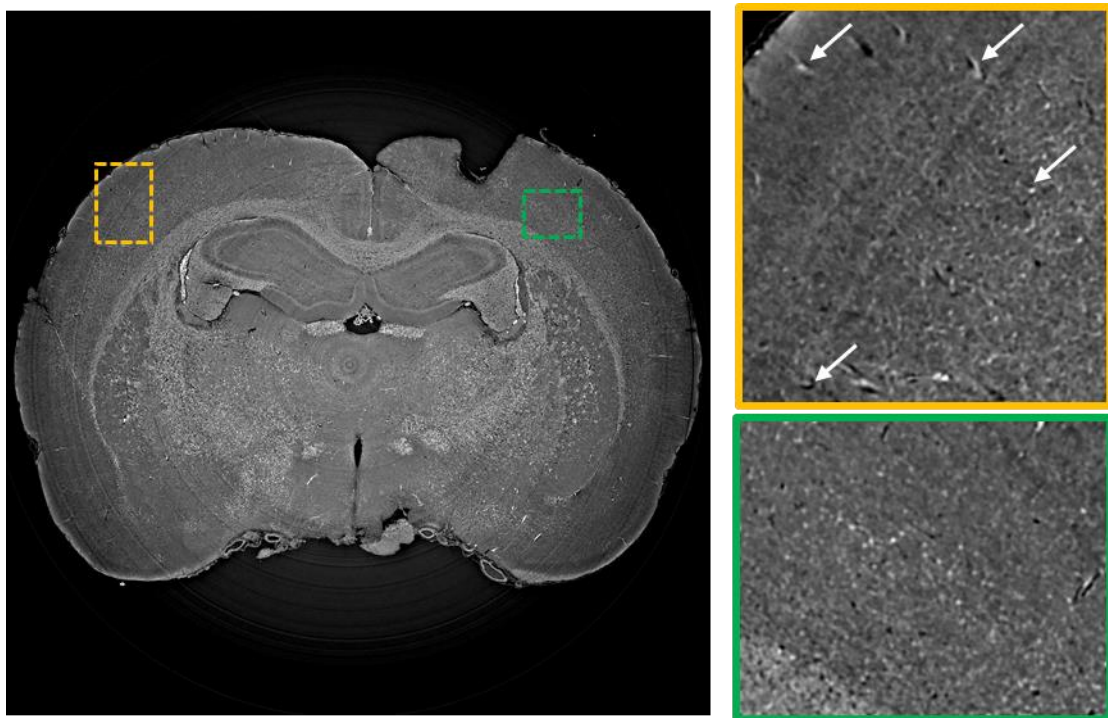


Figure 5.6: example of motion artefacts on a $3.25^3 \mu\text{m}^3$ voxel size XPCI-CT coronal image of a rat brain. The magnified view zooms on a properly reconstructed image part (green box) and on a brain area with wrong reconstruction centre of rotation (half circles) caused by the sample motion during the CT acquisition.

Ring artefacts

Ring artefacts are visible on CT images as concentric rings superimposed on the imaged sample centred around the axis of rotation and can be caused, for instance, by defects of the detecting system such as dead or defective pixels. High degradation of the image can derive from the presence of these rings; thus, its suppression is often implemented in the reconstruction process by introducing refined digital filters. Usually, the ring filtering is applied directly on the sinograms of the projections since, in them, CT rings appear as straight lines and can

be easily isolated in the representation of the image in the Fourier space. This filtering is generally equivalent to a low-pass filter but, in some cases, the truncation of high frequencies can produce secondary artefacts, as partial rings at interfaces within the object (e.g. at tissue-air interfaces), that can be corrected by subsequent interpolation. Other algorithms for ring removal exist and can be found listed in (Massimi, 2018). As an example, algorithms applying the ring filtering on the reconstructed CT images use the image transformation from Cartesian to polar coordinates to display the ring artefacts as stripes according to (Sijbers, 2004) and subsequently apply the wavelet transformation - Fourier transform - Gaussian filtering method described in (Münch, 2009) or use homogeneity criteria for discriminating the object from the artefact contribution (Brun, 2009).

In this Thesis work, ring removal was only applied to the lung images acquired at the TOMCAT beamline by utilizing the sinogram filter described in (Münch, 2009), which is implemented in the *gridrec* reconstruction software.

5.2.2 Stack piling and normalization

In order to obtain a full organ 3D XPCI-CT dataset, some further post-processing is needed on the reconstructed images.

As mentioned before, for the brain specimens, the full organ coverage was obtained with a $3.25^3 \mu\text{m}^3$ voxel size by acquiring several vertical CT stages that then have to be piled and normalized. Normalization is required since each CT stage is saved as an independent image stack with a specific grey value range (a specific windowing). The different normalizations of the single CT stages are due to the composition of the imaged part of the sample and to possible temporal variations of the beam intensity during the imaging session. These effects can shift the grey palette towards different grey values for each CT stage.

To equalize the datasets of the different CT stages, the following procedure is applied:

1. Identification of the CT images corresponding to overlapping imaged regions between any two subsequent vertical CT stages and deletion of the redundant slices;
2. Gathering of all the remaining slices in one folder;

3. Images normalization:
 - a. The mean grey value (m) and the standard deviation (σ) for the full dataset are computed;
 - b. The greyscale of each image is shifted of m and the result is divided by σ enabling an ‘equalized’ visualization of the full organ.
4. Rotation and flip of the CT images to obtain a radiologic view, i.e. coronal slices showing the organ morphology from the point of view of the patient’s feet. The image flipping is only applied when images are not automatically reconstructed with the radiological view because of the software settings or sample positioning during the CT acquisition.
5. Image cropping to reduce at maximum the background and consequently the dataset dimensions.

I implemented this procedure for all the brain samples using an already available *Python* script for image normalization and a custom-made *ImageJ* macro.

Lung CT datasets do not need stack normalization since the samples thickness fits in one single CT vertical stage.

5.2.3 Maximum projection intensity

In some cases, maximum intensity projections (MIPs) were computed for a stack of XPCI-CT slices by means of the maximum intensity projection function of *Fiji*. The MIP is a method that projects the most intense pixels within the stack on a single 2D output image and is used to highlight hyper-dense signals, as visible in Figure 5.7.

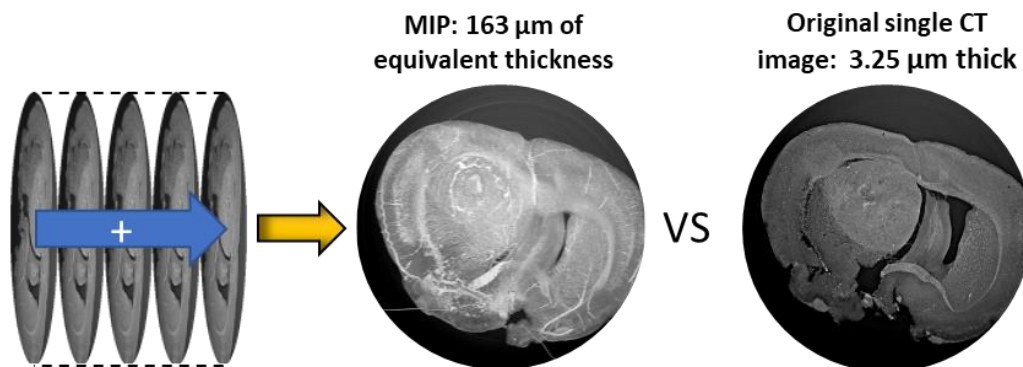


Figure 5.7: from left to right: the representation of the stack of $3.25^3 \mu\text{m}^3$ voxel size XPCI-CT images, the final maximum intensity projection (MIP) obtained by projecting a stack of 50 consecutive slices and one original CT image as a comparison for the MIP signal.

Figure 5.7 schematically represents the process for obtaining a MIP for a brain sample reporting the comparison of the final MIP with one of the original images of the CT stack. As visible in the reported example, hyper-dense signals that were not clearly visible in the single CT slices are enhanced with the MIPs.

5.2.4 Local CT stitching

Lung XPCI-CT images acquired at the TOMCAT beamline with the mosaic modality (see paragraph 4.2.2) are subsequently stitched together by using the procedure described in (Miettinen, 2019) and implemented in published *Python* scripts. This non-rigid stitching procedure is able to correctly stitch CT datasets acquired in adjacent and partially overlapping regions of the samples (yellow circled in the example in Figure 5.8), which may suffer from small local movements, and compensates for these inconsistencies using a local phase correlation.

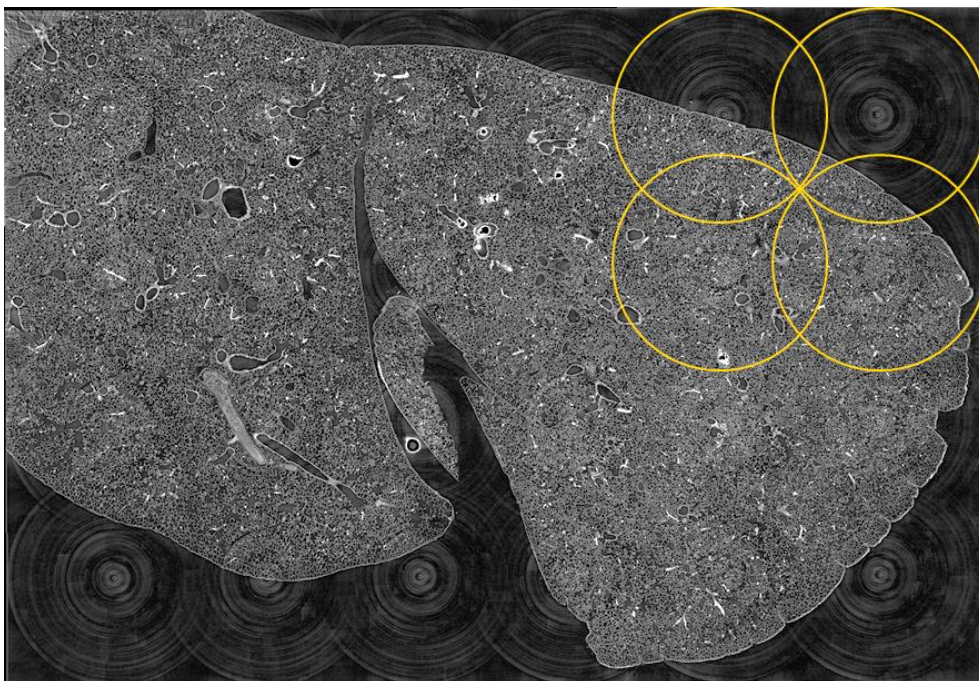


Figure 5.8: 6×4 $1.63^3 \mu\text{m}^3$ voxel size mosaic XPCI-CT coronal image of a healthy lung specimen. The yellow circles showcase the scanning area of each sub-CT. The stitching algorithm is robust in merging the overlapping CT datasets acquired in adjacent-partially overlapping sub-regions of the samples that are not placed at the border of the final image; the result at the borders is sub-optimum due to the lack of data in the overlapping regions (as visible in the top-left corner).

For each overlapping region, a pairwise matching is computed in order to match the structures imaged in multiple sub-sets. Afterwards, a coordinate transformation between the stitched mosaic and each sub-set is defined such that all the overlapping regions of the sub-images become geometrically congruent. Then,

the mosaic image is reconstructed by using all the transformed sub-sets. The result for a lung CT image is shown in Figure 5.8.

5.2.5 Data masking

After all the presented post-processing are applied to the CT images, a masking to remove the background is implemented since, in some cases, the background may present artefacts such as the rings showed in Figure 5.8. Thus, a segmentation procedure is applied to mask the lung or brain parts in the CT images.

Image masking allows for a better visualization of the imaged organ and helps in the segmentation of features of interest avoiding the accounting of unwanted background areas. The masking procedure was performed in this Thesis by means of the *ilastik* (Berg, 2019) ‘carving method’ by manually labelling the background and the imaged organ in 10% of the available slices in one dataset. The program interpolates among the labelled slices to properly mask the residual images. The output images are a series of binary images where the background is displayed in black and the organ tissue in white. This dataset and the original one are processed with the *Fiji* ‘Image Calculator’ using the ‘MIN’ options. This plugin replaces with black pixels the background area (i.e. portions of the original

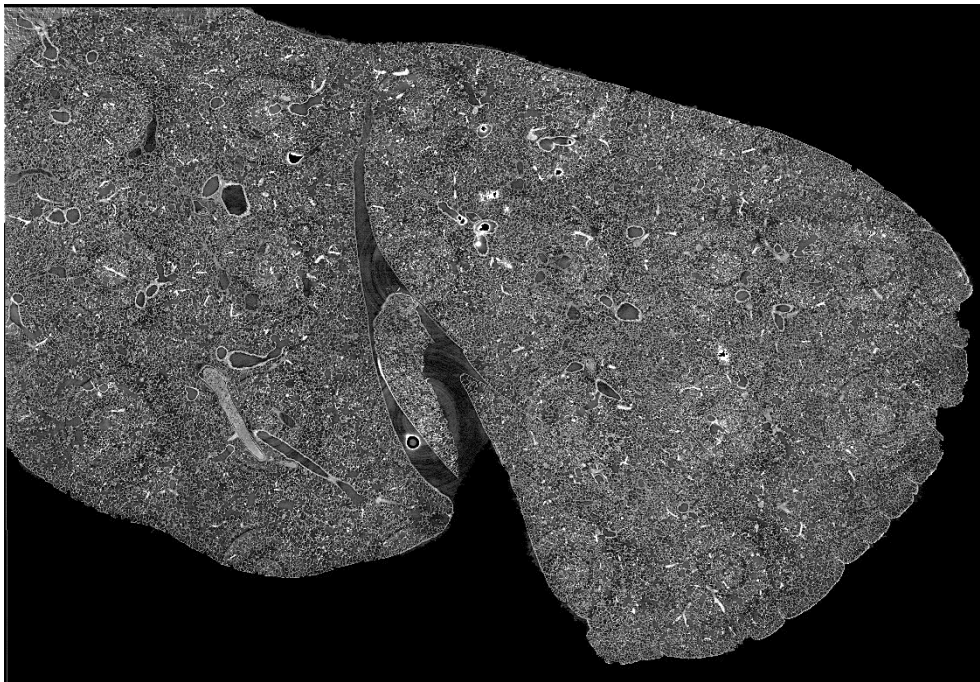


Figure 5.9: masked $6 \times 4 \times 1.63^3 \mu\text{m}^3$ voxel size mosaic XPCI-CT coronal lung image. The background is correctly removed maintaining the lung tissue unalterably visualized.

dataset that are set black in the binary images). The result of the masking procedure applied to the CT image of Figure 5.8 is showed, as an example, in Figure 5.9 where the background is removed and the tissue visualization is preserved. Only a small residual background at the centre of the image is present since, at a different depth, this region is occupied by lung tissue. If needed, the image can be individually further masked.

5.3 Segmentation and quantification of the features of interest within the examined specimens

Segmentation is the procedure of partitioning a digital image into multiple segments and is a crucial step for the analysis of the features of interest within an imaged sample since it allows isolating those structures from the background in which they are embedded. After this procedure is accomplished, 3D rendering and volumetric quantifications can be easily obtained. Ideally, the segmentation procedure should be automatized and as independent as possible from the operator's skills and experience.

Within this Thesis, I segmented the features of interest either by thresholding the grey values palette or by morphological identification of the features on the images. For the latter method I built and put into practice a semi-automatized procedure.

5.3.1 Threshold segmentation

Thresholding is the simplest segmentation method but can only be efficiently used if the structures to be segmented have grey values (i.e. intensity for grey-scale images) that clearly stand out from the background. In this procedure, the value of each pixel of the image is compared to the threshold value (T) and assigned the following new values $I_{new}(x, y)$:

$$I_{new}(x, y) = \begin{cases} 0 & \text{if } I(x, y) \leq T \\ 255 & \text{if } I(x, y) > T \end{cases}$$

where $I(x, y)$ is the original value of the pixel located at x and y within the image. In this case, a lower threshold is applied and all the pixels of which intensity is above T are partitioned. Upper and/or multiple thresholds can be applied too. Threshold values are chosen by displaying and analysing the image histogram

and identifying the grey scale interval of the feature that one wants to segment; thresholds are found in correspondence of local minima.

In this Thesis, the threshold segmentation is used for high absorbing features such as Fe/Ca deposits within the lung or brain tissues. The advantage of a threshold-based segmentation is its rapid execution speed, while the drawback is that features to be partitioned should have grey values that stick out from the other (i.e. high contrasted features), otherwise unwanted pixels may be included in the segmentation, as shown in Figure 5.10d for the segmentation of intra-scar Fe deposits in a lung specimen. Figure 5.10 showcases the workflow of the threshold segmentation I applied to the CT datasets in this Thesis:

- a) the greyscale image is obtained and cropped around the features to be segmented;
- b) the image histogram is displayed via *Fiji* and potential thresholds are found according to the minima location. In this case, a threshold of 254 is chosen;
- c) the chosen threshold is set and pixels above that value are selected and segmented;
- d) a binary image is created. In this image some unwanted structures, which are visible within the red circles, are selected together with the 'actual' Fe deposits;
- e) finally, unwanted segmented pixels are cleared with a masking procedure.

The procedure, here reported for one single CT slice, can be simultaneously applied to an entire CT stage. A unique threshold can be used for all the images or an adaptive threshold value can be selected, i.e. slightly different thresholds are applied to the different images of the stack.

Once the binary images are produced, the segmented features can be quantified using the *Analyze Particles Fiji* plugin, which returns, for each image, the area of each single feature and the total detected-segmented area. The volume of the features is obtained by simply multiplying the area by the slice thickness.

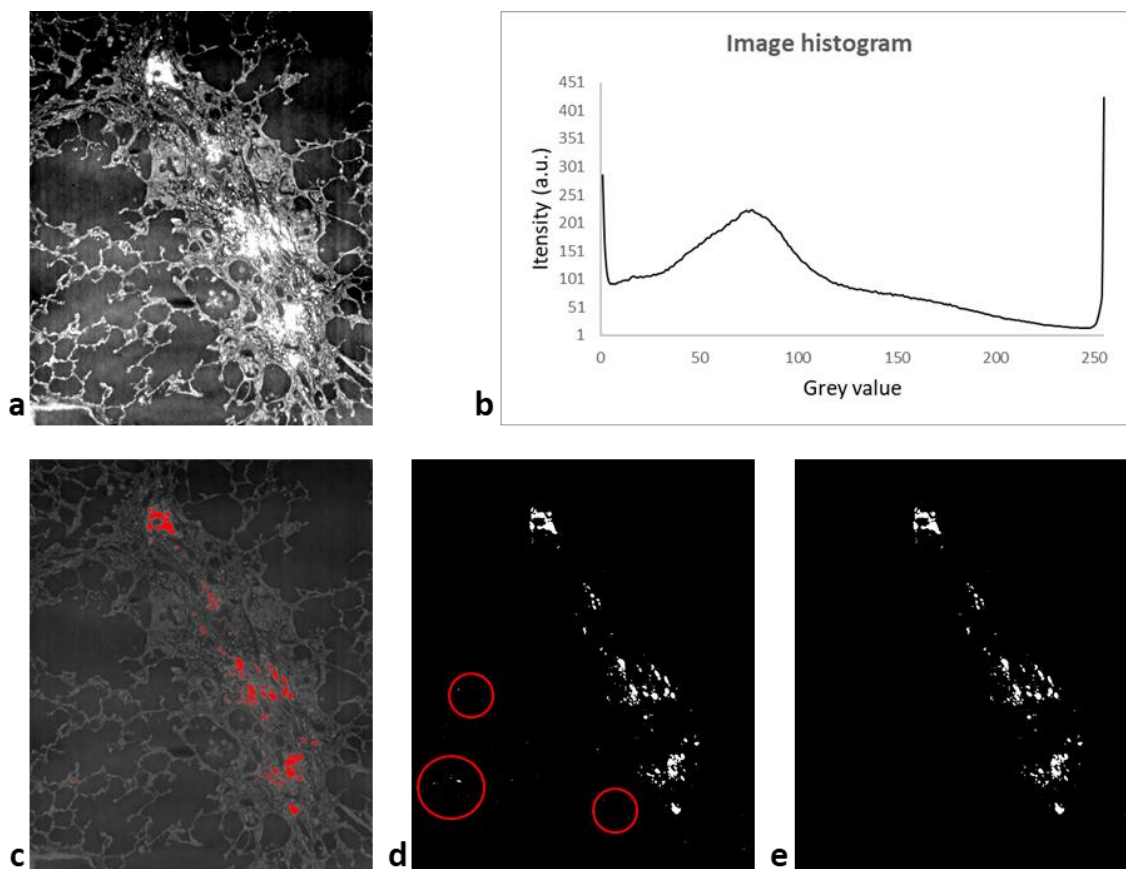


Figure 5.10: threshold-based segmentation procedure showed on a 2D CT lung image. The features to segment are the bright structures (Fe deposits) within the lung scar; the same procedure applies for a 3D dataset. (a) the original XPCI-CT image, an oblique reslicing of a $1.63^3 \mu\text{m}^3$ CT dataset, is cropped; (b) the image histogram is retrieved with Fiji and minima are located as potential thresholds; (c) the selected threshold is applied and pixels of which intensity is above that value are selected in red and segmented; (d) the segmented structures are rendered on a binary image. Some unwanted pixels (in the red circles) are segmented too and are cleared in post-processing (e). Figure (a) is adapted from (Romano, 2021b).

Alternatively, threshold-based segmentation can be obtained with the *3D Object Counter* plugin (Bolte, 2006) of *Fiji* that automatically identifies the volumes of structures with grey values above, or below, the selected threshold as follows:

1. all the 2D images are thresholded individually;
2. the 2D structures belonging to the same feature volume are connected;
3. the volumes of the single features are computed and a binary 2D image dataset is produced with the thresholded volumes.

The *3D Object Counter* plugin can compute several types of information on the segmented volumes and is able to render maps of several properties of the segmented structures such as their volume, surface, centroid and centre of mass

maps. This analysis can be ideally done on the full CT dataset if *Fiji* runs on a sufficiently powerful computer machine; alternatively, the original dataset can be divided into subsets at which the same threshold is applied. Overall, the *Analyze Particles* plugin is faster than the *3D Object Counter* and can be used when only interested in producing binary images of the segmented volumes. In this work, I used the *Analyze Particles* plugin for segmenting the brain tumour in Gd-enhanced MRI images and lung collagen noduli in XPCI-CT datasets, while I applied the *3D Object Counter* to segment the Ca/Fe deposits within the rat brains from XPCI-CT data. I estimated the errors to be associated to the volume assessed after XPCI-CT threshold segmentation by performing the same thresholding on a set of test-dataset and retrieving an overall error (standard deviation of the obtained measurements) to be associated with each segmented feature (i.e. GBM, lung noduli and brain Ca/Fe deposits).

5.3.2 Morphological watershed-based segmentation

The watershed-based segmentation is a robust image processing tool classified as a region-based segmentation approach that was first presented by (Digabel, 1978). The watershed algorithm sees and treats a grey level image as a topographic landscape with ridges and valleys, of which elevation values coincide with the grey values (i.e. intensity values for a grey-scale image) in the corresponding pixels. The image is then decomposed into catchment basins separated by watersheds, with the nomenclature being borrowed by geology, as shown in Figure 5.11.

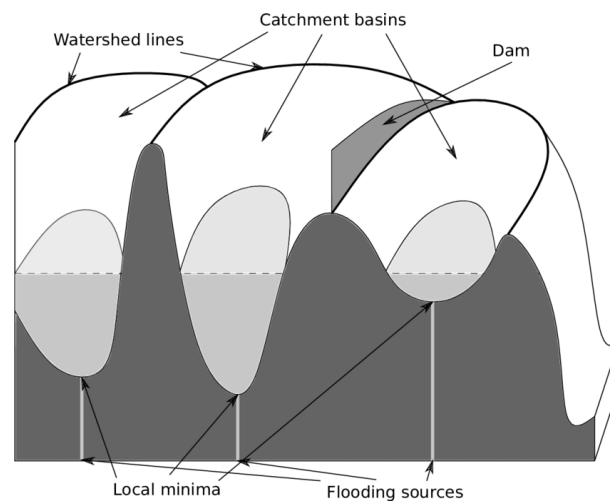


Figure 5.11: watershed segmentation representation. Each local minimum has its own water flooding source and watershed lines divide the catchment basins of the minima. Dams are added to extend the basin borders to avoid water melting from the different minima. Image from (Baran 2018).

To achieve this, after the local minima are identified, a water flood raises from each local minimum and, overall, the water level raises uniformly in the full image until it is fully covered. Dams are added along watershed lines to keep track of the different flooded regions since each area corresponds to a specific grey level and to a portion of the segmented image. A common problem with watershed segmentation is the over-partition of the image. Two main methods have been developed to overcome this problem (El Allaoui, 2012): the hierarchical watershed segmentation and the watershed by markers. The first method merges the segments of which grey levels are within a certain window, while in the latter the flooding starts from the marked minima. The overall result is a reduction of the over-segmentation. Watershed segmentation methods are conveniently used when the features to be segmented have well defined and contrasted borders but poor area contrast (a typical case in XPCI of soft tissues). Thus, the structures to be segmented can be clearly recognized morphologically, but cannot be isolated by means of a threshold of the grey levels.

The *ilastik* software uses an interactive marker-based watershed algorithm to properly segment areas or volumes of interest. Its “*carving method*” was used in this Thesis for brain tumour and fibrotic lung scars segmentation. The workflow I established for semi-automatized segmentation of an entire CT stage is shown in Figure 5.12 and showcased for a brain tumour segmentation:

1. The XPCI-CT images with the feature to be segmented (tumour in this case) are selected;
2. The tumour area is cropped to reduce the data size;
3. A variance filter normalization is applied to each image to enhance the tumour borders and to reduce possible streak artefacts e.g. due to the presence of Ca/Fe deposits;
 - a. For every image, a variance radius of 4 is used leading to a 9x9 square kernel on which, for each pixel, the variance (σ) is calculated according to $\sigma^2 = \frac{1}{n} \sum_{i=1}^n (u_i - \bar{u})^2$, where $n = 81$, u_i is the intensity of the i^{th} pixel and \bar{u} the median intensity (Sarwas, 2015).
 - b. As a result, homogeneous tissues are displayed in black while edges and interfaces are characterized by a brighter grey signal.

4. Every original slice is normalized by its filtered counterpart (i.e. the original slice is divided by its variance filtered version) allowing clearly distinguishing the tumour volume, which is displayed in black, within the surrounding tissue that is characterized by brighter grey values;
5. The obtained dataset is loaded into an *ilastik* “carving method” project where the watershed algorithm separates the images in several watershed segments;
6. The tumour and background volumes are manually labelled with light-blue and yellow markers, respectively. The labelling is performed on the 10% of the images of the stack. In the other slices, the object and background identification are made by interpolation. The procedure of labelling can be iterated to define better and better the volume to be segmented;
7. The area to be segmented, which is detected by the software after the manual labelling, is marked in light-blue as a single segment;
8. The segmented volume is rendered as a binary image dataset;
9. If needed, binary images are used to mask the original dataset to obtain the XPCI-CT tumour volume.

The quantification of the segmented features can be achieved, on the binary dataset, by means of the *Analyze Particles Fiji* plugin and multiplying the values for the slice thickness, as previously described.

This segmentation method was used, in the framework of this Thesis, for segmenting brain tumour volumes and fibrotic scarring lung tissue on XPCI-CT images and the validation of this segmentation procedure is reported in Figure 5.13 and Figure 5.14, where XPCI-CT images are compared to GFAP (for brains) and TRI (for lungs) histology data. For both organs, a good agreement between the *ilastik*-based segmentation and the histology stained tissues is found; infiltrative GBM cells are overestimated by the segmentation procedure (see Figure 5.14d-d’). The error to be associated with the volume estimations after watershed segmentation was obtained by performing the segmentation on a subset of XPCI-CT datasets with and without the variance filtering. The overall standard deviation, given as a percentage of the measured volume, was then chosen as the measurement error.

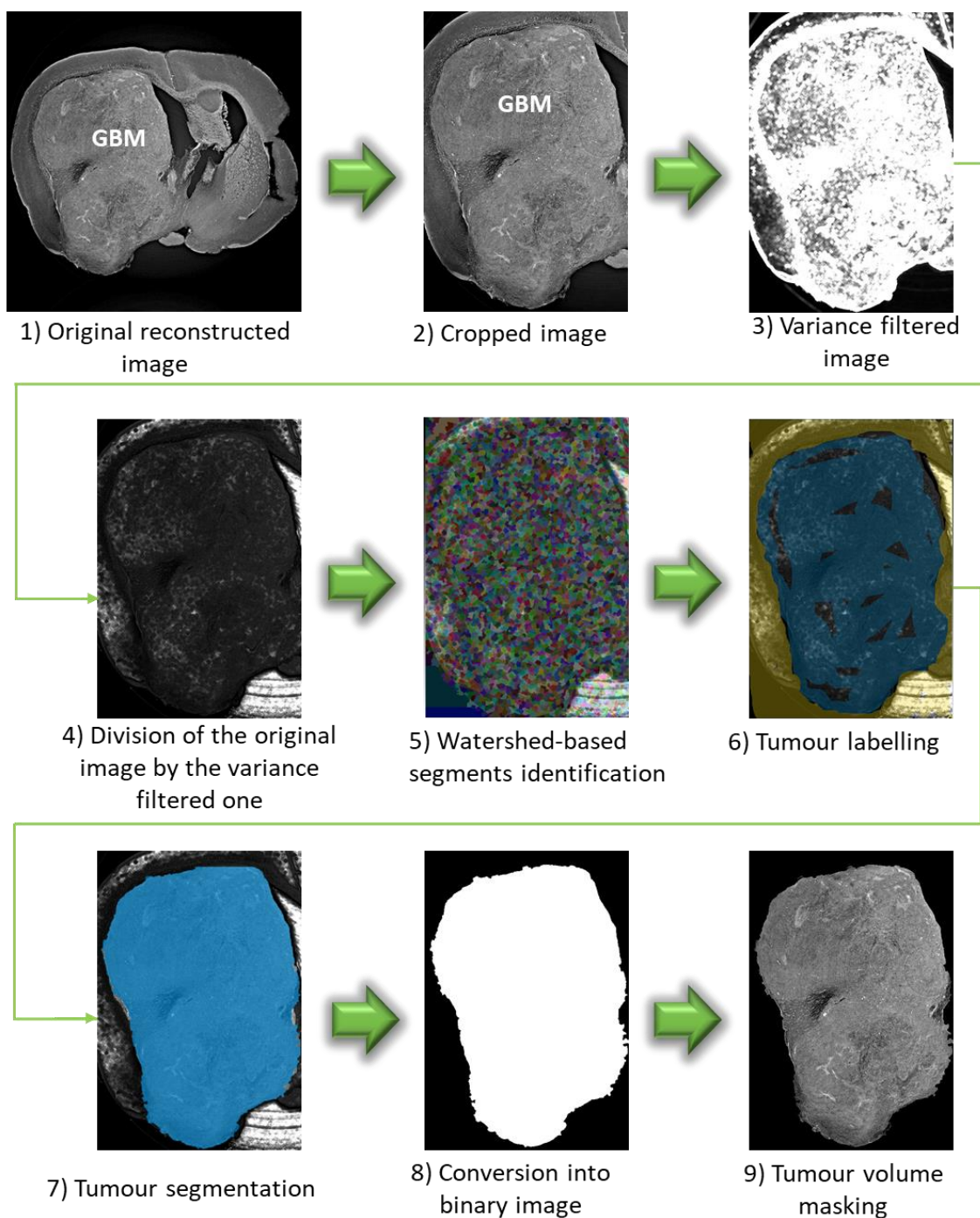


Figure 5.12: the workflow for the ilastik segmentation: showcase on one image of a XPCI-CT dataset of a tumour bearing rat brain. Original 16bit images (1) are used to segment the tumour out and are subsequently cropped for reducing the dataset size (2). A variance filter is applied with a radius of 4 pixels and for enhancing the tumour borders (3), the original image is then divided by the filtered one (4). Thanks to the carving tool of the ilastik software, image segments are identified by the watershed algorithm (5), the object of interest and the background are labelled by the user (6). For a full dataset, it is sufficient to label the 10% of the available slices, the full-volume segmentation will be done by interpolation (7). After the tumour is correctly identified, binary images are produced (8) and used to mask the original dataset (9). Figure modified from (Romano, 2021a).

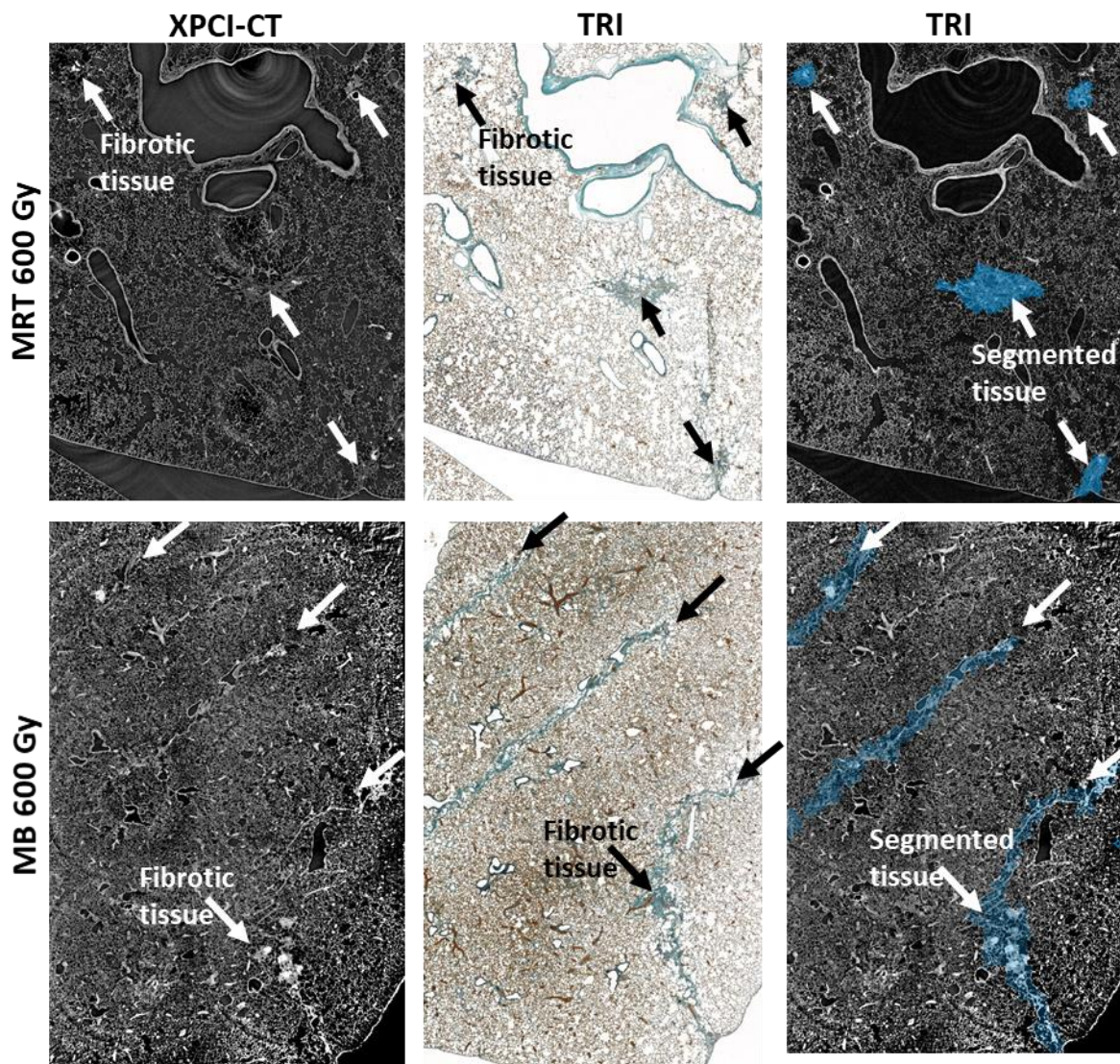


Figure 5.13: examples of the validation of the segmentation procedure of the fibrotic tissue within a rat lung. Two samples (MRT and MB with 600 Gy as peak dose) showcase the validation of the segmentation procedure. Coronal XPCI-CT images acquired with a voxel size of $1.63^3 \mu\text{m}^3$ show a good discrimination between healthy and fibrotic tissue that is confirmed by the Masson-Goldner trichrome (TRI) histology, which stain in green the fibrotic content of the tissue. The outcome of the segmentation procedure (third column) displays good agreement between the real fibrotic tissue (revealed by histology) and the one that XPCI-CT labels as fibrotic tissue. Figure adapted from (Romano, 2021b).

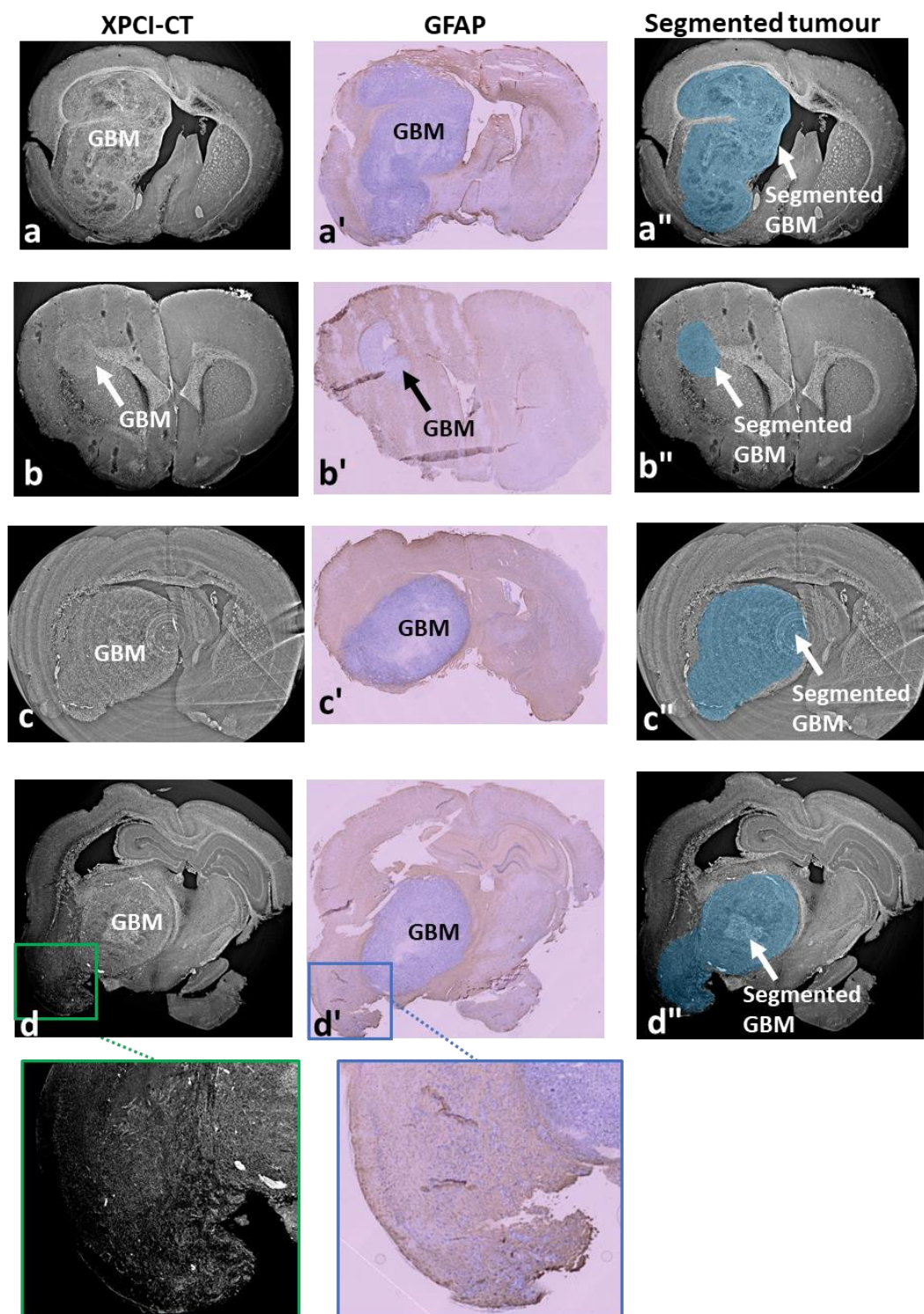


Figure 5.14: *ilastik* brain tumour segmentation validation. For four samples the comparison of XPCI-CT images (first column) and GFAP histology (second column) with the segmented tumour (third column) is given. One slice for each sample is reported. Good agreement is shown for three samples (a)-(a''), (b)-(b'') and (c)-(c''), while for the images (d)-(d'') a good matching is visible for the solid tumour mass, but the *ilastik* segmentation overestimates the GBM infiltrations as shown in the magnified insets. Figure reproduced from (Romano, 2021a).

5.3.3 Volume quantification of under-sampled 3D datasets

In the previous paragraph I have described the methods used to segment XPCI-CT dataset acquired with isotropic voxels of a few micrometres down to sub-micrometre sizes. These spatial resolutions allow for an accurate segmentation and quantification of the anatomical and pathological features of interest. Things get more complicated when the voxel sizes are relatively large with respect to the imaged objects and details. The lack of a sufficiently resolved representation may easily lead to data misinterpretation and imprecise assessments. This is the case of the rat brain *in-vivo* MRI examinations conducted within this Thesis.

Brain tumours are correctly visualized in either the T₂- and T₁-weighted MRI images when an intravenous Gd injection is performed before the T₁ sequence (see Figure 5.15). Tumour volumes assessment was performed on the T₁-weighted 234x234x1000 μm³ voxel size images after the Gd injection, since the Gd acts as a contrast agent for brain tumours. Haemorrhage was excluded by the segmentation procedure since it produces a recognizable signal, i.e. a T₂-weighted signal loss (<https://radiopaedia.org/articles/haemorrhage-on-mri>).

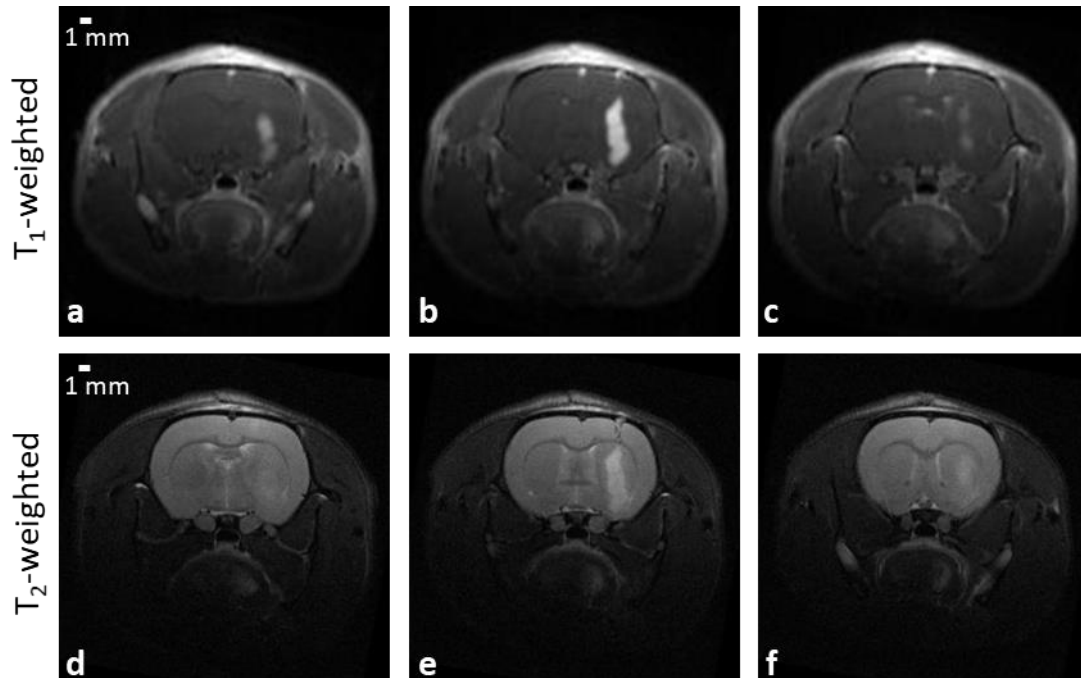


Figure 5.15: *In-vivo* MRI image sequence of a rat brain showing glioblastoma tumour. (a)-(c) are obtained with the T₁-weighted sequence after intravenous Gd injection and (d)-(f) with T₂-weighted sequence. The three reported slices are the only slices, within the acquired datasets, that show brain tumour.

Due to the poor spatial resolution, the tumour contours are not finely resolved in the coronal 2D slices, while in the transverse direction, the tumour is visible in only 2-3 slices, as reported in Figure 5.15. Thus, the tumour cross-sections in the adjacent images have very different sizes. In addition, because of the intra-individual high variability in the tumour growth, no *a priori* knowledge can be used to improve the estimation of the tumour mass volume. Several approaches have been proposed and tested in this work to compute the correct tumour volume by interpolating between the MRI slices with: parallelepipeds, cones and ellipsoids, of which graphic representation is given in Figure 5.16. In all these cases, the 2D MRI coronal slices are first segmented by using the threshold-based segmentation procedure and the tumour areas are computed by means of the "Analyze Particles" plugin in Fiji.

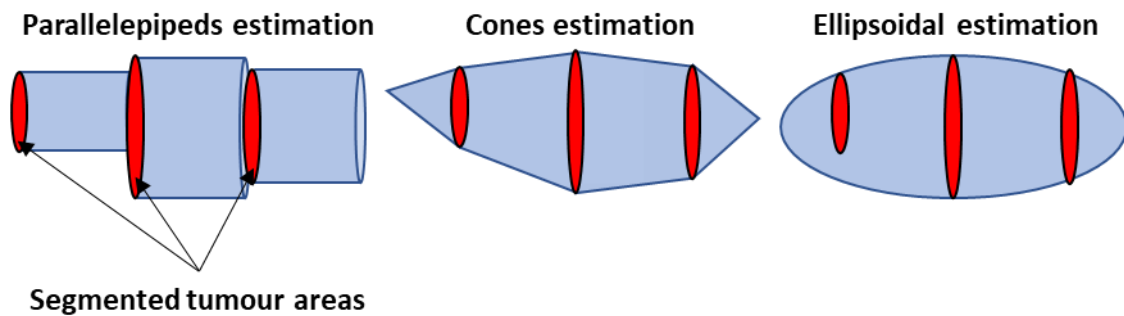


Figure 5.16: schematic 2D representation of the three volume estimation methods of MRI-based segmented tumour volumes. The red areas mimic the segmented tumour areas in the MRI slices and the blue shapes are the 2D views of the volumes that are used to approximate the tumour volume among the slides.

Parallelepipeds estimation

Parallelepipeds volume estimation is a simple and widely used method for volume estimation (Bouchet, 2014; Sezgin, 2013) where the total tumour volume V_t is calculated according to the following formula:

$$V_t = s \cdot \sum_i A_i$$

where s is the slice thickness and A_i are the tumour areas segmented on each MRI image (i) on which the tumour is visible.

Cones estimation

A method I developed to estimate the tumour volume is to approximate the intra-slices tumour shape with cones and truncated cones, as shown in Figure 5.17, thus making the transitions between the individual partial volumes smoother with respect to the parallelepipeds model. Assuming that the tumour is visible in three MRI slices and indicating with A_i the estimated areas of the tumour cross-sections in these slices, a truncated cone is built between $A_1 - A_2$ and $A_2 - A_3$ with height that equals the slice thickness. The tumour rims (built on A_1 and A_3) are simulated as cones with a height equal to half of the slice thickness. This was done to avoid any abnormal (truncated) sharp tumour border.

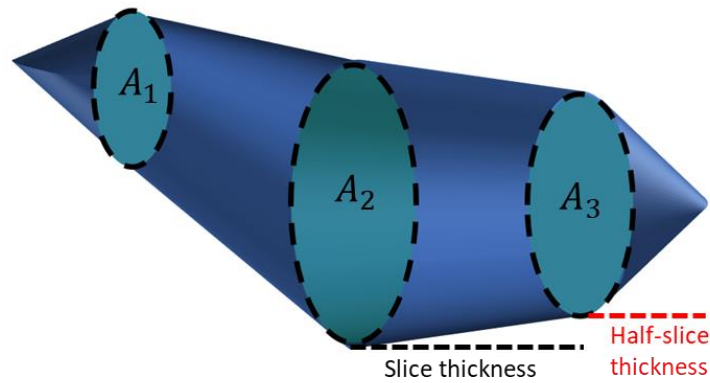


Figure 5.17: scheme of tumour volume estimation by cone and truncated cone volumes. The segmented cross-sectional tumour areas (A_i) are shown in green, while the cone volumes are rendered in blue. Cones and truncated cones have heights equal to the MRI slice thickness and half of the slice thickness, respectively.

The following formula can thus be used to estimate the total volume of the tumour:

$$V_t = \frac{s}{3} \cdot \sum_{i=2}^{N-1} \left[\frac{1}{2} (A_1 + A_N) + (A_i + A_{i+1} + \sqrt{A_i \cdot A_{i+1}}) \right]$$

where the first part of the summation accounts for the cones volume and the second for the truncated cones volumes.

Ellipsoidal estimation

The last tested method is the ellipsoidal model estimation, which use is reported in the literature for the estimation of the volume of other types of tumours such as adenocarcinoma in mice (Sápi, 2015) or mammary tumours in rats (Faustino-Rocha, 2016). Here, the tumour mass is modelled as an ellipsoid with α , β and γ

the radii along the three main axes. To derive α and β , the vertical and lateral tumours half-widths are computed in all the segmented areas and the largest values are selected, as shown in Figure 5.18. γ is the number of slices in which the tumour is visible multiplied by the slice thickness. Thus, the total tumour volume is:

$$V_t = \frac{\pi}{3} \alpha \cdot \beta \cdot \gamma.$$

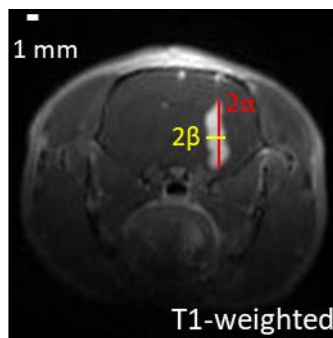


Figure 5.18: example of the derivation of α and β parameters for ellipsoidal tumour volume estimation. The two parameters are chosen as half of the largest vertical and horizontal tumour dimensions, respectively.

I tested the three methods on a set of brain MRI images taken during different sessions (different days post-implantation) and the results of some exemplary cases are reported in Table 5.1. Two different operators, a Master student that I co-supervised and I, performed the MRI tumour segmentation; the standard deviation of the semi-dispersion of the obtained tumour volumes was chosen as the volume error (10% of the value). This high error value reflects both the intra-operator variability in segmenting the features and the poor resolution available for MRI images that impair a precise tumour border definition.

Overall, the parallelepipeds method is the simplest to implement but has the drawback of overestimating the tumour volume since the mass is approximated by a series of parallelepipeds with sharp edges. Cones and ellipsoidal estimations mimic better the natural tumour shape but they are not currently used in the literature for tumour brain volumes estimation.

As visible in Table 5.1, the tumour volumes obtained with the three methods differ one from each other and, due to the lack of high-resolution datasets to be used as a test for assessing which of the three methods is the most accurate, I chose the parallelepipeds method for this Thesis due to its large usage in the literature.

Table 5.1: MRI-based tumour volumes estimation for a subset of rat brain samples obtained with the parallelepipeds, cones and ellipsoidal methods.

Sample Name	Parallelepipeds estimation	Cones estimation	Ellipsoidal estimation
B10	0.80 ± 0.08	0.27 ± 0.03	0.72 ± 0.07
B12	2.1 ± 0.2	0.33 ± 0.03	1.38 ± 0.14
B13	1.32 ± 0.13	0.44 ± 0.04	1.01 ± 0.10
B17	174 ± 17	170 ± 17	185 ± 19
B18	157 ± 15	150 ± 15	158 ± 16
B20	98 ± 10	91 ± 9	99 ± 10
B21	147 ± 15	142 ± 14	190 ± 20
B25	32 ± 3	28 ± 3	43 ± 4
B26	1.81 ± 0.18	0.62 ± 0.06	1.36 ± 0.14
B28	4.6 ± 0.5	2.8 ± 0.3	6.3 ± 0.6
B29	12.9 ± 1.3	8.5 ± 0.9	8.3 ± 0.8
B30	14.7 ± 1.5	9.8 ± 1.0	8.1 ± 0.8
B31	15.4 ± 1.5	12.8 ± 1.3	14.5 ± 1.5

Compatibility study between XPCI- and MRI-based tumour volumes

In order to include in the same analysis the tumour volumes obtained from MRI (*in-vivo*) and XPCI-CT (*ex-vivo*) images, the assessed tumour volumes were normalized by the total brain volume. This volume scaling is necessary to account for modifications (usually shrinkage) of the organ due to the tissue fixation procedures, which is a necessary step for *ex-vivo* experiments to avoid degradation

of biological materials. Before doing so, a compatibility study between the tumour volumes obtained with MRI and XPCI-CT was performed (see paragraph 6.5). The MB350 group was selected for this purpose since all animals in this group died at D15-16, i.e. 3-4 days after an MRI session. Among all the irradiated animal groups, the MB350 is the only one where MRI and XPCI-CT images were acquired a few days apart, thus enabling a good comparison of the tumour volume estimations obtained with the two imaging techniques independently. To compare the assessments of the tumour volumes calculated by XPCI-CT and MRI, and thus to verify the compatibility between the two estimations, the following parameters were computed: *i*) the tumour volumes, normalized to the full-brain volume, for all the seven tumour-bearing animals of the MB350 group computed both by segmenting the MRI and XPCI-CT images, together with the associated error; *ii*) the compatibility reporting the t value, i.e. the difference of the tumour volumes obtained with the two methods divided by the error of the difference; *iii*) the probability $P(t)$ associated with the different values of t according to the Gaussian table; *iv*) the complementary value of $P(t)$, named confidence level (C.L.). Measures with C.L. > 5% are considered to be compatible to each other.

5.4 3D volume rendering

3D rendering of both brain and lung organs were realized with the software *VG Studio Max 3.4* (Volume Graphics GmbH, Heidelberg, Germany). 3D rendering is used to obtain the 3D visualization of radio-induced lesions such as fibrotic content within the lung and micro- and macro-deposits of Ca/Fe within the brain tissue as well as of the brain tumour mass.

Brain tissue 3D rendering

For the 3D rendering of the rat brain datasets, XPCI-CT images need to be processed and segmented using the procedures and methods previously described in this chapter. The brain XPCI-CT slices are masked to remove the background; microcalcifications and tumour volumes are segmented and saved as binary CT datasets. Then, all the volumes are loaded into *VG Studio Max 3.4* in order to exploit at maximum the potential of the XPCI-CT 3D visualization, as shown in Figure 5.19a:

- the full brain organ is rendered in a transparent “*phong*” modality with 80% of opacity allowing the visualization of the co-registered volumes (i.e. the volumes of the brain, of the microcalcifications and of the tumour);
- the segmented microcalcifications are rendered as solid coloured volumes using the “*isosurface render*” modality;
- the segmented tumour volume is rendered with the “*isosurface render*” modality with a 60% of opacity to allow the visualization of the microcalcifications in the surroundings.

Lung tissue 3D rendering

Lung XPCI-CT datasets were processed similarly to the brain samples: the original images were masked to remove the background and rendered in the “*phong*” modality with an opacity of 10%, which was found to be the best rendering density to allow the correct visualization of the co-registered fibrotic tissue. The segmented binary images of the fibrotic tissue were then loaded into the software with the “*isosurface render*” modality, as shown in Figure 5.19b.

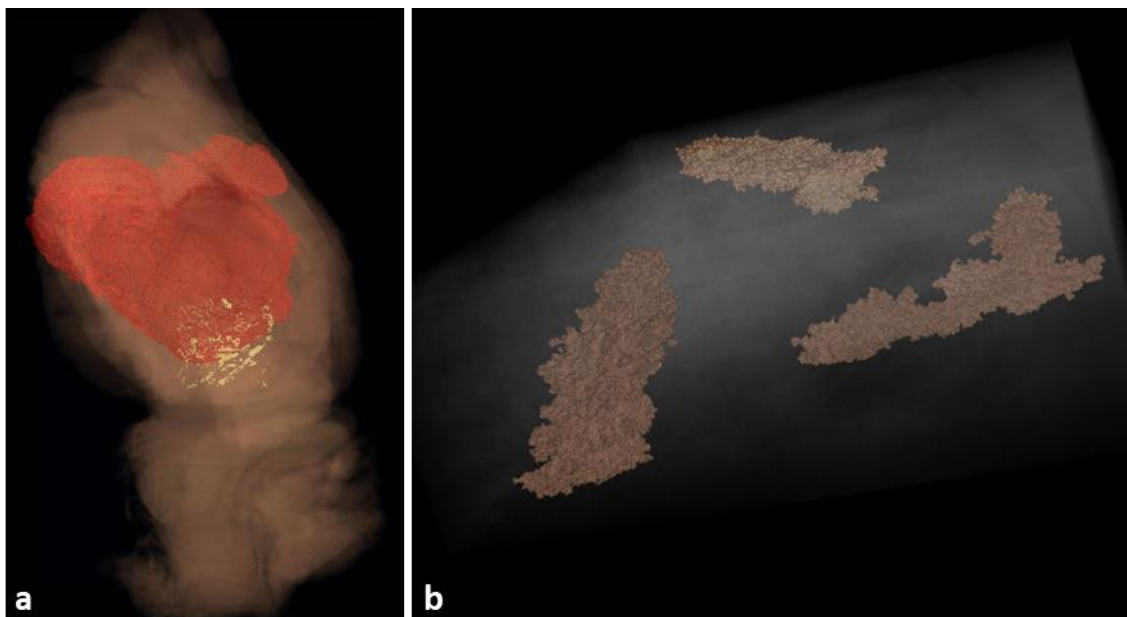


Figure 5.19: 3D XPCI-CT rendering of a BB irradiated rat brain organ (a) and a portion of an MRT-treated lung tissue (b). The organs tissues are rendered in the “*phong*” transparent modality while the brain microcalcifications, the tumour volumes and the lung fibrotic tissue are rendered with the “*isosurface render*” modality. The tumour is set to a 60% opacity to allow the microcalcifications visualization behind the tumour mass.

The image processing and segmentation procedures were carried out with a Fujitsu laptop with 4 Intel Core i7 CPU processors and 2.5 GHz, a Fujitsu workstation with 8 Intel Xeon CPU processors with 4 kernels and 2.6 GHz or via the ESRF Networked Interactive Computing Environment (NICE) when larger computational power was required. A typical XPCI-CT full-brain dataset is composed of about 6000 slices for a total data size of 280 GB (in 16 bit and before data normalization and slice cropping) that reduces to about 150 GB after all the image processing procedures. A typical mosaic XPCI-CT dataset for a lung is composed of one single vertical CT stage (about 2000 slices) and has a dimension of 100-180 GB, depending on the number of sub-regions; one single CT sub-region is about 21 GB. On the NICE cluster, the reconstruction of one single CT brain stage takes about 3-4 hours and the normalization of a full-organ dataset needs about 12 h. The segmentation procedures of a tumour volume on MRI images, on XPCI-CTs and of microcalcifications volumes can take up to about 15 min, 10 h and 50 h, respectively. Tumour segmentations were performed on the Fujitsu laptop or workstation, while microcalcifications segmentation were obtained using the NICE cluster. Usually, when performing microcalcifications segmentation the full dataset is divided in sub volumes that are segmented separately.

5.5 SAXS/WAXS data analysis⁶

To identify characteristic features for each sample, the azimuthally averaged 1D WAXS and SAXS patterns were statistically analysed using a signal-classification method (Lutz-Bueno, 2018) to extract the least-correlated profiles (see paragraph 2.2.1). This procedure was carried out within a collaboration with Dr. O. Bunk and Prof. C. Giannini. In particular, the few 1D WAXS profiles recorded for rat brain slices and selected by this classification procedure, were first indexed by means of the crystallographic software QUALX 2.0 (Altomare, 2015) to identify the crystalline structure that can explain all the diffraction peaks in the pattern. This first analysis allowed to identify the $\text{Ca}_5(\text{PO}_4)_3(\text{OH})$ -HAP (Kay, 1964), as the unique crystallographic structure which best describes the detected WAXS patterns. The next step was to fit the patterns with the whole-profile Rietveld-

⁶ The text of the paragraph is reproduced from (Romano, 2021a)

based program FULLPROF (Rodriguez-Carvajal, 1993), which was used to identify the chemical-physical origin of the crystalline structures originating the measured WAXS patterns and to quantify the crystalline domain size of these structures along precise crystallographic directions. This procedure was only applied to the signals originating from HAP crystals. The crystalline structure composition of the sample, namely the atomic positions, the space group (P 63/m), the hexagonal unit cell sizes $a = b = 9.465 \text{ \AA}$ and $c = 6.9095 \text{ \AA}$ were provided to the program. The inhomogeneous peak broadening of the diffraction peaks was described by a modified Scherrer formula (phenomenological model based on spherical harmonics), with the instrumental resolution function evaluated by fitting the diffraction pattern of a LaB6 NIST standard, recorded under the same experimental conditions, and provided to the program (Giannini, 2016).

Going back to the high throughput data analysis, one can determine, pixel by pixel, the relative abundance of the selected profiles in the imaged sample area. Here, for the WAXS data, a single peak analysis was performed around $q = 2.28 \text{ \AA}^{-1}$, from 2.20 \AA^{-1} to 2.34 \AA^{-1} , which is the location of the most intense diffraction peak characteristic for HAP and that was described as a single Gaussian peak of which position, width and intensity has been determined above a q^{-n} background. This background was chosen as it fits universally both the q^{-4} to q^{-1} signal often present in SAXS and the often locally constant background in WAXS. Once the single peak fitting procedure was repeated for each pixel of the scanned area and for each sample, characteristic values were extracted by calculating for each sample the median peak position and width across all pixels with a reliably detectable HAP peak signal at $q = 2.28 \text{ \AA}^{-1}$. Furthermore, the standard deviation was calculated to characterize the spread of the distribution. For the XRF analysis, the total intensity in the energy range characteristic for the elements Fe, Ca, and P (i.e. 6.2-6.5, 3.4-4.1 and 1.8-2 keV, respectively) was determined for each pixel and values characteristic for each sample were determined by calculating the median and the standard deviation. XRF median signals were both obtained for considering all the available pixels or only the pixels, within a sample, showing WAXS-HAP (or XRF-Ca) signal. To define a threshold for a relevant Ca signal, the median Ca signal for all the scanned pixels was calculated for each sample and then, the median of these values was considered and multiplied by three. This proce-

procedure enables to have a threshold value that is typically above the Ca signal fluctuations observed outside the calcified areas. For each sample, among the pixels with a Ca signal above this threshold, the median P, Ca, and Fe XRF signal were finally calculated and identified as typical values for the calcified areas. To specify the spread of these XRF signals, two types of standard deviations were calculated. The standard deviation over all pixels exhibiting a Ca signal above threshold and the one calculated over the central 50%, when sorting the XRF signal within that area for P, Ca, or Fe by the value of the signal. The standard deviation of the central 50% is mainly characteristic for the spread of the values that determine the specified median value, whereas a normal standard deviation takes into account outliers with equal weight.

Chapter 6

Characterization of the effects of BB, MRT and MB irradiations on rat brains

In this chapter I report on the multi-technique analysis performed on both healthy and GBM-bearing rat brains after treatment with either MRT, MB or standard BB for the assessment and classification of the specific radio-induced effects. Part of the here presented results are included in an **original article** “**Romano et al. 2021**, A multiscale and multi-technique approach for the characterization of the effects of spatially fractionated X-ray radiation therapies in a pre-clinical model *Cancers 13 (19)*” (see Annex 2)⁷. **This work was also presented as a poster at the 9th bioMedical Applications of Synchrotron Radiation conference in 2018, where it received the “Best Poster” award, at the ESRF 2019 user meeting and as an oral talk at the 2019 annual meeting of the Italian Synchrotron Radiation Society** (see Annex 3).

6.1 Introduction

Though histology remains the gold-standard technique for evaluating pathological states at high spatial resolution, it is still limited to a 2D analysis and complete organ inspections need serial cutting of the tissue, which is a labour- and time-consuming practice. XPCI-CT, being able to provide datasets with isotropic micro- and sub-micro-metric spatial resolutions of full organs down to cellular level, is applied as a virtual histology technique for *post-mortem* investigation in 3D of full brain organs and it is here proposed as a valuable method to be included in the follow-up protocol of novel radiotherapies. Previous studies proved that XPCI-CT is a well-suited imaging method for multiscale neuroimaging over a broad range of applications such as Alzheimer’s disease (Connor, 2009; Pinzer, 2012; Massimi, 2020), experimental autoimmune encephalomyelitis (Palermo,

⁷ All the paragraphs of this chapter but paragraph 6.2, are reproduced or adapted from (Romano, 2021a).

2020), brain tumour detection (Pfeiffer, 2007; Barbone, 2018), small animal brain visualization within the skull (Richter, 2009) and human brain nano-anatomy (Khimchenko, 2018) study. Furthermore, a previous pilot study (Barbone, 2018) showed how XPCI-CT displays with high detail and sensitivity the morphology of spatially fractionated RTs, the tumour formation, necrosis and some RT side-effects as tissue ablations. This puts the basis for this multi-technique investigation on MRT, MB and BB treated rat brains. In this study, XPCI-CT is correlated with histology analysis in order to benchmark the findings. On specific regions of interest, the SAXS/WAXS and XRF techniques have permitted to complement the detailed morphological characterization of the samples provided by XPCI-CT with an accurate structural and elemental information on the radio-induced effects of the used therapies.

6.2 Dose maps for BB, MRT and MB brain irradiations

The dose maps obtained for brain irradiations by means of the hybrid MCS presented in Chapter 3, section 3.3, are reported in Figure 6.1 - Figure 6.3 and displayed on both the axial and sagittal planes. For all the used irradiation geometries, the maps are shown for the highest delivered dose value i.e. for the BB15, MRT600 and MB350 groups.

For the BB case (Figure 6.1), the maximum dose release is obtained at the entrance surface and then decreases with the penetration depth. A small lateral dose content due to the lateral scattering is visible in the direction transverse to the beam delivery (dashed lines identify the FOI limits).

BB15

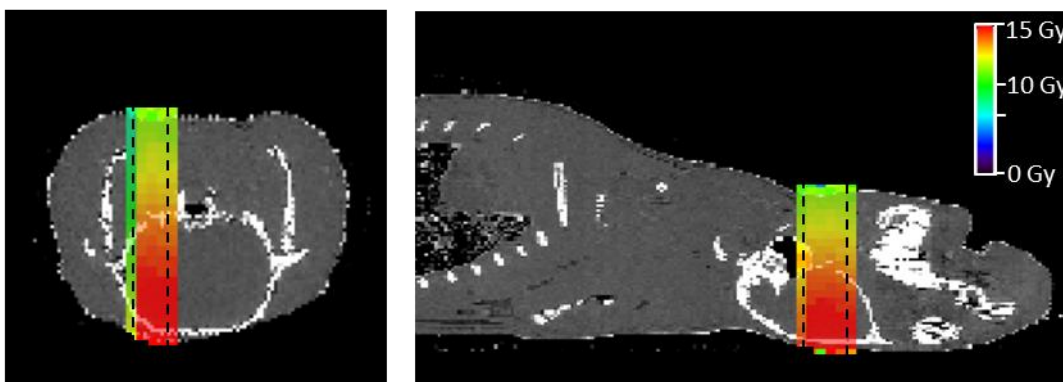


Figure 6.1: dose map for a BB15 irradiated rat brain displayed on the axial and sagittal planes. The dashed black lines indicate the field of irradiation dimensions.

The MRT group is showcased in Figure 6.2, where peak and valley dose maps are given separately. The peak dose delivery is similar to a BB irradiation, while the valley dose map shows an enhancement of dose deposition within the skull bone (about 50% higher than the nominal value) and a smooth lateral fall-off: fraction of the Gray are delivered to the full right-side head and to almost the full brain organ. Due to the fact that the microstructure of the beamlets is not resolved with the hybrid MC calculations, the mean peak distribution over each voxel is plotted in Figure 6.2 and thus, the peak dose resembles a BB-like delivery; the same holds for MBs.

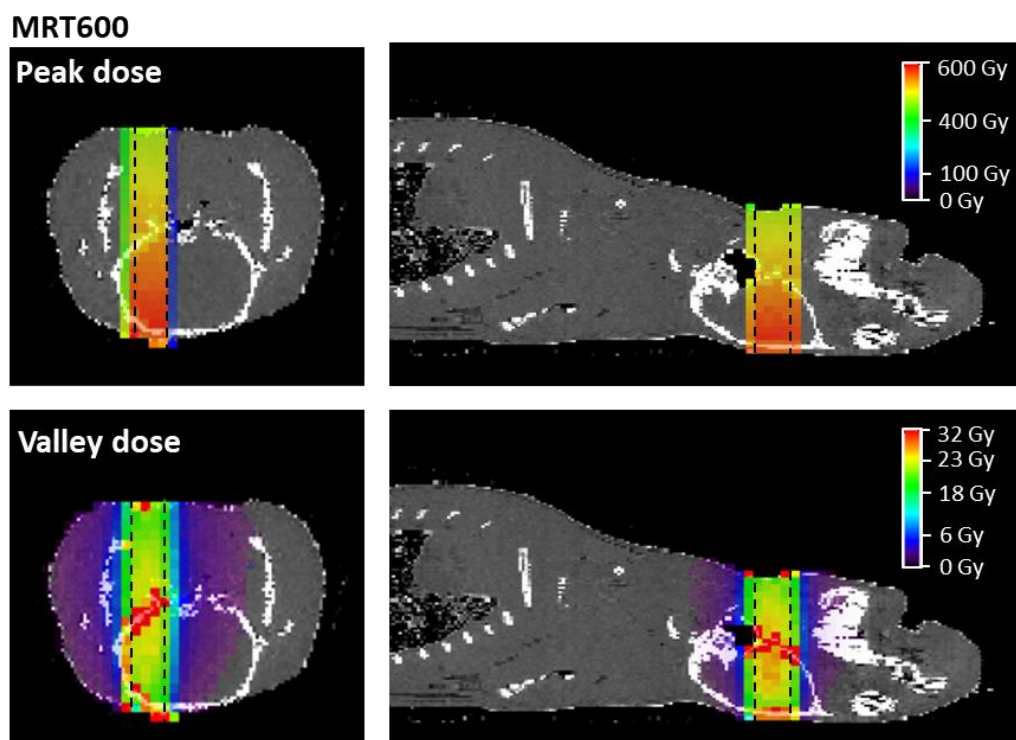


Figure 6.2: peak and valley dose maps for an MRT600-treated rat brain displayed on the axial and sagittal planes. The dashed black lines indicate the field of irradiation dimensions. The scale bar is reported only once per row.

The MB dose maps (Figure 6.3) shows a peak dose distribution similar to the BB and MRT peak cases, while the valley dose has its higher value at the centre of the FOI, and in correspondence to the rat head bone, and decreases in the transverse direction to the beam delivery with the slowest rate if all the three geometries are compared. A dose of few Gray is delivered to the full rat head (axial view) and extends until the rib cage (sagittal view).

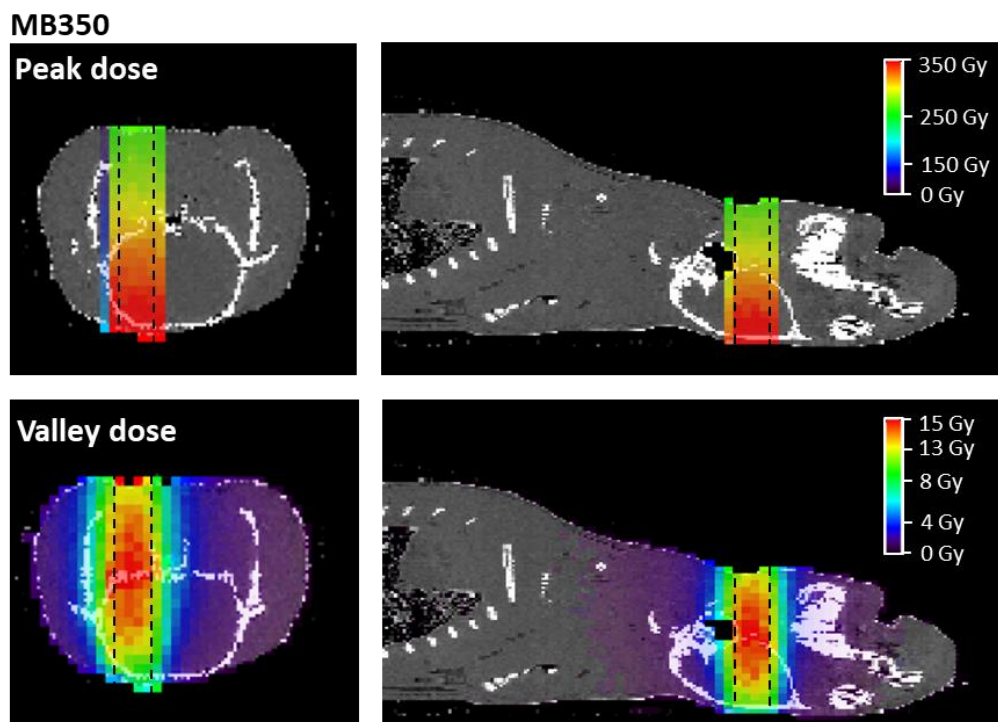


Figure 6.3: peak and valley dose maps for a MB350-treated rat brain displayed on the axial and sagittal planes. The dashed black lines indicate the field of irradiation dimensions. The scale bar is reported only once per row.

6.3 Radio-induced effects on healthy treated samples

XPCI-CT coronal images of healthy BB, MB and MRT irradiated brains acquired with a voxel size of $3.25^3 \mu\text{m}^3$ are presented in Figure 6.4 - Figure 6.8 and correlated to histology results. All the images of these figures are displayed in the radiologic view and are obtained from samples harvested at D138 (with exception for the MB350 group), which was the decided sacrifice point for all the healthy animals. The main effects on the irradiated tissues caused by the three different treatment modalities are visualized with high contrast and detail. XPCI-CT data are then compared with H&E, Ca, Fe and GFAP stained histological images.

No specific alterations in the BB-treated rat brains are visible in XPCI-CT images, where only the irradiated hemisphere is displayed (Figure 6.4a-c). In all the irradiated brain regions only histology could reveal the presence of small structures in the BB10 and BB15-treated samples that were recognized as deposits of ferric ion with lateral dimensions of $\sim 30 \mu\text{m}$ (see the insets of Figure 6.4b-c). Conversely, the BB5 group does not show any pathological change. No RT-induced reactive gliosis, as confirmed by GFAP staining, could be observed in any of the three groups. Some brown-marked areas (indicating the presence of an excess of

astrocytes) are visible in the GFAP histologies of both treated and untreated brain hemispheres, therefore these lesions are not radiation specific and are not necessarily caused by the treatment.

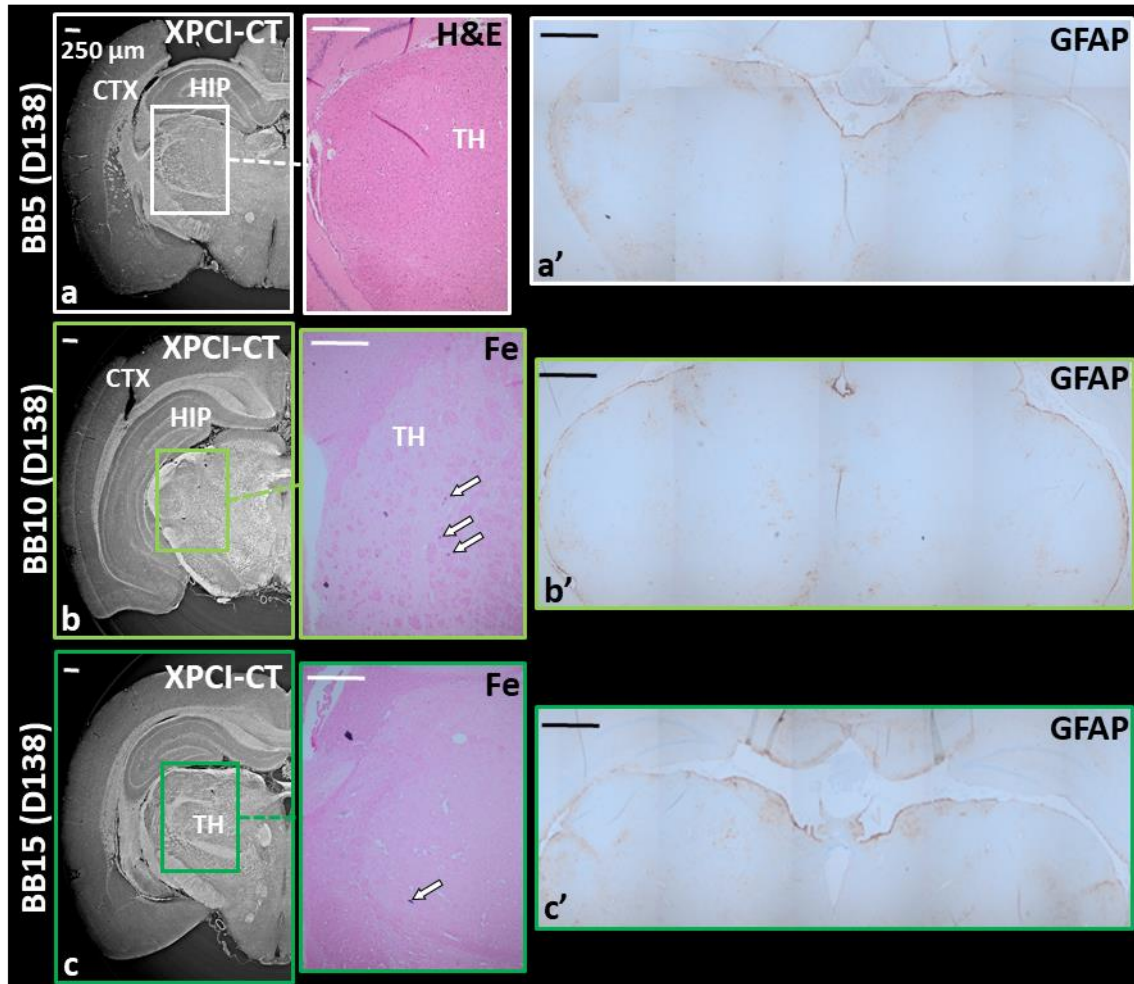


Figure 6.4: healthy BB-treated samples (sacrifice day: D138). Coronal $3.25^3 \mu\text{m}^3$ voxel size XPCI-CT images are compared with histology and immunohistochemistry analysis. When the entire slice is not displayed, only the irradiated hemisphere of the brain is reported. (a) shows an XPCI-CT image for the treated side of a BB5 brain reporting no damages in the cortex (CTX), hippocampus (HIP) and thalamus (TH) as confirmed by its H&E and GFAP (a') stained corresponding tissue slices. BB10 sample is analysed in (b) and (b') where just small Fe deposits are present and marked in blue (see white arrows) in the Fe-stained histology. The GPAF slice reports small reagent uptake in both the hemispheres thus, no RT-induced lesions are revealed. Subfigure (c)-(c') report a BB15 sample analysis where the three different investigations don't show significant pathology: only a small Fe sediment is visible. Also in this case, the GFAP staining features a small gliosis in both the hemispheres. Figure reproduced from (Romano, 2021a).

MB-treated rat brains show evident traces of the dose-delivery geometry (see Figure 6.5 - Figure 6.7). This is clearly visible by comparing the right and left hemispheres of the MB180 brain reported in the coronal XPCI-CT image of Figure 6.5a and the related 3x zoom insets. The scar produced by the minibeam causes a

reshape in the nervous structures in the caudate putamen (CP) as pointed out by blue arrows in the purple-bordered zoom, to be compared with the homogeneously organized tissue in the pink-bordered inset. Furthermore, along the beam path, hyperdense structures are present as bright spots in the XPCI-CT image, as positively-stained structures in H&E, and in the Ca and Fe histologic images (Figure 6.5a-d) as indicated by cyan and white arrows (as in all figures of this chapter), respectively (histologies only show the irradiated hemisphere of the brain). This correlation allows labelling the bright XPCI-CT signal as Ca and Fe deposits.

In addition, the MB delivery causes local cell loss and microcystic degeneration of the tissue (black arrows, as in all figures of this chapter) along the beams path, which are visible in the insets of Figure 6.5b and Figure 6.5d. The 10x zoom of Figure 6.5d shows in detail three Fe mineralizations and some smaller ones in the surroundings. The GFAP staining for the same area, performed on a subsequent slice, shows that Ca deposits (here stained in blue) coexist with Fe ones. In all the images of this chapter, blue arrows indicate the MB path direction.

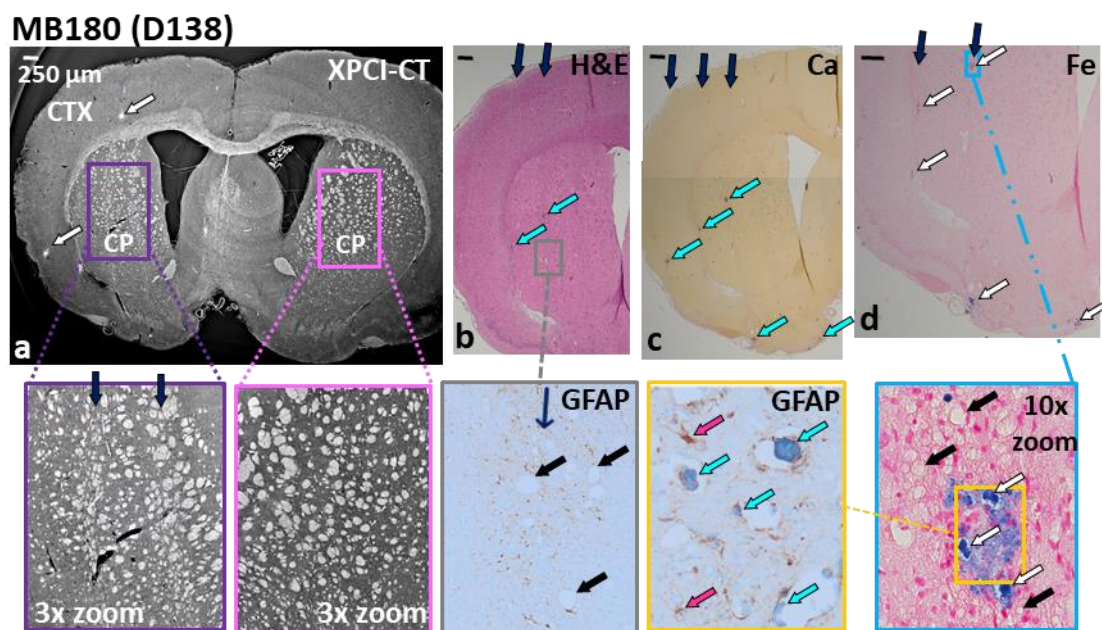


Figure 6.5: $3.25^3 \mu\text{m}^3$ voxel size XPCI-CT, histology and immunohistochemistry analyses for a healthy MB180 sample displaying RT-induced scars along the beam path. In XPCI-CT (a) the lesion is especially visible in the caudate putamen (CP) of the right-side brain and in its 3x zoom. The comparison with the left-side counterpart enhances a reshape in the nervous structures along the MB peak delivery areas (indicated by the blue arrows). Subfigures (b)-(d) and their insets report the presence of Ca and Fe minerals within the MB-driven scar indicated by cyan and white arrows, respectively together with cell-loss findings, microcystic degeneration (black arrows) and small astrocytes next to the calcifications. All the images are displayed in the radiological view. Figure reproduced from (Romano, 2021a).

The same features are visible in another healthy MB180-treated specimen, as visible in Figure 6.6, where a MIP taken over 100 subsequent coronal XPCI-CT slices acquired at $3.25^3 \mu\text{m}^3$ voxels size is shown. The tissue remodelling caused by minibeam is visible together with some hyperdense agglomerates along the area of peak delivery that can be identified with Ca/Fe deposits thanks to the comparison given in Figure 6.5.

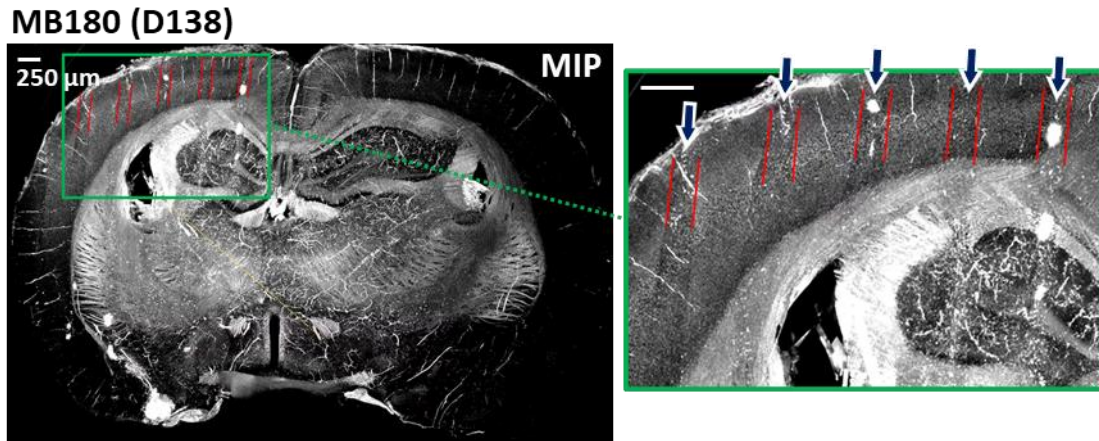


Figure 6.6: maximum intensity projection (MIP) of 100 subsequent coronal XPCI-CT slices, acquired at $3.25^3 \mu\text{m}^3$ voxels size, for a healthy MB180 brain: both tissue reshaping and hyperdense Ca/Fe deposits are visible. The red lines help in identifying the area of peak dose delivery that are indicated by the blue arrows.

By increasing the MB peak dose (e.g. MB350 group), the effects induced on the tissues become more invasive, as shown in Figure 6.7 for an animal died at D16. The minibeam delivered with a peak dose of 350 Gy causes the complete destruction of the irradiated tissues, which is visible in both XPCI-CT and H&E images. The coronal XPCI-CT ($0.65^3 \mu\text{m}^3$ voxel size) and H&E stained histology insets zoom into the hippocampal lesions (yellow arrows) revealing that a very low content in cells is present producing in some cases small microcystic degeneration in the tissue. Both XPCI-CT and H&E images report the irradiated hemisphere only. The GFAP staining shows a reactive gliosis in the cortex areas corresponding to the valley dose delivery; cell loss is predominant in the peak delivery areas.

By analysing the XPCI-CT images of MRT-treated animals (Figure 6.8), tissue micro-ablations, appearing like long micrometre-wide areas with cell losses, are detected in all the irradiated regions of the brain and micro- and macro-deposits of dense materials are visualized, which are identified as Ca and Fe by histologic

analysis. These features are shown in Figure 6.8a-c, where only the irradiated hemispheres are reported.

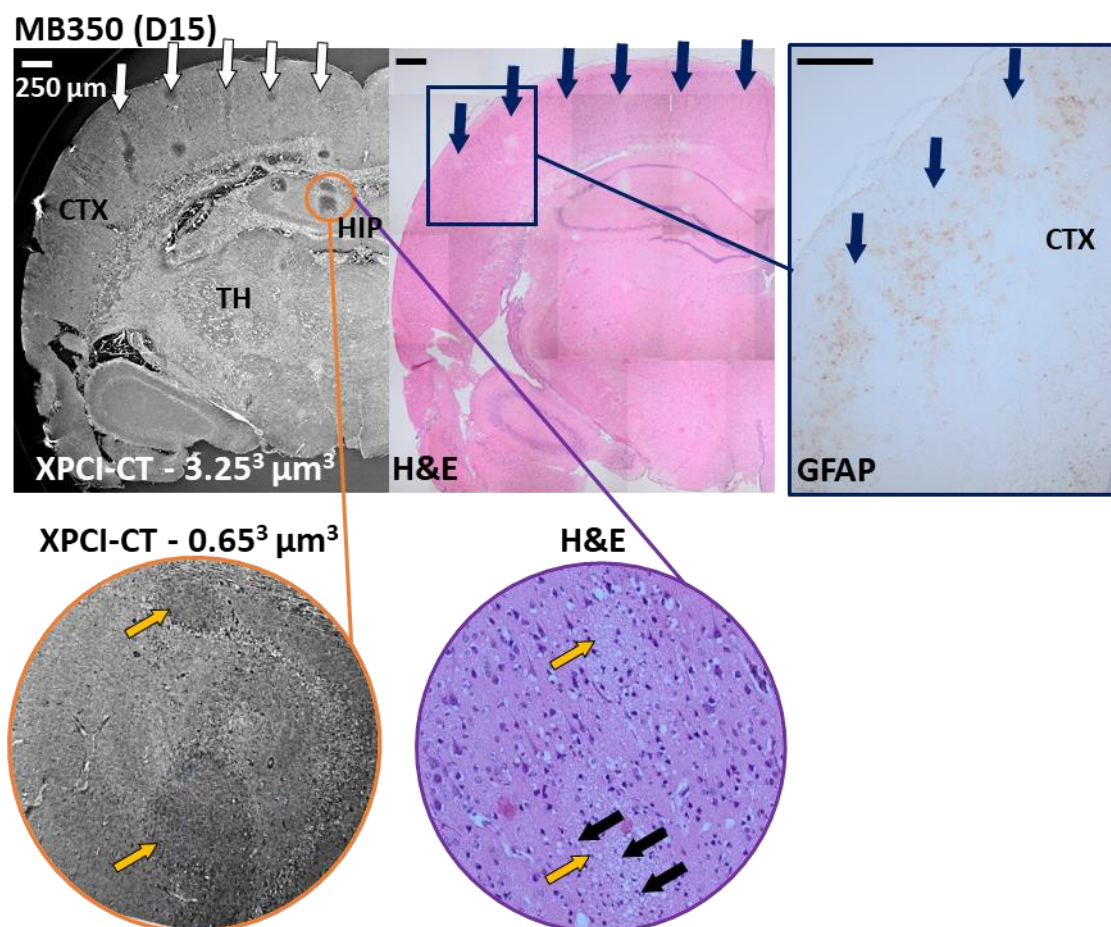


Figure 6.7: XPCI-CT multi-scale approach for a healthy MB350-treated brain and comparison with histology and immunohistochemistry, observed at D15, revealing that the minibeam delivery caused a complete tissue ablation, as visible in the XPCI-CT images and the H&E histology (white and blue arrows point at the minibeam paths). The GFAP cortex (CTX) zoom shows reactive gliosis in the minibeam valleys, while in the peak delivery area the cell loss is predominant. The same effect is seen in the XPCI-CT and H&E hippocampal (HIP) zooms. Black arrows indicate the cell swelling induced by radiation. Figure reproduced from (Romano, 2021a).

Results obtained on an MRT200-treated brain (Figure 6.8a-a') showcase the formation of Ca/Fe deposits in the thalamic area of the right hemisphere along the X-ray microbeam paths (red arrows indicate the MRT delivery direction, as in all figures). On the XPCI-CT image of Figure 6.8a, the presence of hyperdense, highly absorbing structures is shown as bright accumulations in the thalamus (TH), while MRT paths are observable in Figure 6.8a-a' (XPCI-CT and H&E histology images, respectively) in the hippocampus (HIP), amygdala (AMG), thalamus and hypothalamus (HYP). Thanks to the adjusted windowing (AW) inset of

Figure 6.8a it is noticeable that the bright structures are embedded in the thalamus and appear to be aligned along parallel lines corresponding to the MRT microbeam paths. In Figure 6.8a is rather difficult to simultaneously visualize Ca/Fe deposits and the related MRT paths due to the stripe artefacts caused by the abrupt variation of index of refraction between dense deposits and the surrounding soft tissue. The 2x zoom inset of the hippocampus helps recognizing the MRT paths in the XPCI-CT image. The Ca and Fe stained histological slices of the thalamic regions (insets of Figure 6.8a') identify those deposits as Ca/Fe accumulations, which are revealed as red and blue spots, respectively. For this sample, the GFAP stained inset highlights the presence of some reactive gliosis agglomerates (magenta arrows pointing to astrocytes, as in all figures of this chapter) within Ca/Fe deposits.

In the rat brains of the MRT400 group, large mineral deposits are detected in the thalamus (red-bordered rectangle in the coronal XPCI-CT view of Figure 6.8b) and they are present both as micro-deposits and clusters, as it is more clearly highlighted in the AW inset. H&E, Fe, Ca and GFAP histological images (Figure 6.8b') attest the presence of an abundant content of Ca with respect to Fe. A massive astrogliosis is visible around the microcalcifications (GFAP 5x zoomed image) while no astrocytes reaction is evident along the MRT paths unless calcifications are present, as demonstrated in the GFAP-stained cortical zoom (inset of Figure 6.8b').

In the MRT600 group, the hyperdense signal on the coronal XPCI-CT image of Figure 6.8c corresponds again to small deposits and big clusters of granular aggregates (see the AW insert). Those aggregates are mainly composed of Ca, as the different histological stainings also reveal (Figure 6.8c' and insets). For this sample, in both XPCI-CT and H&E histology, MRT microbeam paths can be seen crossing the entire hemisphere from the cortex down to the hypothalamus. In the H&E histology (Figure 6.8c') the MRT paths are not displayed as straight lines in the thalamus but they are bent as a result of the tissue deformation due to the Ca deposits formation (light-blue arrows). The two GFAP antibody stained histology images (insets of Figure 6.8c') demonstrates again the presence of gliosis in the region around the macrocalcifications and next to a blood vessel (BV) that was probably damaged by the MRT transections.

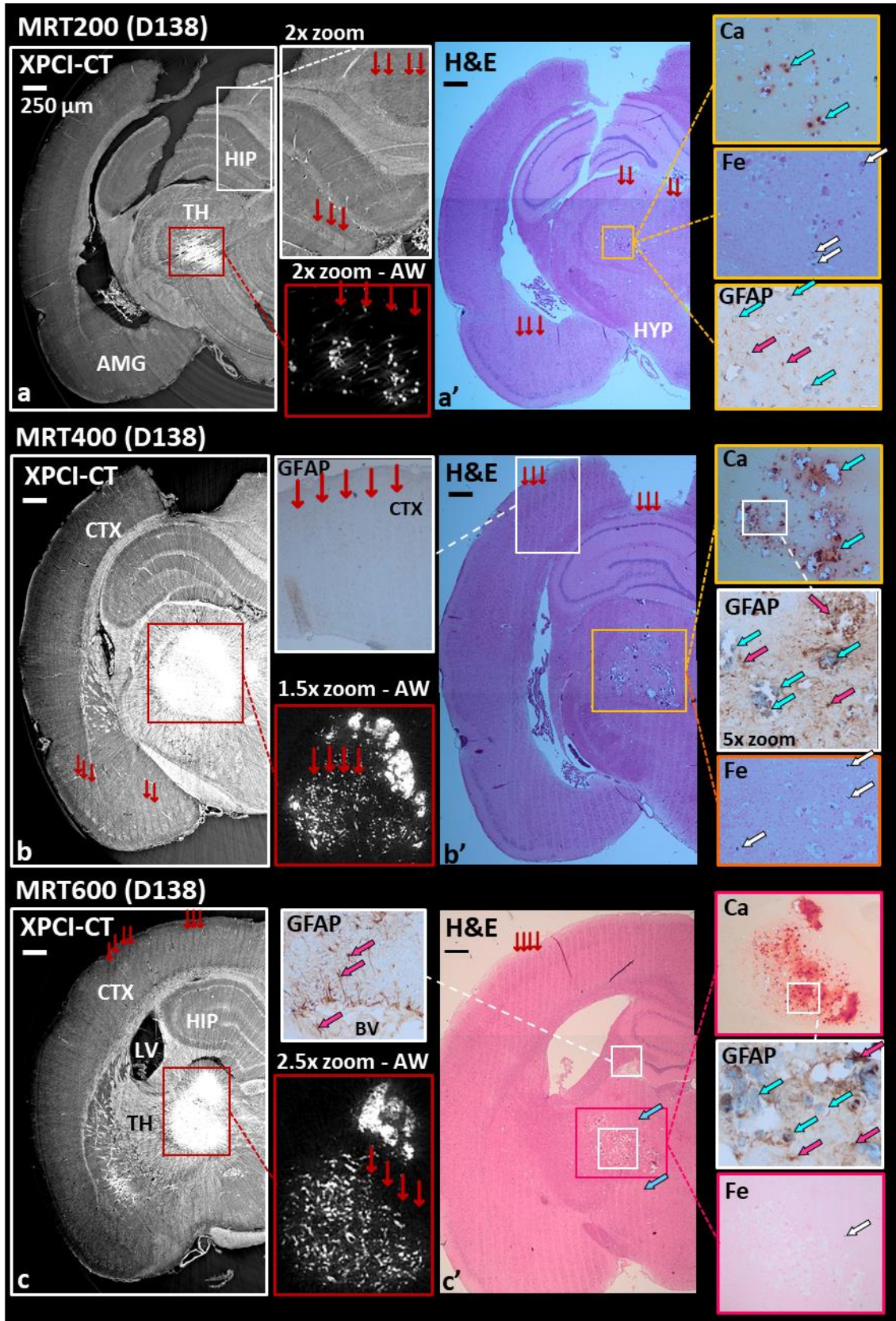


Figure 6.8: MRT-treated healthy samples: coronal $3.25^3 \mu\text{m}^3$ XPCI-CT images compared with histology and immunohistochemistry. Only the irradiated brain hemisphere is reported. ->

-> MRT200 sample reports some hyperdense agglomerates in the thalamus (TH) (a) that are better visible in the adjusted windowing inset and are recognised as Ca and Fe deposits thanks to the H&E, Alzarin Red and Perl's Prussian Blue histologies (a'). Iron deposits are pointed out by white arrows, while red arrows identify the MRT paths. The GFAP staining of the thalamus area (a' inset), shows limited gliosis in two zones. Magenta arrows are for astrocytes and cyan arrows for Ca deposits. MRT paths are visible in both XPCI-CT and histology as tissue ablation in the hippocampus (HIP), thalamus, hypothalamus (HYP) and amygdala (AMG) as visible in the 2x zoom of (a) and in (a'). MRT400 (b) and MRT600 (c) samples manifest big cluster of Ca/Fe deposits together with small dot-shaped ones. The different applied stainings reveal a low content in Fe and massive astrogliosis in the deposit's surroundings (GFAP staining of b' and c'). MRT paths are visible in both XPCI and histologic images. In particular, the cortex (CTX) GFAP inset of (b') demonstrate that no gliosis is induced by MRT irradiation without being entangled to Ca agglomerates. Figure reproduced from (Romano, 2021a).

6.4 Effects of spatially fractionated radiotherapy on glioblastoma-bearing animals

6.4.1 Survival curves

The rats belonging to the MB350 groups, both GBM-implanted and healthy, died at D15-16 and are not included in the survival curves. The healthy-treated animals of the MB180 group and of all the BB and MRT groups lived until the programmed end of the experiment, i.e. D138. Therefore, the survival curves reported in Figure 6.9 only contain data for GBM-bearing animals.

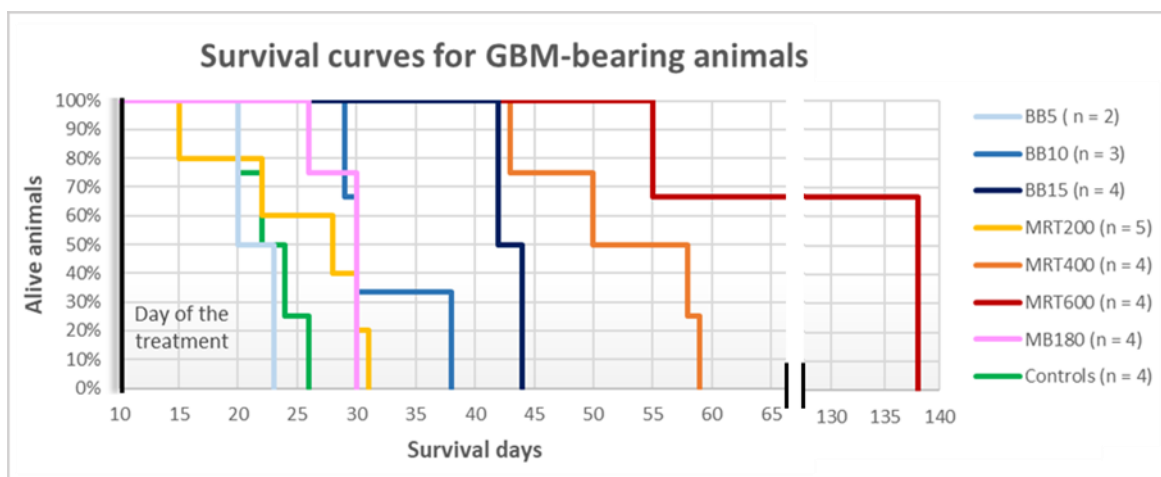


Figure 6.9: survival curves for glioblastoma (GBM)-bearing rats. The curves for the different irradiation groups are given as a percentage of surviving rats as a function of the survival days, counted from the glioblastoma implant day. The legend also reports the total number of animals of each curve. Figure reproduced from (Romano, 2021a).

Healthy-controls, MRT200 and BB5 groups show a similar survival according to the long-rank-test in a 95% C.L., resulting in a median survival of 22, 24 and 21 days from the day of GBM implantation, respectively. MRT400 and MRT600 treatments increase the median survival with respect to the untreated group; a median survival of 52 days for MRT400 and 110 days for the MRT600 group were obtained. The MB180 group shows a median survival of 28 days. Overall, the MRT600 group provides the best survival among the different RTs investigated in this study.

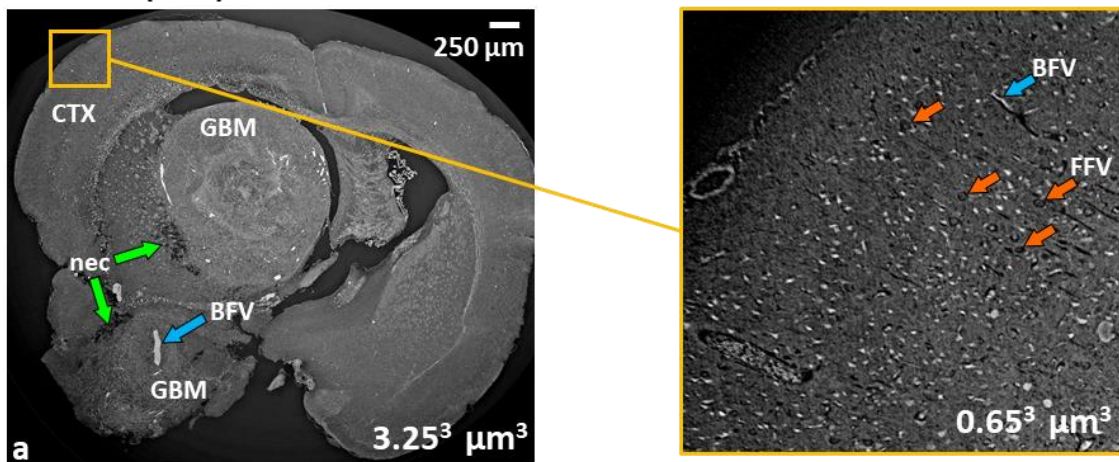
6.4.2 XPCI-CT: a multi-scale imaging approach

The effects of microbeam and minibeam RTs on glioblastoma-bearing rat brains are shown in Figure 6.10 and Figure 6.11 by using a multi-scale approach enabling a hierarchical representation of the treated tissues. Coronal XPCI-CT images acquired at different spatial resolutions (i.e. voxel sizes of 3.25^3 , 1.2^3 and 0.65^3 μm^3) are presented. As first, the volume of GBM tumour is well distinguishable against the surrounding healthy tissue as well as the re-organization and disruption of the overall brain anatomy caused by the presence of the tumour (MRT200 specimen in Figure 6.10a). Necrotic tissue (nec) is displayed with low grey levels (dark area indicated by green arrows) with respect to the other brain tissues, and the tumour and blood-filled vessels (BFV) appear as hyperdense features in the XPCI-CT image within the tumour milieu (light-blue arrows). Blood filled vessel appear brighter than the surrounding tissues as some blood content is still present, as the animals were not perfused and blood cells were not washed out during the sacrifice. The inset of Figure 6.10a shows an area of the brain cortex of Figure 6.10a examined with a voxel size of 0.65^3 μm^3 ; in none of these two images the paths of the 200 Gy-peak microbeams are detectable and, overall, for the MRT200-treated brains no sign of the MRT paths is visible in the cortex, that is the MRT entrance area. The structures in the cortex tissue are homogeneously arranged: cells and both formalin (FFV, orange arrows) and blood-filled vessels are clearly recognizable.

MRT400 brains are showcased in Figure 6.10b where the tumour is grown replacing almost completely the entire right hemisphere and destroying the healthy structures. As a consequence, the brain regions of MRT delivery are replaced by

tumour tissue exception made for a small area in the cortex where the signs due to MRT paths (tissue ablation) are deviated as a result of the tumour growth. Necrotic tissue and intra-tumoral calcifications are visible with a different degree of detail in the 3.25^3 and 1.2^3 μm^3 -voxel size-images (Figure 3b and related inset). The 1.2^3 μm^3 -voxel size XPCI-CT image well discriminates the presence of aggregating cells around a hypocellular zone where a denser lump, with an XPCI-CT signal compatible with Ca (see cyan arrows), appears too. Purple arrows point at the borders of this hypocellular area, while cyan ones indicate the agglomerates.

MRT200 (D30)



MRT400 (D57)

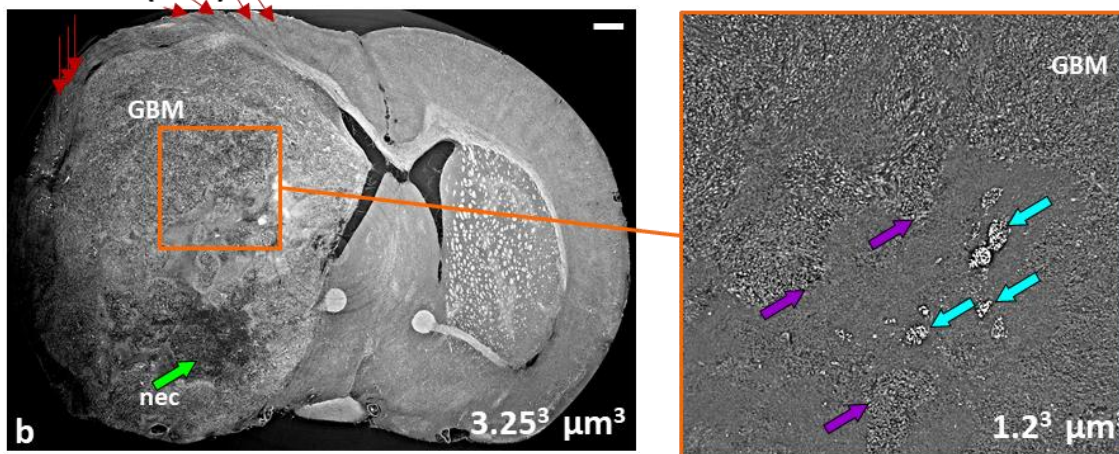


Figure 6.10: multi-scale XPCI-CT coronal images of an MRT200- and MRT400-treated tumour-bearing brain. The two animals were sacrificed at D30 and D57, respectively. The MRT200 sample (a) shows great discrimination between healthy and tumour tissue distinguishing necrosis (nec, green arrows) among the GBM structures. A cortex zoom was realized with a 0.65^3 μm^3 voxel size setup revealing uniform cell content and no MRT path track. Orange and light-blue arrows indicate formalin (FFV) and blood-filled (BFV) vessel. (b) reports an MRT400-treated sample displaying MRT paths induced tissue ablation (red arrows) and necrosis. Its 1.2^3 μm^3 voxel size inset depicts in detail an hypocellular area where calcium deposits are present (cyan arrows). The purple arrows point at the hypocellular area borders. Figure reproduced from (Romano, 2021a).

The multi-scale XPCI-CT images of an MRT600-treated brain extracted at D138 acquired using voxel sizes of 3.25^3 , 1.2^3 and $0.65^3 \mu\text{m}^3$ show that small mineralizations can be only discriminated by using the highest spatial resolutions; a $3.25^3 \mu\text{m}^3$ voxel size is not sufficient to separate individual microcalcifications. Figure 6.11a and a' are two coronal XPCI-CT slices of the same sample illustrating different anatomical areas of the irradiated hemisphere where both MRT paths and large Ca/Fe agglomerates are evident (see the AW insets). The deep pink-bordered inset of Figure 6.11a is a MIP of 50 subsequent XPCI-CT images (corresponding approximately to a voxel size of $1.2 \times 1.2 \times 60 \mu\text{m}^3$) chosen in a way that the slice shown in Figure 6.11a is the centre of the projected stack. This MIP image highlights the presence of small agglomerates, compatible with the microcalcifications found in other anatomical regions, that are not detectable when using a $3.25^3 \mu\text{m}^3$ voxel size. Both the high-resolution insets of Figure 6.11a and Figure 6.11a' display micro agglomerates developing along the MRT peak dose paths.

Finally, XPCI-CT coronal images of a tumour-bearing rat brain treated with MB180 are shown in Figure 6.11b. By applying the multi-scale XPCI-CT approach, it is possible to depict the MB-induced scars (blue arrows) with Ca agglomerates and microcystic-like cell loss regions.

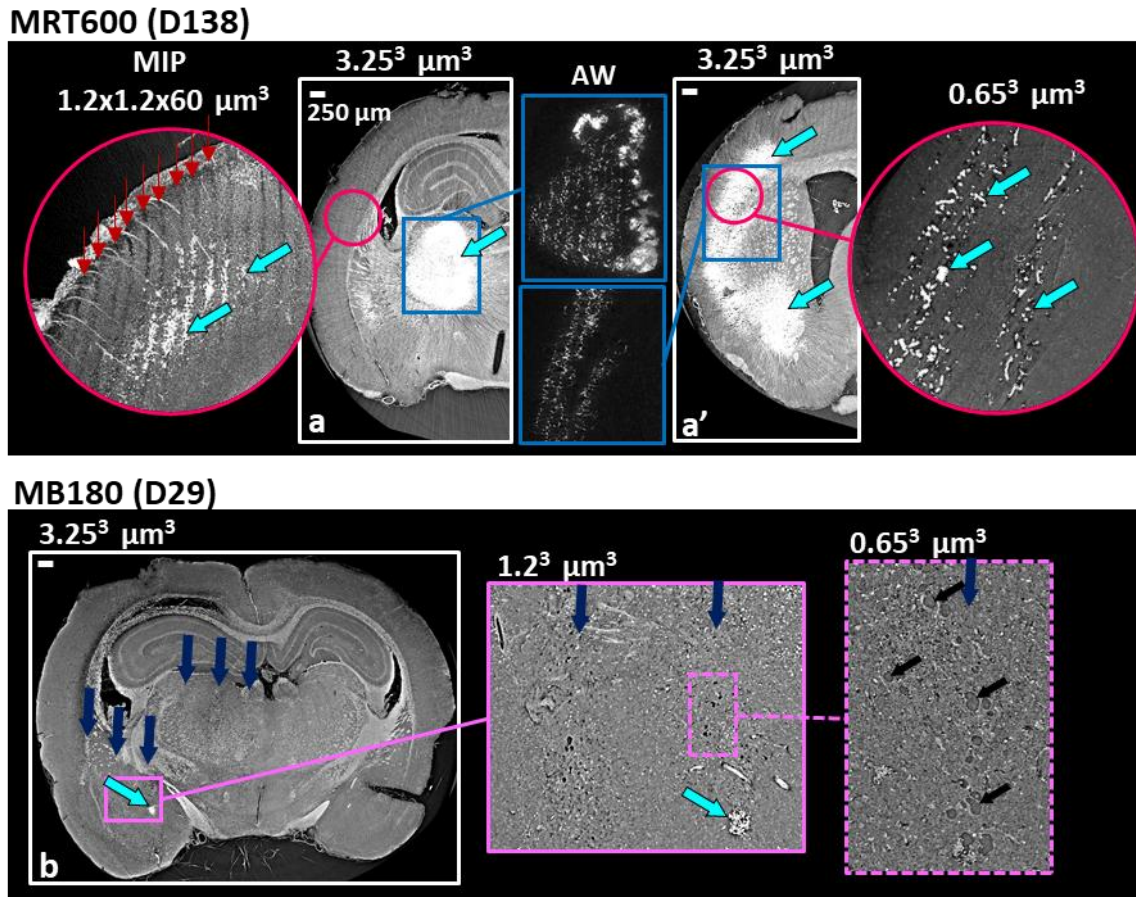


Figure 6.11: multiscale XPCI-CT for an MRT600 and MB180 treated brain extracted respectively at D138 and D29. (a) and (a') present two different coronal views of the same MRT600-treated brain together with their adjusted-windowing insets and high-resolution insets showing in detail that microcalcifications develop along the MRT tracks. The maximum intensity projection (MIP) of 50 subsequent $1.2^3 \mu\text{m}^3$ voxel size XPCI-CT images reveals small deposits that are not visible with a voxel size of $3.25^3 \mu\text{m}^3$. (b) displays in detail the MB180 induced scars together with cells swelling (yellow arrows) and Ca/Fe deposits (cyan arrows) along the minibeam paths. Figure reproduced from (Romano, 2021a).

6.5 Quantitative analysis and 3D rendering

Results of the characterization and quantification study of tumour and microcalcifications for all the irradiation groups are reported in Figure 6.12.

Tumour volumes graphs report both the volumes assessed with MRI and XPCI-CT according to the results of the compatibility test performed as explained in section 5.3.3. The compatibility test between MRI and XPCI-CT tumour volume measurements is reported for the MB350 group in Table 6.1 showing that, overall, the MRI and XPCI-CT segmentation procedures are compatible on 6 out of the 8 considered samples. Furthermore, if the averaged values (last row) of all the computed parameters are considered, MRI- and XPCI-CT-based tumour volumes are

overall within the compatibility. As a result, the values of tumour volumes obtained from *in-vivo* MRI and *ex-vivo* XPCI-CT data can be displayed in the same plot without loss of consistency.

Table 6.1: compatibility study of the MRI- and XPCI-CT-based tumour volumes (T_v) for the MB350 group. The table reports the animal name, the survival counted from the day of glioblastoma implant, XPCI-CT and MRI tumour volumes normalized to the full brain volume with errors and the compatibility evaluation of MRI-XPCI-CT values together with the statistical indicators $P(t)$ and the confidence level (C.L.). MRI-XPCI-CT tumour volumes with $C.L.>5\%$ are considered compatible each other. The last row reports the average of the columns. Table reproduced from (Romano, 2021a).

Sample name	Survival (days)	XPCI-CT T_v (%)	MRI T_v (%)	XPCI-CT – MRI compatibility		
				t	P(t) (%)	C.L. (%)
B33	15	0.84 ± 0.07	0.71 ± 0.11	1.04	61.6	38.4
B34	15	0.45 ± 0.03	0.42 ± 0.07	0.38	27.4	72.6
B35	15	0.41 ± 0.03	0.62 ± 0.10	2.01	94.0	6.0
B36	15	0.30 ± 0.02	0.58 ± 0.09	2.93	99.6	0.5
B37	15	0.26 ± 0.02	0.17 ± 0.03	2.36	96.2	3.8
B23	16	0.78 ± 0.07	0.76 ± 0.12	0.15	10.3	89.7
B24	16	0.88 ± 0.07	1.1 ± 0.2	1.26	73.3	26.7
B27	16	0.92 ± 0.08	1.2 ± 0.2	1.27	76.2	23.8
Average		0.61 ± 0.08	0.69 ± 0.13	1.43	80.6	19.4

The tumour volume values reported in the graphs of Figure 6.12 are also listed in Table 6.2; the volume errors are computed as explained in section 5.3. MRI-based tumour volumes to assess the initial GBM extent are only available for the animals irradiated during the second experimental RT session but, due to the low

intra-animal variability found among the MRI-based assessed initial volumes, the available values are used as a starting point for all the rats belonging to the groups. Only animals involved in the survival study, i.e. not sacrificed at decided time-points, are considered for the tumour volumes study.

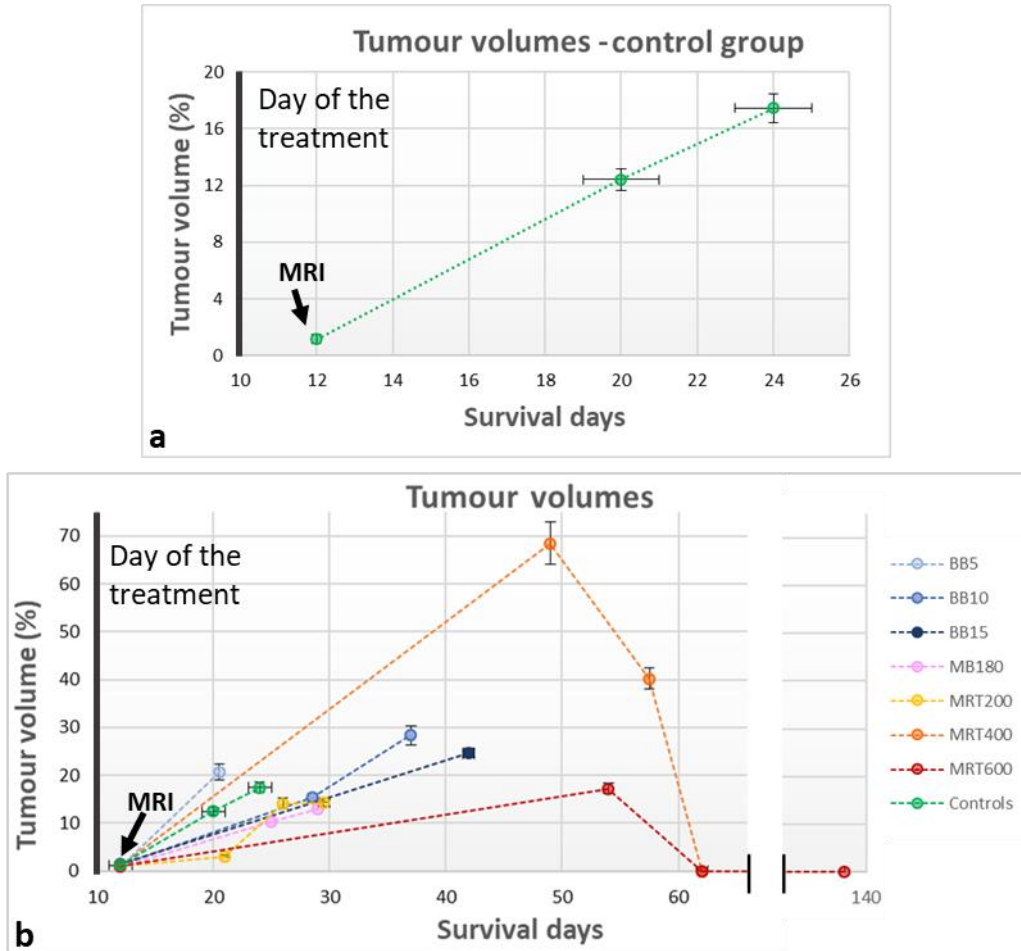


Figure 6.12: quantification of tumour volumes for the GBM-control group (a) and all the groups involved in the study (b) as a function of the survival days, which are counted starting from the GBM cells implantation day (D0). All the values are extracted from XPCI-CT images but the one at day 12, which is in-vivo MRI-based. Tumour volumes are given as a percentage of the entire brain volume; values of animals belonging to the same group with survival within three days are averaged and the mean value is reported in the graphs. Figure reproduced from (Romano, 2021a).

Table 6.2: tumour volumes (T_v), reported as a percentage of the full brain volume, assessed by MRI (2 days post-irradiation, for the rats irradiated in the second RT session) and ex-vivo XPCI-CT. Values of tumour volumes of animals belonging to the same group with survival within three days are averaged.

Group	Sample name	Survival (days)	MRI T_v (%)	XPCI-CT T_v (%)
BB5	C13, C7	20.5 ± 1.5	0.8 ± 0.2	20.6 ± 1.6
BB10	B14, C12	28.5 ± 0.5	1.2 ± 0.3	15.3 ± 0.9
BB10	C14	37		28.3 ± 1.9
BB15	B17, B18, B20, B21	42.0 ± 0.5	1.5 ± 0.4	24.6 ± 1.0
MRT200	C02	21		3.1 ± 0.2
MRT200	B3	26		14.2 ± 1.0
MRT200	C3, B2	29.5 ± 0.5	1.0 ± 0.3	14.4 ± 0.8
MRT400	C8	49		68.5 ± 4.5
MRT400	B25, C6	57.5 ± 0.5	1.0 ± 0.2	40.2 ± 2.1
MRT400	C4	62		0
MRT600	C11	54		17.2 ± 1.1
MRT600	C9, C10	62		0
MRT600	B12, B13	138	1.1 ± 0.3	0
MB180	B31	25		10.3 ± 0.3
MB180	B28 - B30	29	0.8 ± 0.2	13.0 ± 0.7
MB350	B33-B37, B23, B24, B27	15.4 ± 0.5	0.5 ± 0.2	1.1 ± 0.1
Controls	C17, C15	20 ± 1		12.4 ± 0.8
Controls	B11, B32	24 ± 1	1.2 ± 0.3	17.5 ± 1.0

The GBM-control group (Figure 6.12a) as well the BB groups (Figure 6.12b) show a linear trend for the tumour development over time. Furthermore, as noticeable in Figure 6.12b, the MRT200 and MB180 groups have values of tumour volumes similar to those of the BB5 and GBM-control groups. The MRT400 group presents the largest tumour volumes among the different groups and the MRT600-treated brains show the smallest tumour volumes achieved within this study. For animals surviving more than 60 days, no tumour residue is detected on the $3.25^3 \mu\text{m}^3$ -voxel-size XPCI-CT images. Nevertheless, some residual GBM infiltrations are detected with GFAP stained immunohistochemistry, as can be seen in Figure 6.13 and Figure 6.14, meaning that no complete tumour sterilization has been achieved. Here, the tumour is indicated by high cellularity and nuclear pleomorphism, i.e. variability of size, shape and chromatin density of the nuclei.

MRT600 (D138)

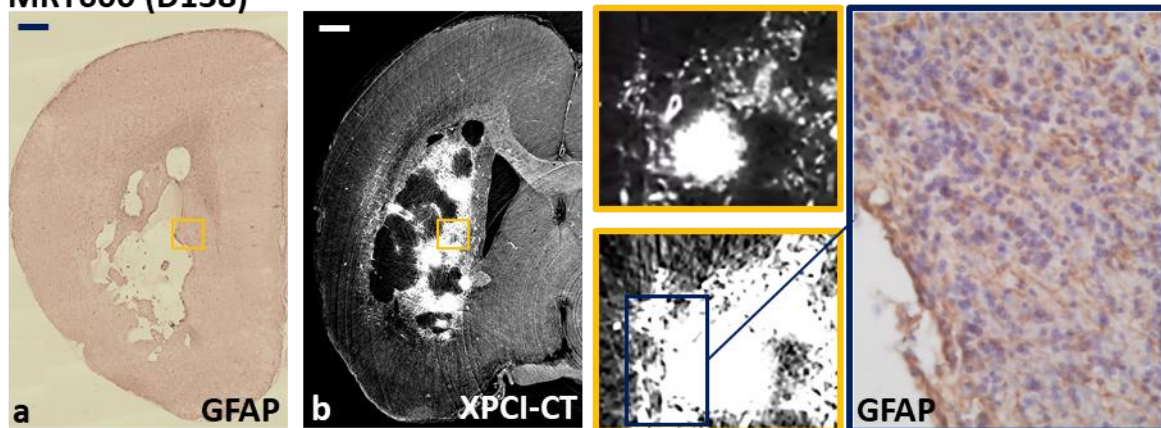


Figure 6.13: GFAP-stained immunohistochemistry (a) and XPCI-CT image (b) comparison for an MRT600-treated tumour-bearing rat brain. XPCI cannot detect any residual tumour (yellow bordered insets), while immunohistochemistry reveals the presence of residual GBM infiltrations with increased cellularity and nuclear pleomorphism (blue bordered inset). Figure reproduced from (Romano, 2021a).

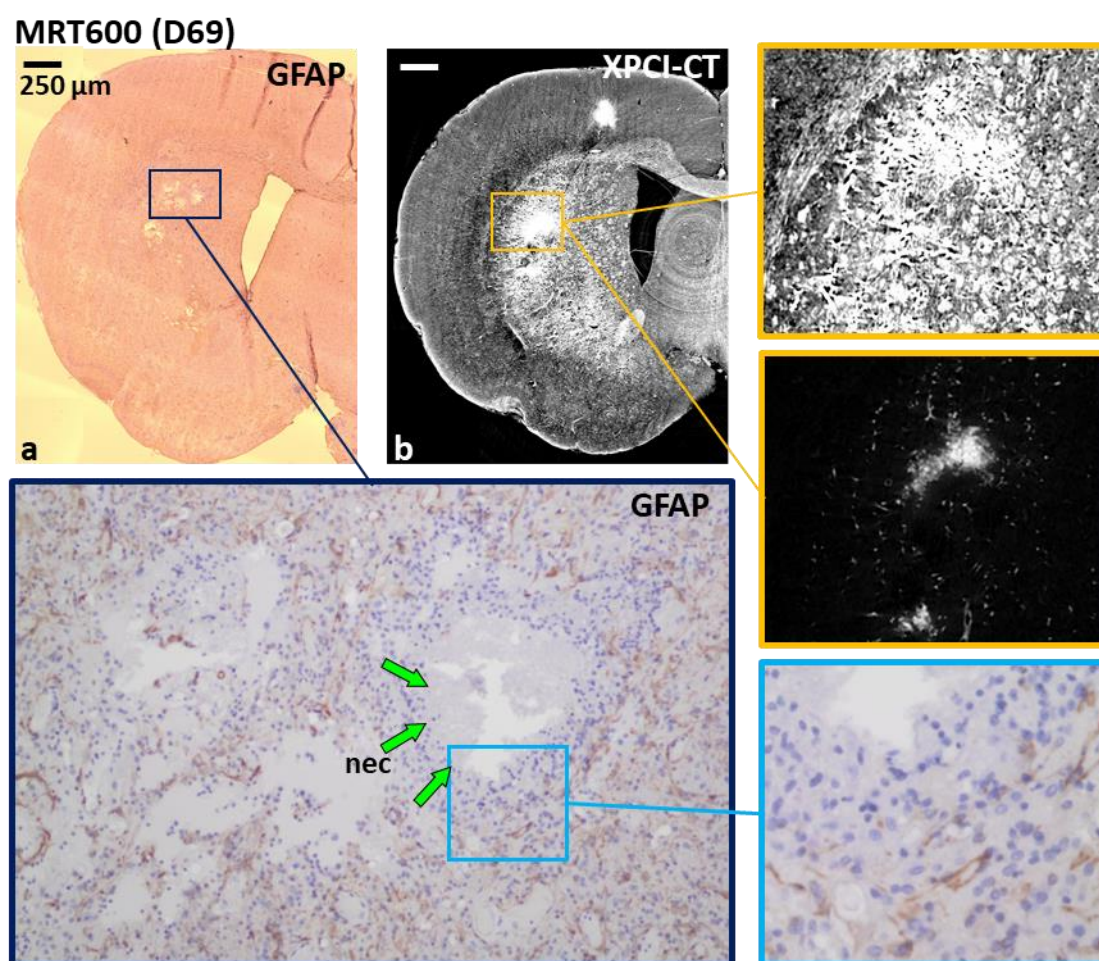


Figure 6.14: coronal XPCI-CT and GFAP immunohistochemistry images comparison for a GBM-bearing MRT600-treated sample sacrificed at D69. Only the implanted hemisphere is shown. (a) is the GFAP stained histology and (b) the respective XPCI-CT image obtained at similar magnification. The insets show, at the maximum available magnification, the residual GBM: the GFAP staining reveals the presence of necrosis (blue bordered inset) and hypercellularity (light-blue bordered box), while the two XPCI-CT insets (yellow borders), obtained with two different windowings, do not show abnormal structures due to the numerous streak artefacts. Figure reproduced from (Romano, 2021a).

As a case in point, Figure 6.15 reports the 3D rendering of one tumour-bearing brain sample of the BB15 and MRT200 groups. Three different views are reported (one axial and two sagittal views). The brain volume is rendered in a semi-transparent mode while the glioblastoma is coloured in red and rendered as a solid mass. The three different views allow identifying how the irregular GBM shape has developed within the organ, shifting the brain mid-line for the BB15 case (axial view).

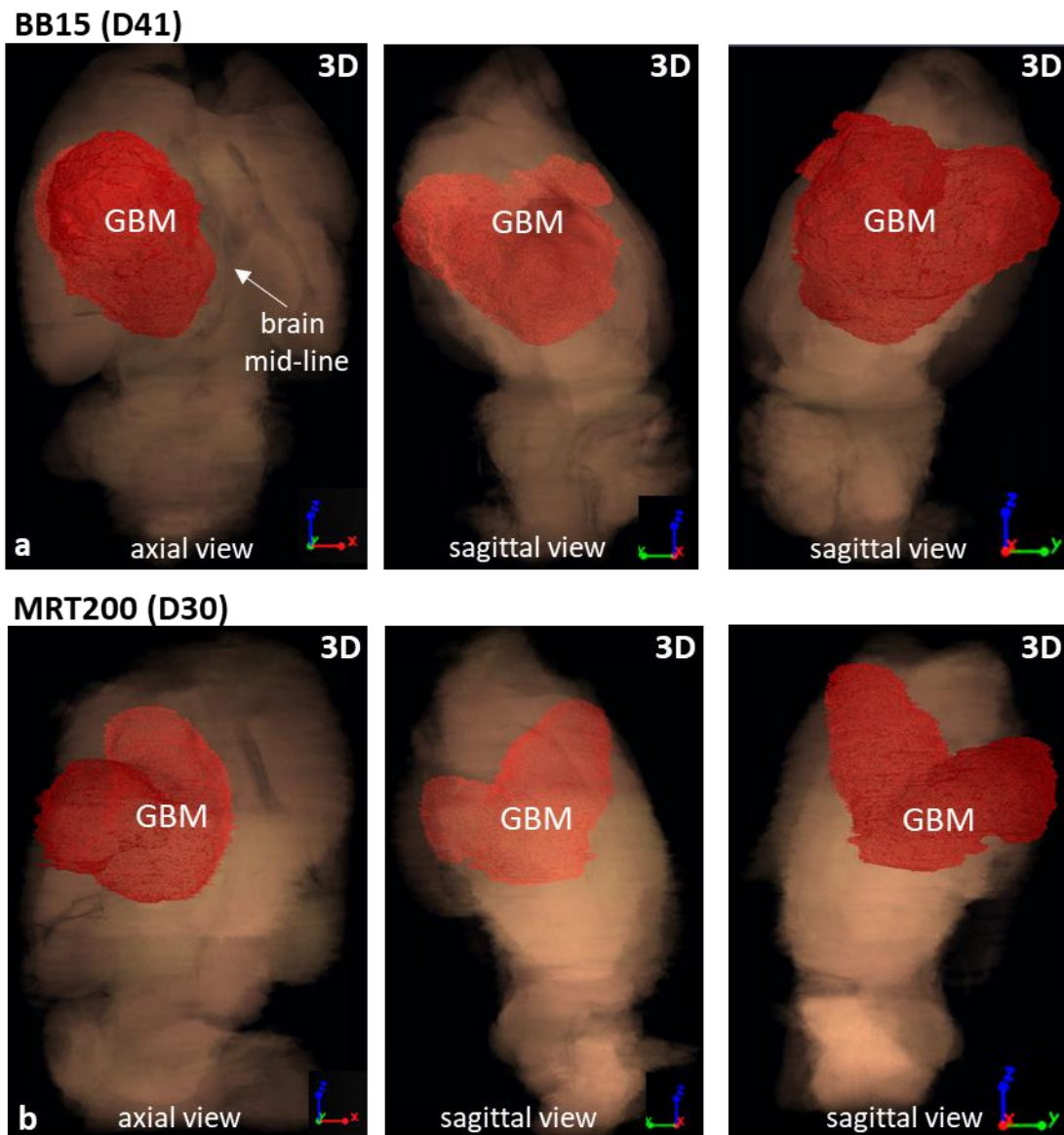


Figure 6.15: 3D renderings of tumour volumes within the brain organ for a BB15 and MRT200 case. The three different orientations (axial and two different sagittal views) of the BB15 (a) and MRT200 (b) irradiated rat show how the tumour develops into the brain volume. BB15 also reports the shifting of the brain mid-line. The full organ dataset is rendered in semi-transparency, while the tumour is coloured in red and co-registered as a solid mass. Figure reproduced from (Romano, 2021a).

As for the **assessment of the volume of the microcalcifications**, all the healthy animals treated with MRT and MB180 show microcalcifications within the irradiated tissues, as reported in the histogram in Figure 6.16a. The MB180 and MRT200 groups have comparable total volumes of microcalcifications; for the MRT-treated groups it increases as the peak dose level rises. All the tumour-bearing animals, exception made for two GBM-controls, show microcalcifications; the total volume of microcalcifications vs the survival days are reported in the plot

in Figure 6.16b. The total volume of microcalcifications in the MRT200, BB5, BB10, MB180 and GBM-control animals present similar values and trends over time, while the MRT400 group has no specific trend and the MRT600 volumes have a quadratic growth over time (see the reported best fit curve). The values reported in the graphs of Figure 6.16 are listed in Table 6.3 and Table 6.4; errors are computed as explained in section 5.3.

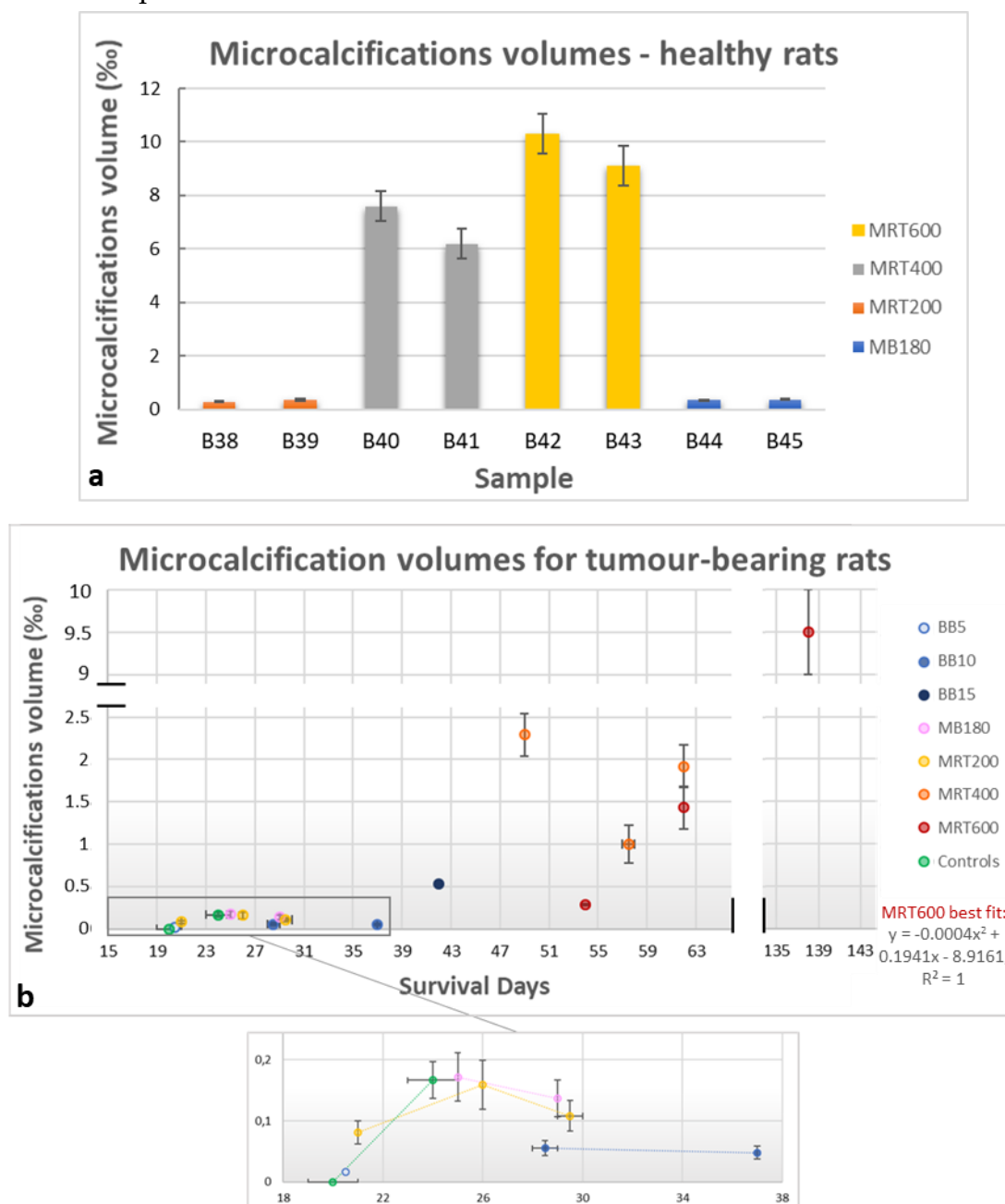


Figure 6.16: graphs of the microcalcifications content in healthy irradiated rats sacrificed at D137-138 (a) and in GBM-bearing animals as a function of the survival days (b). Values are normalized over the field of irradiation. The zoom in (b) better discriminates the values obtained before day 39. Figure reproduced from (Romano, 2021a).

Table 6.3: microcalcifications volumes (V_{mcs}) for the GBM-bearing animals. Volumes are reported as a percentage of the volume of the field of irradiation.

Group	Sample name	Survival (day)	V_{mcs} (%)
BB5	C13, C07	20.5 ± 1.5	0.016 ± 0.004
BB10	B14, C12	28.5 ± 0.5	0.06 ± 0.13
BB10	C14	37	0.05 ± 0.11
BB15	B17, B18, B20, B21	42.0 ± 0.5	0.53 ± 0.13
MRT200	C02	21	0.08 ± 0.02
MRT200	B03	26	0.16 ± 0.04
MRT200	C03, B02	29.5 ± 0.5	0.11 ± 0.03
MRT400	C08	49	2.29 ± 0.25
MRT400	B25, C06	57.5 ± 0.5	1.01 ± 0.22
MRT400	C04	62	1.9 ± 0.3
MRT600	C11	54	0.285 ± 0.007
MRT600	C09, C10	62	1.4 ± 0.3
MRT600	B12, B13	138	9.5 ± 0.5
MB180	B31	25	0.17 ± 0.04
MB180	B28, B29, B30	29	0.14 ± 0.03
MB350	B33, B34, B35, B36, B37, B23, B24, B27	15.4 ± 0.5	0.11 ± 0.03
Control	C17, C15	20 ± 1	0.17 ± 0.03

Table 6.4: microcalcifications volumes (V_{mcs}) for the healthy-treated animals. Volumes are reported as a percentage of the volume of the field of irradiation.

Group	Sample name	Survival (day)	V_{mcs} (%)
MRT200	B38	138	0.29 ± 0.02
MRT200	B39	138	0.37 ± 0.03
MRT400	B40	138	7.6 ± 0.6
MRT400	B41	138	6.20 ± 0.05
MRT600	B42	138	10.30 ± 0.08
MRT600	B43	138	9.11 ± 0.07
MB180	B44	138	0.364 ± 0.007
MB180	B45	138	0.383 ± 0.007

As last, a **3D representation of the distribution of the microcalcifications** (indicated as mcs in the figures) within the whole brain and within the irradiated tissues for an MRT600-treated healthy brain are shown in Figure 6.17a and Figure 6.17b, respectively. Figure 6.17a shows the sagittal view of the whole 3D rendered brain, displayed in semi-transparent modality, and the co-registered segmented microcalcifications volume. Here it is possible to appreciate how microcalcifications are formed within the brain and that they agglomerate in the thalamus, caudate putamen, frontal, parietal and orbital cortex. Furthermore, in the axial view of Figure 6.17b and its inset, the grey-scale 3D rendering of both the organ and microcalcifications allow identifying the location of the structures with respect to the beam paths, indicated by the red arrows. The light-blue arrow points to a region of the tissue where the tracks of the MRT microbeam paths appear “bended” in the proximity of the Ca/Fe deposits. As a comparison, the 3D rendering of an MRT200-treated healthy brain is presented in Figure 6.17c. In this case, the microcalcifications only develop in the thalamus as non-clustered agglomerates of different dimensions.

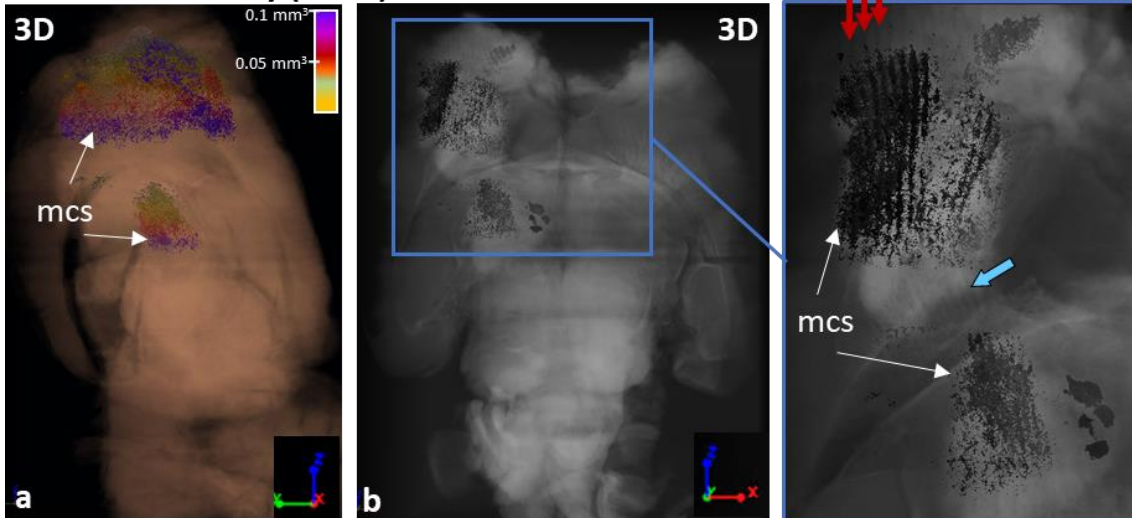
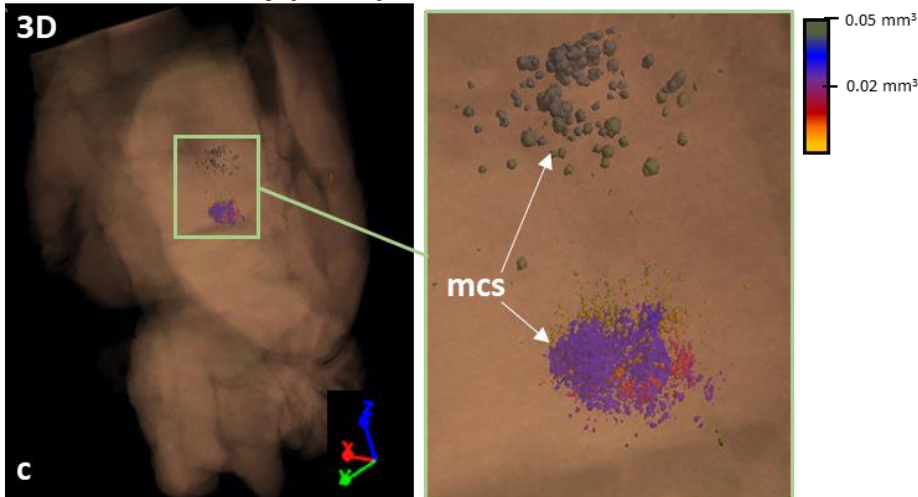
MRT600 – healthy (D138)

MRT200 – healthy (D138)


Figure 6.17: 3D distribution of microcalcifications (mcs) for a healthy MRT600-treated sample in a sagittal (a) and axial (b) view. The zoom (b) enhances that microcalcifications are distributed along the MRT paths (red arrows) and that the MRT paths are bended along their track (green arrow). (c) is the microcalcifications 3D rendering for an MRT200-treated healthy rat brain showcasing that MRT200-induced microcalcifications are mainly present in the thalamus. The brain XPCI-CT datasets are given as semi-transparent volume, while the mcs are reported as coloured solid deposits of dimensions according to the legend. Figure reproduced from (Romano, 2021a).

The **coexistence of tumour and microcalcifications** within the treated brains is shown in Figure 6.18 for different irradiation geometries; all the chosen samples belong to animals involved in the survival study. Images in Figure 6.18a-d report the sagittal view of the 3D rendering of an MRT200, MRT600, BB15 and MB180 samples respectively, while 3D renderings in Figure 6.18e-h are zoomed views of the regions with microcalcifications on an axial orientation, for the same samples. The brain and the tumour volumes are rendered with the same colour code as in

the previous figures, while microcalcifications are here all depicted in white. Similarly to the healthy case, MRT200 samples only show microcalcifications in the thalamus; Figure 6.18e displays the deposits next to the tumour borders, as also seen for the BB15 sample. The MRT600-treated brain, if compared with the MRT200 one, shows more extended calcifications in the area from the thalamus to the cortex. The zoom of Figure 6.18f allows discriminating both micro- and macro-deposits. As last, in the MB180 sample (Figure 6.18d and Figure 6.18h) microcalcifications are clearly arranged along the MB paths (see the arrows) along the entire irradiation field.

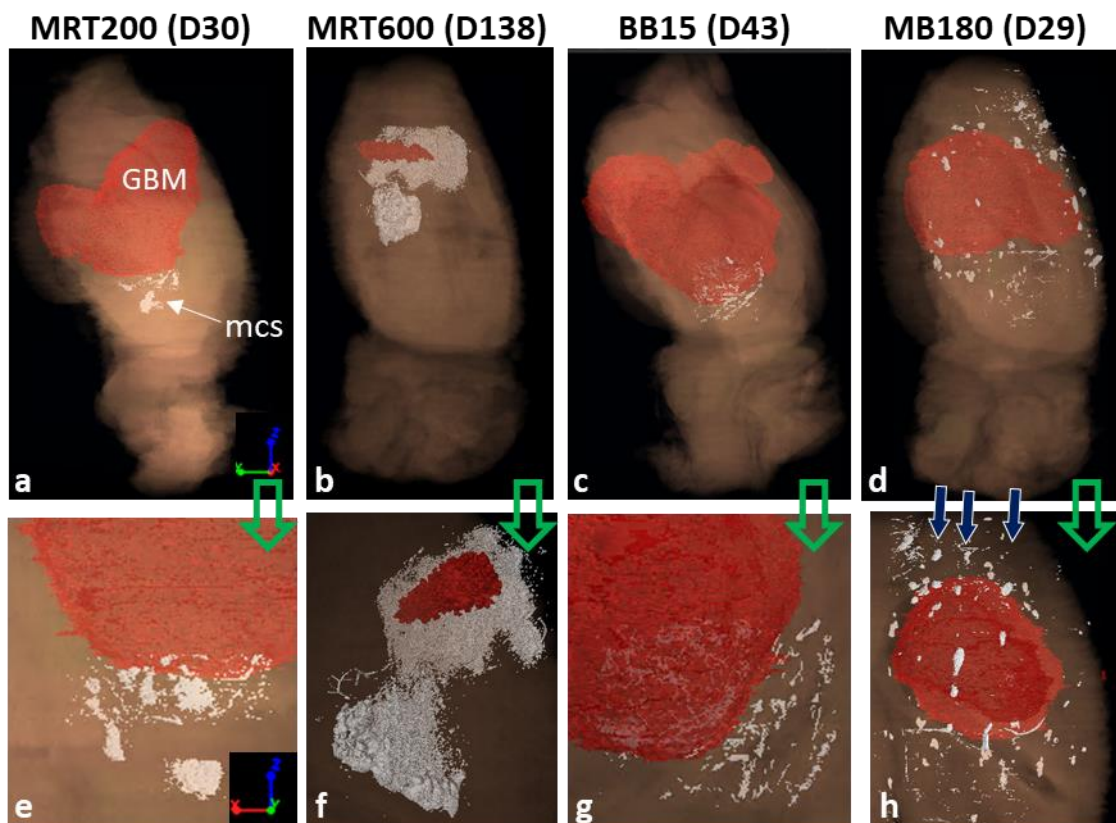


Figure 6.18: tumour and microcalcifications 3D rendering, in a sagittal view, within the entire brain organ for an MRT200, MRT600, BB15 and MB180 - irradiated sample (a)-(d), respectively. (e)-(h) are the zoomed rendering, in axial view, of (a)-(d) respectively. All tumour and brain volumes are given in semi-transparency while microcalcifications are co-registered to the other volumes as solid white deposits. Figure reproduced from (Romano, 2021a).

6.6 SAXS/WAXS and XRF study of microcalcifications

SAXS/WAXS and XRF analysis enabled the structural and chemical classification of microcalcifications for MRT-treated brain samples. In all the investigated specimens showing crystallized Ca, WAXS identified the Ca content as HAP crystals. The HAP peak position, evaluated for the most intense peak ($q \sim 2.28 \text{ \AA}^{-1}$) is reported in Figure 6.19a, showing that all these samples, which are the ones with a crystalline Ca content, include HAP. For the same samples, the median value of the HAP crystalline domain ($\propto 2\pi/\text{peak width}$) evaluated along the most intense peak, are reported in Figure 6.19b, where the median value over all the detected signals is reported. Figure 6.19b shows that, for both healthy and GBM-bearing MRT-treated brains, no specific trend as a function of the delivered MRT peak dose is recognizable and all the samples exhibit the formation of HAP crystals with similar domain sizes. It has to be noticed that the GBM-bearing MRT600 values are from animals that were sacrificed at different time points, while the others were all sacrificed at the last time point. The WAXS-based data used in the graphs of Figure 6.19 are reported in Table 6.5; errors are computed as described in section 5.5.

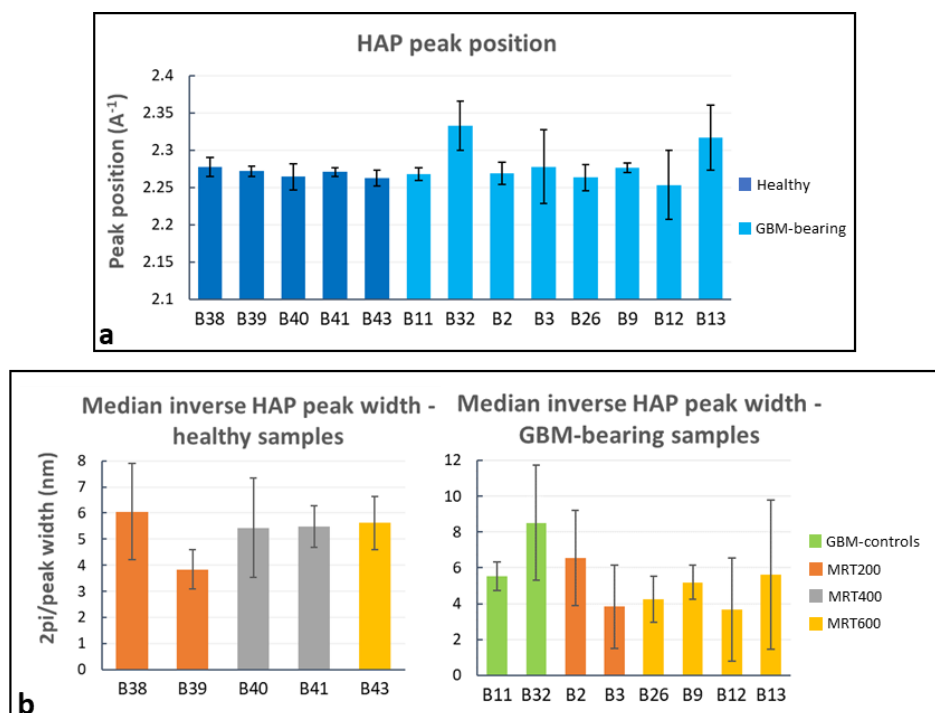


Figure 6.19: WAXS data analysis for controls and MRT-treated samples. (a) peak position graph of the samples showing hydroxyapatite (HAP) as crystallized phase for the Ca content. (b) inverse peak width for healthy and GBM-bearing MRT-treated brains. The reported value is the median over all the detected signals within the q -range from 2.20 \AA^{-1} to 2.34 \AA^{-1} . Figure reproduced from (Romano, 2021a).

Table 6.5: WAXS signals for healthy and GBM-bearing brains. The table reports, for each sample, the number of imaged pixels (i.e. the sample's dimensions), the number of pixels showing crystallized HAP, the median peak position and inverse peak width for the WAXS-HAP signals.

Group	GBM	Sample name	Survival (days)	Imaged pixels	HAP pixels	Peak position (1/Å)	2 π /peak width (nm)
MRT200	NO	B38	138	3721	84	2.277 \pm 0.013	6.1 \pm 1.8
MRT200		B39	138	3477	15	2.271 \pm 0.007	3.8 \pm 0.8
MRT400		B40	138	2911	145	2.264 \pm 0.018	5.4 \pm 1.9
MRT400		B41	138	3721	139	2.271 \pm 0.006	5.5 \pm 0.8
MRT600		B42	138	2091	0	0	0
MRT600		B43	138	4941	711	2.262 \pm 0.011	5.6 \pm 1.0
MRT200	YES	B2	30	3321	89	2.269 \pm 0.015	7 \pm 3
MRT200		B3	26	4141	3	2.28 \pm 0.05	4 \pm 2
MRT400		B8	26	4141	0	0	0
MRT600		B26	41	6161	57	2.263 \pm 0.017	4.2 \pm 1.3
MRT600		B9	69	3111	530	2.276 \pm 0.007	5.2 \pm 1.0
MRT600		B10	69	4941	0	0	0
MRT600		B12	138	3721	3	2.25 \pm 0.05	4 \pm 3
MRT600		B13	138	9272	50	2.32 \pm 0.04	6 \pm 4
Control		B11	23	3721	616	2.268 \pm 0.008	5.5 \pm 0.8
Control		B32	25	3321	30	2.33 \pm 0.03	9 \pm 3

Overall, the graphs of Figure 6.19b report the median values, but large error bars (+/- one standard deviation) reveal that, in some cases, different HAP WAXS profiles are distinguished, corresponding to distinct HAP crystalline domains, i.e. the peaks of the different profiles have different FWHM values. As a showcase, in Figure 6.20 the most representative WAXS signals found within a healthy MRT600-treated sample are reported.

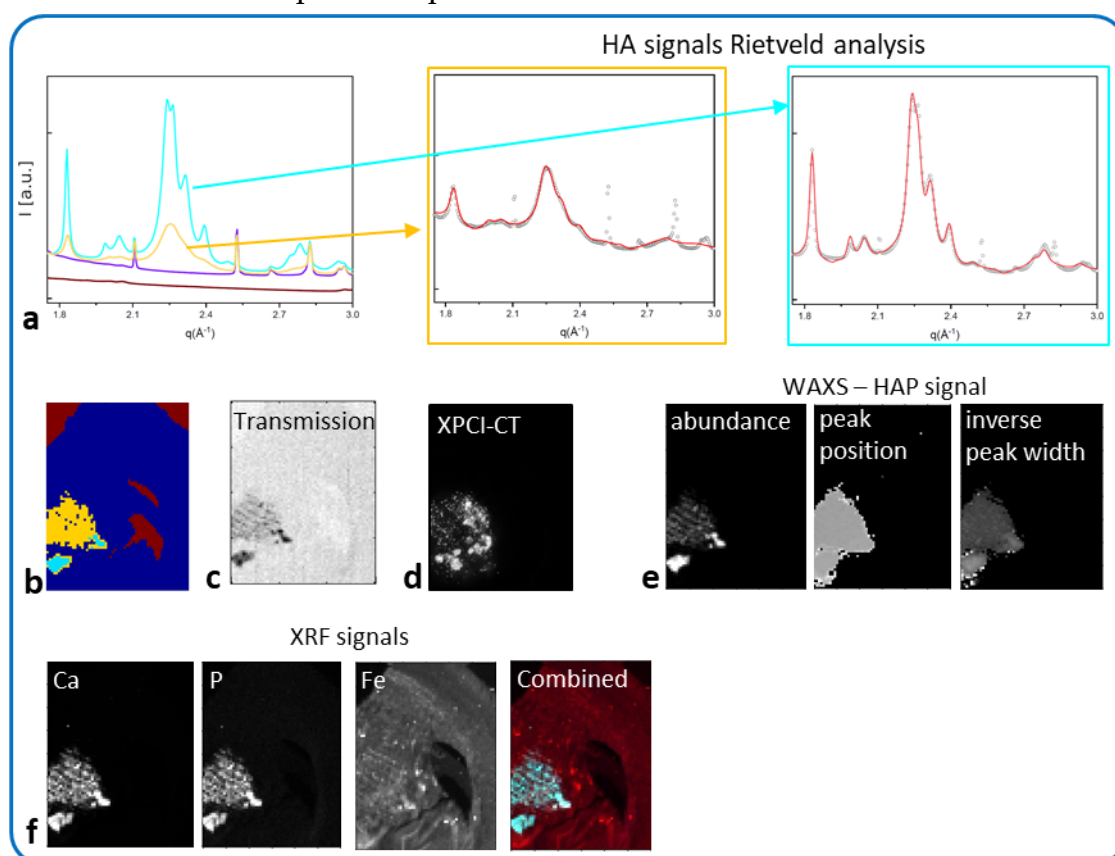


Figure 6.20: showcase of the presence of two different populations of HAP crystals within the same sample (healthy MRT600-treated), which is revealed by the two WAXS signals, the yellow and cyan one, in (a) that are also displayed with their Rietveld analysis. Here, the crystalline domains evaluated along the 002 direction are 11.7 and 27.0 nm. The coloured micrograph (b) helps in identifying the sample areas associated with the detected WAXS signals. Micrographs, obtained for the same specimen, are also available for transmission, XPCI-CT, HAP abundance, peak position and inverse peak width, Ca, P, Fe and combined relevant XRF signals (c)-(f). Figure reproduced from (Romano, 2021a).

Yellow and cyan profiles correspond to HAP and their Rietveld analysis fit is shown in the cyan and yellow-bordered graphs. For these two signals the crystalline domain evaluation along the [002] direction, which is the peak at $q = 1.83 \text{ \AA}^{-1}$, is also reported in the caption. The coloured 2D sample map (Figure 6.20b) helps in identifying the HAP regions and the sub-areas corresponding to the two HAP-WAXS profiles (same colour code in Figure 6.20a and Figure 6.20b).

It is noticeable that the largest crystalline domain value is associated with low signal in the transmission, high XPCI-CT, Ca, Fe and P XRF signals and high values for HAP abundance, peak position and inverse peak width values (Figure 6.20c-f), all expressed in arbitrary units. The “Combined” image reports the combined Fe, Ca and P XRF signals in RGB scale. Thus, the areas in white exhibit the coexistence of the three elements, while cyan areas are rich in Ca and P; the red Fe background present in the entire slice is due to the used stainless-steel microtome blade. A similar behaviour was found in other samples: SAXS/WAXS and XRF collected data are reported in Figure 6.21 for a GBM-control sample, as a further example.

As last, the Fe, P and Ca median XRF signal was extracted for each sample con-

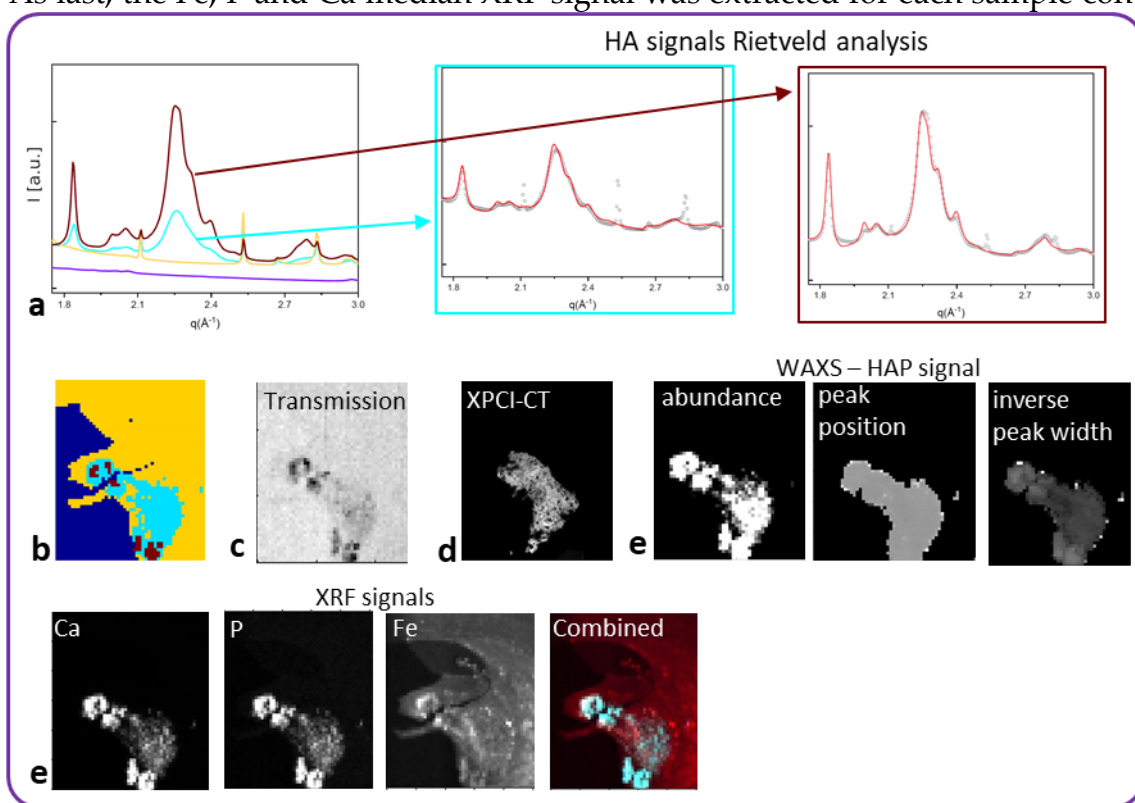


Figure 6.21: two different populations of HAP crystals within a GBM-control brain (cyan and brown WAXS signals in (a) reported together with their Rietveld analysis). Here, the crystalline domains evaluated along the 002 direction are 15 and 21 nm. The coloured micrograph (b) helps in identifying the sample areas associated with the detected WAXS signals. Micrographs, obtained for the same specimen, are also available for transmission, XPCI-CT, HAP abundance, peak position and inverse peak width, Ca, P, Fe and combined XRF signals (c)-(f). Figure reproduced from (Romano, 2021a).

sidering all the pixels showing XRF-Ca content as explained in section 5.5; the values are reported in the graphs of Figure 6.22. For the healthy-treated samples,

no specific trend is visible for the XRF-Fe signal and a large intra-group variability is shown, while for the GBM-bearing brains all values are compatible to each other (Figure 6.22a-b). In these plots, some samples show large error values indicating that the Fe signal detected in the different pixels is spread over a large interval of values. By looking at the GBM-bearing MRT-600-treated samples, a decrease in the mean value for the Fe signal is visible for the animals sacrificed at D138 (samples B12-B13). Ca and P XRF median signals, for both healthy and GBM-bearing samples, are reported in Figure 6.22c-f; no specific trend is visible and large error bars reflect the large intra-signals variability detected in some samples. Data plotted in Figure 6.22 are listed in Table 6.6; errors are computed as described in section 5.5.

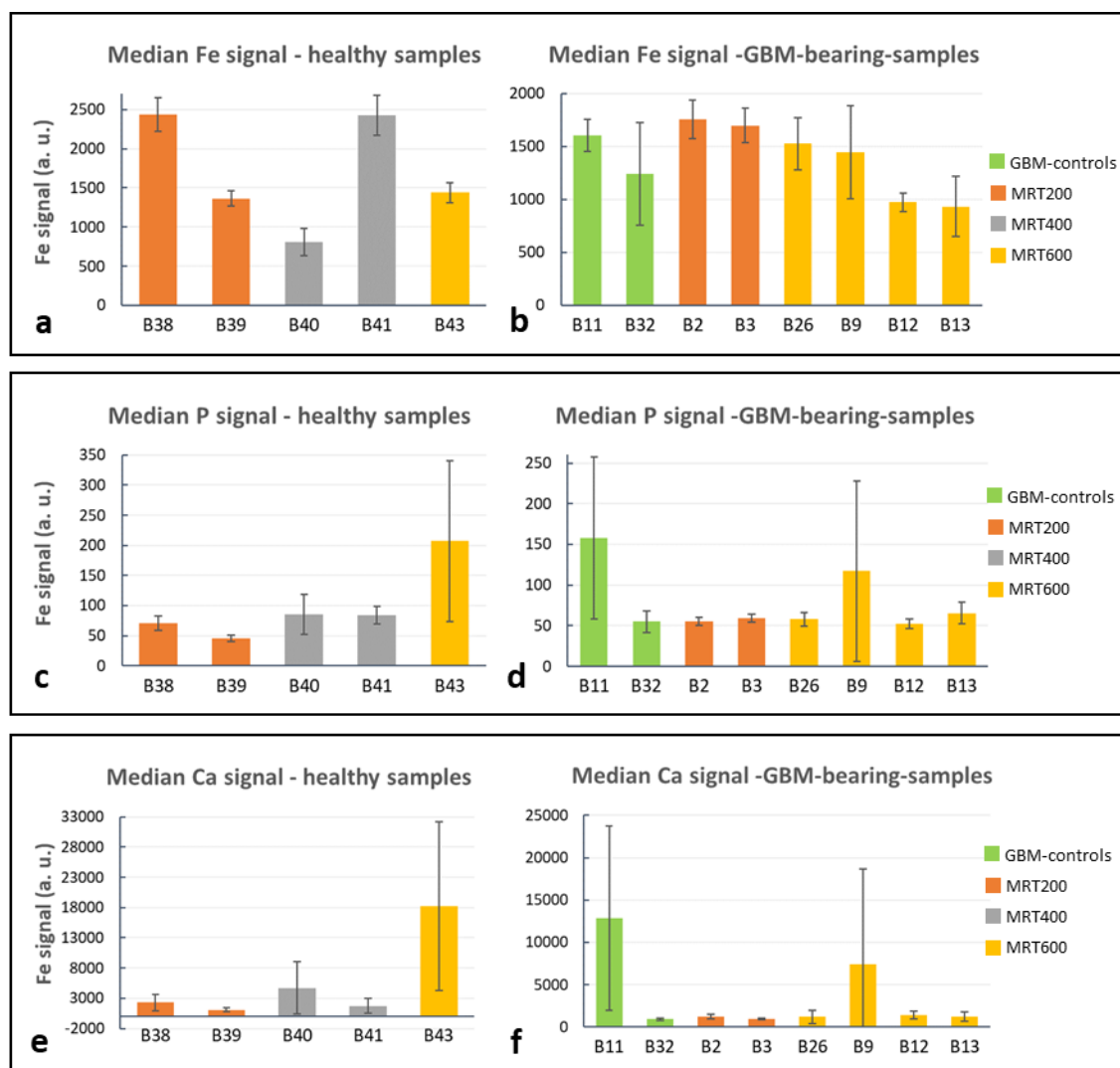


Figure 6.22: median XRF signals for Fe, P and Ca for healthy and GBM-bearing samples. Fe signal was only studied in the image pixels where XRF-Ca signal is detected. Figure reproduced from (Romano, 2021a).

Table 6.6: XRF signals for P, Ca and Fe for both healthy and GBM-bearing brains. The signals are computed over the pixels showing an XRF-Ca content.

Group	GBM	Sample	Survival (days)	XRF-P signal (a. u.)	XRF-Ca signal (a. u.)	XRF-Fe signal (a. u.)
MRT200		B38	138	70 ± 12	2300 ± 1300	2400 ± 200
MRT200		B39	138	46 ± 5	1100 ± 300	1400 ± 100
MRT400	NO	B40	138	90 ± 30	4700 ± 4000	800 ± 170
MRT400		B41	138	80 ± 15	1700 ± 1100	2400 ± 300
MRT600		B43	138	200 ± 130	18000 ± 14000	1400 ± 120
MRT200		B2	30	55 ± 5	1200 ± 300	1760 ± 180
MRT200		B3	26	59 ± 5	950 ± 90	1690 ± 160
MRT600		B26	41	58 ± 9	1200 ± 800	1500 ± 200
MRT600	YES	B9	69	120 ± 90	7400 ± 11000	1400 ± 400
MRT600		B12	138	53 ± 6	1400 ± 500	970 ± 90
MRT600		B13	138	66 ± 13	1211 ± 500	934 ± 300
Control		B11	23	160 ± 80	13000 ± 11000	1600 ± 150
Control		B32	25	55 ± 13	920 ± 150	1200 ± 500

6.7 Discussion

6.7.1 Effects of treated healthy rat brains

The potential of XPCI-CT as a tool for investigating the effects induced by radiotherapy has been shown analysing rat brains treated with both standard and spatially-fractionated RTs. First, the study was performed on healthy brains to access how the brain responds to the different RT protocols. All the delivered BB irradiations (using 5, 10 and 15 Gy) do not determine visible pathological signs or tissue alterations; histological images only reveal a few Fe deposits (see Figure 6.4). The presence of astrocyte excess in the BB-treated brains is likely due to rat age (D138 for all the animals) and do not represent a pathological state as confirmed by a symmetric GFAP uptake in the two hemispheres (Figure 6.4).

MRT-treated samples show more pronounced effects that appear as tissue ablations corresponding to the peak delivery areas together with microcalcifications agglomerates, as visible in Figure 6.8. During the treatment, the following brain areas were irradiated: neocortex, hippocampus, thalamus, hypothalamus, caudate putamen, frontal, parietal and orbital cortex. The MRT-induced ablations are visible in all these areas for the MRT400 and MRT600 groups, while the MRT200-treated animals exhibit ablations mainly in the thalamus and hypothalamus. MRT-induced tissue ablations were already seen in Barbone *et al.* 2018 and Bouchet *et al.* 2016 (Barbone, 2018; Bouchet, 2016), but no preferential effect with the applied dose and the anatomical brain area has been reported. Nonetheless, MRT transection preserve the overall neuroanatomy and some neurons are still visible within the microbeams peak delivery area, as confirmed by histology. Microcalcifications are visible in a small amount in the MRT200-irradiated samples, and the amount of deposits increases by increasing the peak dose value, as visible in the plot of Figure 6.16a. Overall, microcalcifications are observable as old (i.e. advanced stage) and well-organized lesions, probably caused by local microbleeding from blood vessels (see the dedicated paragraph). The MRT200 microcalcifications are mainly found in the thalamus (Figure 6.17c) while for the MRT400 and MRT600 groups they also appear in other anatomical regions (for instance in the caudate putamen and orbitofrontal cortex) accompanied by massive astrogliosis (Figure 6.8, Figure 6.17 and Figure 6.18). **The fact that microcalcifications are only present in specific areas of the brain suggests a different**

radio-sensitivity of the different brain anatomical areas, as discussed later in the paragraph dedicated to the 3D-based information. This is also confirmed by the presence of bended microbeam paths next to Ca/Fe agglomerates in healthy samples (Figure 6.8c' and Figure 6.17b): slow-down of metabolism causes deposits and thus, the MRT bending occurs at the interface with an area with more accelerated metabolism.

MB-treated rat brains present pronounced scar induced by the MB passage, which are characterized by Ca and Fe deposits, in a smaller amount with respect to all the MRT cases, and by low cell density areas (Figure 6.5 and Figure 6.7) that are well distinguishable with both histology and high-resolution XPCI-CT (Figure 6.11b). This latter type of lesion derives from a degradation of the tissue and a neuronal band interruption that are typical signs of old-occurred localised lesions that did not result in a complete tissue destruction nor in a repaired necrosis. MB and MRT groups showcase how the dose-volume effect determines very different outcomes in spatially fractionated RTs depending on the size of the field of irradiation. Limited to the investigated cases, microbeams are well tolerated by the brain tissues for radiation doses up to 600 Gy of peak, while minibeam cause important damages (see Figure 6.7) even if the peak and valley doses are both lower than in the MRT600 case. As last, it has to be considered that the MB350 valley dose is compatible with the uniformly delivered dose in the BB15 case, where no substantial effects are found. Thus, **the peak delivered doses for MB350 animals showed toxic effects on healthy tissues and represents a dose limit that should not be exceeded when planning the minibeam RT with 1 mm of spacing**. This evidence is corroborated by the fact that all the MB350-treated animals, both healthy and tumour-bearing, died at D15-16.

6.7.2 Effects on GBM-bearing rat brains

The main visible effects of the RTs on tumour-bearing animals concerns the tumour control, i.e. the regression or progression of the tumoral entity, to be interpreted together with the analysis of survival curves and the occurrence of microcalcifications. The high sensitivity of XPCI-CT with respect to the nervous tissue structures allows for an **optimal GBM discrimination**, as previously demonstrated in the literature (Barbone, 2018; Lwin, 2016; Ricciardi, 2021). This capability is evident in Figure 6.10 where the GBM tissue and necrosis are appreciable,

as in (Rong, 2006), at different length scales enabling the establishment of a solid and precise pipeline for tumour segmentation that can be also applied to other animal models. The implemented *ilastik*-based segmentation tool exploits the 3D nature of the XPCI-CT data providing, isotropically, greater precision in tumour segmentation with respect to the one achievable with histology or MRI. Indeed, histologic-based tumour quantification is intrinsically 2D (the thickness of the cut slices determines the spatial resolution in the third dimension), and the MRI-based one has the drawback of being based on low spatial resolution data, especially in the third dimension where is limited by the inter-space between two subsequent slices (Bouchet, 2014; Bouchet, 2016; Laissue, 1998). Thanks to the implemented segmentation procedure, it was possible to build the graphs of Figure 6.12 reporting the tumour development over time. The first plot reports a tumour volume trend for the GBM-controls compatible with the linear growth found in (Bouchet, 2016; Lemasson, 2015) and the second show the computed tumour volume for all the different groups. As in (Bouchet, 2016), the tumour volumes for BBs and MRT200 groups have an upward trend as a function of time and overall, for the BB groups, the median survival is increased as the delivered dose increases. The MRT400 group shows large values of the tumour volumes that are not in accordance with the available literature. Probably, this is due to the low statistics since those values represent data from only one or two animals. The MRT600 group shows the best tumour control achieved in this study and, for animals surviving more than 60 days, no traces of GBM are detected by inspection with $3.25^3 \mu\text{m}^3$ voxel size XPCI-CT. However, GFAP staining histology reveals small GBM traces in all these samples (Figure 6.13 and Figure 6.14), meaning that these **tumour infiltrations are below the $3.25^3 \mu\text{m}^3$ voxel size detectability limit**. Figure 6.18b and Figure 6.18f showcase in 3D the MRT600 induced tumour shrinkage and regression.

6.7.3 Microcalcification study

By analysing the microcalcifications content in the different samples, it is possible to see that those deposits are both radio- and tumour-induced. Healthy MB180- and MRT-treated animals exhibit pure radio-induced accumulations (Figure 6.8 and Figure 6.16a), GBM-controls display pure tumour-induced mineralizations and GBM-bearing treated animals feature the presence of both types of sediments

(Figure 6.16b). On the contrary, healthy-controls do not show any Ca/Fe accumulation. In the literature, the presence of microcalcifications has been demonstrated in MRT-treated GBM-bearing and healthy brains (Dilmanian, 2002; Régnard, 2008a) and on healthy MB-treated brains (Prezado, 2015) with different geometrical parameters or applied radiation doses. Although in this study the segmentation was performed on the full-organ $3.25^3 \mu\text{m}^3$ voxel size CT datasets, the multi-scale approach applied in targeted regions allows for a better identification of small deposits, as shown in Figure 6.11a-a'.

Microcalcifications are a well-known post-irradiation effect. Ca deposits are classified as a late effect of cranial irradiation in childhood (Suzuki, 2000). This effect is known as mineralizing microangiopathy, an autoimmune reaction localized to the irradiated area that is associated with vasculitis and hyalinization (Lee, 1977). Thus, hypersensitivity of the vessels after irradiation produces vascular damages with hypoxia that results in Ca mineralization. Mineralizing microangiopathy found after child and adult cranial irradiations is mainly present in the basal ganglia and is asymptomatic in most cases (Srinivasan, 2010). These observations strengthen the XPCI-CT based evidence of microcalcifications mainly occurring in the thalamus and caudate putamen that are strictly connected or part of the basal ganglia, respectively (Figure 6.8 and Figure 6.17 - Figure 6.18). XPCI-CT enables the full-organ 3D analysis with great detail and sensitivity allowing the investigation of RT-induced effects and their localization. Histological examination of the mineralizing microangiopathy deposits showed a strong positive stain for Ca and a weak positive stain for Fe (Boyko, 1992), as also seen in our cases (histologies of Figure 6.4 and Figure 6.8). Furthermore, brain irradiation was found to cause microbleeding in survivors irradiated during childhood (Phillips, 2020), which is likely to increase during the follow-up, and is classified as a small vessel disease (Remes, 2020). Thus, **microbleeding and mineralizing microangiopathy can be seen as the responsible for microcalcifications formation in the irradiated animals of our study.**

For the first time an in-depth analysis of the chemical and crystalline nature of the microcalcifications was realized by means of SAXS/WAXS and XRF tools. Interestingly, many MRT-treated samples showed a **crystallized phase of Ca** that was **identified with HAP crystals** by means of the WAXS analysis (Figure 6.19a).

The microcalcifications content for healthy MRT-treated samples show an increasing trend with the peak dose (Figure 6.16a), but no visible trend for their crystalline domain values or XRF Fe intensity signal is retrievable. It is worth to note that in Figure 6.19b the plotted values of crystalline domains are the typical (median) values obtained for each sample, but the **coexistence of different HAP populations** in the same specimen is detected (Figure 6.20a and Figure 6.21a) suggesting an heterogeneous formation of HAP deposits within the brain tissue. As last, all samples containing HAP crystals exhibit the coexistence of Ca, Fe and P in the same sites (see Figure 6.20e and Figure 6.21e). Nevertheless, some GBM-bearing samples were found to contain Fe (from XRF measurements) and no crystallized HAP (as from WAXS analysis) in the region where there is a XPCI-CT signal compatible with that of microcalcifications. Probably, an X-ray amorphous phase of HAP is present, thus corroborating the evidence that no specific values of crystalline domains can be associated with each MRT group. In the literature, the presence of HAP calcifications on humans is reported in various pathological cases (see (Vidavsky, 2021; Vanna, 2020; Giannini, 2019)), where mineralizations are associated with cells injury, explaining the radio-induced calcifications, or with apoptosis and necrosis, which cause a pathological release of high concentrations of calcium and phosphate that can explain the detected GBM-induced microcalcifications.

6.7.4 A full 3D characterization and quantification of RT-induced effects

The 3D rendering of the distribution of the tumour and microcalcifications within the studied organ shown in Figure 6.15, Figure 6.17 and Figure 6.18 displays how **XPCI-CT enables an accurate volumetric visualization of anatomical structures and pathological states**. From the tumour volume rendering it is possible to see how the tumour develops inside the full brain for the three different radiotherapy protocols (BB, MRT and MB) shifting, in some cases, the brain midline and consequently displacing the healthy surrounding tissues.

As for the microcalcifications 3D rendering, in Figure 6.17 and Figure 6.18, it is possible to have a visual and qualitative assessment of the different radio-sensitivity of brain anatomical regions depending on the applied RT protocol. As it can be seen in Figure 6.18c and Figure 6.18g, BB cases show microcalcifications

in the thalamic area if only associated with tumour presence. This could be explained considering that tumour areas are characterized by a fragile vasculature where microbleeding is more likely to happen and thus Ca/Fe deposits can build in. Healthy BB-treated animals do not show evident clusters of Ca/Fe and only isolated deposits are present (see Figure 6.4). MB-treated brains do not display evident differences in radio-sensitivity for microcalcifications formation. Clusters of mineralizations are present along the full FOI reproducing the MB path with discontinuity (see Figure 6.18d and Figure 6.18h). Healthy-treated brains show about three times more Ca/Fe deposits with respect to the GBM-bearing ones, exception made for the MRT600 group. This is probably due to the tumour growth within the organ and to metabolic processes that remodel the presence of microcalcifications and their formation within the brain with respect to the healthy cases. The MRT-treated brains have a very different content in microcalcifications depending on the delivered dose (see Figure 6.16 and Figure 6.17). Nevertheless, **the thalamus is the most sensitive brain area to X-ray MRT irradiation** (as also confirmed by the aforementioned studies on mineralizing microangiopathy): microcalcifications are present in all the MRT-treated brains (200-600 Gy of peak dose) regardless the peak dose. Analysing the distribution of microcalcifications on MRT400 and MRT600-treated animals, they appear also to be visible in the caudate putamen and in some cortex areas. Furthermore, it is noticeable that only MRT200-treated animals do not show clustered deposits. At the best of my knowledge, no previous work reported experimental 3D results on the induced effects of RTs and thus on the different radio-sensitivity within the different brain areas.

6.8 Data exclusion from the study

The brain RT study used, as already said, irradiations with BB, MRT and two different MB geometries. In this chapter no results related to the MB150 and MB450 groups (i.e. with the minibeam spaced by 2 mm) are reported. Animals belonging to these groups show a survival similar to the GBM-control groups. After animals' euthanasia and *ex-vivo* XPCI-CT experiments, it was seen that the chosen geometry was not well-suited for the implanted tumours, which had dimensions of a few millimetres at D10 (see MRI images of Figure 5.15). As a result, tumours were either only partially irradiated or not irradiated at all. In order to

avoid this problem, in the second RT experiment, an MRI session was performed at a time close to the irradiation in order to verify the size and shape of the tumours and the minibeam c-t-c distance was set to 1 mm.

6.9 Limitations of the study

The main limitations of this study are related to the low statistics in terms of number of animals available for each RT group. Other RT experimental sessions have been foreseen to improve the results statistics, especially for the tumour and microcalcifications volumes assessment, but were not realized due to the spread of COVID-19 that causes a long ESRF shutdown just after the restarting period after the EBS-ESRF upgrade. Furthermore, SAXS/WAXS and XRF analyses were only performed on one tissue slice per each sample and a second experimental session to complement the investigations by scanning additional tissues slices was not possible because of SLS COVID-19 related closure.

It has also to be added that synchrotron beamtime demand a long-term preparation and anticipated beamtime schedule; proposals for obtaining an experimental session are submitted with more than six months of advance and thus allow limited rescheduling and almost no possibility of obtaining additional experimental sessions in a short time range.

6.10 Conclusions and future perspective

This study proves that the XPCI-CT imaging technique is well suited for visualizing *ex-vivo*, with a label-free, 3D full organ approach the neuroanatomy of irradiated brains and side effects after radiotherapy. The effects of standard and novel radiotherapies on both healthy and tumour-bearing rat brains are visualized with high sensitivity, quantified and classified by a multi-technique approach. The comparison of XPCI-CT with histology, immunohistochemistry, SAXS/WAXS and XRF analyses enabled the morphological, structural and chemical categorization of radio-induced effects on brain tissues.

This is the first study that compares X-ray BB, MRT and MB treatment protocols, provides an accurate 3D visualization and quantification of tumour and microcalcifications volumes and demonstrates a non-uniform radio-sensitivity of the different brain areas. Microcalcifications are also identified, from a multi-tech-

nique approach, as HAP with a coexistence of Fe, Ca and P. Supplementary investigations are necessary to study if the microcalcifications crystalline structures varies depending on the brain area in which they develop and to compare the presented results with behavioural studies. The qualitative and quantitative methodologies here presented are of high value for an accurate and precise evaluation of the efficacy of treatments. Additional experimental sessions are planned to improve the statistical significance of the results of this study and to extend the analysis of the evolution over time of the radio-induced effects of these spatially-fractionated radiotherapies.

Overall, this study proves that XPCI-CT is a valuable imaging technique for a *post-mortem* follow-up of full organs at high resolution. It also puts the basis for channelling studies of *in-vivo* applications for monitoring RT effects.

Chapter 7

Evaluation of healthy lung alterations after BB, MRT and MB irradiation

This chapter reports on a study in which, for the first time, the effects of both standard and novel RT methods on rat lungs were investigated, characterized and quantified by using XPCI-CT as a label-free 3D, *ex-vivo* X-ray imaging-based virtual histology technique.

This Chapter reports the results included in **an original article published as “Romano *et al.* 2021, X-ray Phase Contrast 3D virtual histology: evaluation of lung alterations after micro-beam irradiation *International Journal of Radiation Oncology, Biology, Physics*”** (see Annex 2)⁸. These scientific results were **presented as an oral talk at the European Congress of Radiology 2021 and at the 2021 annual meeting of the Italian Synchrotron Radiation Society** (see Annex 3).

7.1 Introduction

Lung tissue is ideally suited to XPCI because it consists of air sacs (approximately 80% by volume at end expiration) separated by thin tissue layers (mainly water) (Hooper, 2009). The air-tissue interfaces produce significant phase shifts (i.e. X-ray refraction) and thus small airways are visualized with high contrast despite of their weakly absorbing power. Small animal lungs have been investigated in several applications as dynamic identification of airway liquid clearance in newborn rabbits (Lewis, 2005; Hooper, 2009) and quantitative imaging of airway structure and regional lung ventilation with spatial resolution down to $\sim 1.0 \mu\text{m}$, allowing *in-vivo* and *ex-vivo* (Lovric, 2017a) studies in small animal models (Fardin, 2121; Broche, 2019).

⁸ All the paragraphs of this chapter, but paragraph 7.3, are reproduced or adapted from (Romano, 2021b).

In this study, standard BB, MRT and MB RTs were applied focusing on the effects of different X-ray beam geometries on healthy rat lungs, being the radio-tolerance of normal tissue the limiting factor of any cancer treatment. A proof of concept experiment on a mouse model already showed no acute response after the MRT irradiation with peak doses up to 400 Gy (Schültke, 2021) by monitoring physiological parameters and using immunohistochemistry. Up to now, the potential of XPCI-CT to investigate RT effects has been proven on MRT-treated rat brains (Barbone, 2018) as already mentioned in Chapter 6. Based on these successful studies, we aimed at visualizing and comparing via XPCI-CT the effects of MRT, MB and conventional BB RTs on healthy lung tissue. The final goal is to validate XPCI-CT as a 3D imaging technique for the follow-up of *ex-vivo* and then *in-vivo* studies of spatially fractionated X-ray RT for lung tumour treatment.

7.2 XPCI-CT for healthy rat lung anatomy

The capability of XPCI-CT to depict lung anatomic details with high sensitivity is shown in the $1.63^3 \mu\text{m}^3$ voxel size images of two control (healthy, non-irradiated) rat samples (Figure 7.1 and Figure 7.2). The comparison between XPCI-CT and H&E, TRI and Fe stainings allows a validation of the structures visualized with XPCI-CT. Small variations between the structures visible in XPCI-CT and histology images are due to the histologic cutting procedures and a possible angle of misalignment between the two slices.

In the $1.63^3 \mu\text{m}^3$ voxel size XPCI-CT coronal image (Figure 7.1a), the uniform alveolarization of the tissue with regular septa is clearly visualized and blood vessels (yellow arrows, as in all figures of this chapter) and airways (sky-blue arrows, as in all figures of this chapter) of different dimensions are depicted, as validated by histology (Figure 7.1b-d) confirming the absence of pathological signs. At different anatomical levels, based on the appearance of their inner surface, the XPCI-CT technique can distinguish between blood vessels (smooth walls) and airways (wrinkled walls). This can be appreciated in the insets of Figure 7.1a-d, where the development of a bronchiole into alveolar duct and alveolar acini is presented next to a blood vessel. Blood filled vessel appear in XPCI-CT as bright structures and are intense red in H&E images (Figure 7.1b), while airways appear to be empty cavities with green walls in TRI images (Figure 7.1c). The Fe stained histology reveals no pathological areas but only small deposits ($\sim 25 \mu\text{m}$

large) between blood vessels and bronchi walls (Figure 7.1d and related inset). Generally, vessels are blood filled since no perfusion was applied before euthanasia, while airways are paraffin filled.

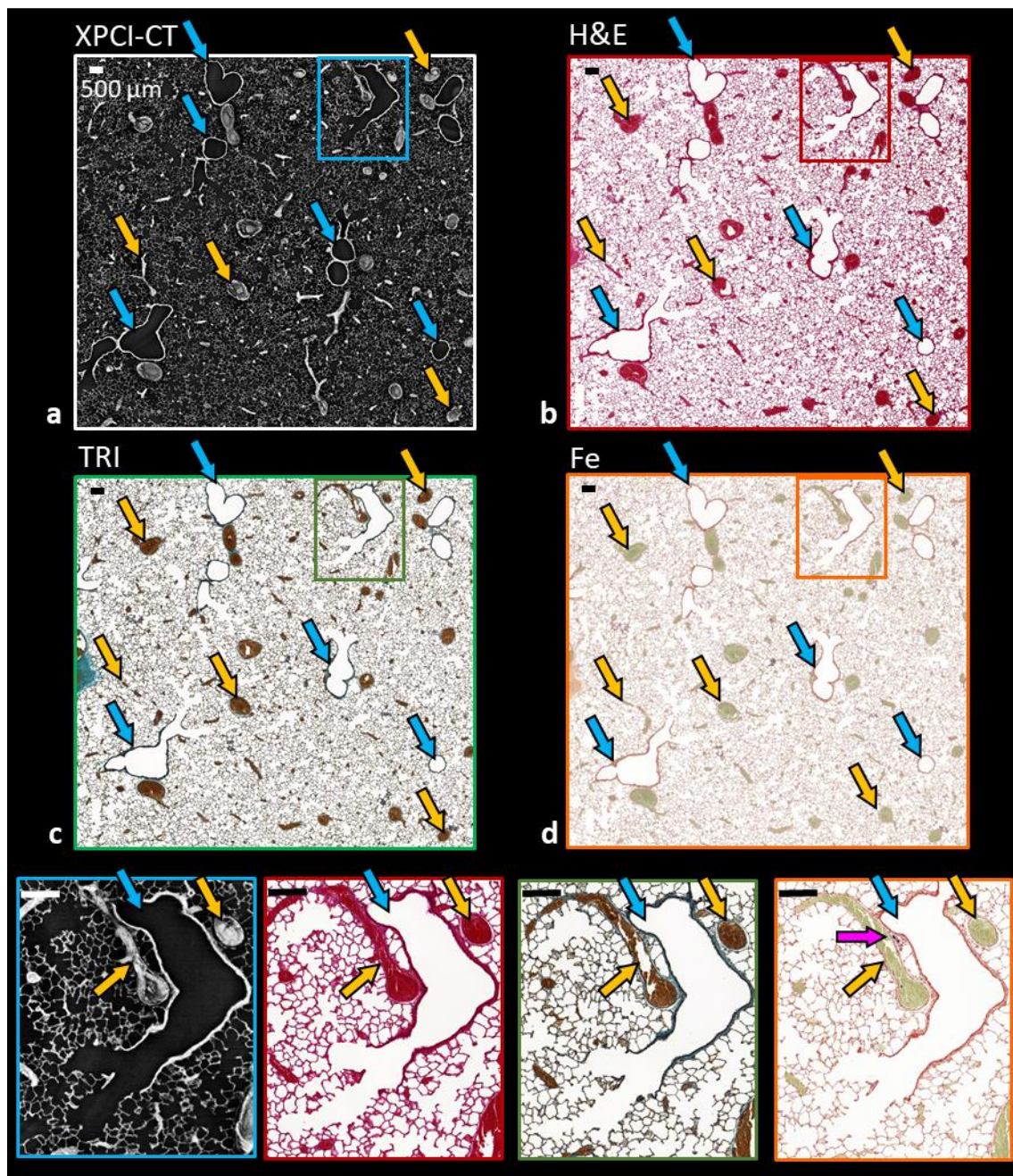


Figure 7.1: XPCI-CT images at $1.63^3 \mu\text{m}^3$ voxel size and histologic comparison for a healthy lung. (a) is a portion of a 3x3 stitched, $1.63^3 \mu\text{m}^3$ voxel size XPCI-CT coronal image displaying vessels and airways of different dimensions on a regular alveolar pattern; (b) the correspondent H&E, (c) the Masson-Goldner trichrome (TRI) and (d) the Fe stained histologic slices. Each inset show, in a magnified view, the development of the bronchioles and the capillaries. The Fe insets reveal the presence of a small Fe deposit developed between the bronchiole and blood vessel walls (magenta arrow) Sky-blue arrows point at the airways, while yellow arrows indicate the blood filled vessels. Figure adapted from (Romano, 2021b).

Figure 7.2a shows a portion of a $1.63^3 \mu\text{m}^3$ voxel size XPCI-CT coronal image of another control lung tissue and Figure 7.2b-d are the correspondent H&E, TRI and Fe stained histologies. Here, a big blood vessel is displayed entangled to a bronchus. The regular alveolar pattern (typical of a normal, non-pathological condition) is better visualized in the magnified insets. The correlation between XPCI-CT and histology given in Figure 7.1 and Figure 7.2 makes it possible to validate the XPCI-CT signal for nonpathological features such as bronchi, vessels and alveoli.

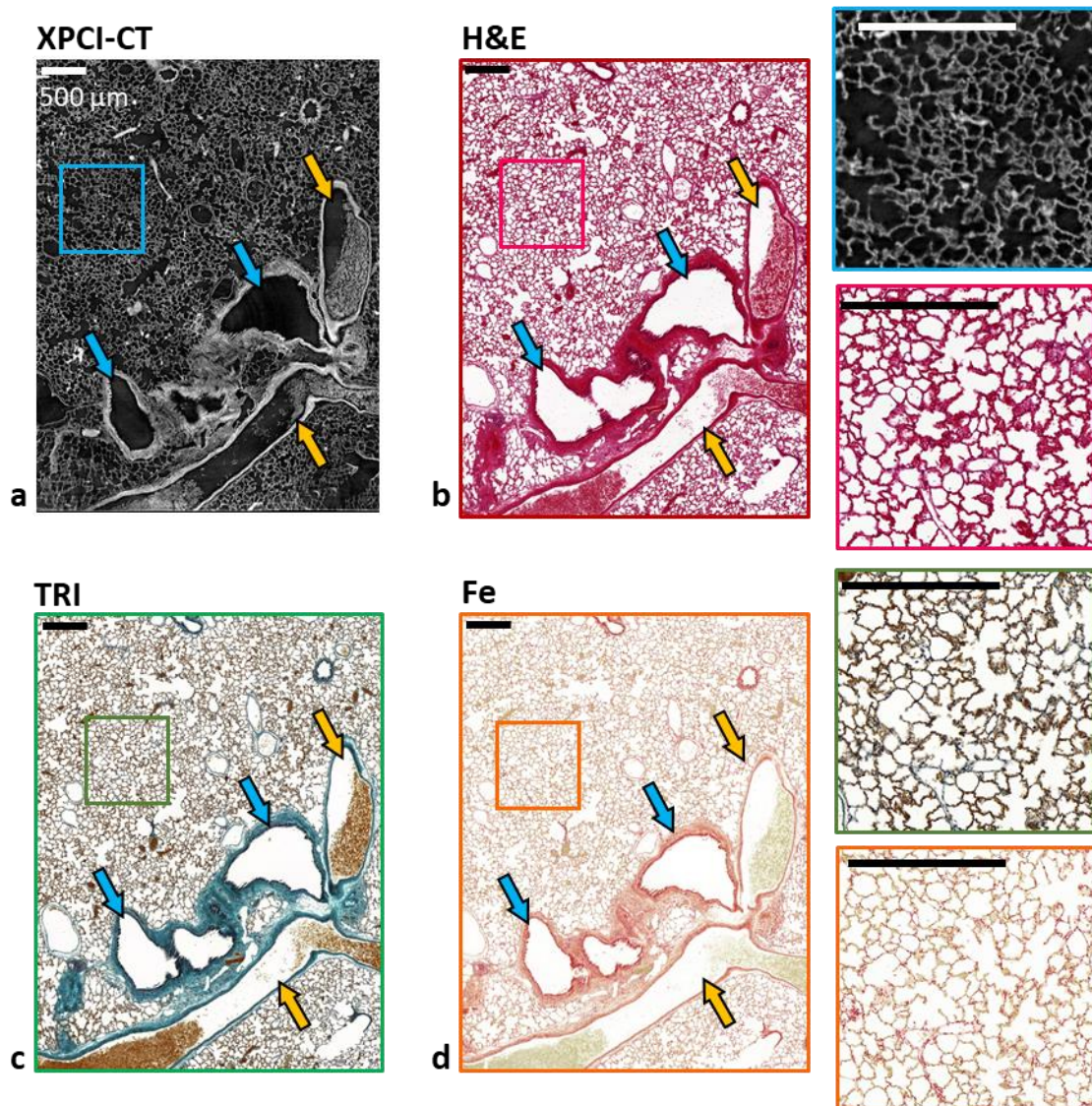


Figure 7.2: a healthy lung sample in a portion of a 4×2 stitched, $1.63^3 \mu\text{m}^3$ voxel size XPCI-CT coronal image (a), H&E (b), Masson-Goldner trichrome (TRI) (c) and Fe (d) histologic stainings allowing the validation of the XPCI-CT signal for alveoli, blood vessels and bronchi. The entanglement of a big blood vessel and an airway is shown, while the insets zoom in the regular alveolar pattern of the sample. Sky-blue arrows point at the airways while yellow arrows indicate the blood filled vessels. Figure adapted from (Romano, 2021b).

7.3 Dose maps for BB, MRT and MB irradiations

The dose maps obtained by means of the hybrid MC method explained in Chapter 3, section 3.3, are reported in Figure 7.3, Figure 7.4 and Figure 7.5 and are displayed on both the axial and sagittal planes. For all the used irradiation geometries, the maps are shown for the highest delivered dose value, i.e. 50 Gy for BBs and 600 Gy-peak for MRTs and MBs. As a showcase, the dose distribution for the BB50 displays, as expected, that the maximum dose is released at the entrance on the skin and decreases with the depth. The dashed lines (Figure 7.3) identify the beam dimensions: a small amount of lateral scattering is registered in the transverse direction to the beam delivery.

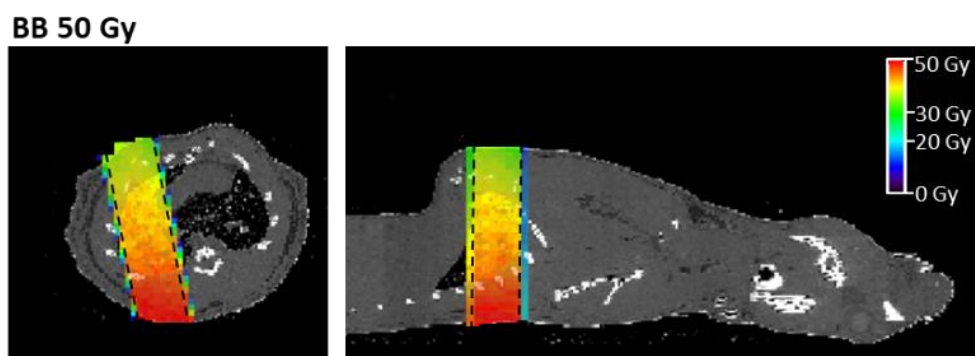


Figure 7.3: dose map for a BB50 irradiated rat displayed on the axial and sagittal planes. The dashed black lines indicate the field of irradiation.

For the MRT600 group, the peak and valley dose distributions are reported separately in Figure 7.4. Due to the fact that the microstructure of the beamlets is not resolved with the hybrid MC calculations, the mean peak distribution over each voxel is obtained and resembles the BB case. The valley dose shows instead a less regular pattern: a background of about half of the nominal valley dose value is scored along the FOI together with small local dose deposition variations within it. Outside the FOI, and in the transverse direction to the beam delivery, which borders are delimited by the dashed black lines, the dose sharply falls to about 30-35% of the nominal value and reaches a value below 1 Gy at a distance of 8 mm from the FOI border in the transverse direction, computed on both the axial and sagittal planes. A small dose fraction is given to a large amount of healthy surrounding tissues.

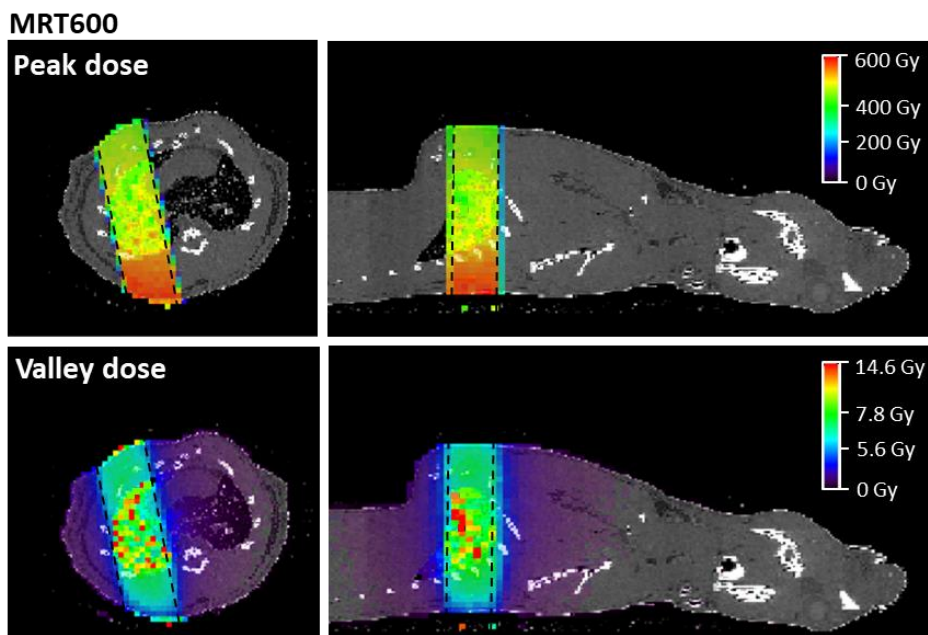


Figure 7.4: peak and valley dose maps for an MRT600-treated rat displayed on the axial and sagittal planes. The dashed black lines indicate the field of irradiation dimensions. The scale bar is reported only once per row.

The MB case is showcased by the MB600 group in Figure 7.5 where the peak dose uniformly decreases with the depth along the beam delivery direction. As for the valley dose distribution, a clear dose enhancement is visible after the beam passes through the bone of the rib cage and a large content of scattered dose is present in the transverse direction, outside the FOI.

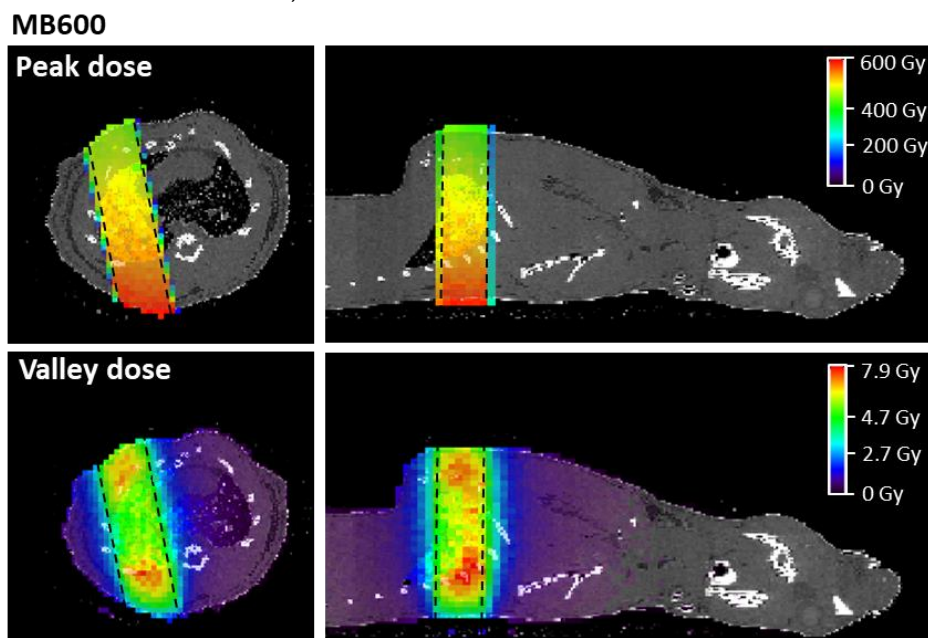


Figure 7.5: peak and valley dose maps for an MB600-treated rat displayed on the axial and sagittal planes. The dashed black lines indicate the field of irradiation dimensions. The scale bar is reported only once per row.

To compare the peak and valleys for the different RTs, a line profile, or depth-dose curve, was obtained with *Amide* and the resulting graphs are shown in Figure 7.6. The MRT and MB peak doses decrease with the depth similarly to the BB deposition, while the MRT and MB valleys have respectively an irregular trend and a double peak shape, due to the dose enhancement after the beam passes the bone.

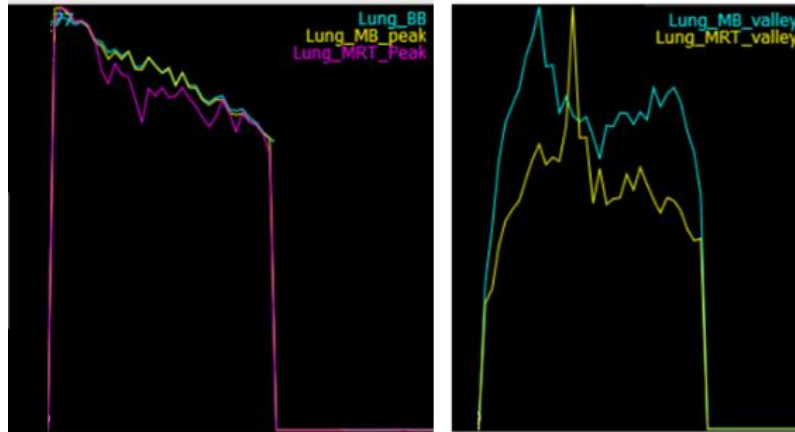


Figure 7.6: depth-dose curves for peaks and valleys computed at the centre of the field of irradiation. The MB and MRT peak doses have a trend similar to the BB dose deposit and uniformly decreases with depth. The MRT and MB valley doses have different behaviour: the MB curve shows two different peaks corresponding to the areas where a dose enhancement is registered, while the MRT curve has a more irregular shape. The curves are normalized to 1 for display purposes.

7.4 Imaging of the effects of MRT on lungs

1.63³ μm³ voxel size XPCI-CT images of MRT treated rat lungs are reported in Figure 7.7, Figure 7.8 and Figure 7.9. Within those samples, as confirmed by histology, only isolated scars with Fe mineralization are visible together with some collagen noduli and the calcification of the vessel endothelium. The tissue anatomy of all the three examined MRT50-treated lungs appear very similar to the one of control animals: no significant evidence of the irradiation was found (see Figure 7.7a). The effects of the irradiation with MRT100 on the lungs are shown in the XPCI-CT coronal image in Figure 7.7b: overall the tissue appears as healthy exception made for the presence of a small collagen nodulus (volume of $\sim 2 \cdot 10^{-3}$ mm³) as proved by H&E histology (insets of Figure 7.7b). Within the same specimen, another nodulus of similar dimensions was found. These two collagen noduli both grow in the vicinity of a blood vessel (yellow arrows in Figure 7.7b).

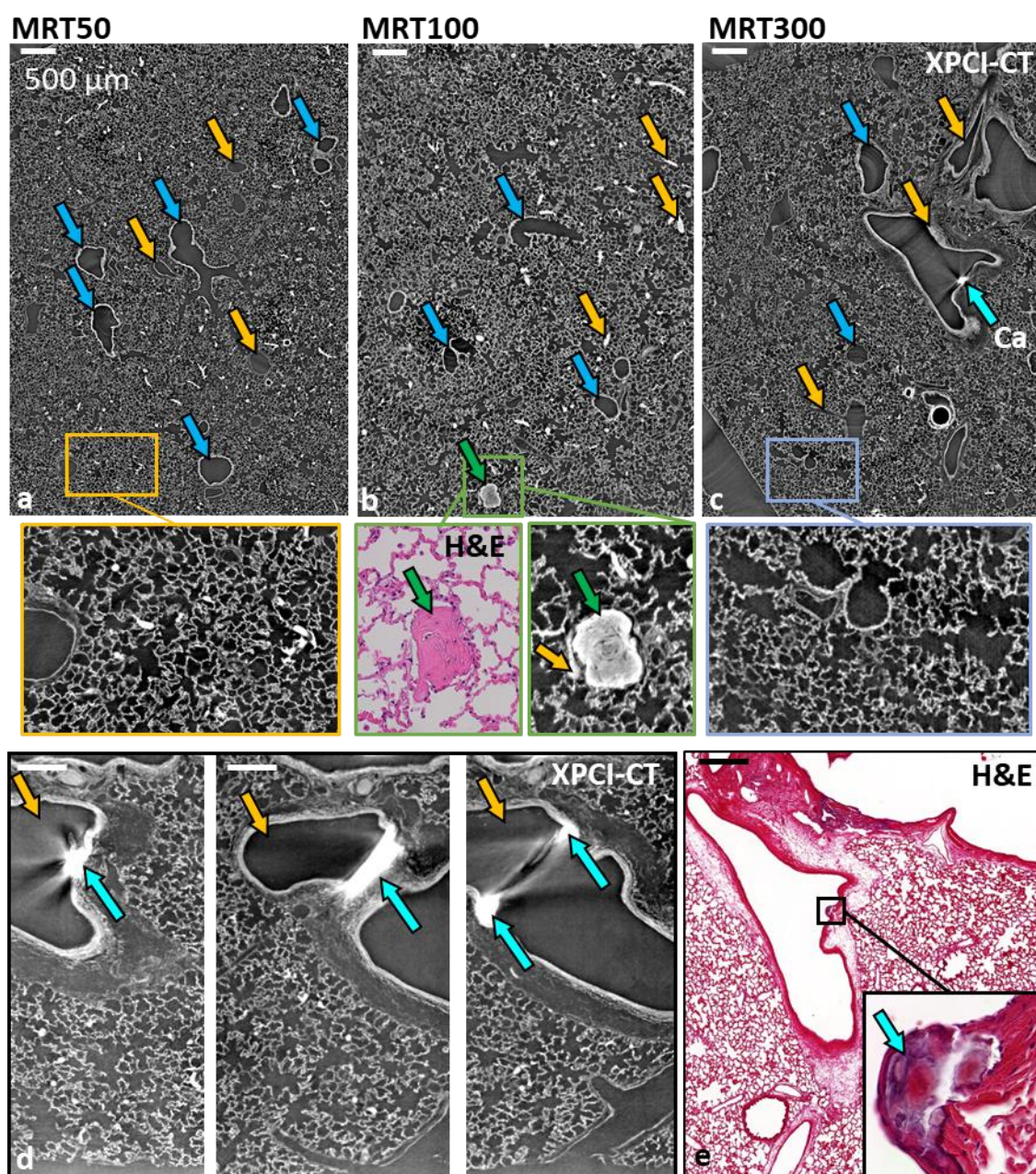


Figure 7.7: MRT irradiated samples with 50, 100 and 300 Gy as peak dose imaged at $1.63^3 \mu\text{m}^3$ voxel size. Subfigure (a), (b) and (c) show portions of a stitched, $1.63^3 \mu\text{m}^3$ voxel size XPCI-CT coronal image of an MRT50, MRT100 and MRT300 sample respectively. The tissue structures of the three samples are comparable with the healthy ones, exception made for a specific feature for the last two samples. The insets of each figure show a normal alveolarization in all the cases and a collagen nodule found in the MRT100 sample pointed by a green arrow and validated with its respective H&E histology. The blood vessel it is entangled with, is indicated with a yellow arrow. The inset of (c) reports the replacement of a portion of endothelium by a calcification. (d) show the same feature at three different depths on the sagittal plane. The H&E histology in (e) confirms that the structure found in (c) is a calcium deposit produced by the impinging radiation on a blood vessel. Cyan arrows indicate the calcification, yellow and sky-blue ones are for the blood vessels and airways. Figure adapted from (Romano, 2021b).

Figure 7.7c-d represent an MRT300-treated specimen. In the coronal image in Figure 7.7c the only feature recognizable as an effect of the treatment is a hyperdense structure laying on the endothelium of a blood vessel. The H&E histologic analysis (Figure 7.7e) identifies this dense structure as a calcification that replaced a part of the endothelium. This is a clear sign of a radiation-induced damage that can be followed in 3D along the endothelium, as shown in the sagittal planes at three different depths within the sample (Figure 7.7d). In each of these figures, we see a blood vessel and some calcifications that appear as white spots (cyan arrows) indicating that the feature is much denser than the surrounding tissue. The streak-like artefacts on the image background originate from the abrupt variation in the refractive index between the soft tissue and the calcification.

XPCI-CT images in Figure 7.8 and Figure 7.9 showcase the radiation-driven features detected in one of the samples of the MRT600 group. The $1.63^3 \mu\text{m}^3$ voxel size XPCI-CT coronal image (Figure 7.8a) shows isolated scars (red arrows) within the lung tissue. Images in Figure 7.8a'-a''' report, respectively, the 3x zoom of the scar visible in the centre of Figure 7.8a (green dashed box), its axial view and a $0.65^3 \mu\text{m}^3$ voxel size XPCI-CT coronal image of the same feature at a different depth with respect to Figure 7.8a within the lung tissue. The fibrotic nature of the visualized scars is validated by the TRI histology of Figure 7.8b. The intra-scar Fe deposits, as identified by histology (inset of Figure 7.8b), are pointed out by magenta arrows and appear as blue after Fe staining. Other visible effects of the irradiation in this group are the thickening of the alveolar septa (Figure 7.9a and corresponding TRI histology in Figure 7.9a') and again the formation of collagen noduli, as visualized with high detail in the $0.65^3 \mu\text{m}^3$ voxel size CT images in Figure 7.9b-b''. Those subfigures show the same CT slice with and without phase retrieval and for the latter case, with two different windowing. The noduli structure appears different among these images. In the no-phase retrieved image (Figure 7.9b) the edges of the nodulus and of the different morphological details (such as alveoli and vessels) are enhanced and visible at once. The phase retrieved images provide a better area contrast and depending on the windowing adjustment, it is possible to clearly visualize either the collagen part and cells (small dark spots) of the nodulus (Figure 7.9b') or the surrounding tissue (Figure 7.9b'').

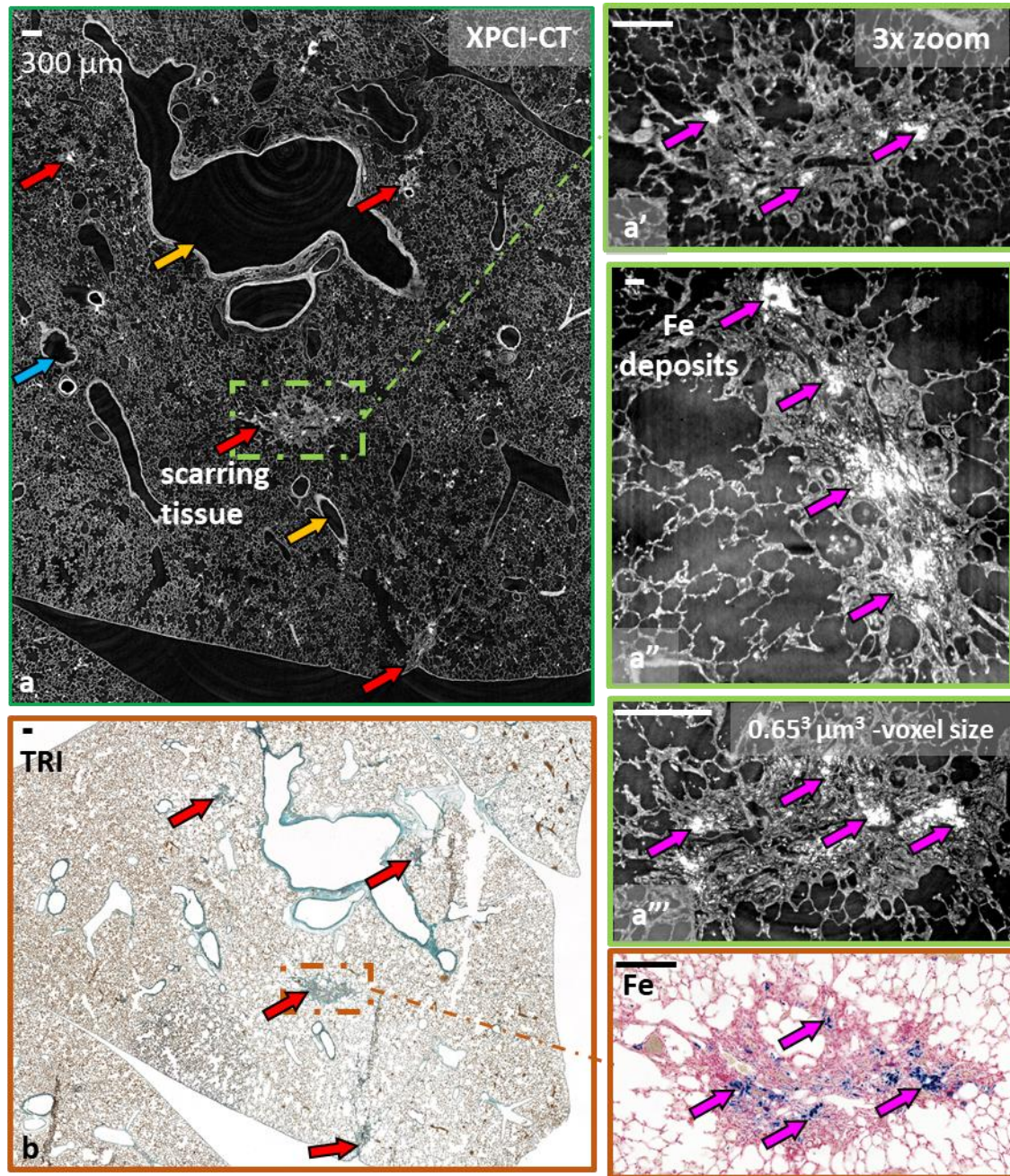


Figure 7.8: MRT600 treated rat. All the CT images are taken with $1.63^3 \mu\text{m}^3$ voxel size, if not differently specified. (a) is a 3×3 stitched, $1.63^3 \mu\text{m}^3$ voxel size XPCI-CT coronal image: the tissue has only few signs of the irradiation as isolated scars indicated by the red arrows. The central scar englobes some hyperdense structures as pointed out by the magenta arrows in the 3x zoom in (a'), in a reslice along the axial plane (a'') and in a $0.65^3 \mu\text{m}^3$ voxel size coronal image of the same scar at a different depth in the tissue. The Masson-Goldner trichrome (TRI) histology (b) of the same lung tissue area of (a) shows collagen structures, and thus fibrotic tissue, where XPCI reveals scars. Its inset is an Fe-stained histology labelling the hyperdense structured detected by XPCI-CT images as Fe deposits. Sky-blue and yellow arrows are for the airways and blood vessels. Figure adapted from (Romano, 2021b).

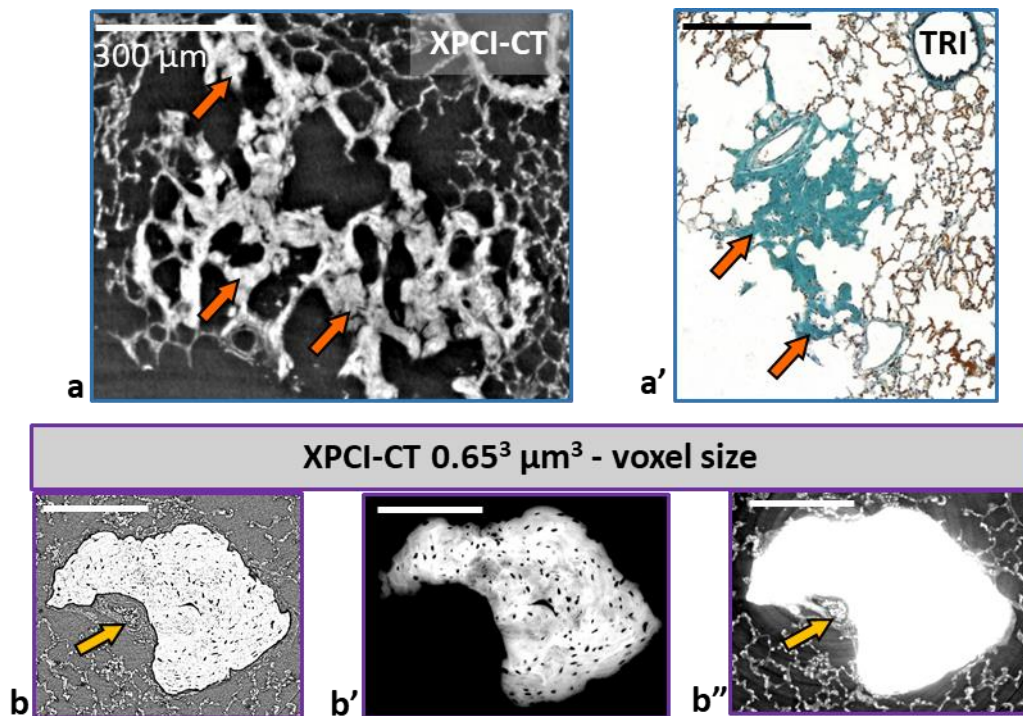


Figure 7.9: Alveolar wall thickening (a-a') and collagen nodule (b-b'') detected for an MRT600 treated rat. (a) and (a') are a portion of a 1.63³ μm³ voxel size XPCI-CT coronal image and the Masson-Goldner trichrome (TRI) histology, respectively for thick alveolar walls (orange arrows). (b), (b') and (b'') are respectively the reconstruction in absorption mode and phase retrieved XPCI-CT with two different windowing of a collagen nodule, where the small dark spots are cells and yellow arrows point at the blood vessel entangled to the nodule. Figure adapted from (Romano, 2021b).

7.5 Imaging of the effects of MB on lungs

Findings in the lung samples of rats irradiated by MB are reported in 1.63³ μm³ voxel size XPCI-CT images of Figure 7.10-Figure 7.12. An extended scarring area within the tissue of a MB50-treated rat lung is visible in the coronal image in Figure 7.10a (red arrow) together with its 2x zoom inset. The complete rearrangement of the alveolar spaces and the septa thickening are depicted, while, in the rest of the sample, the overall structure of the lung tissue seems preserved and looks similar to the one of control rats (Figure 7.1 and Figure 7.2). In the coronal XPCI-CT image in Figure 7.10b, a large blood vessel within a sample belonging to the MB100 group is observable. This image includes four dense structures on the endothelium layer (cyan arrows) that can be identified as Ca formations as in Figure 7.7. The cyan arrows indicate the direction of the MB paths, i.e. the two parallel lines lying horizontally on the coronal plane, along which calcifications are visible.

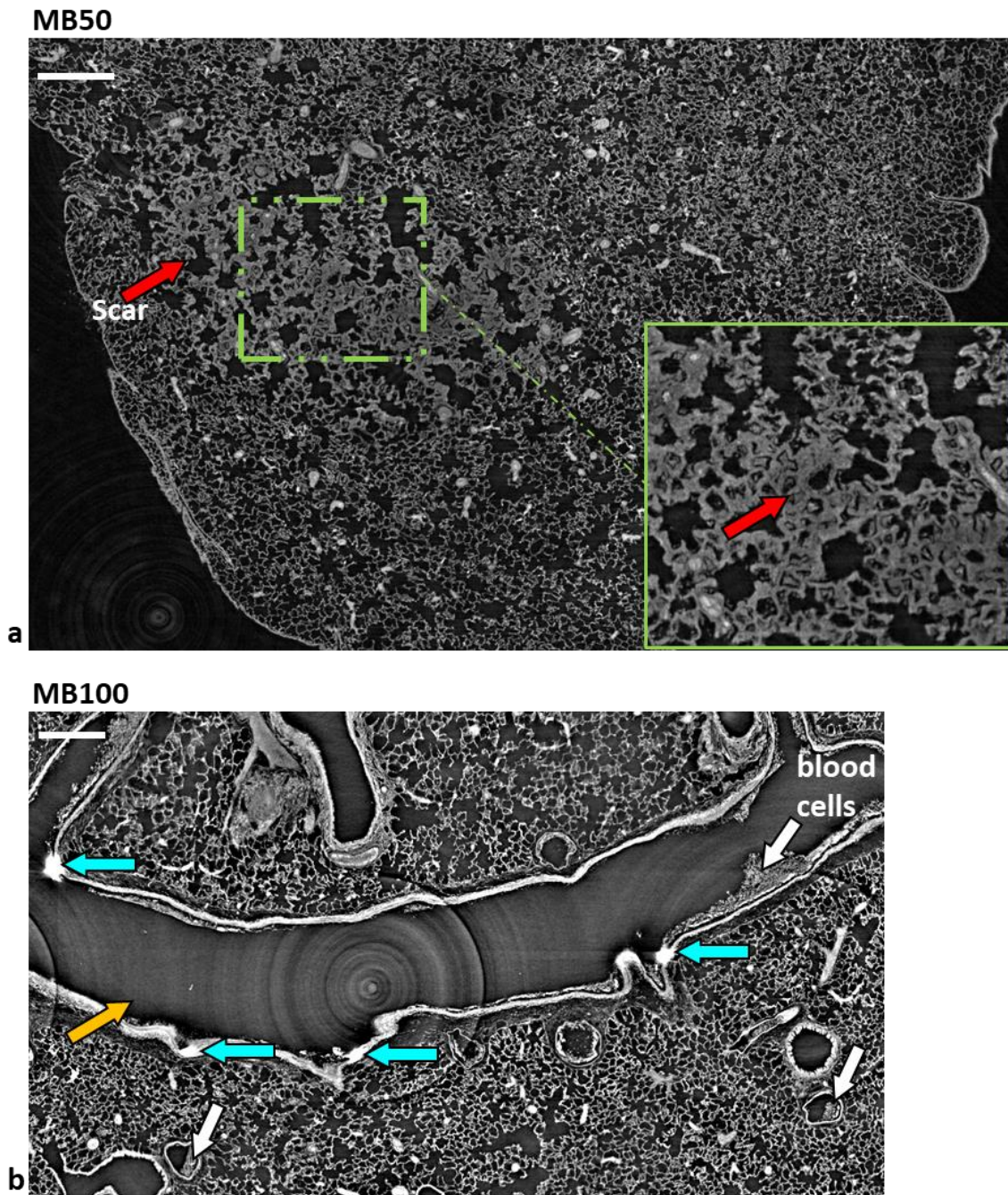


Figure 7.10: MB-treated samples with 50 and 100 Gy as peak dose. (a) is a portion of a 6x4 stitched, $1.63^3 \mu\text{m}^3$ voxel size XPCI-CT coronal image of a MB50 irradiated sample. The red arrow indicates an extended scar on the tissue and its 2x zoom in the inset better shows the thickening of the alveoli septa. The calcifications of a blood vessel caused by the impinging of a 100 Gy-peak minibeam on the epithelium layer is reported in (b) on a portion of a 4x3 stitched, $1.63^3 \mu\text{m}^3$ voxel size XPCI-CT coronal image. Each calcification is pointed out by a cyan arrow indicating the direction of the beam delivery. The white arrow shows some blood cells left inside the vessel, which is indicated by the yellow arrow. Figure adapted from (Romano, 2021b).

Figure 7.11a shows a $1.63^3 \mu\text{m}^3$ voxel size XPCI-CT coronal image of a sample of the MB300 group. The deep-pink arrowheads help identifying the stripe-scars that are also evident in the TRI histology of Figure 7.11b, where collagenous, green stained, scars are visible. Figure 7.11 reports only two out of the three MB scars and the magnified view in the XPCI-CT inset shows the details within the scar.

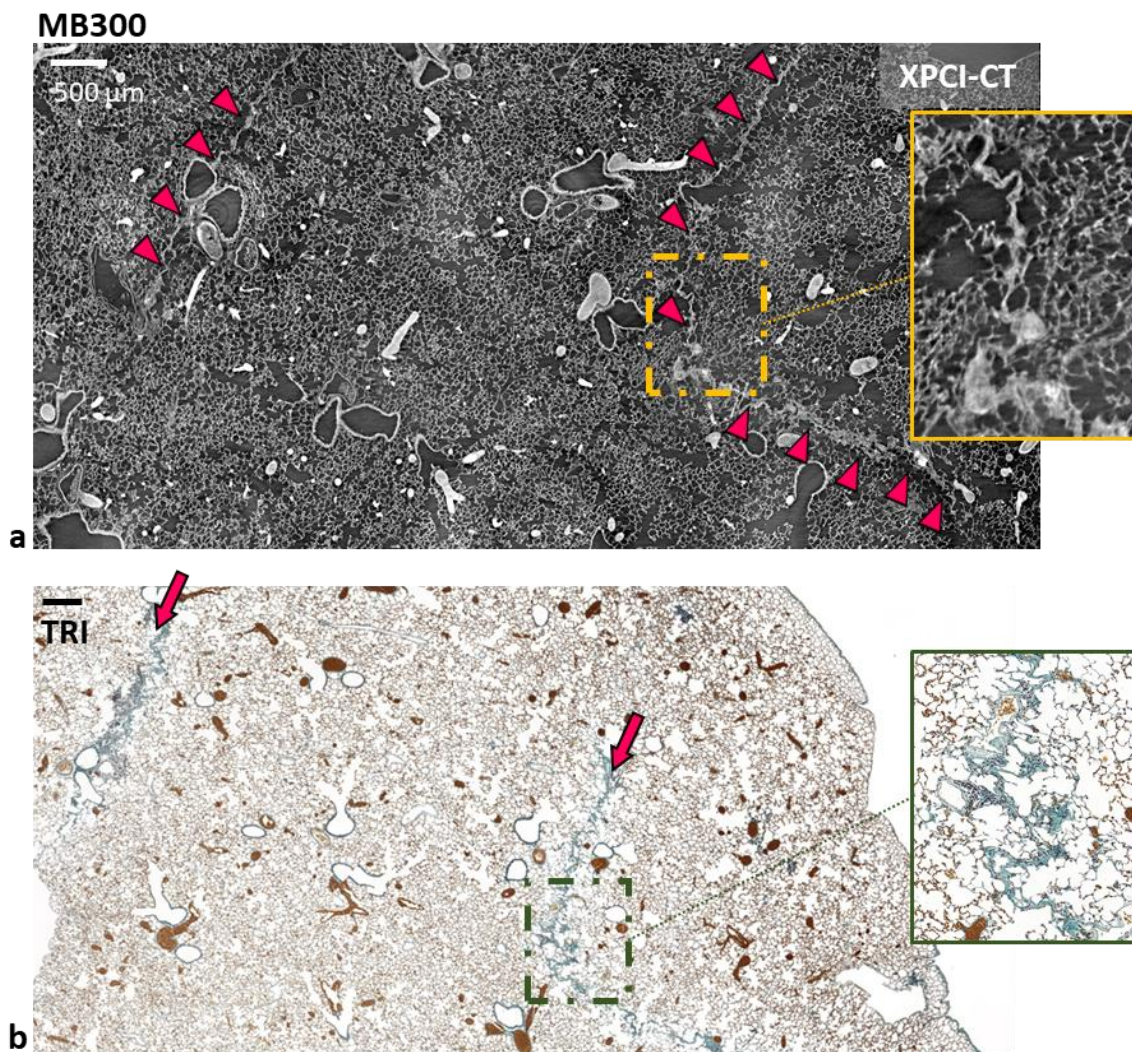


Figure 7.11: effects of the MB300 irradiation on healthy lung. (a) is a portion of a 2x4 stitched, $1.63^3 \mu\text{m}^3$ voxel size XPCI-CT coronal image of a MB300-treated lung showing two of the three minibeam paths as stripe-shaped scars and (b) is its TRI histology confirming the presence of fibrotic tissue in the scars. The 3x zoom inset are a magnification of the scarring tissue produced by a 500 μm-wide minibeam. Figure adapted from (Romano, 2021b).

In the XPCI-CT coronal image of a MB600 irradiated lung (Figure 7.12a) all the minibeam paths are visible as stripe-shaped scars that develop straight in depth as visualized in the oblique reslicing (Figure 7.12b). In some cases, as also visible

in the showcases of the MB300 and MB600 groups, minibeam scars do not appear always as a straight line but as “bent” (“L”- shaped). The scars due to the minibeam are recognizable within the tissue in the TRI histologies as green structures (Figure 7.12c), while the Fe-stained histology (Figure 7.12d) reveals the presence of Fe deposits within the scars, validating the bright XPCI-CT signal of (Figure 7.12a-b).

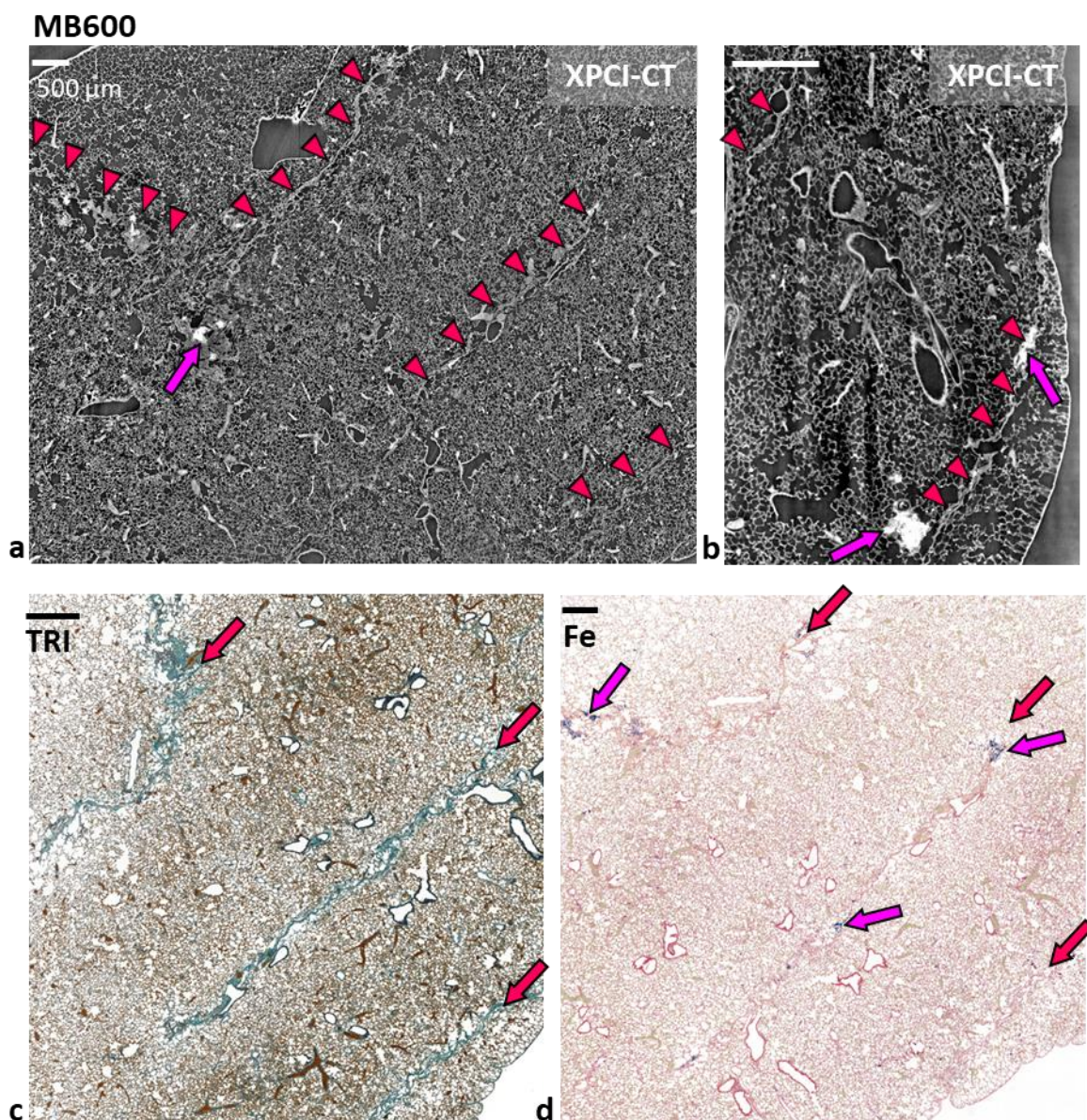


Figure 7.12: XPCI-CT and histologic comparison for a MB600-treated lung. (a) is a 3x2 stitched, $1.63^3 \mu\text{m}^3$ voxel size XPCI-CT coronal image where the three MB paths are visible; (b) is its oblique reslice that clarifies how the scars develop in depth throughout the sample. Some Fe contents are visible and indicated by magenta arrows. The deep-pink arrowheads are placed next to the stripe-scars to help in their visualization. (c) and (d) are the TRI and Fe-stained histology of the XPCI-CT coronal image confirming the presence of fibrotic tissue and intra-scar Fe deposits. Figure adapted from (Romano, 2021b).

7.6 Imaging of the effects of BB radiotherapy on lungs

The lung tissue alterations due to BB irradiation with doses of 30 and 50 Gy are reported in Figure 7.13 and Figure 7.14, respectively. The scarring tissue induced by irradiation with BB30 is shown on the coronal and sagittal images in Figure 7.13a-b. The irradiated tissue presents a quasi-uniform alveolarization with scars appearing in limited regions and the 3x zoom image in the inset of Figure 7.13a reveals a thickening of the alveolar walls with respect to the case of healthy alveoli (see Figure 7.2). In the sagittal view, it is possible to observe an extended tissue damage appearing as a reshaping of the alveolar spaces (white arrows).

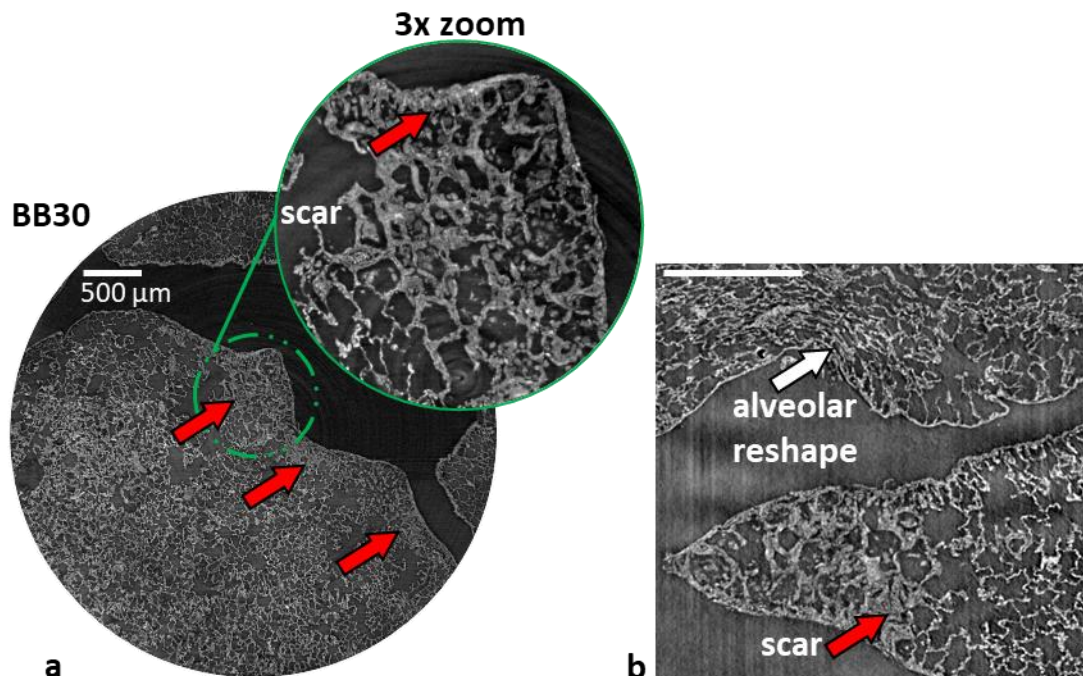


Figure 7.13: BB30 irradiated lung imaged at $1.63^3 \mu\text{m}^3$ voxel size on a coronal (a) and sagittal (b) view. The scarring tissue is pointed out by the red arrows and emphasized in the 3x zoomed inset, while the white arrow indicates a general alveolar rearrangement. Figure adapted from (Romano, 2021b).

Figure 7.14 presents XPCI-CT data of lung tissue irradiated with BB50: a more invasive damage is visible with respect to the 30 Gy case. The morphological changes within the lung tissue are clearly discernible in XPCI-CT images: the interface and discontinuity between the irradiated and non-irradiated portions of the tissue is marked by the dashed red line in Figure 7.14b. In the irradiated region, the alveolar sacs are destroyed and the typical regular tissue structure is lost. Within this scarring tissue, highly absorbing features are detected (magenta

arrows), identified as Fe deposits by the correlation with histology. The non-irradiated portion of the tissue presents more regular alveoli and septa similarly to the control cases. The reslicing (Figure 7.14c) of the XPCI-CT dataset, obtained along the cyan line of Figure 7.14a, shows that the scar presents thicker alveolar walls on the surface of the sample. As we move inside the lung, another highly absorbing feature (green arrow) is visible. By adjusting the image windowing (inset of Figure 7.14c), it is possible to recognize the inner structure of a collagenous nodulus.

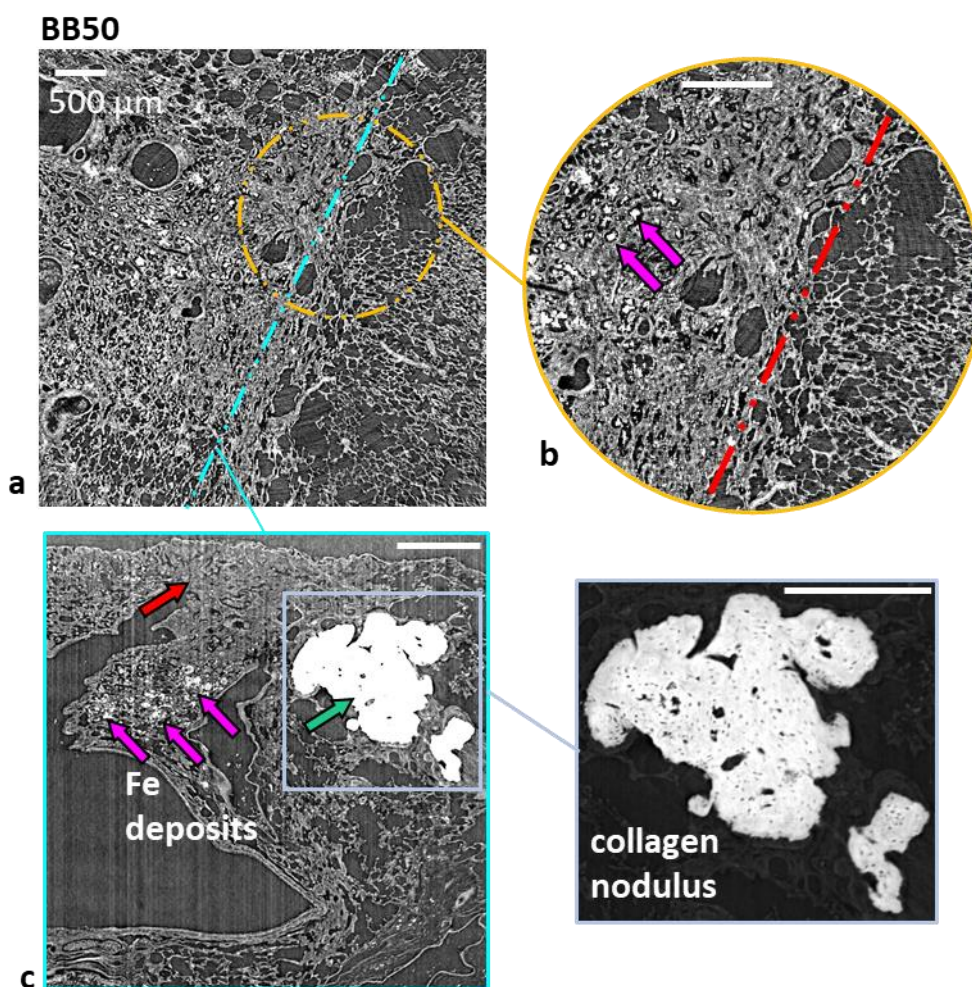


Figure 7.14: BB50 irradiated sample XPCI-CT images at $1.63^3 \mu\text{m}^3$ voxel size. In the coronal view (a) a sharp discontinuity between irradiated and not irradiated tissue is visible. The 2x zoom (b) goes into the details of the edge between the two zones, which is identified by the red dashed line, and of the presence of Fe deposits indicated by the magenta arrows. (c) is the reslicing of (a) along the cyan line and reveals the presence of a collagen nodulus (green arrow), fibrotic tissue (red arrow) and several Fe deposits distributed in depth (magenta arrows). The collagen nodulus is reported in the inset of (c) with a different windowing to reveal its inner structure. Figure adapted from (Romano, 2021b).

7.7 Segmentation of the scarring tissue

The quantification of the total amount of fibrotic tissue over the available imaged volume was performed following 3D segmentation and rendering of the segmented scars over the surrounding tissue (Figure 7.15a). The segmentation discriminated both the extended scar produced by a BB, isolated spot-like and planar shaped scars typical of MRT and MB, respectively.

One representative sample per group was chosen to build a chart of the fibrotic tissue detected over the full imaged volume of Figure 7.15b. The plotted values are reported in Table 7.1 as a percentage of the scarring tissue over the imaged lung volume to get rid of the differences of imaged volumes among the samples.

Table 7.1: values for one representative sample per group of the segmented scarring volume within the area imaged with XPCI-CT at $1.63^3 \mu\text{m}^3$ voxel size.

Group name	Fibrotic tissue content (%)
BB30	1.55 ± 0.08
BB50	34.1 ± 1.7
MRT50	0
MRT100	0.0045 ± 0.0002
MRT300	0
MRT600	1.23 ± 0.06
MB50	0.30 ± 0.02
MB100	0
MB300	2.01 ± 0.10
MB600	8.4 ± 0.4
Controls	0

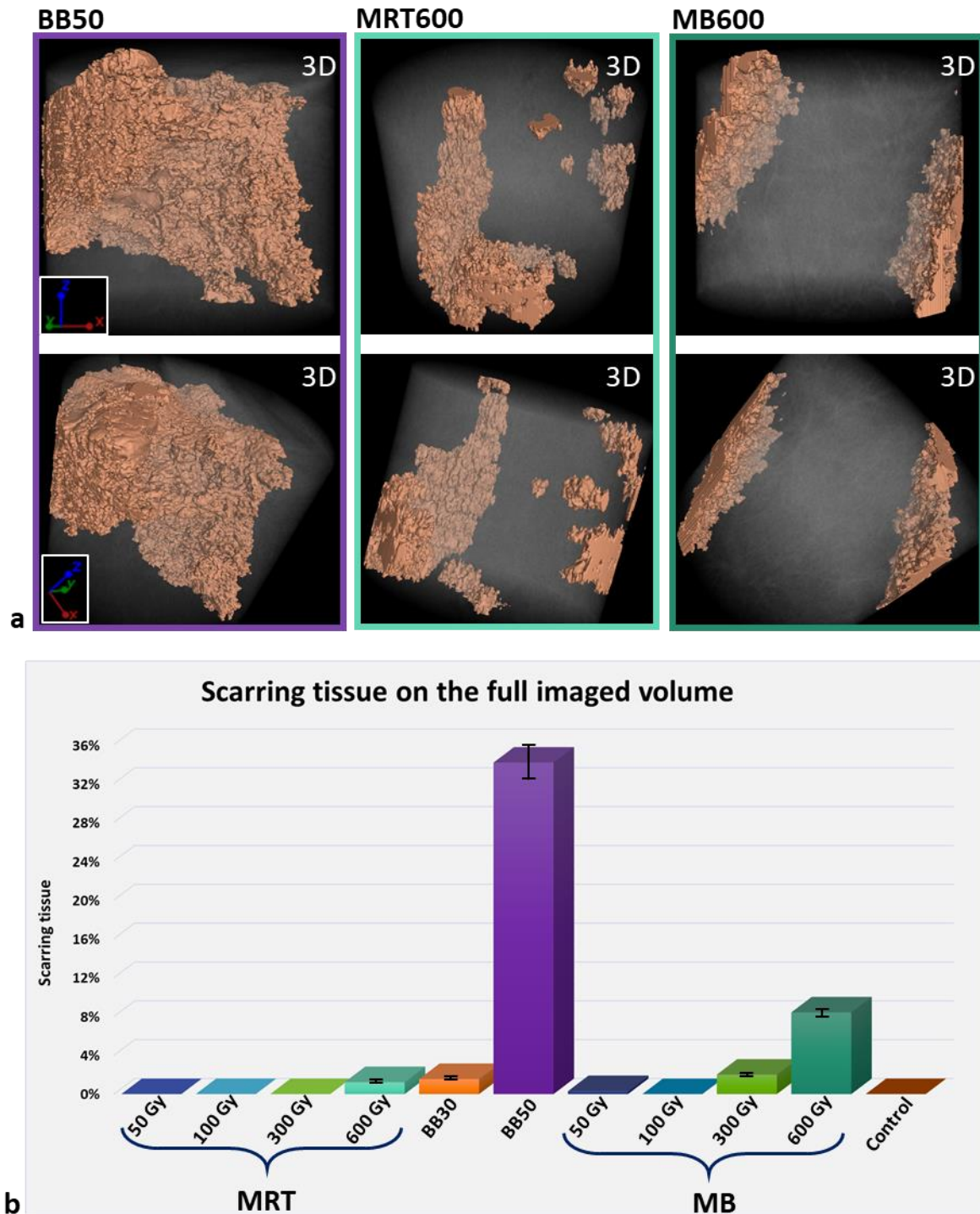


Figure 7.15: scarring tissue 3D representation and graph of the total fibrotic tissue quantification for a representative sample for each radiotherapy protocol. (a) 3D rendering of a BB50, MRT600 and MB600 lung specimen showing, in two different orientations, how the fibrotic tissue is distributed within the imaged lung portions for the different cases. The fibrotic content is displayed as solid and coloured feature, while the rest of the sample is shown in a transparent grey modality. BB only produces one extended clustered scar, MRT treated lung shows isolated small scars while for the MB specimen the planar shape of the fibrotic tissue is visible. (b) reports the total amount of segmented fibrotic tissue as a percentage of the total available volume. One representative sample was chosen for each group to build the graph. Figure adapted from (Romano, 2021b).

Errors were assessed by repeating the segmentation for one sample per RT geometry (BB, MRT and MB) for three times during different days. The average error was estimated to be the 5% of the segmented volume. The obtained results confirm that the BB50 irradiated samples are the ones showing the largest amount of fibrotic tissue while for MRT and MB treated samples, the highest peak doses produce the severest damage.

7.8 Discussion

XPCI-CT enables 3D imaging of lung tissue from full organs down to a sub-micrometric resolution, showing, with high detail, the tissue anatomy from alveolar volumes down to acini levels (Figure 7.1 and Figure 7.2). Airways and blood vessels can be followed in 3D and alveolar septa are clearly resolved. The high detail of lung XPCI-CT data allow for sophisticated 3D quantitative examinations (Broche, 2019) enabling as well saccular volume computation and topological analysis of the air-to-tissue surface (Lovric, 2017b). *Post-mortem* semi-quantitative XPCI-CT was applied as a label-free density-based 3D morphological technique for high resolution and high sensitivity lung imaging. The distinctive effects on the tissue following the administration of RTs characterized by different beam geometries were investigated and visualized.

This study shows for the first time XPCI-CT data of the effects of BB, MRT and MB RTs on lung tissue delivered *in-vivo* using both $1.63^3 \mu\text{m}^3$ and $0.65^3 \mu\text{m}^3$ voxel size XPCI-CT images with a resolution similar to histology, demonstrating the high diagnostic power of this technique. Overall, the $1.63^3 \mu\text{m}^3$ voxel size allows detecting and distinguishing several features within the irradiated tissue, while the $0.65^3 \mu\text{m}^3$ voxel size images show the same details but with an increased quality of the image in terms of sharpness. Nevertheless, the FOV of CT images decreases as the spatial resolution increases and $1.63^3 \mu\text{m}^3$ voxel size was found as the optimum compromise between image quality and FOV for rat lung tissue analysis.

XPCI-CT showed that BB irradiation induces scars within the treated lung areas with extending dimensions as the dose increases. Overall, the alveolarization appears less regular in BB-irradiated lung with respect to control tissues (Figure 7.13 and Figure 7.14 vs Figure 7.2). The interface between the irradiated and not-irradiated areas is clearly demarked as a sharp edge in the BB50 case (Figure 7.14).

Indeed, the dose map for the BB group shows a sharp falloff for the lateral dose distribution (see Figure 7.3 and Figure 7.6). The collagen nodule of the BB50 sample in Figure 7.14c is ~ 10 times bigger than those detected in the MRT and MB-treated lungs, thus confirming that **the BB irradiation at 50 Gy is the most aggressive among the here presented treatments**. This result is also confirmed by the fibrosis segmentation study, of which graphical representation is given in Figure 7.15a and by the histogram of Figure 7.15b showing that the BB50 irradiation produces the largest fibrotic content within all the considered cases.

As shown in Figure 7.7 - Figure 7.9, **the MRT irradiation causes isolated scars with Fe deposits and small collagen noduli within the tissue**. All the MRT50-treated lungs are comparable, in terms of alveolar shape and dimensions, to the control samples, while MRT100 lungs only show radio-induced collagen noduli. Two out of the three specimens of the MRT300 group are also comparable to controls in terms of tissue morphology; only one lung tissue presents an extended calcification that replaced a portion of the endothelium on a blood vessel (Figure 7.7d). The three rat lungs irradiated with MRT600 contain scars, Fe particles, collagen noduli and thicker alveolar septa (Figure 7.8 and Figure 7.9) if compared to the healthy tissues. **In all the MRT-treated samples no microbeam paths are detected**; given the fact that all the animals have been sacrificed 12 months after the irradiation, **this could be a sign that lung tissue can repair micrometric damages** without showing extended scarring or damaged tissue even if the delivered dose is locally up to hundreds of Gray.

With respect to MRT-irradiated lungs, the effects on MB-treated tissues are found to be more pronounced. Even when using 50 Gy, i.e. the lowest peak dose, collagen noduli, blood vessel calcification and scarring tissue are clearly visible in all the examined specimens and, **as the dose increases, MB paths become progressively more noticeable as stripe-shaped scars** (Figure 7.11 and Figure 7.12). Here, the scars prevalently have a straight planar shape if visualized in 3D. Nevertheless, in few cases it is possible to observe a folded stripe-MB path: these distortions are likely due to the sample manipulation during the extraction and fixation procedures. In principle, all the MB-induced scars should present a planar shape reproducing the straight path of the delivered X-ray beam array. However, in some cases, this forecast is not met for *ex-vivo* images since the sample under-

went some local morphological alterations during the extraction and fixing procedures that are detectable with the accuracy provided by XPCI-CT. The great advantage upon histology is that XPCI-CT is a dissection-free technique that does not need further tissue manipulation after the fixing procedure. Hence, the used technique is free from tearing and stretching artefacts caused by the tissue cutting and can retrieve the information of the sample manipulation, while histology, requiring the tissue to be cut in thin slices, is affected by additional artefacts and could lack in providing some information that can only be given with a 3D virtual histology method. While XPCI-CT technique provides great and highly detailed anatomical representation of full specimens, its signal is biologically nonspecific and can only differentiate and delineate with accuracy structures on the basis of their electronic density difference. Correlation with standard histology is a crucial step in the analysis process, which can help identifying the nature of unknown structures. This is important in particular in the training phase of XPCI-CT data interpretation. Furthermore, **XPCI-CT can be exploited to identify and accurately localize the region of interest within the fixed samples without sample sectioning**. This knowledge could then guide the following examination via histology limiting the sectioning and staining procedures only to the part of interest.

The quantification study based on the segmentation of the fibrotic tissue gives clear evidence on how XPCI-CT enables an accurate 3D rendering of the effects of the radiation on lungs and allows enhanced visualization and characterization of the features of interest e.g. fibrosis within the full organ. Furthermore, this 3D full organ analysis confirms that **the irradiation geometries that impact the most the healthy tissue are BB50, BB30, MRT600 and MB with 300 and 600 Gy as peak doses**, as reported in Wright et al. (Wright, 2021). Overall, XPCI appears as a technique that allows imaging soft tissues and especially lungs at high spatial and contrast resolutions and shows the potential to become a complementary and/or alternative tool to standard histology and premises for *in-vivo*, full organ coverage method for disease and treatment monitoring filling the gaps of the currently available lung imaging techniques, as discussed in Chapter 1.

7.9 Limitations of the study

Overall, the main limitation of the study is that lungs were not extracted in a standardized way, i.e. using an *in-situ* fixation via vascular perfusion while held at 20-25 cm H₂O airway pressure (Weibel, 1984; Hsia, 2010). A non-standard lung extraction causes the collapse of the alveolar sacs. Therefore, the quantification of alveolar spacing remodelling caused by the different radiotherapies could not be studied and considered as a reliable parameter for the assessment of the severity of RT side-effects.

Furthermore, the XPCI-CT imaged volume does not cover the full lung organ (and different imaged volumes are obtained for each sample) due to the fact that samples were imaged with XPCI-CT after undergoing some standard analysis procedures e.g. histology, which is sample destructive.

7.10 Conclusion and future perspectives

This study proves that the used methodology allows visualizing *ex-vivo* with high contrast and detail and in 3D radiation-driven features specific of the delivered beam configurations in lungs. It was possible to recognize RT-induced stripe-shaped scars, alveolar wall thickening, fibrotic tissue as collagenous structures and hyperdense structures corresponding to be Fe deposits and calcifications on blood vessels, as validated by histological analysis. Thus, XPCI based virtual histology, when included in the workflow of pathological assessment of tissue samples currently performed by means of standard histology, is able to quantify fibrotic lesions within the lung organ. Providing that standard histology is the gold standard for the identification of the imaged structures, XPCI-CT can give the complementary information of a 3D detailed anatomical and structural view of the sample and can act as a guidance tool for conventional histology owing to its 3D capabilities and the possibility of virtually navigating within samples.

Proven that MRTs and MBs are well tolerated by healthy tissue up to 600 Gy of peak, this study puts the basis for an *ex-vivo* investigation on the effects and the curing power of MRT and MB RTs applied to lung cancer, but the method has the potential for *in-vivo* XPCI-CT investigations, which are already part of the long-term perspective of this research.

Conclusions

The scientific investigations carried out within this Ph.D. Thesis had the overall common objective of developing an accurate 3D imaging-based methodology, complementary to standardly used analysis tools, for the follow-up of the efficacy of novel radiotherapies (RTs) in small animal models. X-ray Phase Contrast Imaging - Computed Tomography (XPCI-CT) is here proposed as an imaging technique that can distinguish and identify, with high sensitivity and at multiple spatial resolutions (down to sub-micrometre), the side effects of spatially fractionated vs conventional broad beam RTs. XPCI-CT has been used in combination with other techniques, such as Magnetic Resonance Imaging, histology, immunohistochemistry, Small- and Wide-Angle X-ray Scattering and X-ray fluorescence, with the objective of helping and validating the data interpretation as well as of obtaining a complete (morphological, structural and elemental) characterization of the radio-induced side effects on rat brains and lungs. A full pipeline of experimental and data processing procedures has been designed, tested and implemented to establish a solid methodology that can bring complementary valuable information in serving preclinical radio-oncology research.

The main results obtained in this Thesis can be summarized as follows:

1. **XPCI-CT produces highly detailed and contrasted images that allow visualizing healthy brain and lung anatomy as well as simultaneously depicting tumour morphology on a full-organ scale.** The produced datasets provide isotropic histology-like spatial resolution on the entire volumes (3D) of the imaged tissue. The mosaic CT reconstruction used with lung specimens showcased the possibility of achieving a full-organ coverage with sub-micrometric voxel sizes overcoming the problem of the limited detector field of view and filling the gap, in terms of resolution and sensitivity to soft tissues, of the techniques currently used in clinical practice.
2. XPCI-CT is a well-suited imaging technique for *ex-vivo* RT follow-up for brain and lung with the **capability of discriminating among MRT, MB and BB dose delivery-induced effects**, enabling also the quantification of

anatomical and pathological features of interest (e.g. tumour volumes, microcalcifications and fibrotic tissue).

3. **For the first time, a back-to-back comparison of XPCI-CT images, histology and immunohistochemistry enabled the classification of RT-induced lesions on lung tissues** such as BB-induced extended fibrotic tissue, MRT-driven isolated scars with **intra-scar Fe deposits** and planar MB fibrotic lesions.
4. **The XPCI-CT vs. histology correlation on irradiated rat brain tissues** enabled the identification of **MRT- and MB-induced tissue ablations, Ca/Fe micro- and macro-deposits** within the peak dose delivery areas and associated **reactive gliosis**.
5. Small and wide-angle X-ray scattering and X-ray fluorescence data obtained on both healthy and glioblastoma-bearing rat brains allowed **characterizing, for the first time, the chemical and structural composition of intra-tumour and MRT-driven microcalcifications** that were identified as **hydroxyapatite crystals**.
6. The high sensitivity and detail provided by XPCI-CT analysis on the full brain organs made it **possible, for the first time, to clearly recognize and distinguish the different response of the brain regions to the radiation (i.e. different radio-sensitivity) of the diverse anatomical regions within the brain**.
7. An **optimized procedure for XPCI-CT data processing** was set up and a **semi-automatized procedure for XPCI-CT images morphological segmentation** has been established for studying the glioblastoma multiforme evolution following different RT protocols and for quantifying the extent of iatrogenic lung fibrosis. Accurate threshold segmentation of the microcalcifications in brains were also performed.
8. Ultimately, an **ideal protocol for the follow-up of novel RTs in pre-clinical applications has been outlined and proposed**.

After having used different experimental tools, having analysed different tissues with multiple methods and having collected a series of successful and unsuccessful attempts, I setup a methodological pipeline on the basis on what I have

learned during my Ph.D. Thesis work. I have realized a final ‘product’ consisting in a protocol for preclinical radiotherapy follow-up on small-animal models, which is reported in the Annex 1. In this protocol, I suggest a ‘to-do’ list of the different steps that are required to thoroughly study the effects of RTs by using the methodology proposed in this Ph.D. Thesis.

Besides the scientific results of this Ph.D., which have been reported in 3 manuscripts published as scientific articles and presented in oral contributions at 3 international conferences (see Annex 1 and Annex 2), this protocol is one of the final products of this Ph.D. work and represents a guide for future pre-clinical investigations of RT effects.

The ultimate goal of this study is to **advance towards the *in-vivo* application of XPCI-CT as an auxiliary monitoring imaging technique for RT effects, which can fill the gaps existing in the standard follow-up protocols used in preclinical RT research with small animal models.** Aspects that need to be addressed and optimized in view of the *in-vivo* application of XPCI-CT are the dose issue related to the use of ionizing radiation and the linked questions of the maximum possible spatial resolution and the scan acquisition time. The doses currently delivered when imaging *post-mortem* soft tissues are strongly dependent, among the different parameters, on the chosen voxel size. As an example, for a single CT performed at ESRF-ID17 with a monochromatic beam of 35 keV, the dose delivered to an excised soft-tissue sample (e.g. a rat brain) is about 150 Gy with a voxel size of $3.25^3 \mu\text{m}^3$, while for voxel sizes of $6^3\text{-}8^3 \mu\text{m}^3$ the dose ranges from hundreds of milliGray to few Gray, which is in line with the delivered doses in conventional micro-CT full-animal scans (Bartling, 2007; Molinos, 2019). The dose can be further lowered if e.g. iterative or machine learning methods are used for CT reconstruction: these algorithms can keep the image reconstruction consistent even when a reduced number of angular projections are acquired or when low X-ray fluxes are used for imaging.

Another aspect to be taken into account is linked to the physiological motions of the living organism during *in-vivo* CT acquisitions. The smaller the used voxel size, the more sensitive is the technique to the small movements of the animal and to motions within the animal’s body (breathing, heart beat...) and the higher

is the risk of image artefacts that can jeopardise the quality of the resulting images. Overall, voxel sizes of the order of $6^3\text{-}10^3 \mu\text{m}^3$ are a good candidate for the first XPCI-CT *in-vivo* application.

Additional limitations may arise when the soft tissue to be examined is surrounded by bone, as in the case of *in-vivo* brain imaging. In this case, the presence of the skull impairs the visibility of the soft cerebral structures. The limits encountered in imaging complex organisms due to the presence of both soft and hard tissues can be mitigated by the use of multi-material phase retrieval algorithms, which first applications have been already published by (Croton, 2018). Previous works by our group already demonstrated that XPCI-CT may facilitate a more complete evaluation of the complex samples and organisms by providing concurrent comprehensive information about soft and hard tissue (Barbone, 2020b; Horng, 2014).

In conclusion, this doctoral work demonstrated that XPCI-CT can be used as a part of a multi-technique approach for *post-mortem*, and possibly in future for *in-vivo*, follow-up of novel RTs being able to distinguish different radio-induced effects at high spatial and contrast resolution.

Bibliography

<https://www.esrf.fr>

<https://radiopaedia.org/articles/haemorrhage-on-mri>

<https://www.euro.who.int>

https://www.pco.de/fileadmin/user_upload/pco-product_sheets/pco.edge_55_data_sheet.pdf

Agostinelli, S., Allison, J., Amako, K., Apostolakis, J., Araujo, H. et al. **2003**. “Geant4—a simulation toolkit.” *Nuclear Instruments and Methods in Physics Research Section A* 506 (3).

Albers, J., Pacilé, S., Markus, M. A., Wiart, M., Vande Velde, G., Tromba, G. and Dullin, C. **2018a**. “X-ray-Based 3D Virtual Histology-Adding the Next Dimension to Histological Analysis.” *Molecular Imaging and Biology* 20.

Albers, J., Markus, M. A., Alves, F. and Dullin, C. **2018b**. “X-ray based virtual histology allows guided sectioning of heavy ion stained murine lungs for histological analysis.” *Scientific Reports* 8.

Alliance, National Guideline. **2018**. “Evidence reviews for the investigation, management and follow-up of glioma: Brain tumours (primary) and brain metastases in adults: Evidence Report A.” *NICE Guideline, No. 99*.

Altomare, A., Corriero, N., Cuocci, C., Falcicchio, A., Moliterni, A. and Rizzi, R. **2015**. “QUALX2.0: a qualitative phase analysis software using the freely available database POW_COD.” *Journal of Applied Crystallography* 48.

Altunbas, M. C., Shaw, C. C., Chen, L., Lai, C., Liu, X., Han, T., Wang, T. **2007**. “A post-reconstruction method to correct cupping artifacts in cone beam breast computed tomography.” *Medical Physics* 34 (7).

Ando, M. and Hosoya, S. **1971**. “Proceedings of the 6th International Conference of X-Ray Optics and Microanalysis.” Osaka.

- Arfelli, F., Bonvicini, V., Bravin, A., Cantatore, G., Castelli, E., Palma, L. D., Michiel, M. D., Fabrizioli, M., Longo R, Menk RH, Olivo A, Pani S, Pontoni D, Poropat P, Prest M, Rashevsky A, Ratti M, Rigon L, Tromba G, Vacchi A, Vallazza E, Zanconati F. **2000**. "Mammography with Synchrotron Radiation: Phase-Detection Techniques." *Radiology* 215 (1).
- Baran, M. **2018**. "Pattern recognition in superpixel graphs, PhD Thesis." *AGH University of Science and Technology in Kraków*.
- Barbone, G. E., Bravin A., Romanelli P., Mittone A., Bucci D., Gaass T., le Duc G., Auweter S., Reiser M. F., Kraiger M. K., de Angelis M. H., Battaglia G. and Coan P. **2018**. "Micro-imaging of Brain Cancer Radiation Therapy Using Phase-contrast Computed Tomography." *International Journal of Radiation Oncology, Biology, Physics* 101.
- Barbone, G. E., Bravin, A., Mittone, A., Kraiger, M. J., Hrabě de Angelis, M., Bossi, M., Ballarini, E., Rodriguez-Menendez, V., Ceresa, C., Cavaletti, G., Coan, P. **2020a**. "Establishing sample-preparation protocols for X-ray phase-contrast CT of rodent spinal cords: Aldehyde fixations and osmium impregnation." *Journal of Neuroscience Methods*.
- Barbone, G. E., Bravin, A., Mittone, A., Grosu, S., Ricke, J., Cavaletti, G., Djonov, V., Coan, P. **2020b**. "High-Spatial-Resolution Three-dimensional Imaging of Human Spinal Cord and Column Anatomy with Postmortem X-ray Phase-Contrast Micro-CT." *Radiology* 298 (1).
- Barrett, J. F. and Keat, N. **2004**. "Artifacts in ct: recognition and avoidance." *Radiographics* 24.
- Barnett, G. C., West, C. M., Dunning, A. M., Elliott, R. M., Coles, C. E., Pharoah, P. D., and Burnet, N. G. **2009**. "Normal tissue reactions to radiotherapy." *Nature Reviews Cancer* 9 (2).
- Bartels, M., Krenkel, M., Cloetens, P., Möbius, W., Salditt, T.,. 2015. "Myelinated mouse nerves studied by X-ray phase contrast zoom tomography." *Journal of Structural Biology* **192** (3).
- Barth, R. F. **1999**. "Rat brain tumor models in experimental neuro-oncology: the 9L, C6, T9, F98, RG2 (D74), RT-2 and CNS-1 gliomas." *Journal of Neuro-Oncology* 36 (1).

- Bartling, S. H., Stiller, W., Semmler, W. and Kiessling, F. **2007**. "Small Animal Computed Tomography Imaging." *Current Medical Imaging Reviews* 3 (1).
- Bartzsch, S., Corde, S., Crosbie, J. C., Day, L., Donzelli, M., Krisch, M., Lerch, M., Pellicioli, P., Smyth, L. M. L. and Tehei, M. **2020**. "Technical advances in x-ray microbeam radiation therapy." *Physics in Medicine and Biology* 65.
- Baskar, R., Lee, K. A., Yeo, R. and Yeoh, K.-W. **2012**. "Cancer and Radiation Therapy: Current Advances and Future Directions." *International Journal of Medical Sciences* 9 (3).
- Bayat, S., Porra, L., Suhonen, H., Nemoz, C., Suortti, P., Sovija, A. R. A. **2006**. "Differences in the time course of proximal and distal airway response to inhaled histamine studied by synchrotron radiation CT." *Journal of Applied Physiology* 100.
- Bayat, S., Strengell, S., Porra, L., Janosi, T. Z., Petak, F., Suhonen, H., Suortti, P., Hantos, Z., Sovijarvi, A. R. A., and Habre, W. **2009**. "Methacholine and Ovalbumin Challenges Assessed by Forced Oscillations and Synchrotron Lung Imaging." *American Journal of Respiratory and Critical Care Medicine* 180.
- Berg, S., Kutra, D., Kroeger, T., Straehle, C. N., Kausler, B. X., Haubold, C., Schiegg, M., Ales, J., Beier, T., Rudy, M., Eren, K., Cervantes, J. I., Xu, B., Beuttenmueller, F., Wolny, A., Zhang, C., Koethe, U., Hamprecht, F. A. and Kreshuk, A. **2019**. "ilastik: interactive machine learning for (bio)image analysis." *Nature Methods* 16.
- Bernhardt, M., Priebe, M., Osterhoff, M., Wollnik, C., Diaz, A., Salditt, T., Rehfeldt, F. **2016**. "X-Ray Micro- and Nanodiffraction Imaging on Human Mesenchymal Stem Cells and Differentiated Cells." *Biophysical Journal* 110.
- Beyer, T., Bidaut, L., Dickson, J., Kachelriess, M., Kiessling, F., Leitgeb, R., Ma, J., Sundar, L. K. S., Theek, B. and Mawlawi, O. **2020**. "What scans we will read: imaging instrumentation trends in clinical oncology." *Cancer Imaging* 20 (38).
- Blocker, S. J., Holbrook, M. D., Mowery, Y. M., Sullivan, D. C., Badea, C. T. **2020**. "The impact of respiratory gating on improving volume measurement of murine lung tumors in micro-CT imaging." *PLoS ONE* 15.

- Bolte, S. and Cordelières, F. P. **2006**. "A guided tour into subcellular colocalization analysis in light microscopy." *Journal of Microscopy* 244 (3).
- Bolze, J., Kogan, V., Beckers, D., and Fransen, M. **2018**. "High-performance small- and wide-angle X-ray scattering (SAXS/WAXS) experiments on a multi-functional laboratory goniometer platform with easily exchangeable X-ray modules." (Review of Scientific Instruments) 89.
- Bonse, U. and Hart, M. **1965**. "An x-ray interferometer." *Applied Physics Letters* 6.
- Borisova, E., Lovric, G., Miettinen, A., Fardin, L., Bayat, S., Larsson, A., Stampanoni, M., Schittny, J. C., and Schlepütz, C. M. **2020**. "Micrometer-resolution X-ray tomographic full-volume reconstruction of an intact post-mortem juvenile rat lung." *Histochemistry and Cell Biology*.
- Born, M., Wolf, E. **1999**. *Principles of Optics: Electromagnetic Theory of Propagation, Interference and Diffraction of light 7th Edition*. Elsevier.
- Bouchet, A., Lemasson, B., Le Duc, G., Maisin, C., Bräuer-Krisch, E., Siegbahn, E. A., Renaud, L., Khalil, E., Rémy, C., Poillot, C., Bravin, A., Laissue, J. A., Barbier, E. L., Serduc, R. **2010**. "Preferential Effect of Synchrotron Microbeam Radiation Therapy on Intracerebral 9L Gliosarcoma Vascular Networks." *International Journal of Radiation Oncology, Biology, Physics* 78 (5).
- Bouchet, A., Lemasson, B., Christen, T., Potez, M., Rome, C., Coquery, N., Le Clec'h, C., Moisan, A., Bräuer-Krisch, E., Leduc, G., Rémy, C., Laissue, J. A., Barbier, E. L., Brun, E., Serduc, R. **2013**. "Synchrotron microbeam radiation therapy induces hypoxia in intracerebral gliosarcoma but not in the normal brain." *Radiotherapy and Oncology* 108.
- Bouchet, A., Bidart, M., Miladi, I., Le Clec'h, C., Serduc, R., Coutton, C., Regnard, P., Khalil, E., Dufort, S., Lemasson, B., Laissue, J. A., Pelletier, L., Le Duc, G. **2014**. "Characterization of the 9L gliosarcoma implanted in the Fisher rat: an orthotopic model for a grade IV brain tumor." *Tumor Biology*.
- Bouchet, A., Bräuer-Krisch, E., Prezado, Y., El Atifi, M., Rogalev, L., Le Clec'h, C., Laissue, J. A., Pelletier, L. and Le Duc, G. **2016**. "Better Efficacy of Synchrotron Spatially Microfractionated Radiation Therapy Than

- Uniform Radiation Therapy on Glioma." *International Journal of Radiation Oncology, Biology, Physics*.
- Bouhemad, B., Zhang, M., Lu, Q. and Rouby, J. J. **2007**. "Clinical review: Bedside lung ultrasound in critical care practice." *Critical care* 11.
- Boyko, O. B., Burger, P. C., Shelburne, J. D., Ingram, P. 1992. "Non-heme mechanisms for T1 shortening: pathologic, CT, and MR elucidation." *American Journal of Neuroradiology* 13.
- Brahme, A. **1984**. "Dosimetric Precision Requirements in Radiation Therapy." *Acta Radiologica: Oncology* 23 (5).
- Bräuer-Krisch, E., Bravin, A., Lerch, M., Rosenfeld, A., Stepanek, J., Di Michiel, M., and Laissue, J. A. **2003**. "MOSFETdosimetry for microbeam radiation therapy at the European Synchrotron Radiation Facility." *Medical Physics* 30.
- Bräuer-Krisch, E., Requardt, H., Régnard, P., Corde, S., Siegbahn, E., LeDuc, G., Brochard, T., Blattmann, H., Laissue, J. A. and Bravin, A. **2005**. "New irradiation geometry for microbeam radiation therapy." *Physics in Medicine & Biology* 50 (13).
- Bräuer-Krisch, E., Requardt, H., Brochard, T., Berruyer, G., Renier, M., Laissue, J. A. and Bravin, A. **2009**. "New technology enables high precision multislit collimators for microbeam radiation therapy." *Review of scientific instruments* 80.
- Bräuer-Krisch, E., Serduc, R., Siegbahn, E. A., Le Duc, G., Prezado, Y., Bravin, A., Blattmann, H., Laissue, J. A. **2010**. "Effects of pulsed, spatially fractionated, microscopic synchrotron X-ray beams on normal and tumoral brain tissue." *Mutation Research* 704 (1-3).
- Bravin, A., Coan, P. and Suortti, P. **2013**. "X-ray phase-contrast imaging: from pre-clinical applications towards clinics." *Physics in Medicine and Biology* 58.
- Bravin, A., Olko, P., Schültke, E., Wilkens, J. J. **2015**. "SYRA3 COST Action – Microbeam radiation therapy: Roots and prospects." *Physica Medica* 31.

- Bray, F., Ferlay, J., Soerjomataram, I., Siegel, R. L., Torre, L. A., Jemal, A. 2018. "Global Cancer Statistics 2018: GLOBOCAN Estimates of Incidence and Mortality Worldwide for 36 Cancers in 185 Countries." *Cancer Journal for Clinicians* 68.
- Broche, L., Pisa, P., Porra, L., Degrugilliers, L., Bravin, A., Pellegrini, M., Borges, J. B., Perchiazzi, G., Larsson, A., Hedenstierna, G., Bayat, S. 2019. "Individual Airway Closure Characterized In Vivo by Phase-Contrast CT Imaging in Injured Rabbit Lung." *Critical Care Medicine* 47 (9).
- Brun, F., Kourousias, G., Dreossi, D., Mancini, L. 2009. "An improved method for ring artifacts removing in reconstructed tomographic images." *World Congress on Medical Physics, Biomedical Engineering, September 7–12, 2009. Munich, Germany: IFMBE Proceedings*.
- Bunk, O., Bech, M., Jensen, T.H., Feidenhans'I, R., Binderup, T., Menzel, A. and Pfeiffer, F. 2009. "Multimodal x-ray scatter imaging." *New Journal of Physics* 11.
- Burvall, A., Lundström, U., Takman, P. A. C., Larsson, D. H. and Hertz, M. H. 2011. "Phase retrieval in X-ray phase-contrast imaging suitable for tomography." *Optics express* 19 (11).
- Caiazzo, A., Ramis-Conde, I. 2015. "Multiscale modelling of palisade formation in glioblastoma multiforme." *Journal of Theoretical Biology* 383.
- Cao, Y., Yin, X., Zhang, J., Wu, T., Li, D., Lu, H., and Hu, J. 2106. "Visualization of mouse spinal cord intramedullary arteries using phase- and attenuation-contrast tomographic imaging." *Journal of Synchrotron Radiation* 23.
- Castelli, E., Tonutti, M., Arfelli, F., Longo, R., Quaia, E., Rigon, L., Sanabor, D., Zanconati, F., Dreossi, D., Abrami, A., Quai, E., Bregant, P., Casarin, K., Chenda, V., Menk, R. H., Rokvic, T., Vascotto, A., Tromba, G., Cova, M. A. 2011. "Mammography with Synchrotron Radiation: First Clinical Experience with Phase-Detection Technique." *Radiology* 259 (3).
- Cedola, A., Bravin, A., Bukreeva, I., Fratini, M., Pacureanu, A., Mittone, A., Massimi, L., Cloetens, P., Coan, P., Campi, G., Spanò, R., Brun, F., Grigoryev, V., Petrosino, V., Venturi, C., Mastrogiacomo, M., de Rosbo, N.

- K. and Uccelli, A. **2017**. "X-Ray Phase Contrast Tomography Reveals Early Vascular Alterations and Neuronal Loss in a Multiple Sclerosis Model." *Scientific Reports* 7.
- Center, M. M., Jemal, A., Lortet-Tieulent, J., Ward, E., Ferlay, J., Brawley, O., Bray, F. **2012**. "International Variation in Prostate Cancer Incidence and Mortality Rates." *European Urology* 61 (6).
- Chakravarty, M. M., Bertrand, G., Descouteaux, M., Sadikot, A. F. and Collins, D. L. **2003**. "The Creation of a Brain Atlas for Image Guided Neurosurgery Using Serial Histological Data." Edited by Springer Berlin Heidelberg.
- Chiumello, D., Froio, S., Bouhemad, B., Camporota, L. and Coppola, S. **2013**. "Clinical review: Lung imaging in acute respiratory distress syndrome patients - an update." *Critical Care* 17.
- Clarke, J. **2014**. Accessed 04 27, 2021. <https://www.cockcroft.ac.uk/wp-content/uploads/2014/12/Lecture-1.pdf>.
- Cloetens, P., Barretty, R., Baruchel, J., Guigayz, J-P., and Schlenker, M. **1996**. "Phase objects in synchrotron radiation hard x-ray imaging." *Journal of Physics D: Applied Physics* 29 (133).
- Coan, P., Peterzol, A., Fiedler, S., Ponchut, C., Labiche, J. C. and A. Bravin, A. **2006**. "Evaluation of imaging performance of a taper optics CCD 'FReLoN' camera designed for medical imaging." *Journal of Synchrotron Radiation* 13.
- Coan, P., Mollenhauer, J., Wagner, A., Muehleman, C., Bravin, A. **2008**. "Analyzer-based imaging technique in tomography of cartilage and metal implants: A study at the ESRF." *European Journal of Radiology* 68 (3).
- Coan, P., Bamberg, F., Diemoz, P. C., Bravin, A., Timpert, K., Mützel, E., Raya, J. G., Adam-Neumair, S., Reiser, M. F., Glaser, C. **2010**. "Characterization of osteoarthritic and normal human patella cartilage by computed tomography X-ray phase-contrast imaging: a feasibility study." *Investigative radiology* 45 (7).
- Coan, P., Bravin, A. and Tromba, G. **2013**. "Phase-contrast x-ray imaging of the breast: recent developments towards clinics." *Journal of Physics D: Applied Physics* 46.

- Connor, D. M., Benveniste, H., Dilmanian, F. A., Kritzer, M. F., Miller, L. M., Zhong, Z. **2009**. "Computed tomography of amyloid plaques in a mouse model of Alzheimer's disease using diffraction enhanced imaging." *NeuroImage* 46 (4).
- Connor, D. M., Cole, E. B., Zhong, Z., Parham, C. A. and Pisano, E. D. **2012**. "Preliminary performance measurements from a second generation diffraction enhanced." *Proceedings of SPIE* 8313.
- Cooper, D. M. L., Erickson, B., Peele, A. G., Hannah, K., Thomas, C. D. L., Clement, J. G. **2011**. "Visualization of 3D osteon morphology by synchrotron radiation micro-CT." *Journal of Anatomy* 219 (4).
- Crosbie, J. C., Anderson, R. L., Rothkamm, K., Restall, C. M., Cann, L., Ruwanpura, S., Meachem, S., Yagi, N., Svalbe, I., Lewis, R. A., Williams, B. R., Rogers, P. A. **2010**. "Tumor cell response to synchrotron microbeam radiation therapy differs markedly from cells in normal tissues." *International Journal of Radiation Oncology, Biology and Physics* 77 (3).
- Croton, L. C. P., Morgan, K. S., Paganin, D. M., Megan, L. T. K., Wallace, M. J., Crossley, K. J., Miller, S. L., Yagi, N., Uesugi, K., Hooper, S. B. and Kitchen, M. J. **2018**. "In situ phase contrast X-ray brain CT." *Scientific Reports* 8.
- Curtis, H. J. **1967**. "The use of deuteron microbeam for simulating the biological effect of heavy cosmic-ray particles." *Radiation Research Supplement* 7.
- Danilchenko, S. N., Kukharenko, O. G., Moseke, C., Protsenko, I. Yu., Sukhodub, L. F., Sulkio-Cleff, B. **2002**. "Determination of the Bone Mineral Crystallite Size and Lattice Strain from Diffraction Line Broadening." (*Crystal Research and Technology*) 37 (11).
- David, W. I. F., Leoni, M. and Scardi P. **2010**. "Domain Size Analysis in the Rietveld Method." (*Materials Science Forum*) 651.
- Davis, T. J., Gureyev, T. E., Gao, D., Stevenson, A. W. and Wilkins, S. W. **1994**. "X-Ray Image Contrast from a Simple Phase Object." *Physical Review Letters* 74.
- Dawson, L. A., Sharpe, M. B. **2006**. "Image-guided radiotherapy: rationale, benefits, and limitations." *The Lancet Oncology* 7 (10).

- De Felici, M., Felici, R., Sanchez del Rio, M., Ferrero, C., Bacarian, T., Dilmanian, F. A. **2005**. "Dose distribution from x-ray microbeam arrays applied to radiation therapy: An EGS4 Monte Carlo study." *Medical Physics* 32 (8).
- Debus, C., Oelfke, U. and Bartzsch. S., **2017**. "A point kernel algorithm for microbeam radiation therapy." *Physics in Medicine and Biology* 62 (21).
- del Rio, M. S. and Roger, J. D. **2004**. "A New Version of the X-ray Optics Software Toolkit." *AIP Conference Proceedings* 705 (1).
- Delgado-Lopez, P. D., Corrales-Garcia, E. M. **2016**. "Survival in glioblastoma: A review on the impact of treatment modalities." *Clinical and Translational Oncology* 18.
- Desai, R. and Rich, K. M. **2020**. "Therapeutic Role of Gamma Knife Stereotactic Radiosurgery in Neuro-Oncology." *Missouri Medicine* 117 (1).
- DeSantis, C. E., Bray, F., Ferlay, J., Lortet-Tieulent, J., Anderson, B. O., Jemal, A. **2015**. "International variation in female breast cancer incidence and mortality rates." *Cancer Epidemiology, Biomarkers and Prevention* 24 (10).
- DeVita, V. T. Jr. and Chu, E. **2008**. "A History of Cancer Chemotherapy." *Cancer Research* 68.
- Diemoz, P. C., Bravin, A., Glaser, C., and Coan, P., **2010**. "Comparison of analyzer-based imaging computed tomography extraction algorithms and application to bone-cartilage imaging". *Physics in Medicine and Biology*, 55(24).
- Digabel, H. and Lantuejoul, C. **1978**. "iterative Algorithms. Proceedings of the 2nd European Symposium Quantitative Analysis of Microstructures." *Material Science, Biology and Medicine*.
- Dilmanian, F. A., Button, T. M., Le Duc, G., Zhong, N., Peña, L. A., Smith, J. A. L., Martinez, S. R., Bacarian, T., Tammam, J., Baorui, R. B., Farmer, P. M., Kalef-Ezra, J., Micca, P. L., Nawrocky, M. M., Niederer, J. A., Recksiek, F. P., Fuchs, A. and Rosen, E. **2002**. "Response of rat intracranial 9L gliosarcoma to microbeam radiation therapy." *Neuro-Oncology*.

- Donnelly, P., Hiller, L., Bathers, S., Bowden, S., Coleman, R. **2007**. "Questioning specialists' attitudes to breast cancer follow-up in primary care." *Annals of Oncology* 18 (9).
- Donzelli, M., Bräuer-Krisch, E., Oelfke, U., Wilkens, J. J. and Bartzsch, S. **2018**. "Hybrid dose calculation: a dose calculation algorithm for microbeam radiation therapy." *Physics in Medicine and Biology* 63.
- Dreossi, D., Abrami, A., Arfelli, F., Bregant, P., Casarin, K., Chenda, V., Cova, M. A., Longo, R., Menk, R.-H., Quai, E., Quaia, E., Rigon, L., Rokvic, T., Sanabor, D., Tonutti, M., Tromba, G., Vascotto, A., Zanconati, F., Castelli, E. **2008**. "The mammography project at the SYRMEP beamline." *European Journal of Radiology* 68 (3).
- Drury, H. C. **1896**. "Dermatitis caused by Roentgen X-rays." *British medical journal* 2.
- Du, J., Li, W., Lu, K., Xiao, B. **2015**. "An overview of multi-modal medical image fusion." *Neurocomputing* 215.
- El Allaoui, A., Nasri M. **2012**. "Medical Image Segmentation by Evolutionary Approach and Watershed Morphology." *International Journal of Computer Applications* 47 (24).
- Elleau, H., Charvet, A. M., Berkvens, P., Berruyer, G., Brochard, T., Dabin, Y., Dominguez, M. C., Draperi, A., Fiedler, S., Goujon, G., Le Duc, G., Mattenet, M., Nemoz, C., Perez, M., Renier, M., Schulz, C., Spanne, P., Suortti, P., Thomlinson, W., Esteve, F., Bertrand, B., Le Bas, J. F. **1999**. "Instrumentation of the ESRF medical imaging facility." *Nuclear Instruments and Methods in Physics Research Section A: Accelerators, Spectrometers, Detectors and Associated Equipment* 428 (2-3).
- Endrizzi, M. **2018**. "X-ray phase-contrast imaging." *Nuclear Instruments and Methods in Physics Research, A* 878.
- Fain, S., Schiebler, M. L., McCormack, D. G. **2010**. "Imaging of Lung Function Using Hyperpolarized Helium-3 Magnetic Resonance Imaging: Review of Current and Emerging Translational Methods and Applications." *Journal of Magnetic Resonance Imaging* 32.

- Fardin, L., Broche, L., Lovric, G., Mittone, A., Stephanov, O., Larsson, A., Bravin, A. and Bayat, S. **2021**. "Imaging atelectrauma in Ventilator-Induced Lung Injury using 4D X-ray microscopy." *Scientific Reports* 11 (1).
- Faustino-Rocha, A. I., Gama, A., Oliveira, P. A., Alvarado, A., Fidalgo-Gonçalves, L., Ferreira, R., Ginja, M. **2016**. "Ultrasonography as the Gold Standard for In Vivo Volumetric Determination of Chemically-induced Mammary Tumors." *In Vivo* 30 (4).
- Fedorov, A., Beichel, R., Kalpathy-Cramer, J., Finet, J., Fillion-Robin, J.-C., Pujol, S., Bauer, C., Jennings, D., Fennessy, F., Sonka, M., Buatti, J., Aylward, S., Miller, J. V., Pieper, S. and Kikinis, R. **2012**. "3D Slicer as an Image Computing Platform for the Quantitative Imaging Network." *Magnetic resonance imaging* 30 (9).
- Felder, J., Celik, A. A., Choi, C. H., Schwan, S. and Shah, N. J. **2017**. "9.4 T small animal MRI using clinical components for direct translational studies." *Journal of Translational Medicine* 15.
- Förster, E., Goetz, K. and Zaumseil P. **1980**. "Double crystal diffractometry for the characterization of targets for laser fusion experiments." *Kristall und Technik* 15.
- Fratzl, P., Jakob, H. F., Rinnerthaler, S., Roschger, P. **1997**. "Position-Resolved Small Angle X-Ray Scattering of." *Journal of Applied Crystallography* 30.
- Friedrich, W., Knipping, P., Laue, M. **1912**. "Interferenz-Erscheinungen bei Röntgenstrahlen." *München: Verlassen der Königlich Bayerische Akademie der Wissenschaften*.
- Furnari, F. B., Fenton, T., Bachoo, R. M., Mukasa, A., Stommel, J. M., Stegh, A., Keith, W. H., Ligon, L., Louis, D. N., Brennan, C., Chin, L., De Pinho, R. A., Cavenee, W. K. **2007**. "Malignant astrocytic glioma: genetics, biology, and paths to treatment." *Genes & development* 21 (21).
- Ghods, A. J., Irvin, D., Liu, G., Yuan, X., Abdulkadir, R. I., Tunici, P., Konda, B., Wachsmann-Hogiu, S., Black, K. L., Yu, J. S. **2007**. "Spheres Isolated from 9L Gliosarcoma Rat Cell Line Possess Chemoresistant and Aggressive Cancer Stem-Like Cells." *Stem Cells* 25 (7).

- Giannini, C., Siliqi, D., Bunk, O., Beraudi, A., Ladisa, M., Altamura, D., Stea, S. and Baruffaldi, F. **2012**. "Correlative Light and Scanning X-Ray Scattering Microscopy of Healthy and Pathologic Human Bone Sections." *Scientific Reports* 2 (435).
- Giannini, C., Siliqi, D., Ladisa, M., Altamura, D., Diaz, A., Beraudi, A., Sibillano, T., De Caro, L., Stea, S., Baruffaldi F., and Bunk O. **2014**. "Scanning SAXS–WAXS microscopy on osteoarthritis-affected bone – an age-related study." *Journal of Applied Crystallography* 47.
- Giannini, C., Ladisa, M., Altamura, D., Siliqi, D., Sibillano, T. and De Caro, L. **2016**. "Diffraction: A Powerful Technique for the Multiple-Length-Scale Structural Analysis of Nanomaterials." *Crystals* 6 (87).
- Giannini, C., Ladisa, M., Lutz-Bueno, V., Terzi, A., Ramella, M., Fusaro, L., Altamura, D., Siliqi, D., Sibillano, T., Diaz, A., Boccafoschi, F. and Bunk, O. **2019**. "X-ray scanning microscopies of microcalcifications in abdominal aortic and popliteal artery aneurysms." *IUCrJ* 6 (2).
- Gompel, G. V., Tisson, G., Dyck, D. V., Sijbers, J. **2004**. "A new algorithm for 2D region of interest tomography." *Proceedings of SPIE - The International Society for Optical Engineering* 5370.
- Goodman, A. M., Szaflarski, J. P. **2021**. "Recent Advances in Neuroimaging of Epilepsy." *Neurotherapeutics*.
- Gragoudas, E. S., Lane, A. M., Kim, I. K. **2013**. "Chapter 146 - Charged-Particle Irradiation of Uveal Melanoma." In *Retina (Fifth Edition)*, by S. J. Ryan. Elsevier Saunders.
- Gureyev, T. E., Nesterets, Y. I., Stevenson, A. W., Miller, P. R., Pogany, A. and Wilkins, S. W. **2008**. "Some simple rules for contrast, signal-to-noise and resolution in in-line x-ray phase-contrast imaging." *Optics Express* 16 (5).
- Gureyev, T.E., Mayo, S. C., Myers, D. E., Nesterets, Ya., Paganin, D. M., Pogany, A., Stevenson, A. W., Wilkins, S. W. **2009**. "Refracting Röntgen's rays: Propagation-based x-ray phase contrast for biomedical imaging." *Journal of Applied Physics* 105.

- Hellbach, K., Yaroshenko, A., Meinel, F. G., Yildirim, A. Ö., Conlon, T. M., Bech, M., Mueller, M., Velroyen, A., Notohamiprodjo, M., Bamberg, F., Auweter, S., Reiser, M., Eickelberg, O., Pfeiffer, F. **2015**. “In Vivo Dark-Field Radiography for Early Diagnosis and Staging of Pulmonary Emphysema.” *Investigative Radiology* 50 (7).
- Hémonnot, C. Y. J., Reinhardt, J., Saldanha, O., Patommel, J. **2016**. “X-Rays Reveal the Internal Structure of Keratin Bundles in Whole Cells.” *ACS Nano* 10.
- Hémonnot, C. Y. J. and Köster, S. **2017**. “Imaging of Biological Materials and Cells by X-ray Scattering and Diffraction.” *ACS Nano* 11 (9).
- Henrich, B., Bergamaschi, A., Broennimann, C., Dinapoli, R., Eikenberry, E.F., Johnson, I., Kobasb, M., Kraft, P., Mozzanica, A., Schmitt, B. **2009**. “PILATUS: A single photon counting pixel detector for X-ray applications.” *Nuclear Instruments and Methods in Physics Research A* 607.
- Herrmann, K. A., Kohan, A. A., Gaeta, M. C., Rubbert, C., Vercher-Conejero, J. L., Paspulati, R. M., Antonis, K., Mansoori, B., Faulhaber, P. F., Avril, N., and Ros, P. R. **2013**. “Applications in Clinical Imaging.” *Current Radiology Reports* 1.
- Hong, T. S., Ritter, M. A., Tomé, W. A. and Harari, P. M. **2005**. “Intensity-modulated radiation therapy: emerging cancer treatment technology.” *British Journal of Cancer* 92 (10).
- Hooper, S. B., Kitchen, M. J., Siew, M. L. L., Lewis, R. A., Fouras, A., te Pas, A. B., Siu, K. K. W., Yagi, N., Uesugi, K. and Wallace, M. J. **2009**. “Imaging lung aeration and lung clearance at birth using Phase Contrast X-ray Imaging.” *Clinical and Experimental Pharmacology and Physiology* 36.
- Horng, A., Brun, E., Mittone, A., Gasilov, S., Weber, L., Geith, T., Adam-Neumair, S., Auweter, S. D., Bravin, A., Reiser, M. F., Paola, C. **2014**. “Cartilage and Soft Tissue Imaging Using X-rays.” *Investigative Radiology* 49 (9).
- Hsia, C. C. W., Hyde, D. M., Ochs, M. and Weibel, E. R. **2010**. “An Official Research Policy Statement of the American Thoracic Society/European Respiratory Society: Standards for Quantitative Assessment of Lung Structure.” *American Journal of Respiratory and Critical Care Medicine* 181 (4).

- IAEA, International Atomic Energy Agency. **2005**. *Absorbed dose determination in external beam radiotherapy An international code of practice for dosimetry based on standards of absorbed dose to water*. Vienna, (Austria): International Atomic Energy Agency (IAEA): IAEA.
- ICRU. **1976**. "Report 24." *Journal of the International Commission on Radiation Units and Measurements* 13 (1).
- Johnson, G. A., Cofer, G. P., Gewalt, S. L., Hedlund, L. W. **2002**. "Morphologic Phenotyping with MR Microscopy: The Visible Mouse." *Radiology* 222.
- Kay, M. I., Young, R. A., Posner, A. S. **1964**. "Crystal structure of hydroxyapatite." *Nature* 205.
- Keyriläinen, J., Bravin, A., Fernández, M., Tenhunen, M., Virkkunen, P., and Suortti, P. **2010**. "Phase-contrast X-ray imaging of breast." *Acta Radiologica*.
- Khimchenko, A., Bikis, C., Pacureanu, A., Hieber, S. E., Thalmann, P., Deyhle, H., Schweighauser, G., Hench, J., Frank, S., Müller-Gerbl, M., Schulz, G., Cloetens, P. and Müller, B. **2018**. "Hard X-Ray Nanoholotomography: Large-Scale, Label-Free, 3D Neuroimaging beyond Optical Limit." *Advanced Science* 5.
- Kitchen, M. J., Paganin, D., Lewis, R. A., Yagi, N., Uesugi, K. **2005**. "Analysis of speckle patterns in phase-contrast images of lung tissue." *Nuclear Instruments and Methods in Physics Research A* 548.
- Krenkel, M., Töpperwien, M., Dullin, C., Alves, F. **2016**. "Propagation-based phase-contrast tomography for high-resolution lung imaging with laboratory sources." *AIP Advances* 6.
- la Fougère, C., Suchorska, B., Bartenstein, P., Kreth, F. W., Tonn, J. C. **2011**. "Molecular imaging of gliomas with PET: opportunities and limitations." *Neuro-Oncology* 13 (8).
- Labriet, H., Berujon, S., Broche, L., Fayard, B., Bohic, S., Stephanov, O., Paganin, D. M. Lhuissier, P., Salvo, L., Bayat, S., Brun, E. **2019**. "3D histopathology speckle phase contrast imaging: from synchrotron to conventional sources." *Proceedings of SPIE* 10948.

- Laissue, J. A., Spanne, P., Dilmanian, F. A., Gebbers, J.-O., and Slatkin, D. N. **1992**. "Zell- und Gewebeläsionen nach räumlich fraktionierter Mikro-Bestrahlung des ZNS mit Synchrotron-Photonen." *Schweizerische medizinische Wochenschrift* 122.
- Laissue, J. A., Geiser, G., Spanne, P. R., Dilmanian, F. A., Gebbers, J.-O., Geiser, M., Wu, X.-Y., Makar, M. S., Micca, P. L., Nawrockym, M., Joel, D. D. and Slatkin, D. N. **1998**. "Neuropathology of ablation of rat gliosarcomas and contiguous brain tissues using a microplanar beam of synchrotron-wiggler-generated x rays." *International Journal of Cancer* 78.
- Laissue, J. A., Lyubimova, N., Wagner, H.-P., Archer, D. W., Slatkin, D. N., Di Michiel, M., Nemoz, C., Renier, M., Brauer, E., Spanne, P. O., Gebbers, J.-O., Dixon, K., Blattmann, H. **1999**. "Microbeam radiation therapy." *Proceedings of SPIE* 3770.
- Laissue, J. A., Blattmann, H., Michiel, D., Slatkin, D. N., Lyubimova, N., Guzman, R., Zimmermann, A., Birrer, S., Bey, T., Kircher, P., Stettler, R., Fatzer, R., Jaggy, A., Smilowitz, H. M., Bräuer-Krisch, E., Bravin, A., Le Duc, G., Nemoz, C., Renier, M., Thomlinson, W., Stepanek, J. and Wagner, H. P. **2001**. "The weanling piglet cerebellum: a surrogate for tolerance to MRT (microbeam radiation therapy) in pediatric neuro-oncology." *Proceedings of SPIE*.
- Laissue, J. A., Blattmann, H., Wagner, H. P., Grotzer, M. A., Slatkin, D. N. **2007**. "Prospects for microbeam radiation therapy of brain tumours in children to reduce neurological sequelae." *Developmental Medicine and Child Neurology* 49.
- Larsson, D. H., Lundstrom, U., Westermark, U., Takman, P. A. C., Burvall, A., Arsenian Henriksson, M. and Hertz, H. M. **2012**. "Small-animal tomography with a liquid-metal-jet x-ray source." *Proceeding of SPIE* 8313.
- Larsson, D. H., Lundstrom, U., Westermark, U., Takman, P. A. C., Burvall, A., Arsenian Henriksson, M. and Hertz, H. M. **2012**. "Small-animal tomography with a liquid-metal-jet x-ray source." *Proceeding of SPIE* 8313.

- Larsson, D. H., Vågberg, W., Yaroshenko, A., Yildirim, A. O. and Hertz, H. M. **2016**. "High-resolution short-exposure small-animal laboratory x-ray phase-contrast tomography." *Scientific Reports* 6.
- Leao, D. J., Craig, P. G., Godoy, L. F., Leite, C. C. and Policeni, B. **2020**. "Response Assessment in Neuro-Oncology Criteria for Gliomas: Practical Approach Using Conventional and Advanced Techniques." *American journal of Neuroradiology* 41 (1).
- Lecoq, P. **2020**. *Detectors in Medicine and Biology*. Vol. 2, Chap. 20 in *Particle Physics Reference Library*, by C., Schopper, H. Fabjan. Springer.
- Lee, K. F. and Ho Su, J. **1977**. "CT evidence of grey matter calcification secondary to radiation therapy." *Computerized Tomography* 1.
- Lemasson, B., Bouchet, A., Maisin, C., Christen, T., Le Duc, G., Rémy, C., Barbier, E. L., Serduc, R. **2015**. "Multiparametric MRI as an early biomarker of individual therapy effects during concomitant treatment of brain tumours." (*NMR in Biomedicine*) 28 (9).
- Lewis, R. A. **2004**. "Medical phase contrast x-ray imaging: current status and future prospects." *Physics in Medicine & Biology* 49.
- Lewis, R. A., Yagi, N., Kitchen, M. J., Morgan, M. J., Paganin, D., Siu, K. K. W., Pavlov, K., Williams, I., Uesugi, K., Wallace, M. J., Hall, C. J., Whitley, J. and Hooper, S. B. **2005**. "Dynamic imaging of the lungs using x-ray phase contrast." *Physics in Medicine and Biology* 50.
- Lewis, R. A., Neal, R. D., Williams, N. H., France, B., Hendry, M., Russell, D., Hughes, D. A., Russell, I., Stuart, N. S., Weller, D. and Wilkinson, C. **2009**. "Follow-up of cancer in primary care versus secondary care: systematic review." *The British Journal of general practice* 59 (564).
- Li, J., Zhong, Z., Lidtke, R., Kuettner, K. E., Peterfy, C., Aliyeva, E., Muehleman, C. **2003**. "Radiography of soft tissue of the foot and ankle with diffraction enhanced imaging." *Journal of Anatomy* 202 (5).
- Lichtenstein, D., Goldstein, I., Mourgeon, E., Cluzel, P., Grenier, P., Rouby, J. J. **2004**. "Comparative diagnostic performances of auscultation, chest

- radiography, and lung ultrasonography in acute respiratory distress syndrome." *Anesthesiology* 100.
- Linton, O. W. **1995**. "Medical applications of x-rays." *SLAC Beam Line* 25N2.
- Liu, L., Boldon, L., Urquhart, M. and Wang, X. **2013**. "Small and Wide Angle X-Ray Scattering Studies of Biological Macromolecules in Solution." (Journal of Visualizes Experiments: JoVE) 71.
- Lloyd, S. P. **1982**. "Least Squares Quantization in PCM." (IEEE Transactions on Information Theory) 28 (2).
- Loening, A. M., Gambhir, S. S. **2003**. "AMIDE: a free software tool for multimodality medical image analysis." *Molecular Imaging* 2 (3).
- Lombardo, D., Calandra, P. and Kiselev, M. A. **2020**. "Structural Characterization of Biomaterials by Means of Small Angle X-rays and Neutron Scattering (SAXS and SANS), and Light Scattering Experiments." *Molecules* 25.
- Loureiro, J. L., Himmelbach, M., Ethofer, T., Pohmann, R., Martin, P., Bause, J., Grodd, W., Scheffler, K., Hagberg, G. E. **2018**. "In-vivo quantitative structural imaging of the human midbrain and the superior colliculus at 9.4T." *NeuroImage* 177.
- Lovric, G., Mokso, R., Arcadu, F., Vogiatzis Oikonomidis, I., Schittny, J. C., Roth-Kleiner, M. and Stampanoni, M. **2017a**. "Tomographic in vivo microscopy for the study of lung physiology at the alveolar level." *Scientific reports* 7.
- Lovric, G., Oikonomidis, I. V., Mokso, R., Stampanoni, M., Roth-Kleiner, M., Schittny, J. C. **2017b**. "Automated computer-assisted quantitative analysis of intact murine lungs at the alveolar scale." *PLoS ONE* 12 (9).
- Lundström, U. **2014**. *Phase-Contrast X-Ray Carbon Dioxide Angiography*. PhD thesis, Stockholm: KTH Royal Institute of Technology.
- Lutz-Bueno, V., Arboleda, C., Leu, L., Blunt, M.J., Busch, A., Georgiadis, A., Bertier, P., Schmatz, J., Varga, Z., Villanueva-Perez, P., Wang, Z., Lebugle, M., David, C., Stampanoni, M., Diaz, A., Guizar-Sicairosa, M. and Menzel A. **2018**. "Model-free classification of X-ray scattering signals applied to image segmentation." *Journal of Applied Crystallography* 51.

- Lwin, T.-T., Yoneyama, A., Hara, A., Ohbu, M., Maruyama, H., Taguchi, M., Esashi, S., Matsushima, T., Terazaki, K., Hyodo, K., Takeda, T. **2016**. "Spontaneous brain tumor imaging of aged rat by crystal X-ray interferometer-based phase-contrast X-ray CT." *Acta Radiologica Open*.
- Manglik, A., Kruse, A. C., Kobilka, T. S., Thian, F. S., Mathiesen, J. M., Sunahara, R. K., Pardo, L., Weis, W. I., Kobilka, B. K., Granier, S. **2012**. "Crystal structure of the μ -opioid receptor bound to a morphinan antagonist." *Nature* 485.
- Marenzana, M., Hagen, C. K., Das Neves Borges, P., Endrizzi, M., Szafraniec, M. B., Ignatyev, K. and Olivo, A. **2012**. "Visualization of small lesions in rat cartilage by means of laboratory-based x-ray phase contrast imaging." *Physics in Medicine and Biology* 57 (24).
- Marone, F., Stampanoni, M. **2012**. "Regridding reconstruction algorithm for real-time tomographic imaging." *Journal Synchrotron Radiation* 19.
- Marone, F., Studer, A., Sala, L. and Stampanoni, M. **2017**. "Towards on-the-fly data post-processing for real-time tomographic imaging at TOMCAT." *Advanced Structural and Chemical Imaging* 3.
- Massimi, L., Brun, F., Fratini, M., Bukreeva, I. and Cedola, A. **2018**. "An improved ring removal procedure for in-line xrayphase contrast tomography." *Physics in Medicine and Biology* 63.
- Massimi, L., Pieroni, N., Maugeri, L., Fratini, M., Brun, F., Bukreeva, I., Santamaria, G., Medici, V., Poloni, T. E., Balducci, C., and Cedola, A. **2020**. "Assessment of plaque morphology in Alzheimer's mouse cerebellum using three-dimensional X-ray phase-based virtual histology." *Scientific Reports* 10.
- MATLAB. **2010**. "version 7.10.0 (R2010a)." *The MathWorks Inc., Natick, Massachusetts*.
- Mayo, S. C., Stevenson, A. W. and Wilkins, S. W. **2012**. "In-Line Phase-Contrast X-ray Imaging and Tomography for Materials Science." *Materials* 5.

- McDonald, S. A., Marone, F., Hintermüller, C., Mikuljan, G., David, C., Pfeiffer, F., and Stampanoni, M. **2009**. “Advanced phase-contrast imaging using a grating interferometer.” *Journal of Synchrotron Radiation* 16.
- McGee-Russell, S. M. **1958**. “Histochemical methods for calcium.” *Journal of Histochemistry & Cytochemistry* 6 (1).
- Miettinen, A., Oikonomidis, I. V., Bonnin, A., Stampanoni, M. **2019**. “NRStitcher: non-rigid stitching of terapixel-scale volumetric images.” *Bioinformatics* 35.
- Mirone, A., Gouillart, E., Brun, E., Tafforeau, P., Kieffer, J. **2014**. “PyHST2: a hybrid distributed code for high speed tomographic reconstruction with iterative reconstruction and a priori knowledge capabilities.” *Nuclear Instruments and Methods B* 324.
- Mittone, A., Manakov, I., Broche, L., Jarnias, C., Coan, P. and Bravin, A. **2017**. “Characterization of a sCMOS-based high-resolution imaging system.” *Journal of Synchrotron radiation* 24.
- Mittone, A., Fardin, L., Di Lillo, F., Fratini, M., Requardt, H., Mauro, A., Homs-Regojo, R. A., Douissard, P.-A., Barbone, G. E., Stroebel, J., Romano, M., Massimi, L., Begani-Provinciali, G., Palermo, F., Bayat, S., Cedola, A., Coan, P. and Bravin, A. **2020**. “Multiscale pink-beam microCT imaging at the ESRF-ID17 biomedical beamline.” *Journal of Synchrotron Radiation* 27.
- Molinos, C., Sasser, T., Salmon, P., Gsell, W., Viertl, D., Massey, J. C., Mińczuk, K., Li, J., Kundu, B., K., Berr, S., Correcher, C., Bahadur, A., Attarwala, A. A., Stark, S., Junge, S., Himmelreich, U., Prior, J. O., Laperre, K., Van Wyk, S. and Heiden. **2019**. “Low-Dose Imaging in a New Preclinical Total-Body PET/CT Scanner.” *Frontiers in Medicine* 6.
- Momose, A., Takeda, T., Itai, Y., and Hirano, K. **1996**. “Phase-contrast X-ray computed tomography for observing biological soft tissues.” *Nature Medicine* 2.
- Momose, A. **2020**. “X-ray phase imaging reaching clinical uses.” *Physica Medica* 79.

- Monshi, A., Foroughi, M. R., Monshi, M. R. **2012**. "Modified Scherrer Equation to Estimate More Accurately Nano-Crystallite Size Using XRD." (World Journal of Nano Science and Engineering,) 2 (3).
- Moosmann, J., Ershov, A., Weinhardt, V., Baumbach, T., Prasad, M. S., La Bonne, C., Xiao, X., Kashef, J. and Hofmann, R. **2014**. "Time-lapse X-ray phase-contrast microtomography for in vivo imaging and analysis of morphogenesis." *Nature Protocols* 9.
- Mori, K., Hyodo, K., Shikano, N. and Ando, M. **1999**. "First Observation of Small Fractures on a Human Dried Proximal Phalanx by Synchrotron X-Ray Interference Radiography." *Japanese Journal of Applied Physics* 38 (11B).
- Muehleman, C., Majumdar, S., Issever, A. S., Arfelli, F., Menk, R.-H., Rigon, L., Heitner, G., Reime, B., Metge, J., Wagner, A., Kuettner, K. E. and Mollenhauer, J. **2004**. "X-ray detection of structural orientation in human articular cartilage." *OsteoArthritis and Cartilage* 12.
- Müller, M., Kimm, M. A., Ferstl, S., Allner, S., Achterhold, K., Herzen, J., Pfeiffer, F. and Busse, M. **2018**. "Nucleus-specific X-ray stain for 3D virtual histology." *Scientific Reports* 8.
- Münch, B., Trtik, P., Marone, F. and Stampanoni, M. **2009**. "Stripe and ring artifact removal with combined wavelet – Fourier filtering." *Optics Express* 17 (10).
- Muschelli, J. **2020**. "A Publicly Available, High Resolution, Unbiased CT Brain Template." *Nature Public Health Emergency Collection*.
- Najmudin, Z., Kneip, S., Bloom, M. S., Mangles, S. P. D., Chekhlov, O., Dangor, A. E., Dopp, A., Ertel, K., Hawkes, S. J., Holloway, J., Hooker, C. J., Jiang, J., Lopes, N. C., Nakamura, H., Norreys, P. A., Rajeev, P. P., Russo, C., Streeter, M. J. V., Symes, D. R., Wing, M. **2014**. "Compact laser accelerators for X-ray phase-contrast imaging." *Philosophical Transactions of the Royal Society A* 372.
- NCI, National Cancer Institute. n.d. <https://www.cancer.gov/publications/dictionaries/cancer-terms/>.

- Nemoz, C., Kibleur, A., Hyacinthe, J. N., Berruyer, G., Brochard, T., Bräuer-Krisch, E., Le Duc, G., Brun, E., Elleaume, H. and Serduc, R. **2016**. “In vivo pink-beam imaging and fast alignment procedure for rat brain tumor radiation therapy.” *Journal of Synchrotron Radiation* 23.
- Norvik, C., Westöö, C. K., Peruzzi, N., Lovric, G., van der Have, O., Mokso, R., Jeremiasen, I., Brunnström, H., Galambos, C., Bech, M. and Tran-Lundmark, K. **2019**. “Synchrotron-based phase-contrast micro-CT as a tool for understanding pulmonary vascular pathobiology and the 3-D microanatomy of alveolar capillary dysplasia.” *American Journal of Physiology-Lung Cellular and Molecular Physiology* 318.
- Ogurreck, M., Wilde, F., Herzen, J., Beckmann, F., Nazmov, V., Mohr, J., Haibel, A., Müller, M. and Schreyer, A. **2013**. “The nanotomography endstation at the PETRA III Imaging Beamline.” *Journal of Physics: Conference Series* 425.
- Oliva, P., Bacci, A., Bottigli, U., Carpinelli, M., Delogu, P., Ferrario, M., Giulietti, D., Golosio, B., Petrillo, V., Serafini, L., Tomassini, P., Vaccarezza, C., Vicario, C. and Stefanini, A. **2010**. “Start-to-end simulation of a Thomson source for mammography.” *Nuclear Instruments and Methods in Physics Research Section A* 615 (1).
- Olivo, A. and Speller, R. **2007**. “A coded-aperture technique allowing x-ray phase contrast imaging with conventional sources.” *Applied Physics Letters* 91.
- Olivo, A., Gkoumas, S., Endrizzi, M., Hagen, C. K., Szafraniec, M. B., Diemoz, P. C., Munro, P. R. T., Ignatyev, K., Johnson, B., Horrocks, J. A., Vinnicombe, S. J., Jones, J. L. and Speller, R. D. **2013**. “Low-dose phase contrast mammography with conventional x-ray sources.” *Medical Physics* 40 (9).
- Ostrom, Q. T., Cote, D. J., Ascha, M., Kruchko, C., Barnholtz-Sloan, J. S. **2018**. “Adult Glioma Incidence and Survival by Race or Ethnicity in the United States From 2000 to 2014.” *JAMA Oncology* 4 (9).
- Paganin, D., Mayo, S. C., Gureyev, T. E., Miller, P. R., and Wilkins, S. W. **2002**. “Simultaneous phase and amplitude extraction from a single defocused image of a homogeneous object.” *Journal of Microscopy* 206 (1).
- Paganin, D. **2006**. *Coherent X-Ray Optics*. Oxford University Press on Demand.

- Paganin, D., Pelliccia, D. **2019**. *Tutorials on X-ray Phase Contrast Imaging: Some Fundamentals and Some Conjectures on Future Developments*. arXiv: Image and Video Processing.
- Palermo, F., Pieroni, N., Maugeri, L., Begani Provinciali, G., Sanna, A., Massimi, L., Catalano, M., Olbinado, M. P., Bukreeva, I., Fratini, M., Uccelli, A., de Rosbo, N. R., Balducci, C. and Cedola, A. **2020**. "X-ray Phase Contrast Tomography Serves Preclinical Investigation of Neurodegenerative Diseases." *Frontiers in Neurosciences* 14.
- Parsai, E. I., Shvydka, D., Gopalakrishnan, D. P. M., Feldmeier, J. J. **2008**. "Surface and build-up region dose analysis for clinical radiotherapy photon beams." *Applied Radiation and Isotopes* 66 (10).
- Peli, E. **1990**. "Contrast in Complex Images." *Journal of the Optical Society of America A* 7 (10).
- Pfeiffer, F., Weitkamp, T., Bunk, O. and David C. **2006**. "Phase retrieval and differential phase-contrast imaging with low-brilliance X-ray sources." *Nature Physics* 2.
- Pfeiffer, F., Bunk, O., David, C., Bech, M., Le Duc, G., Bravin, A. and Cloetens, P. **2007**. "High-resolution brain tumor visualization using three-dimensional x-ray phase contrast tomography." *Physics in Medicine and Biology* 52.
- Phillips, N. S., Hillenbrand, C. M., Mitrea, B. G., Yan, J., Li, C., Scoggins, M. A., Merchant, T. E., Armstrong, G. T., Srivastava, D., Pui, C.-H., Robison, L. L., Hudson, M. M., Krull, K. R. and Sabin, N. D. **2020**. "Cerebral microbleeds in adult survivors of childhood acute lymphoblastic leukemia treated with cranial radiation." *Scientific Reports* 10.
- Pinzer, B. R., Cacquevel, M., Modregger, P., McDonald, S. A., Bensadoun, J. C., Thuering, T., Aebischer, P., Stampanoni, M. **2012**. "Imaging brain amyloid deposition using grating-based differential phase contrast tomography." *NeuroImage* 61 (4).
- Pisano, E. D., Johnston, R. E., Chapman, D., Geradts, J., Iacocca, M. V., Livasy, C. A., Washburn, D. B., Sayers, D. E., Zhong, Z., Kiss, M. Z., Thomlinson, W. C. **2000**. "Human breast cancer specimens: diffraction-enhanced imaging

- with histologic correlation-improved conspicuity of lesion detail compared with digital radiography." *Radiology* 214 (3).
- Podgorsak, E. B. **2005**. "External Photon Beams: Physical Aspects." In *Radiation Oncology Physics: A Handbook for Teachers and Students*, by International Atomic Energy Agency IAEA.
- Prasad, K. N. **2004**. "Multiple Dietary Antioxidants Enhance the Efficacy of Standard and Experimental Cancer Therapies and Decrease Their Toxicity." *Integrative Cancer Therapies*.
- Prezado, Y., Martí'nez-Rovira, I., Thengumpallil, S., Deman, P. **2011a**. "Dosimetry protocol for the preclinical trials in white-beam minibeam radiation therapy." *Medical Physics* 39 (9).
- Prezado, Y., Vautrin, M., Martí'nez-Rovira, I., Bravin, A., Estève, F., Elleaume, H., Berkvens, P., Adam, J. F. **2011b**. "Dosimetry protocol for the forthcoming clinical trials in synchrotron stereotactic radiation therapy (SSRT)." *Medical Physics* 38.
- Prezado, Y., Deman, P., Varlet, P., Jouvion, G., Gil, S., Le Clec'h, C., Bernard, H., Le Duc, G. and Sarun, S. **2015**. "Tolerance to Dose Escalation in Minibeam Radiation Therapy Applied to Normal Rat Brain: Long-Term Clinical, Radiological and Histopathological Analysis." *Radiation Research* 184 (3).
- Priebe, M., Bernhardt, M., Blum, C., Tarantola, M., Bodenschatz, E., Salditt, T. **2014**. "Scanning X-Ray Nanodiffraction on Dictyostelium discoideum." *Biophysical Journal* 107.
- Quartuccio, N., Laudicella, R., Vento, A., Pignata, S., Mattoli, M. V., Filice, R., Comis, A. D., Arnone, A., Baldari, S., Cabria, M., Cistaro, A. **2020**. "The Additional Value of 18F-FDG PET and MRI in Patients with Glioma: A Review of the Literature from 2015 to 2020." *Diagnostics* 10 (6).
- Régnard, P, Bräuer-Krisch, E., Tropès, I., Keyriläinen, J., Bravin, A., Le Duc, G. **2008a**. "Enhancement of survival of 9L gliosarcoma bearing rats following intracerebral delivery of drugs in combination with microbeam radiation therapy." *European Journal of Radiology* 68.

- Régnard, P., Le Duc, G., Bräuer-Krisch, E., Troprés, I., Siegbahn, E. A., Kusak, A., Clair, C., Bernard, H., Dallery, D., Laissue, J. A. and Bravin, A. **2008b**. "Irradiation of intracerebral 9L gliosarcoma by a single array of microplanar x-ray beams from a synchrotron: balance between curing and sparing." *Physics in Medicine and Biology* 35.
- Rehman, J., Zahra Ahmad, N., Khalid, M., Asghar, H. M. N. H. K., Gilani, Z. A., Ullah, I., Nasar, G., Akhtar, M.M., Usmani, M. N. **2018**. "Intensity modulated radiation therapy: A review of current practice and future outlooks." *Journal of Radiation Research and Applied Sciences* 11 (4).
- Remes, T. M., Suo-Palosaari, M. H., Koskenkorva, P., K. T., Sutela, A. K., Toiviainen-Salo, S.-M., Arikoski, P. M., Arola, M. O., Heikkilä, V.-P., Kapanen, M., Lähteenmäki, P. M., Lönnqvist, T. R. I., Niiniviita, H. et al. **2020**. "Radiation-induced accelerated aging of the brain vasculature in young adult survivors of childhood brain tumors." *Neuro-Oncology Practice* 7 (4).
- Requardt, H., Bravin, A., Prezado, Y., Bräuer-Krisch, E., Renier, M., Brochard, Th., Berkvens, P., Estève, F., Elleaume, H., Adam, J.-F., Blattmann, H., Laissue, J. A., Kaser-Hotz, B., Nemoz, C., Berruyer, G. **2010**. "The Clinical Trials Program at the ESRF Biomedical Beamline ID17: Status and Remaining Steps." AIP Conference Proceedings.
- Ricciardi, L., Chatterjee, S., Palermo, G., Szerb, E. I., Sanna, A., Palermo, F., Pieroni, N., Fratini, M., Bartolino, R., Cedola, A., La Deda, M. and Strangi, G. **2021**. "Glioblastoma Treatments with Photo-Nanotherapeutics Induce Massive Devascularization and Tumor Elimination." *arXiv:2101.05152*.
- Richter, C.-P., Shintani-Smith, S., Fishman, A., David, C., Robinson, I., Rau, C. **2009**. "Imaging of cochlear tissue with a grating interferometer and hard X-rays." *Microscopy Research and Technique* 72 (12).
- Rodriguez-Carvajal, J. **1993**. "Recent advances in magnetic structure determination by neutron powder diffraction." *Physica B: Condensed Matter* 192 (1-2).
- Romano, M., Bravin, A., Mittone, A., Eckhardt, A., Barbone, G. E., Sancey, L., Dinkel, J., Bartzsch, S., Ricke, J., Alunni-Fabbroni, M., Hirner-Eppeneder,

- H., Karpov, D., Giannini, C., Bunk, O., Bouchet, A., Ruf, V., Giese, A., Coan, P. **2021a**. "A Multi-Scale and Multi-Technique Approach for the Characterization of the Effects of Spatially Fractionated X-ray Radiation Therapies in a Preclinical Model." *Cancers* 13 (19).
- Romano, M., Bravin, A., Wright, M. D., Jacques, L., Miettinen, A., Hlushchuk, R., Dinkel, J., Bartzsch, S., Laissue, J. A., Djonov, V., Coan, P. **2021b**. "X-Ray Phase Contrast 3D Virtual Histology: Evaluation of Lung Alterations After Microbeam Irradiation." *International Journal of Radiation Oncology, Biology, Physics*.
- Rong, Y., Durden, D. L., Van Meir, E. G. **2006**. "'Pseudopalisading' Necrosis in Glioblastoma: A Familiar Morphologic Feature That Links Vascular Pathology, Hypoxia, and Angiogenesis." *Journal of Neuropathology & Experimental Neurology*.
- Röntgen, W. C. **1895**. "Über eine neue Art von Strahlen. Vorläufige Mittheilung." *Sitzungsberichte der Physikalisch-Medizinischen Gesellschaft zu Würzburg*.
- Rose, P. W. **2009**. "What is the value of routine follow-up after diagnosis and treatment of cancer?" *British Journal of General Practice* 59 (564).
- Rousseeuw, P. J. **1987**. "Silhouettes: a graphical aid to the interpretation and validation of cluster analysis." (*Journal of Computational and Applied Mathematics*) 20.
- Russo, P. **2017**. *Handbook of X-ray Imaging Physics and Technology*. CRC Press Taylor & Francis Group.
- Sacomano, M., Albers, J., Tromba, G., Dobrivojevic Radmilovic, M., Gajovic, S., Alvesa, F. and Dullina, C. **2018**. "Synchrotron inline phase contrast uCT enables detailed virtual histology of embedded soft-tissue samples with and without staining." *Journal of Synchrotron Radiation* 25.
- Sadaghiani, M. S., Sheikhabaei, S., Rowe, S. P., Pomper, M. G., Solnes, L. B. **2021**. "Cellular and Molecular Imaging with SPECT and PET in Brain Tumors." *Radiologic Clinics of North America* 59 (3).

- Sápi, J., Kovács, L., Drexler, D. A., Kocsis, P., Gajári, D., Sápi, Z. **2015**. "Tumor Volume Estimation and Quasi-Continuous Administration for Most Effective Bevacizumab Therapy." *PLoS ONE* 10 (11).
- Sarikaya, I. **2015**. "PET studies in epilepsy." *American Journal of Nuclear Medicine and Molecular Imaging* 5 (5).
- Sarwas, G., Skoneczny, S. **2015**. *Processing & Communications Challenges* 6. Springer.
- Sayers, Z., Avsar, B., Cholak, E., Karmous, I. **2017**. "Application of advanced X-ray methods in life sciences." *Biochimica et Biophysica Acta* 1861.
- Scherrer, P. **1918**. "Bestimmung der Grösse und der inneren Struktur von Kolloidteilchen mittels Röntgenstrahlen." (Nachrichten von der Gesellschaft der Wissenschaften, Göttingen).
- Schindelin, J., Arganda-Carreras, I., Frise, E., Kaynig, V., Longair, M., Pietzsch, T., Preibisch, S., Rueden, C., Saalfeld, S., Schmid, B., Tinevez, J. Y., White, D. J., Hartenstein, V., Eliceiri, K., Tomancak, P. and Cardona, A. **2010**. "Fiji: an open-source platform for biological-image analysis." *Nature Methods* 9.
- Schültke, E., Bayat, S., Bartzsch, S., Bräuer-Krisch, E., Djonov, V., Fiedler, S., Fernandez-Palomo, C., Jaekel, F., Pelliccioli, P., Trappetti, V., Hildebrandt, G. **2021**. "A mouse model for microbeam radiotherapy of the lung." *International Journal of Radiation Oncology, Biology, Physics*.
- Schulz, G., Weitkamp, T., Zanette, I., Pfeiffer, F., Beckmann, F., David, C., Rutishauser, S., Reznikova, E., Müller, B. **2010**. "High-resolution tomographic imaging of a human cerebellum: comparison of absorption and grating-based phase contrast." *Journal of the Royal Society, Interface* 7 (53).
- Schulze, R., Heil, U., Groß, D., Bruellmann, D. D., Dranischnikow, E., Schwanecke, U. and Schoemer, E. **2011**. "Artefacts in CBCT: a review." *Dentomaxillofacial Radiology* 40.
- Schuster, D. P., Kovacs, A., Garbo, J. and Piwnica-Worms, D. **2004**. "Recent Advances in Imaging the Lungs of Intact Small Animals." *American Journal of Respiratory Cell and Molecular Biology* 30.

- Serduc, R., Christen, T., Laissue, J. A., Fario, R., Bouchet, A., van der Sanden, B., Segebarth, C., Bräuer-Krisch, E., Le Duc, G., Bravin, A. **2008**. "Brain tumor vessel response to synchrotron microbeam radiation therapy: a short-term in vivo study." *Physics in Medicine & Biology* 53.
- Serduc, R., Bouchet, A., Bräuer-Krisch, E., Laissue, J. A., Spiga, J., Sarun, S., Bravin, A., Fonta, C., Renaud, L., Boutonnat, J., Siegbahn, E. A., Estève, F. and Le Duc, G. **2009**. "Synchrotron microbeam radiation therapy for rat brain tumor palliation—influence of the microbeam width at constant valley dose." *Physics in Medicine and Biology* 54.
- Serduc, R., Berruyer, G., Brochard, T., Renier, M., and Nemoz, C. **2010**. "In vivo pink-beam imaging and fast alignment procedure for rat brain lesion microbeam radiation therapy." *Journal of Synchrotron Radiation* 17.
- Sezgin, Ö. S., Kayıpmaz, S., Sahin, B. **2013**. "The Effect of Slice Thickness on the Assessment of Bone." *Journal of Digital Imaging* 26.
- Shovkun, V. Y. and Kumakhov, M. A. **2006**. *Phase contrast imaging with micro focus X-ray tube*. Vol. 5943. Proceedings of SPIE.
- Siegel, R., DeSantis, C., Jemal, A. **2014**. "Colorectal cancer statistics, 2014." *CA: A Cancer Journal for Clinicians* 64 (2).
- Sijbers, J. and Postnov, A. **2004**. "Reduction of ring artefacts in high resolution micro-CT reconstructions." *Physics in Medicine and Biology* 49 (14).
- Slatkin, D. N., Spanne, P., Dilmanian, F. A., Sandborg, M. **1992**. "Microbeam radiation therapy." *Medical Physics* 19 (6).
- Slatkin, D. N., Spanne, P., Dilmanian, F. A., Gebbers, J. O., Laissue, J, A. **1995**. "Subacute neuropathological effects of microplanar beams of x-rays from a synchrotron wiggler." *Proceedings of the National Academy of Sciences* 92 (19).
- Snigirev, A., Snigireva, I., Kohn, V., Kuznetsov, S., Schelokov, I. **1995**. "On the possibilities of X-ray phase contrast microimaging by coherent high-energy synchrotron radiation." *Review of Scientific Instruments* 66.

- Spiga, J., Siegbahn, E. A., Bräuer-Krisch, E., Randaccio, P., Bravin, A. **2007**. "The GEANT4 toolkit for microdosimetry calculations: Application to microbeam radiation therapy (MRT)." *Medical Physics* 34 (11).
- Srinivasan, K. G., Ramprabanth, S., Ushanandhini, K. P., Srividya, S., Praveen Kumar, M. **2010**. "Radiation-Induced Mineralizing Microangiopathy in a Case of Recurrent Craniopharyngioma A Case Report." *The Neuroradiology Journal* 32.
- Stampanoni, M., Groso, A., Isenegger, A., Mikuljan, G., Chen, Q., Bertrand, A., Henein, S., Betemps, R., Frommherz, U., Böhler, P., Meister, D., Lange, M., Abela, R. **2006**. "Trends in synchrotron-based tomographic imaging: the SLS experience." *Developments in X-Ray Tomography V, Proceedings of the Society of Photo-Optical Instrumentation Engineers (Spie)* 6318.
- Stampanoni, M., Groso, A., Isenegger, A., Mikuljan, G., Chen, Q., Meister, D., Lange, M., Betemps, R., Henein, S. and Abela, R. **2007**. "TOMCAT: A beamline for Tomographic Microscopy and Coherent rAdiology experimenTs." *AIP Conference Proceedings* 879.
- Stampanoni, M., Wang, Z., Thuring, T., David, C., Roessl, E., Trippel, M., Kubik-Huch, R. A., Singer, G., Hohl, M. K. and Hauser, N. **2011**. "The first analysis and clinical evaluation of native breast tissue using differential phase-contrast mammography." *Investigative Radiology* 46 (12).
- Stevenson, A. W., Crosbie, J. C., Hall, C. J., Häusermann, D., Livingstone, J. and Lye, J. E. **2017**. "Quantitative characterization of the X-ray beam at the Australian Synchrotron Imaging and Medical Beamline (IMBL)." *Journal of Synchrotron Radiation* 24.
- Stokes, A. R., Wilson, A. J. C., Bragg, W. L. **1942**. "A method of calculating the integral breadths of Debye-Scherrer lines." (Proceedings of the Cambridge Philosophical Society) 38 (3).
- Sullivan, R., Alatisé, O. I., Anderson, B. O., Audisio, R., Autier, P., Aggarwal, A., Balch, C., Brennan, M. F., Dare, A., D'Cruz, A. et al. **2015**. "Global cancer surgery: delivering safe, affordable, and timely cancer surgery." *The Lancet Oncology* 16 (11).

- Sung, H., Ferlay, J., Siegel, R. L., Laversanne, M., Soerjomataram I., Jemal, A., Bray, F. **2021**. “Global cancer statistics 2020: GLOBOCAN estimates of incidence and mortality worldwide for 36 cancers in 185 countries.” *CA: A Cancer Journal for Clinicians*.
- Suzuki, S., Nishio, S., Takata, K., Morioka, T., and Fukui, M. **2000**. “Radiation-Induced Brain Calcification: Paradoxical High Signal Intensity in T1-Weighted MR Images.” *Acta Neurochirurgica* 142.
- Swan, M. S., Piccolroaz, A., Bigoni, D. **2017**. “Application of tomographic reconstruction techniques for density analysis of green bodies.” *Ceramics International* 43 (1).
- Tanaka, T., Honda, C., Matsuo, S., Noma, K., Oohara, H., Nitta, N., Ota, S., Tsuchiya, K., Sakashita, Y., Yamada, A., Yamasaki, M., Furukawa, A., Takahashi, M., Murata, K. **2005**. “The First Trial of Phase Contrast Imaging for Digital Full-Field Mammography Using a Practical Molybdenum X-Ray Tube.” *Investigative Radiology* 40 (7).
- Tanaka J, Nagashima M, Kido K, Hoshino Y, Kiyohara J, Makifuchi C, Nishino S, Nagatsuka S, Momose A. **2013**. “Cadaveric and in vivo human joint imaging based on differential phase contrast by X-ray Talbot-Lau interferometry.” *Zeitschrift für Medizinische Physik* 23 (3).
- Taylor, A., and Powell, M. E. B. **2004**. “Intensity-modulated radiotherapy – what is it?” *Cancer Imaging* 4.
- Teague, M. R. **1983**. “Deterministic phase retrieval: a Green’s function solution.” *Journal of the Optical Society of America* 73 (11).
- Töpperwien, M., van der Meer, F., Stadelmann, C. and Salditta, T. **2018a**. “Three-dimensional virtual histology of human cerebellum by X-ray phase-contrast tomography.” *Proceedings of the National Academy of Sciences of the United States of America* 115 (27).
- Töpperwien, M., Gradl, R., Keppeler, D., Vassholz, M., Meyer, A., Hessler, R., Achterhold, K., Gleich, B., Dierolf, M., Pfeiffer, F., Moser, T. and Salditt, T. **2018b**. “Propagation-based phase-contrast x-ray tomography of cochlea using a compact synchrotron source.” *Scientific Reports* 8.

- Turkheimer, F. E., Rizzo, G., Bloomfield, P. S., Howes, O., Zanotti-Fregonara, P., Bertoldo, A., Veronese, M. **2015**. "The methodology of TSPO imaging with positron emission tomography." *Biochemical Society Transactions* 43 (4).
- Van Heekeren, J., Kostenko, A., Hanashima, T., Yamada, H., Stallinga, S., Offerman, S. E. and Van Vliet, L. J. **2011**. "Characterization of an x-ray phase contrast imaging system based on the miniature synchrotron MIRRORCLE-6X." *Medical Physics* 38 (9).
- van Herk, M. **2007**. "Different Styles of Image-Guided Radiotherapy." *Seminars in Radiation Oncology* 17 (4).
- van Rikxoort, E. M., van Ginneken, B. **2013**. "Automated segmentation of pulmonary structures in thoracic computed tomography scans: a review." *Physics in Medicine and Biology* 58.
- Vanna, R., Morasso, C., Marcinnó, B., Piccotti, F., Torti, E., Altamura, D., Albasini, S., Agozzino, M., Villani, L., Sorrentino, L., Bunk, O., Leporati, F., Giannini, C. and Fabio Corsi, F. **2020**. "Raman Spectroscopy Reveals That Biochemical Composition of Breast Microcalcifications Correlates with Histopathologic Features." *Cancer Research* 8.
- Vidavsky, N, Kunitake, J. A. M. R. and Estroff, L. A. **2021**. "Multiple Pathways for Pathological Calcification in the Human Body." *Advanced Healthcare Materials* 10.
- Voskrebenezv, A., Vogel-Claussen, J. **2020**. "Proton MRI of the Lung: How to Tame Scarce Protons and Fast Signal Decay." *Journal of Magnetic Resonance Imaging*.
- Wagner, A., Aurich, M., Sieber, N., Stoessel, M., Wetzels, W.-D., Schmuck, K., Lohmann, M., Reime, B., Metge, J., Coan, P., Bravin, A., Arfelli, F., Rigon, L., Menk, R.-H., Heitner, G., Irving, T., Zhong, Z., Muehleman, C., Mollenhauer, J. A. **2005**. "Options and limitations of joint cartilage imaging: DEI in comparison to MRI and sonography." *Nuclear Instruments and Methods in Physics Research Section A: Accelerators, Spectrometers, Detectors and Associated Equipment* 548 (1-2).

- Wang, S., Liu, Y., Feng, Y., Zhang, J., Swinnen, J., Li, Y. and Ni, Y. **2019a**. “A Review on Curability of Cancers: More Efforts for Novel Therapeutic Options Are Needed.” *Cancers (Basel)* 11 (11).
- Wang, S., Zan, G., Wang, Q., Liu, S. **2019b**. “Preliminary demonstration of flexible dual-energy X-ray phase-contrast imaging.” *Optical Engineering* 58 (11).
- Weibel, E. R. **1984**. *Morphometric and stereological methods in respiratory physiology including fixation techniques (Techniques in respiratory physiology)*. Elsevier.
- Weinhausen, B., Nolting, J.-F., Olendrowitz, C., Langfahl-Klabes, J., Reynolds, M., Salditt, T., Köster, S. **2012**. “X-Ray Nano-Diffraction on Cytoskeletal Networks.” *New Journal of Physics* 14.
- Weitkamp, T., Diaz, A., David, C., Pfeiffer, F., Stampanoni, M., Cloetens, P. and Ziegler, E. **2005**. “X-ray phase imaging with a grating interferometer.” *Optics Express* 13 (16).
- WHO, World Health Organization. **2018**. “Global health estimates 2016: deaths by cause, age, sex, by country and by region, 2000–2016.”
- Wiedemann, H. **2015**. *Particle Accelerator Physics*. Springer, Cham.
- Wild, C. P., Weiderpass, E., Stewart, B. W. **2020**. *World Cancer Report: Cancer Research for Cancer Prevention*. Lyon, France: International Agency for Research on Cancer. <http://publications.iarc.fr/586>.
- Wilde, F., Ogurreck, M., Greving, I., Hammel, J. U., Beckmann, F., Hipp, A., Lottermoser, L., Khokhriakov, I., Lytaev, P., Dose, T., Burmester, H., Müller, M. and Schreyer, A. **2016**. “Micro-CT at the Imaging Beamline P05 at PETRA III.” *AIP Conference Proceedings* 1741.
- Wilkins, S. W., Gureyev, T. E., Gao, D., Pogany, A. and Stevenson, A. W. **1995**. “Phase-contrast imaging using polychromatic hard X-rays.” *Nature* 384.
- Wilkins, S. W., Gureyev, T. E., Gao, D., Pogany, A. & Stevenson, A. W. **1996**. “Phase-contrast imaging using polychromatic hard X-rays.” *Nature*.
- Willer, K., Fingerle, A., Noichl, W., De Marco, F., Frank, M., Urban, T., Schick, R., Gustschin, A., Gleich, B., Herzen, J., Koehler, T., Yaroshenko, A., Pralow, T., Zimmermann, G., Renger, B., Sauter, A., Pfeiffer, D., Makowski, M., Rummeny, E., Grenier, P., Pfeiffer, F. **2021**. “X-ray Dark-Field Chest

- Imaging can Detect and Quantify Emphy-sema in COPD Patients." *medRxiv* 2021.01.15.21249798.
- Witthayanuwat, S., Pesee, M., Supaadirek, C., Supakalin, N., Thamronganantasakul, K., Krusun, S. **2018**. "Survival Analysis of Glioblastoma Multiforme." *Asian Pacific Journal of Cancer Prevention* 19 (9).
- Wright, M. D., Romanelli, P., Bravin, A., Le Duc, G., Bräuer-Krisch, E., Requardt, H., Bartzsch, S., Hlushchuk, R., Laissue, J. A., Djonov, V. **2021**. "Non-conventional Ultra-High Dose Rate (FLASH) Microbeam Radiotherapy Provides Superior Normal Tissue Sparing in Rat Lung Compared to Non-conventional Ultra-High Dose Rate (FLASH) Radiotherapy." *Cureus* 13 (11).
- Xu, T., Zhang, X., Zhang, S, Liu, C., Fu, W., Zeng, C. and Chen, Y. **2020**. "Imaging features and prognostic value of 18F-FDG PET/CT detection of soft-tissue metastasis from lung cancer: a retrospective study." *BMC Cancer* 20 (596).
- Yaroshenko, A., Hellbach, K., Yildirim, A. Ö., Conlon, T. M., Fernandez, I. E., Bech, M., Velroyen, A., Meinel, F. G., Auweter, S., Reiser, M., Eickelberg, O., Pfeiffer, F. **2015**. "Improved In vivo Assessment of Pulmonary Fibrosis in Mice using X-Ray Dark-Field Radiography." *Scientific reports* 5.
- Yoshioka, H., Kadono, Y., Kim, Y. T., Oda, H., Maruyama, T., Akiyama, Y., Mimura, T., Tanaka, J., Niitsu, M., Hoshino, Y., Kiyohara, J., Nishino, S., Makifuchi, C., Takahashi, A., Shinden, Y., Matsusaka, N., Kido, K., Momose, A. **2020**. "Imaging evaluation of the cartilage in rheumatoid arthritis patients with an x-ray phase imaging apparatus based on Talbot-Lau interferometry." *Scientific Reports* 10.
- Zeman, W., Curtis, H. and Baker, C. **1961**. "Histopathologic Effect of High-Energy-Particle Microbeams on the Visual Cortex of the Mouse Brain." *Radiation Research* 15 (4).
- Zhou, S.-A., Brahme, A. **2008**. "Development of phase-contrast X-ray imaging techniques and potential medical applications." *Physica Medica* 24.
- Zhou, T., Wang, H., Connolley, T., Scott, S., Baker, N. and Sawhney, K. **2018**. "Development of an X-ray imaging system to prevent scintillator

degradation for white synchrotron radiation." *Journal of Synchrotron Radiation* 25 (3).

Annexes

Annex 1: An ideal protocol for preclinical radiotherapy follow-up

1. RT protocols conceptualization:
 - a. Definition of the irradiation geometries and dose levels (seamless and/or spatially fractionated);
 - b. MCS for deciding the most appropriate doses to be delivered on the basis of the peak and valley dose values for MRT and MB. Dose maps are also needed to study the dose spread over the animal body;
 - c. Organization of the animals among the different RT session. It is convenient to distribute animals of each group over separate RT sessions. In this way, problems during one experimental session will not hamper the overall study;
 - d. Organization of the experimental sessions for the application of the different analysis techniques.
2. RT preparation:
 - a. Tumour or other animal model cells culture and implant (if required by the study). The implant is performed at D0;
 - b. Pre-RT *in-vivo* MRI session for checking the status of the animals and the progression of the induced disease (D9);
 - c. Recalibration of the irradiation protocol based on MRI images (e.g. adapting the beamlets size and c-t-c distance to the tumour sizes).
3. RT experiment:
 - a. Dosimetry procedures (as described in section 3.2.2);
 - b. Animal anaesthesia, positioning and image-guided irradiation (see section 3.2.3);
4. Animal follow-up:
 - a. Daily cares and weekly weight check;

- b. *In-vivo* MRI sessions at different time points post-treatment.
5. Samples collection:
 - a. Animal sacrifice and organ extraction in a standardized way;
 - b. Sample fixation in a solution of 4% PFA for at least one week;
 - c. PFA replacement with ethanol baths of increasing concentrations (e.g. for brains) or sample inclusion in paraffin blocks (see section 4.1.1). Ethanol and other liquid solutions are viable options for storing samples for a limited period of time.
6. XPCI-CT experiments (see section 4.2):
 - a. Samples to be either imaged using 86% ethanol as a liquid or buffer or embedded in paraffin blocks with smoothed edges;
 - b. Full-organ CT and imaging of specific ROIs at sub-micron resolution.
7. Histology and immunohistochemistry analysis (see section 4.3): XPCI-CT can act as a guidance tool to virtually navigate through samples and help deciding the orientation and position of the cutting.
8. SAXS/WAXS and XRF experiment (see section 4.4): serial 80 μm - thick slices in Ultralene sachets;
9. Data analysis (see Chapter 5):
 - a. XPCI-CT datasets inspection, findings validation by correlation with histology and immunohistochemistry, segmentation and quantification of features of interest;
 - b. SAXS/WAXS and XRF for chemical and structural classification.

Annex 2: List of publications produced within this Ph.D. work

Peer-reviewed articles:

- **Romano, M.**, Bravin, A., Mittone, A., Eckhardt, A., Barbone, G. E., Sancey, L., Dinkel, J., Bartzsch, S., Ricke, J., Alunni-Fabbroni, M., Hirner-Eppeneder, H., Giannini, C., Bunk, O., Bouchet, A., Ruf, V., Giese, A., Coan, P. 2021 “A multiscale and multi-technique approach for the characterization of the effects of spatially fractionated X-ray radiation therapies in a preclinical model” *Cancers*, 19(13). <https://doi.org/10.3390/cancers-13194953>;
- **Romano, M.**, Bravin, A., Wright, M. D., Jacques, L., Miettinen, A., Hlushchuk, R., Dinkel, J., Bartzsch, S., Laissue, J. A., Djonov, V., Coan, P. 2021 “X-ray Phase Contrast 3D virtual histology: evaluation of lung alterations after micro-beam irradiation” DOI: 10.1016/j.ijrobp.2021.10.009;
- Mittone, A., Fardin, L., Di Lillo, F., Fratini, M., Requardt, H., Mauro, A., Homs-Regajo, R., Douissard, P., Barbone, G., Stroebel, J., **Romano, M.**, Massimi, L., Begani-Provinciali, G., Palermo, F., Bayat, S., Cedola, A., Coan, P., Bravin, A. 2020. “Multiscale pink-beam microCT imaging at the ESRF-ID17 biomedical beamline” *Journal of Synchrotron Radiation*, 27(5). doi 10.1107/S160057752000911X.

Submitted articles:

- Barbone, G. E., Bravin, A., Mittone, A., Alexandra Pacureanu, A., Mascio, G., Paola Di Pietro, P., Kraiger, M. J., Marina Eckermann, M., **Romano, M.**, Martin Hrabě de Angelis, M., Cloetens, P., Bruno, V., Battaglia, G., Paola Coan, P. “A multiscale 3D method for post-mortem detection and quantification of cellular neurodegeneration in experimental Alzheimer’s disease”.

Annex 3: list of oral talk and poster presentations related to this Thesis work

Oral talks:

- Italian Synchrotron Radiation Society meeting 2019: *“High resolution X-ray Phase Contrast Imaging for studying the effects of novel radiotherapies”*;
- European Congress of Radiology 2021: *“Micro-beam vs broad-beam radiation-driven effects on lungs studied by X-ray phase contrast 3D virtual histology”*;
- Italian Synchrotron Radiation Society meeting 2021: *“Micro-beam vs broad-beam radiation-driven effects on lungs studied by X-ray phase contrast 3D virtual histology”*.

Poster presentations:

- 9th bioMedical Applications of Synchrotron Radiation 2018 conference: *“High resolution X-ray phase contrast imaging for studying MRT effects on 9L glioblastoma in rats”* (best poster prize award);
- ESRF student day: *“High resolution X-ray phase contrast imaging for studying MRT effects on 9L glioblastoma in rats”*;
- The IEE 2018 Nuclear Science Symposium and Medical Imaging Conference: *“Experimental benchmarking of a Geant4 application for radiation therapy dosimetry using uniform monochromatic X-ray beams”*, Speaker: J. Spiga;
- ESRF User Meeting 2019: *“High resolution X-ray phase contrast imaging for studying MRT effects on 9L glioblastoma in rats”*;
- European Congress of Radiology 2020: *“High resolution X-ray Phase Contrast Imaging for studying the effects of novel radiotherapies”*.